

**Titre:** Towards Understanding Stall Cells and Transonic Buffet Cells  
Title:

**Auteur:** Frédéric Plante  
Author:

**Date:** 2020

**Type:** Mémoire ou thèse / Dissertation or Thesis

**Référence:** Plante, F. (2020). Towards Understanding Stall Cells and Transonic Buffet Cells  
Citation: [Ph.D. thesis, Polytechnique Montréal]. PolyPublie.  
<https://publications.polymtl.ca/5541/>

 **Document en libre accès dans PolyPublie**  
Open Access document in PolyPublie

**URL de PolyPublie:** <https://publications.polymtl.ca/5541/>  
PolyPublie URL:

**Directeurs de  
recherche:** Éric Laurendeau, & Julien Dandois  
Advisors:

**Programme:** Génie mécanique  
Program:

**POLYTECHNIQUE MONTRÉAL**  
affiliée à l'Université de Montréal  
ET  
**ÉCOLE DOCTORALE N°391 : SCIENCES MÉCANIQUES, ACOUSTIQUE,  
ÉLECTRONIQUE ET ROBOTIQUE DE PARIS**  
**SORBONNE UNIVERSITÉ**

**Towards understanding stall cells and transonic buffet cells**

**FRÉDÉRIC PLANTE**  
Département de génie mécanique

Thèse présentée en vue de l'obtention du diplôme de *Philosophiæ Doctor*  
Génie mécanique

Décembre 2020

**POLYTECHNIQUE MONTRÉAL**  
affiliée à l'Université de Montréal  
ET  
**ÉCOLE DOCTORALE N°391 : SCIENCES MÉCANIQUES, ACOUSTIQUE,  
ÉLECTRONIQUE ET ROBOTIQUE DE PARIS**  
**SORBONNE UNIVERSITÉ**

Cette thèse intitulée :

**Towards understanding stall cells and transonic buffet cells**

présentée par **Frédéric PLANTE**  
en vue de l'obtention du diplôme de *Philosophiæ Doctor*  
a été dûment acceptée par le jury d'examen constitué de :

Jérôme **VÉTEL**, président  
Éric **LAURENDEAU**, membre et directeur de recherche  
Julien **DANDOIS**, membre et directeur de recherche  
Philippe **SPALART**, membre  
Jeffrey **CROUCH**, membre  
Daniella **RAVEH**, membre externe

## ACKNOWLEDGEMENTS

*The research presented in this thesis was realized in a joint project between the laboratory of Professor Éric Laurendeau at Polytechnique Montréal and the Département Aérodynamique, Aéroélasticité et Acoustique (DAAA) of the Office National d'Études et de Recherches Aérospatiales (ONERA). It was supported by the Natural Sciences and Engineering Research Council of Canada (NSERC/CRSNG) through the Alexander Graham Bell Canada Graduate Scholarship - Doctoral (CGS D) award. Computational resources were provided by ONERA HPC clusters, Compute Canada and the GENCI CINES facilities under the Grant DARI No.A0042A10423.*

To begin, I would like to thank my research director, Professor Éric Laurendeau with whom I have been working since 2015 through my master and Ph.D. studies. He always provided me with guidance to align my research project and space to explore my own path. He also opened great opportunities for me. I also want to thank my research director Julien Dandois for his ideas, the support he provided me and his interest throughout this research project. To both of you, thank you for the great opportunity which was this research project and your help in carrying it out.

I would also like to thank Denis Sipp and Samir Beneddine for their inputs and support for the stability analyses presented in this thesis. I am also grateful to the DAAA team at ONERA Meudon for their warm welcome and technical support. Coffee breaks were always a nice part of the day Simon, Edoardo, Ilias, Fulvio, Andrea, Maxime, Alan, Frédéric, Michel, Gerald, Antoine, Camille, ... thanks to you all.

I also want to acknowledge my colleagues and friends for many years at Polytechnique Montréal, Simon Bourgault-Côté, Matthieu Parenteau, Pierre Lavoie, Anthony Bouchard and the rest of the team which have come and gone through the years. Coffee breaks were a good occasion to have meaningful conversation about our research projects (and other topics I must say), sadly they no longer occur in the COVID-19 context. Your comments on this thesis were much welcomed.

Finally, I want to thank my parents, Lucie and Claude, who supported me since the beginning.

## RÉSUMÉ

L'enveloppe de vol des avions civils est contrainte par plusieurs phénomènes aérodynamiques. Parmi ceux-ci figurent le décrochage et le tremblement. Le décrochage est défini comme une perte de portance causée par la séparation de l'écoulement sur une voilure. Il survient le plus souvent à faible vitesse et à un angle d'attaque élevé, influençant donc les performances au décollage et à l'atterrissage. Le tremblement est quant à lui une vibration de la structure de l'appareil causée par des efforts aérodynamiques instationnaires. Plus spécifiquement, le tremblement transsonique est défini comme une instabilité aérodynamique causant une oscillation de la position de l'onde de choc sur une aile. Il se produit à haute vitesse, cause un chargement instationnaire et des vibrations, et limite la vitesse maximale de l'aéronef. Ces deux phénomènes nuisent au contrôle de l'appareil et doivent être évités. Cependant, le tremblement et le décrochage demeurent mal compris et difficiles à prédire. Pour ces raisons, les avionneurs utilisent des lois empiriques pour prédire ces limites de l'enveloppe de vol, qui sont par la suite vérifiées lors des tests en vol. Une meilleure compréhension de ces phénomènes permettrait donc de réduire les incertitudes sur leur prédiction et de réduire les marges par rapport aux limites de décrochage et de tremblement lors de la conception, et ainsi d'améliorer les performances des prochaines générations d'avions.

Le décrochage basse vitesse implique des dynamiques complexes, parmi lesquelles les cellules de décrochage. Ces dernières sont une variation de la position de la séparation d'une section en envergure de l'aile à l'autre. Elles sont associées à une structure en forme de champignon formée de tourbillons contrarotatifs. Des expériences réalisées sur des modèles s'étendant sur la largeur d'une soufflerie et des simulations sur des ailes infinies ont montré leur présence. Cela indique la présence d'une instabilité qui transforme l'écoulement bidimensionnel en un écoulement tridimensionnel. Dans le régime transsonique, le tremblement est caractérisé par une oscillation de la position de l'onde de choc le long de la corde causée par une interaction entre l'onde de choc et une couche limite décollée. La visualisation de l'écoulement sur des cas tridimensionnels montre la présence de structures formées par une variation de la position du choc le long de l'envergure. Ce phénomène a été nommé cellule de tremblement et présente une structure en forme de champignon similaire à celle qui est observée en condition basse vitesse. Cette observation mène à l'idée d'étudier les deux phénomènes avec les mêmes méthodes. Cette thèse vise l'amélioration de la compréhension du décrochage et du tremblement en étudiant ces cellules. L'hypothèse soutenant ce travail est que les cellules de décrochage et de tremblement sont en fait le même phénomène sous

deux régimes d'écoulement distincts.

Pour examiner cette hypothèse, les cellules sont d'abord caractérisées avec des calculs instationnaires des équations de Navier-Stokes en moyenne de Reynolds (URANS) et des simulations zonales des tourbillons décollés (ZDES). Des configurations formées par des ailes infinies sont sélectionnées afin d'exclure l'effet de la géométrie et des conditions aux limites sur la présence d'un écoulement tridimensionnel. Ces configurations sont obtenues en fermant le domaine de calcul avec des conditions de périodicité dans la direction de l'envergure. Ces simulations montrent la présence de cellules de décrochage et de tremblement. Ces dernières sont stationnaires pour le cas des ailes sans flèche et les cellules sont convectées dans la direction de l'envergure lorsqu'un angle de flèche est ajouté. La vitesse de cette convection est proportionnelle à la vitesse de l'écoulement en champ lointain, projetée dans la direction du bord d'attaque de l'aile. Le nombre de cellules augmente avec l'envergure. De plus, la visualisation des lignes de frottement pariétal montre une topologie d'écoulement en forme de champignon. Les simulations du décrochage sur les ailes sans flèche permettent d'obtenir des cellules de décrochage stationnaires. Dans le cas du tremblement, une instabilité bidimensionnelle est présente ce qui induit un écoulement instationnaire pour tous les angles de flèche. Cependant, cette étude n'exclut pas la possibilité d'observer des cellules de tremblement stationnaire. Ces résultats permettent de distinguer deux effets dominant le tremblement tridimensionnel. Le premier est l'instabilité de tremblement bidimensionnel classique qui survient à une fréquence constante, peu importe l'angle de flèche. Le second est une convection des cellules de tremblement avec une fréquence proportionnelle à l'angle de flèche. Cela explique la fréquence de tremblement plus élevé sur les avions civils que les cas bidimensionnels, puisque ces ailes ont un angle de flèche élevé.

Pour supporter l'hypothèse de base et proposer un modèle expliquant l'origine des cellules de décrochage et de tremblement, elles ont aussi été étudiées à l'aide d'analyses de stabilité globale. Ces analyses permettent de caractériser la transition entre une solution bidimensionnelle stationnaire vers un état instationnaire et/ou tridimensionnel dans le régime linéaire. La méthodologie utilisée dans cette étude suppose que les perturbations autour de l'état de base sont périodiques dans la direction de l'envergure afin de réduire le coût de calcul. Ces analyses montrent qu'un mode globalement instable est responsable de la transition d'un état bidimensionnel vers une solution tridimensionnelle. Ce mode a une fréquence nulle pour le cas de l'aile sans flèche, et a une fréquence d'oscillation pour le cas des ailes en flèche. Cette fréquence est cohérente avec celle des structures convectées aux vitesses trouvées dans les simulations URANS. Dans le cas du décrochage, la longueur d'onde de ces cellules est aussi

bien prédite. Ce faisant, la fréquence est aussi bien prédite. Cependant, les longueurs d'onde trouvées pour les cas de tremblement ne corroborent avec celles obtenues dans les simulations instationnaires. Toutefois, on observe que les simulations instationnaires bifurquent vers un état tridimensionnel en suivant la longueur d'onde présente dans les analyses de stabilité. Ainsi, des effets non linéaires sont probablement responsables du changement de longueur d'onde. On observe aussi que la présence de cellules de décrochage et de tremblement coïncide avec une pente négative de la relation entre le coefficient de portance et l'angle d'attaque des solutions utilisées comme champs de base pour les études de stabilité. Cela est aussi observé dans les calculs URANS où les solutions demeurent invariantes en envergure tant que cette pente est positive. Des analyses de stabilité sont aussi réalisées pour un cas à haut nombre de Reynolds et pour des nombres de Mach allant du régime subsonique au transsonique. Un mode tridimensionnel instable est trouvé pour tous les nombres de Mach et un dimensionnement par l'épaisseur de la séparation est appliqué avec succès pour comparer la longueur d'onde de ces modes.

Pour finir, un modèle non visqueux (surface portante) avec correction de viscosité est utilisé pour étudier les cellules de décrochage. Ce modèle est capable de reproduire les principales caractéristiques des cellules de décrochage, comme leur nombre sur une aile ayant un rapport d'aspect donné. Ce modèle prédit la présence de cellules dès que la pente de la portance selon l'angle d'attaque devient négative. Il permet aussi de penser que les cellules ne seront observées que pour des décrochages du bord de fuite, pour lesquels la séparation se propage progressivement du bord de fuite vers le bord d'attaque lorsque l'angle d'attaque augmente. Cette conclusion est faite puisqu'un décrochage de bord d'attaque est caractérisé par une perte soudaine de portance et que la plage d'angle d'attaques où la pente de la portance est négative est infiniment mince. Cette conclusion est pour un cas parfait et le comportement sur une géométrie complexe comme celle d'un avion devrait être plus complexe. Ce modèle basse fidélité permet d'obtenir des solutions aillant le même nombre de cellules que des expériences sur des ailes rectangulaires. Un point intéressant de ce modèle est le fait que les effets visqueux sont traités de façon macroscopique à travers une polaire de portance. Le modèle n'inclut aucune information sur la topologie de l'écoulement décollé. Pour cette raison, on peut conclure qu'une instabilité de la distribution de la circulation permet d'expliquer les cellules de décrochage, et par extension les cellules de tremblement puisqu'elles ont été reliées à une instabilité similaire.

Ensemble, ces résultats montrent que le tremblement bidimensionnel et tridimensionnel sont deux phénomènes différents. Ce dernier a plus de similarité avec l'instabilité causant

les cellules de décrochage qu'avec une instabilité entre l'onde de choc et la couche limite décollée. Il ne faudrait donc pas l'appeler tremblement tridimensionnel, mais plutôt cellules de décrochage. Ces résultats montrent aussi que les cellules de décrochage/tremblement sont reliées à une instabilité de la circulation sur l'aile (cf. théorie de la ligne portante). Les idées et les méthodes présentées dans cette thèse pourront être utilisées dans un cadre industriel pour améliorer la modélisation de ces phénomènes, et améliorer l'efficacité et la sécurité du transport aérien.



## ABSTRACT

The flight envelope of civil aircraft is bounded by several complex aerodynamic phenomena, of those the stall and the buffeting of lifting surfaces. Stall is defined as a loss of lift caused by flow separation. This usually occurs at low speed and high angle of attack, thus influencing the take-off and landing performances. Buffeting is a vibration of the airframe caused by unsteady aerodynamic loads. More specifically, the transonic buffet phenomenon causes an oscillation of the shock position on an aircraft wing. It occurs at high speed, induces unsteady loads and vibrations, and limits the maximum speed of aircraft. Both phenomena are detrimental to aircraft handling and must be avoided. However, transonic buffet and stall remain misunderstood and difficult to predict. For these reasons, aircraft manufacturer use empirical relations to predict these flight envelope limits, which are later verified in flight tests. Improving the comprehension of these phenomena will allow to reduce the uncertainty on the buffet and stall margins in the design stages and thus to improve the performances of future aircraft.

Low speed stall involves complex dynamics, of which the stall cells. The latter are a variation of the chordwise separation point from one spanwise section to the other. This is associated with a complex vortical flow structure which has a mushroom shape. Experiments on wings spanning from one wind tunnel wall to the other and idealized infinite wing numerical simulations, which are essentially two-dimensional configurations, show their occurrence. This points to a flow instability which causes the two-dimensional separated flow to become three-dimensional. On the other hand, transonic buffet is characterized by an oscillation of the shock wave position caused by an interaction between the shock wave and a shock induced flow separation. Flow visualizations show three-dimensional flow features in the form of a variation of the chordwise shock position between spanwise wing stations (i.e. buffet cells). These buffet cells have a mushroom shape similar to the stall cells, which leads to the idea of studying both phenomena with the same methods. This thesis aims to improve our understanding of stall and buffet by studying these cells. The primary hypothesis on which this work is based is that the stall cells and the buffet cells are in fact the same flow phenomenon in two different flow regimes.

To assess this hypothesis, the behavior of the cells is first characterized using Unsteady Reynolds Averaged Navier-Stokes (URANS) simulations and Zonal Detached Eddy Simulations (ZDES). Infinite swept wing configurations are selected to exclude influence of the

geometry and boundary conditions on the occurrence of three-dimensional flow features. Such configurations are achieved numerically by closing the computational domain with periodicity boundary conditions in the wing spanwise direction. Results from these simulations exhibit similar behavior between the stall cells and the buffet cells. Both are stationary for unswept wings and convected in the spanwise direction when the wings are swept. The convection speed is proportional to the magnitude of the projection of the free stream velocity along the leading edge direction. The number of buffet and stall cells increases with the span of the computational domain. Moreover, visualizations of the skin friction lines in both flow conditions exhibit a similar mushroom shape flow topology. In the simulation of the subsonic stall, fully converged steady solutions with stall cells are obtained on the unswept wings. In the case of the transonic buffet, the classic two-dimensional buffet instability is still present and causes the flow to be unsteady, even on unswept wings. However, the present study does not exclude the possibility to observe steady buffet cells on unswept wings. These results also allow to clearly distinguish between two dominant features of the three-dimensional buffet phenomenon. The first one is a two-dimensional buffet instability which occurs at a constant frequency, no matter the sweep angle. The second one is the convection of buffet cells at a frequency proportional to the sweep angle. This explains why the buffet of civil aircraft wings has a higher frequency than the two-dimensional buffet instability, since these wings are highly swept.

In order to support the primary hypothesis and to work towards a model explaining the stall cell and buffet cell phenomena, they are also studied using global linear stability analyses about steady two-dimensional base-flows. These analyses allow to study the bifurcation from the two-dimensional base-flows towards an unsteady and/or a three-dimensional behavior, in the linear regime. The methodology used in this study assumes the instability will be periodic in the spanwise direction to reduce the computational cost. These analyses show that a globally unstable mode is responsible for a transition from the two-dimensional state towards a three-dimensional one. This mode is non-oscillatory for unswept wing and has a non-zero frequency for swept wing cases. This frequency is consistent with the one of flow structures convected at the speed observed in the URANS simulations. In the case of the subsonic stall, the wavelength of the stall cells is correctly predicted by the stability analyses and so is the frequency. In the case of the transonic buffet, the wavelengths found in the stability analyses do not match the one of the URANS simulations. However, it is found that the URANS simulations indeed diverge from the two-dimensional state with the wavelength of the stability analysis. Hence, nonlinear effects are probably responsible for this shift in the wavelength. Finally, it is observed that stall cells and buffet cells occur when the slope of the

lift versus angle of attack curve of the two-dimensional steady base-flows becomes negative (i.e. onset of the stall). This is observed in the results of the stability analyses as well as in the URANS simulations where the flow stays spanwise invariant as long as this slope stays positive. These analyses are also carried out for a case at high Reynolds number and a three-dimensional unstable mode is identified for every Mach number from the incompressible to the transonic regime. Moreover, a scaling of the spanwise wavelength of the mode by the separation thickness is successfully used to link the results from all these Mach numbers, at least near the onset of the three-dimensional instability.

Finally, the behavior of a simple inviscid model (lifting surface) coupled with a viscous correction is studied to explain the stall cell phenomenon. This model is able to reproduce the main characteristics of the stall cell such as the number of cells over a wing of a given aspect ratio. This model predicts the onset of stall cells as soon as the slope of the lift versus angle of attack curve is negative. This model also allows to infer that the stall cells will only be observed for a trailing edge type of stall where the flow separation progressively moves from the trailing edge to the leading edge of the wing as the angle of attack is increased. This conclusion is made since a leading edge type of stall results in a sharp reduction of the lift in the post stall regime. Hence, the range of angles of attack for which the lift slope is negative is infinitely small and the entire wing will jump from a two-dimensional attached flow to a two-dimensional separated flow. Of course, this conclusion is for an idealized case and the flow behavior is expected to be more complex for real aircraft applications. An interesting point is the fact that the viscous effects are treated in a macroscopic way in the inviscid model. In fact, this model contains no information about the flow topology of the separated flow, it only takes into account the lift versus angle of attack polar of an airfoil. For this reason we can conclude that an instability in the lifting line or lifting surface theory can explain the stall cells and by extension the buffet cells since they have been shown to relate to similar instabilities.

Together, these results shed light on the fact that the two-dimensional and three-dimensional buffet are two different phenomena, the latter being more akin to the stall cells than to a shock induced separation instability. They also emphasize that the stall/buffet cells are linked to an instability of the circulation distribution on a wing (i.e. lifting line theory). The ideas and methods put forward in the thesis can be used in the industry towards more accurate modeling of these phenomena, and to increase air transport efficiency and safety.

## TABLE OF CONTENTS

ACKNOWLEDGEMENTS . . . . .	iii
RÉSUMÉ . . . . .	vii
ABSTRACT . . . . .	x
TABLE OF CONTENTS . . . . .	x
LIST OF TABLES . . . . .	xiv
LIST OF FIGURES . . . . .	xv
LIST OF APPENDICES . . . . .	xxii
LIST OF SYMBOLS AND ABBREVIATIONS . . . . .	xxiii
CHAPTER 1 INTRODUCTION . . . . .	1
1.1 Context . . . . .	1
1.2 Computational Fluid Dynamics . . . . .	2
1.2.1 Numerical simulation of steady and unsteady flow . . . . .	3
1.2.2 Modal analyses . . . . .	8
1.3 Subsonic stall . . . . .	12
1.3.1 Two-dimensional stall classification . . . . .	12
1.3.2 Stall cells . . . . .	13
1.3.3 Partial conclusion . . . . .	20
1.4 Transonic buffet . . . . .	21
1.4.1 Two-dimensional buffet . . . . .	21
1.4.2 Three-dimensional buffet . . . . .	28
1.4.3 Buffet models . . . . .	35
1.5 Research objectives . . . . .	37
1.6 Outline . . . . .	38
CHAPTER 2 ARTICLE 1 : SIMILARITIES BETWEEN CELLULAR PATTERNS OCCURRING IN TRANSONIC BUFFET AND SUBSONIC STALL	40
2.1 Introduction . . . . .	41

2.2	Numerical method . . . . .	45
2.3	Numerical results . . . . .	48
2.3.1	Transonic buffet . . . . .	48
2.3.2	Subsonic stall . . . . .	61
2.4	Conclusion . . . . .	69
CHAPTER 3 ZONAL DETACHED EDDY SIMULATIONS . . . . .		70
3.1	Numerical methods . . . . .	70
3.2	Two-dimensional buffet . . . . .	71
3.3	Three-dimensional buffet . . . . .	72
3.4	Conclusion . . . . .	77
CHAPTER 4 ARTICLE 2 : LINK BETWEEN SUBSONIC STALL AND TRAN- SONIC BUFFET ON SWEPT AND UNSWEPT WINGS: FROM GLOBAL STABILITY ANALYSIS TO NONLINEAR DYNAMICS .		79
4.1	Introduction . . . . .	81
4.2	Physical and numerical set-up . . . . .	86
4.2.1	Configurations . . . . .	86
4.2.2	Governing equations . . . . .	88
4.2.3	Numerical discretisation and algorithms . . . . .	89
4.3	Unsteady Reynolds-Averaged simulations . . . . .	92
4.3.1	Subsonic stall . . . . .	92
4.3.2	Transonic buffet . . . . .	95
4.3.3	Partial conclusion . . . . .	100
4.4	Global stability analyses . . . . .	102
4.4.1	Subsonic stall . . . . .	102
4.4.2	Transonic buffet . . . . .	110
4.4.3	Partial conclusion . . . . .	117
4.5	From linear to non-linear regime . . . . .	118
4.5.1	NACA4412 at $\alpha = 15^\circ$ and $\delta = 0^\circ$ . . . . .	118
4.5.2	OALT25 at $\alpha = 4^\circ$ and $\delta = 20^\circ$ . . . . .	118
4.6	Link between stall and buffet cells . . . . .	119
4.7	Conclusion . . . . .	124
CHAPTER 5 ARTICLE 3 : STALL CELL PREDICTION USING A LIFTING SURFACE MODEL . . . . .		127

5.1	Introduction . . . . .	128
5.2	Methodology . . . . .	130
5.2.1	Non-linear lifting line model . . . . .	131
5.2.2	Lifting surface model - Vortex Lattice Method . . . . .	132
5.3	Numerical verification . . . . .	135
5.4	Analysis of the lift cell . . . . .	138
5.4.1	Lifting line - Infinite Wing . . . . .	138
5.4.2	Lifting surface - Elliptic wing . . . . .	140
5.4.3	Lifting surface - Rectangular wing . . . . .	146
5.4.4	Lifting surface - Infinite wing . . . . .	149
5.5	Conclusion . . . . .	153
CHAPTER 6 GENERAL DISCUSSION . . . . .		155
CHAPTER 7 CONCLUSION . . . . .		160
REFERENCES . . . . .		162
APPENDICES . . . . .		179

## LIST OF TABLES

Table 1.1	Experimental studies of stall cells . . . . .	17
Table 1.2	Numerical studies of stall cells . . . . .	17
Table 1.3	Experimental studies of two-dimensional buffet . . . . .	22
Table 1.4	Numerical studies of two-dimensional buffet . . . . .	23
Table 1.5	Numerical studies of three-dimensional buffet . . . . .	29
Table 1.6	Experimental studies of three-dimensional buffet . . . . .	32
Table 2.1	Effect of the sweep angle. . . . .	54
Table 2.2	Effect of the span. . . . .	55
Table 4.1	Characteristics of the grids. . . . .	89
Table 4.2	Stall cells convection frequency for several wing spans and sweep angles (NACA4412, $M = 0.2$ , $Re = 350\,000$ , $\alpha = 15^\circ$ ). . . . .	96
Table 4.3	Buffet cells convection frequency for several sweep angles (OALT25, $M = 0.7352$ , $Re = 3 \times 10^6$ , $\alpha = 4^\circ$ ). . . . .	101
Table 5.1	Parameters of the lift polar. . . . .	145
Table 5.2	Number of stall cells compared to the experiments. . . . .	148
Table A.1	Description of the recirculation bubble associated with the NACA4412 base-flows . . . . .	182
Table A.2	Description of the recirculation bubble associated with the OALT25 base-flows . . . . .	182
Table A.3	Description of the recirculation bubble associated with the NACA0012 base-flows . . . . .	182
Table C.1	Summary of the convection speed and spanwise wavelength associated with specific frequencies in the pressure spectrum (OALT25, $M =$ $0.7352$ , $Re = 3 \times 10^6$ , $\alpha = 4^\circ$ , $\delta = 10^\circ$ , $x = 0.4$ ) . . . . .	197
Table C.2	Summary of the convection speed and spanwise wavelength associated with specific frequencies in the pressure spectrum (OALT25, $M =$ $0.7352$ , $Re = 3 \times 10^6$ , $\alpha = 4^\circ$ , $\delta = 20^\circ$ , $x = 0.4$ ) . . . . .	197
Table C.3	Summary of the convection speed and spanwise wavelength associated with specific frequencies in the pressure spectrum (OALT25, $M =$ $0.7352$ , $Re = 3 \times 10^6$ , $\alpha = 4^\circ$ , $\delta = 30^\circ$ , $x = 0.4$ ) . . . . .	198

## LIST OF FIGURES

Figure 1.1	Aircraft flight envelope limit (taken from Abbas-Bayoumi and Becker (2011)) . . . . .	2
Figure 1.2	Classification of typical flow problems, associated ZDES modes and examples of applications (taken from Deck <i>et al.</i> (2014)) . . . . .	7
Figure 1.3	Application of hybrid RANS/LES at flight conditions (taken from Deck <i>et al.</i> (2014)) . . . . .	8
Figure 1.4	Computational Fluid Dynamics models (adapted from Gallay (2016))	9
Figure 1.5	Stall types: $C_L - \alpha$ curves for 5 airfoils geometries (taken from McCullough and Gault (1951)) . . . . .	13
Figure 1.6	Stall cells for various aspect ratio (reproduction of Winkelmann and Barlow (1980), taken from Disotell and Gregory (2015)) . . . . .	14
Figure 1.7	Time-averaged pressure coefficient over the OAT15A airfoil . . . . .	28
Figure 1.8	Numerical solutions of RBC12 configuration in buffet conditions (taken from Sartor and Timme (2017)) . . . . .	30
Figure 1.9	Pressure coefficient time history measured with unsteady pressure sensitive paint (taken from Sugioka <i>et al.</i> (2016)) . . . . .	35
Figure 2.1	Three-dimensional mesh obtained from the extrusion of a two-dimensional grid. . . . .	46
Figure 2.2	OALT25 grid refinement study. . . . .	47
Figure 2.3	Lift coefficient for the 2.5D cases. . . . .	49
Figure 2.4	Time-averaged surface pressure coefficient for 2.5D cases. . . . .	50
Figure 2.5	RMS of the surface pressure fluctuations for 2.5D cases. . . . .	50
Figure 2.6	Time evolution of the pressure coefficient and skin friction lines for infinite swept wings ( $\delta = 20$ deg.). . . . .	51
Figure 2.7	Effect of the sweep angle on the pressure coefficient and skin friction lines for infinite swept wings. . . . .	52
Figure 2.8	Wing span effect on the number of buffet cells for a sweep angle of 20 deg. . . . .	53
Figure 2.9	Tentative model for the convection speed and buffet cells frequency. .	54
Figure 2.10	Extraction of the pressure on a line parallel to the leading edge near $x'/l_{ref} = 0.4$ . . . . .	54
Figure 2.11	Buffet cells convection speed model. . . . .	55
Figure 2.12	Fourier coefficients of the pressure coefficient of four Fourier modes. .	56



Figure 2.13	Effect of the sweep angle on the sectional lift coefficient power spectral density . . . . .	57
Figure 2.14	Global lift coefficient power spectral density . . . . .	58
Figure 2.15	Effect of the span on the sectional lift coefficient power spectral density	59
Figure 2.16	Spanwise grid refinement for a sweep angle of 30 deg. . . . .	60
Figure 2.17	Stall cells flow topology . . . . .	62
Figure 2.18	Pressure coefficient over the NACA4412 airfoil. . . . .	62
Figure 2.19	Lift coefficient of the NACA4412 airfoil. . . . .	64
Figure 2.20	Contour of $u/v_{ref}$ and streamtraces. . . . .	64
Figure 2.21	Surface pressure coefficient and skin friction lines with 224 (left) and 112 (right) spanwise cells ( $\alpha = 15.0$ deg.). . . . .	65
Figure 2.22	Surface pressure coefficient and skin friction lines for a wing of aspect ratio 12. . . . .	65
Figure 2.23	Two-dimensional and three-dimensional sectional surface pressure coefficient. . . . .	65
Figure 2.24	Effect of the sweep angle on the surface pressure coefficient and skin friction lines. . . . .	67
Figure 2.25	Sectional lift coefficient. . . . .	67
Figure 2.26	Extraction of the pressure on a line parallel to the leading edge near $x'/l_{ref} = 0.4$ for a sweep angle of 20 deg. . . . .	68
Figure 2.27	Convection speed model for buffet cells and stall cells. . . . .	68
Figure 3.1	C-H type grid with repartition of the model type (only one point out of four shown) . . . . .	71
Figure 3.2	Pressure distribution of the 2D URANS ZDES simulations. . . . .	72
Figure 3.3	Time-averaged pressure distribution of three-dimensional buffet on swept wings. . . . .	73
Figure 3.4	Q-criterion iso-surface of level 60.0 colored by density and density contour on the plane $z/c = 4$ and the wing surface. . . . .	74
Figure 3.5	In X-Y plane location of the probes for the ZDES simulation. . . . .	75
Figure 3.6	Power spectral density of the pressure in the large span ZDES simulation.	75
Figure 3.7	Cross-spectrum analysis in the spanwise direction for the Field002 probes.	77
Figure 3.8	Inverse Fourier modes. . . . .	77
Figure 4.1	Infinite swept wing configuration . . . . .	86
Figure 4.2	Lift curve for the 2-D and 3-D steady solutions (NACA4412, $Re = 350\,000$ , $M = 0.2$ , $\delta = 0^\circ$ ). . . . .	94

Figure 4.3	Surface pressure coefficient and skin friction lines of 3-D steady solution with 224 (left) and 112 (right) spanwise grid cells (NACA4412, $M = 0.2$ , $Re = 350\,000$ , $\alpha = 15^\circ$ , $\delta = 0^\circ$ , $L_z = 6$ ). . . . .	94
Figure 4.4	Instantaneous surface pressure coefficient and skin friction lines over a swept wing (NACA4412, $M = 0.2$ , $Re = 350\,000$ , $\alpha = 15^\circ$ , $L_z = 6$ ). . . . .	95
Figure 4.5	Stall and buffet cells convection model. . . . .	95
Figure 4.6	Time-averaged wall pressure coefficient for spanwise invariant solution with several sweep angle (OALT25, $M = 0.7352$ , $Re = 3 \times 10^6$ , $\alpha = 4^\circ$ ). . . . .	97
Figure 4.7	Instantaneous surface pressure coefficient and skin friction lines for URANS simulations of infinite swept wings with two sweep angles (OALT25, $M = 0.7352$ , $Re = 3 \times 10^6$ , $\alpha = 4^\circ$ , $L_z = 6$ ). . . . .	97
Figure 4.8	Sectional lift coefficient power spectral density (OALT25, $M = 0.7352$ , $Re = 3 \times 10^6$ , $\alpha = 4^\circ$ , $\delta = 30^\circ$ ). . . . .	99
Figure 4.9	Effect of the sweep angle on the global and sectional lift coefficient power spectral density (OALT25, $M = 0.7352$ , $Re = 3 \times 10^6$ , $\alpha = 4^\circ$ ). . . . .	99
Figure 4.10	Extraction of the pressure on a line parallel to the leading edge near $x'/c = 0.43$ (OALT25, $M = 0.7352$ , $Re = 3 \times 10^6$ , $\alpha = 4^\circ$ , $\delta = 30^\circ$ ). . . . .	100
Figure 4.11	Convection speed of stall (NACA4412, $M = 0.2$ , $Re = 350\,000$ , $\alpha = 15^\circ$ ) and buffet (OALT25, $M = 0.7352$ , $Re = 3 \times 10^6$ , $\alpha = 4^\circ$ ) cells. . . . .	101
Figure 4.12	Eigenspectrum (NACA4412, $M = 0.2$ , $Re = 350\,000$ , $\alpha = 15.0^\circ$ , $\delta = 0.0^\circ$ ). . . . .	103
Figure 4.13	Effect of spanwise grid density and the wavenumber on the growth rate of the unstable mode (NACA4412, $M = 0.2$ , $Re = 350\,000$ , $\alpha = 15.0^\circ$ , $\delta = 0.0^\circ$ ). . . . .	104
Figure 4.14	Flow visualisation of the (a): base-flow and (b): 3-D unstable mode (NACA4412, $M = 0.2$ , $Re = 350\,000$ , $\alpha = 15.0^\circ$ , $\delta = 0.0^\circ$ ). . . . .	104
Figure 4.15	Effect of the angle of attack on the growth rate of the unstable mode (NACA4412, $M = 0.2$ , $Re = 350\,000$ , $\delta = 0.0^\circ$ ). . . . .	105
Figure 4.16	Flow visualisation of the 3-D unstable mode for several angle of attack on the two branches of the lift hysteresis (NACA4412, $M = 0.2$ , $Re = 350\,000$ , $\delta = 0.0^\circ$ ). . . . .	106
Figure 4.17	Effect of the sweep angle on the growth rate and frequency of the 3-D unstable mode (NACA4412, $M = 0.2$ , $Re = 350\,000$ , $\alpha = 15.0^\circ$ , black: stability analysis, red: URANS simulations). . . . .	107
Figure 4.18	Effect of the angle of attack on the spectra of the 2-D unstable mode (NACA4412, $M = 0.2$ , $Re = 350\,000$ , $\delta = 0.0^\circ$ , $\beta = 0$ ). . . . .	108

Figure 4.19	Flow visualisation of the (a,b): base-flow and (c,d): 2-D unstable mode on the two branches of the lift hysteresis (NACA4412, $M = 0.2$ , $Re = 350\,000$ , $\alpha = 18.0^\circ$ , $\delta = 0.0^\circ$ , $\beta = 0.0$ ). . . . .	109
Figure 4.20	Effect of the wavenumber on the 2-D wake instability mode (NACA4412, $M = 0.2$ , $Re = 350\,000$ , $\alpha = 18.0^\circ$ ). . . . .	110
Figure 4.21	Eigenspectrum in 2-D and 3-D (OALT25, $M = 0.7352$ , $Re = 3 \times 10^6$ , $\alpha = 4.0^\circ$ , $\delta = 0.0^\circ$ ). . . . .	112
Figure 4.22	Effect of the wavenumber $\beta$ on the 3-D mode (OALT25, $M = 0.7352$ , $Re = 3 \times 10^6$ , $\delta = 0.0^\circ$ ) . . . . .	113
Figure 4.23	Lift coefficient of the steady 2-D flow (OALT25, $M = 0.7352$ , $Re = 3 \times 10^6$ , $\delta = 0.0^\circ$ ). . . . .	113
Figure 4.24	Effect of the sweep angle on the 3-D mode (OALT25, $M = 0.7352$ , $Re = 3 \times 10^6$ , $\alpha = 4.0^\circ$ , black: stability analysis, red: URANS simulations). . . . .	114
Figure 4.25	Flow visualisation of the (a): base-flow, (b,c) 2-D and 3-D unstable modes (OALT25, $M = 0.7352$ , $Re = 3 \times 10^6$ , $\alpha = 4.0^\circ$ , $\delta = 30^\circ$ ). . . . .	115
Figure 4.26	Effect of the angle of attack on the 2-D unstable mode (OALT25, $M = 0.7352$ , $Re = 3 \times 10^6$ , $\delta = 0.0^\circ$ , $\beta = 0.0$ ). . . . .	116
Figure 4.27	Effect of the wavenumber on the 2-D buffet mode (OALT25, $M = 0.7352$ , $Re = 3 \times 10^6$ , $\alpha = 4.0^\circ$ ). . . . .	117
Figure 4.28	Snapshots of the surface pressure coefficient and skin friction lines of the URANS simulations (NACA4412, $M = 0.2$ , $Re = 350\,000$ , $\alpha = 15.0^\circ$ , $\delta = 0^\circ$ , $L_z = 6$ ). . . . .	119
Figure 4.29	Snapshots of the surface pressure coefficient and skin friction lines of the URANS simulations (OALT25, $M = 0.7352$ , $Re = 3 \times 10^6$ , $\alpha = 4.0^\circ$ , $\delta = 20^\circ$ , $L_z = 6$ ). . . . .	119
Figure 4.30	Base-flow Mach number field at several Mach number and angle of attack (NACA0012, $Re = 10^7$ , $\delta = 0^\circ$ ) . . . . .	121
Figure 4.31	Effect of the Mach number and angle of attack on the growth rate of the 3-D mode (NACA0012, $Re = 10^7$ , $\delta = 0^\circ$ ). . . . .	122
Figure 4.32	Flow visualisation of the 3-D $\hat{\rho}^e/\rho_{e\infty}$ unstable mode (NACA0012, $Re = 10^7$ , $\delta = 0^\circ$ ). . . . .	123
Figure 4.33	Effect of the angle of attack on the 2-D unstable mode (NACA0012, $M = 0.72$ , $Re = 10^7$ , $\delta = 0.0^\circ$ , $\beta = 0.0$ ). . . . .	123
Figure 4.34	Effect of the sweep angle on the 3-D mode frequency. . . . .	124
Figure 5.1	VLM computational setup. . . . .	133

Figure 5.2	Infinite wing Vortex Lattice Method with periodicity assumption. . .	134
Figure 5.3	Viscous coupling applied to the VLM model. . . . .	135
Figure 5.4	Infinite wing solution of the NL-VLM . . . . .	136
Figure 5.5	Effect of the span on the lift distribution of wing with periodic twist.	137
Figure 5.6	Solution of the wing with periodic twist using the periodicity assumption.	138
Figure 5.7	$\Gamma$ distribution over the periodic wing with 1 and 10 chordwise panels.	138
Figure 5.8	Lift distribution and effective angle of attack of Spalart's lifting line model. . . . .	139
Figure 5.9	Lift distribution of Spalart's lifting line model without the Gaussian filter. . . . .	140
Figure 5.10	Effect of the dissipation coefficient $\mu$ on the lift distribution (elliptic wing, $AR = 16.0$ , $\alpha = 18^\circ$ ). . . . .	142
Figure 5.11	Effect of the dissipation coefficient $\mu$ on the effective angle of attack (elliptic wing, $AR = 16.0$ , $\alpha = 18^\circ$ ). . . . .	142
Figure 5.12	Effect of the dissipation coefficient $\mu$ on the lift coefficient interpolated at the effective angle of attack (elliptic wing, $AR = 16.0$ , $\alpha = 18^\circ$ ). . .	143
Figure 5.13	$\Gamma$ distribution at several angle of attack (elliptic wing, $AR = 16.0$ ). .	143
Figure 5.14	Lift coefficient distribution of several aspect ratios at several angles of attack (elliptic wing). . . . .	144
Figure 5.15	Selection of manufactured lift curves. . . . .	145
Figure 5.16	Effect of the lift polar on the lift distribution (elliptic wing, $AR = 16.0$ , $\alpha = 18^\circ$ ). . . . .	146
Figure 5.17	Effect of the lift polar on the effective angle of attack (elliptic wing, $AR = 16.0$ , $\alpha = 18^\circ$ ). . . . .	147
Figure 5.18	Effect of the aspect ratio on the lift coefficient distribution (rectangular wing, $\alpha = 20^\circ$ , polar 5). . . . .	148
Figure 5.19	Effect of the aspect ratio on the effective angles of attack (rectangular wing, $\alpha = 20^\circ$ , polar 5). . . . .	148
Figure 5.20	Manufactured lift curve for the Clark Y airfoil based on the experiments (Lyon <i>et al.</i> , 1997). . . . .	149
Figure 5.21	Effect of the aspect ratio on the lift coefficient with the experimental lift curve (rectangular wing, $\alpha = 18.4^\circ$ , polar 6). . . . .	149
Figure 5.22	Effect of the angle of attack on the lift distribution (infinite wing, $AR = 2.0$ ). . . . .	150
Figure 5.23	Effect of the angle of attack on the sectional effective angle distribution (infinite wing, $AR = 2.0$ ). . . . .	151

Figure 5.24	Effect of the number of spanwise period on the lift distribution (infinite wing, $AR = 2.0$ ). . . . .	151
Figure 5.25	Effect of the aspect ratio on the lift distribution of infinite wings. . .	152
Figure 5.26	Effect of the artificial dissipation on the lift distribution (infinite wing, $AR = 2.0$ ). . . . .	152
Figure 5.27	Effect of the artificial dissipation on the effective angle distribution (infinite wing, $AR = 2.0$ ). . . . .	153
Figure A.1	Effect of the wavenumber of the 2-D buffet mode (OAT15A, $Re = 3 \times 10^6$ , $\alpha = 3.5^\circ$ , $\delta = 0^\circ$ ). . . . .	180
Figure A.2	Density contours of the base-flow (OALT25, $M = 0.7352$ , $Re = 3 \times 10^6$ , $\alpha = 4.0^\circ$ , $\delta = 0^\circ$ ). . . . .	181
Figure A.3	Effect of the Mach number and angle of attack on the growth rate of the three-dimensional mode (NACA0012, $Re = 10^7$ , $\delta = 0^\circ$ ). . . . .	184
Figure A.4	Scaling of the three-dimensional modes by the separation height. . . . .	185
Figure B.1	Continuation method. (Adapted from Wales <i>et al.</i> (2012)) . . . . .	188
Figure B.2	Lift curve for the 2-D steady solutions with the pseudo-arclength method (NACA4412, $Re = 350\,000$ , $M = 0.2$ ). . . . .	189
Figure B.3	Flow visualisation of the (a): base-flow and (b): 2-D unstable mode on the two branches of the lift hysteresis (NACA4412, $M = 0.2$ , $Re = 350\,000$ , $\alpha = 18.0^\circ$ , $\delta = 0.0^\circ$ , $\beta = 0.0$ ). . . . .	190
Figure B.4	Effect of the angle of attack on the spectra of the 2-D unstable mode (NACA4412, $M = 0.2$ , $Re = 350\,000$ , $\delta = 0.0^\circ$ , $\beta = 0$ ). . . . .	191
Figure B.5	Effect of the angle of attack on the growth rate of the unstable mode (NACA4412, $M = 0.2$ , $Re = 350\,000$ , $\delta = 0.0^\circ$ ). . . . .	191
Figure B.6	Effect of the sweep angle on the growth rate and frequency of the 3-D unstable mode (NACA4412, $M = 0.2$ , $Re = 350\,000$ , $\alpha = 18.0^\circ$ , upper branch, black: stability analysis, red: URANS simulations ( $\alpha = 15.0^\circ$ )).	192
Figure B.7	Effect of the sweep angle on the growth rate and frequency of the 3-D unstable mode (NACA4412, $M = 0.2$ , $Re = 350\,000$ , $\alpha = 18.0^\circ$ , middle branch, black: stability analysis, red: URANS simulations ( $\alpha = 15.0^\circ$ )).	192
Figure C.1	Extraction of the pressure on a line parallel to the leading edge (OALT25, $M = 0.7352$ , $Re = 3 \times 10^6$ , $\alpha = 4^\circ$ , $\delta = 10^\circ$ ). . . . .	193
Figure C.2	Extraction of the pressure on a line parallel to the leading edge (OALT25, $M = 0.7352$ , $Re = 3 \times 10^6$ , $\alpha = 4^\circ$ , $\delta = 20^\circ$ ). . . . .	194
Figure C.3	Extraction of the pressure on a line parallel to the leading edge (OALT25, $M = 0.7352$ , $Re = 3 \times 10^6$ , $\alpha = 4^\circ$ , $\delta = 30^\circ$ ). . . . .	194

Figure C.4	Power spectral density of the pressure coefficient at several position along the chord (OALT25, $M = 0.7352$ , $Re = 3 \times 10^6$ , $\alpha = 4^\circ$ , $\delta = 10^\circ$ ). . . . .	199
Figure C.5	Cross-spectrum analysis for a line of sensors at $x/c = 0.4$ (OALT25, $M = 0.7352$ , $Re = 3 \times 10^6$ , $\alpha = 4^\circ$ , $\delta = 10^\circ$ ). . . . .	200
Figure C.6	Inverse Fourier mode on the wing suction side at the dominant frequencies (OALT25, $M = 0.7352$ , $Re = 3 \times 10^6$ , $\alpha = 4^\circ$ , $\delta = 10^\circ$ ). . . . .	200
Figure C.7	Cross-spectrum analysis for a line of sensors at $x/c = 0.4$ (OALT25, $M = 0.7352$ , $Re = 3 \times 10^6$ , $\alpha = 4^\circ$ , $\delta = 20^\circ$ ). . . . .	201
Figure C.8	Inverse Fourier mode on the wing suction side at the dominant frequencies (OALT25, $M = 0.7352$ , $Re = 3 \times 10^6$ , $\alpha = 4^\circ$ , $\delta = 20^\circ$ ). . . . .	201
Figure C.9	Cross-spectrum analysis for a line of sensors at $x/c = 0.4$ (OALT25, $M = 0.7352$ , $Re = 3 \times 10^6$ , $\alpha = 4^\circ$ , $\delta = 30^\circ$ ). . . . .	202
Figure C.10	Inverse Fourier mode on the wing suction side at the dominant frequencies (OALT25, $M = 0.7352$ , $Re = 3 \times 10^6$ , $\alpha = 4^\circ$ , $\delta = 30^\circ$ ). . . . .	202

**LIST OF APPENDICES**

Appendix A	Appendice to article 2 . . . . .	180
Appendix B	Newton continuation . . . . .	186
Appendix C	Stall cell convection analysis in the transonic buffet case . . . . .	193

## LIST OF SYMBOLS AND ABBREVIATIONS

## Symbols

$a$	speed of sound ( $m.s^{-1}$ )
$\mathbf{A}$	RANS equation linear operator
$\hat{\mathbf{A}}$	modified RANS equation linear operator
$A, B$	coefficients of the Fourier series of the circulation
$A_{i,j}$	coefficients of the VLM influence matrix
$A'_{i,j}$	coefficients of the modified VLM influence matrix
$b$	wing span ( $m$ )
$c, c_{3D}$	chord length in 2D or mean aerodynamic chord in 3D ( $m$ )
$c_{2D}$	chord in the plane normal to the leading edge ( $m$ )
$c_f$	Gaussian filter width
$C_l$	sectional lift coefficient
$C_{l_\alpha}$	derivative of $C_l$ with respect to $\alpha$
$C_{l_{inv}}$	inviscid lift coefficient
$C_{l_{vis}}$	viscous lift coefficient
$C_L$	lift coefficient
$C_P$	pressure coefficient
$e$	internal energy ( $m^2.s^{-2}$ )
$f$	frequency ( $Hz$ )
$k_0$	wavenumber
$l_{ref}$	reference length, which is equal to the chord in the plane normal to the leading edge ( $m$ )
$Lz$	wing span ( $m$ )
$Lz'$	length of the leading edge ( $m$ )
$M$	Mach number ( $V/a$ )
$M_{2D}$	Mach number in the plane normal to the leading edge ( $V_{ref}/a$ )
$M_{3D}$	free stream Mach number ( $V_\infty/a$ )
$N$	number of VLM mesh panels
$\vec{n}$	normal vector
$n_i, n_j$	number of grid cells in the $i$ and $j$ direction
$n_{p.s.}, n_{s.s.}, n_{t.e.}$	number of grid cells on the pressure side, suction side and trailing edge
$N_{cells}$	number of stall/buffet cells



$P$	VLM collocation point
$p_{rms}$	RMS of the pressure fluctuations ( $kg.m^{-1}.s^{-2}$ )
$q_{\infty}$	free stream dynamic pressure ( $kg.m^{-1}.s^{-2}$ )
$\vec{q}$	velocity induced by a vortex segment ( $m \cdot s^{-1}$ )
$\vec{r}$	distance vector ( $m$ )
$\mathbf{R}$	residual vector
$Re, Re_c$	Reynolds number ( $\rho_{\infty} V_{ref} l_{ref} / \mu_{\infty}$ )
$Re_{2D}$	Reynolds number in the plane normal to the leading edge ( $\rho_{\infty} V_{ref} l_{ref} / \mu_{\infty}$ )
$Re_{3D}$	free stream Reynolds number ( $\rho_{\infty} V_{\infty} c / \mu_{\infty}$ )
$Re_{MAC}$	free stream Reynolds number based on the mean aerodynamic chord
$S_{ref}$	reference surface ( $m^2$ )
$St$	Strouhal number ( $f l_{ref} / V_{ref}$ )
$t$	time ( $s$ )
$T$	spanwise period
$\bar{t}$	nondimensional time ( $t V_{ref} / l_{ref}$ )
$u, v, w$	velocity in the $x, y, z$ directions ( $m.s^{-1}$ )
$\mathbf{u}$	perturbation vectors to extract the Jacobian matrix
$V_{2min}$	minimum takeoff speed
$\mathbf{V}$	diagonal matrix of the cells volume
$V_{ref}, V_{\infty, 2D}$	free stream velocity in the plane normal to the leading edge ( $m.s^{-1}$ )
$V_{REF}$	landing approach speed
$V_{S1g}$	stall speed in 1 $g$ flight
$V_{\infty}, V_{\infty, 3D}$	free stream velocity ( $m.s^{-1}$ )
$V_c$	convection speed ( $m.s^{-1}$ )
$V_x, V_y, V_z$	free stream velocities in the $x, y, z$ referential ( $m.s^{-1}$ )
$V'_x, V'_y, V'_z$	free stream velocities in the $x', y', z'$ referential ( $m.s^{-1}$ )
$\mathbf{W}$	conservative variables ( $[\rho, \rho u, \rho v, \rho w, \rho e, \rho \tilde{v}]^t$ )
$\mathbf{W}_0$	conservative variables of base-flow (converged steady solution)
$\mathbf{W}'$	conservative variables perturbation
$\hat{\mathbf{W}}$	conservative variable eigenvector
$x, y, z$	Cartesian coordinates
$x', y', z'$	Cartesian coordinates with $z'$ aligned with the leading edge
$\alpha$	angle of attack (deg.)
$\alpha_{2D}$	angle of attack in the plane normal to the leading edge (deg.)
$\alpha_{3D}$	free stream angle of attack (deg.)
$\alpha_{eff}$	effective angle of attack (deg.)

$\alpha_i$	induced angle of attack (deg.)
$\alpha_{inv}$	inviscid angle of attack (deg.)
$\alpha_t$	twist angle (deg.)
$\beta$	wavenumber
$\delta$	sweep angle (deg.)
$\Delta_z$	spanwise grid spacing
$\Delta x^+, \Delta y^+, \Delta z^+$	dimensionless grid size
$\Delta x_{s.f.}$	grid spacing across the shock wave
$\Delta y_w$	grid wall spacing
$\Delta y_{f.f.}$	farfield distance
$\Delta$	SFD filter width
$\Delta\alpha$	angle of attack correction (deg.)
$\epsilon$	finite difference linearisation coefficient or convergence tolerance
$\eta$	dimensionless spanwise position
$\Gamma$	circulation ( $m^2.s^{-1}$ )
$\lambda$	eigenvalue ( $\sigma + i\omega$ )
$\lambda_t$	twist period ( $m$ )
$\lambda_z$	wavelength ( $m$ )
$\phi$	phase angle ( $rad.$ ) or velocity potential
$\rho_\infty$	free stream density ( $kg.m^{-3}$ )
$\sigma$	growth rate
$\mu$	artificial viscosity coefficient
$\mu_\infty$	free stream dynamic viscosity ( $kg.m^{-1}.s^{-1}$ )
$\omega$	frequency $\omega = 2\pi f$ ( $rad.$ ) or relaxation factor
$\chi$	SFD proportional controller coefficient

## Abbreviations

AR	Aspect Ratio
CC	Compressibility Correction
CFD	Computational Fluid Dynamics
CFL	Courant-Friedrichs-Lewy
CINES	<i>Centre Informatique National de l'Enseignement Supérieur</i>
CRM	Common Research Model
CTA	Constant Temperature Anemometry
CPU	Central Processing Unit
DAAA	<i>Département Aérodynamique, Aéroélasticité et Acoustique</i>

DARI	<i>Demande d'Attribution de Ressources Informatique</i>
DES	Detached Eddy Simulation
DDES	Delayed Detached Eddy Simulation
DMD	Dynamic Mode Decomposition
DNS	Direct Numerical Simulation
DPSP	Dynamic Pressure Sensitive Paint
DTS	Dual Time Stepping
elsA	<i>ensemble logiciel de simulation Aérodynamique</i>
EDW	Edwards-Chandra
EVM	Eddy Viscosity Model
FastS	Fast aerodynamic solver technology Structured
GENCI	<i>Grand Équipement National de Calcul Intensif</i>
GIS	Grid Induced Separation
GMRES	Generalized Minimal Residual Method
HPC	High Performance Computing
IDDES	Improved Delayed Detached Eddy Simulation
ILES	Implicit Large Eddy Simulation
ILU	Incomplete Lower-Upper
JST	Jameson-Shmidt-Turkel
LBM	Lattice Boltzmann Method
LES	Large Eddy Simulation
LU	Lower-Upper
LU-SSOR	Lower-Upper Symmetric Successive Overrelaxation
MAC	Mean Aerodynamic Chord
MSD	Modeled-Stress Depletion
MUSCL	Monotonic Upwind Scheme for Conservation Laws
NACA	National Advisory Committee for Aeronautics
NASA	National Aeronautics and Space Administration
NL-VLM	Non-Linear Vortex Lattice Method
NSERC/CRNSG	Natural Sciences and Engineering Research Council
ONERA	<i>Office National d'Études et de Recherches Aérospatiales</i>
PANS	Partially Averaged Navier-Stokes
POD	Proper Orthogonal Decomposition
PITM	Partially Integrated Transport Model
PSP	Pressure Sensitive Paint
QDNS	Quasi Direct Numerical Simulation

RANS	Reynolds Averaged Navier-Stokes
RC	Curvature Correction
RMS	Root Mean Square
RSM	Reynolds Stress Models
SA	Spalart-Allmaras
SFD	Selective Frequency Damping
SORSM	Stress-Omega Reynolds Stress Model
SST	Shear Stress Transport
STVD	Symmetric Total Variant Diminishing
URANS	Unsteady Reynolds Averaged Navier-Stokes
VG	Vortex Generator
VLES	Very Large Eddy Simulation
VLM	Vortex Lattice Method
WENO	Weighted Essentially Non Oscillatory
WMLES	Wall Modeled Large Eddy Simulation
WRLES	Wall Resolved Large Eddy Simulation
ZDES	Zonal Detached Eddy Simulation

## CHAPTER 1 INTRODUCTION

### 1.1 Context

For safety reasons, civil aircraft must operate within a flight envelope bounded by several aerodynamic phenomena. Such phenomena include transonic buffet and stall (Figure 1.1). Stall is characterized by a loss of lift caused by flow separation. Most of the time, stall occurs at low-speed and at high angle of attack, and involves complex physics: laminar to turbulent transition, flow separation and reattachment, unsteadiness, etc. Transonic buffet is a specific phenomenon resulting from an interaction between the shock wave and the separation of the boundary layer induced by the shock. This interaction causes an oscillation of the position of the shock and of the separated boundary layer. This induces oscillations of the aerodynamic forces. Transonic buffet and stall can cause vibrations of the airframe called buffeting, and are detrimental to the handling of the aircraft. Knowing that in-flight loss of control is one of the largest cause of aviation accidents and fatalities (Boeing Commercial Airplanes, 2014), these phenomena must be avoided in aircraft operations.

Since the flight envelope of aircraft is bounded by transonic buffet and stall, these two phenomena must be taken into account in aircraft design. In practice buffeting speed is qualitatively evaluated by test pilots. However it is sometimes defined as the speed in 1.0  $g$  condition at which vibrations reach  $\pm 0.050g$ . Then a safety maneuver margin of 0.3  $g$  is added to get the actual flight envelope limit (Piccola, 2012). In aircraft certification the stall speed  $V_{S1g}$  is defined as the minimum speed at which the aircraft can maintain a 1.0  $g$  flight. This speed defines important parameters of an aircraft performance, like the minimum takeoff safety speed ( $V_{2min} = 1.13V_{S1g}$ ) and the minimum landing approach speed ( $V_{REF} = 1.23V_{S1g}$ ) (Bolds-Moorehead *et al.*, 2013). However, the physics involved is still not fully understood and these phenomena are still a challenge for state-of-the-art CFD techniques (Abbas-Bayoumi and Becker, 2011; Spalart and Venkatakrishnan, 2016; Deck *et al.*, 2014). Hence, the transonic buffeting and stall limits are predicted using empirical relations and safety margins are used (Bérard and Isikveren, 2009) in the design stage, and are later verified in flight test. This can result in limitations to the design space of modern aircraft. Hence, a better comprehension of these complex physics is required by the aerospace industry to design more efficient aircraft while maintaining safety.

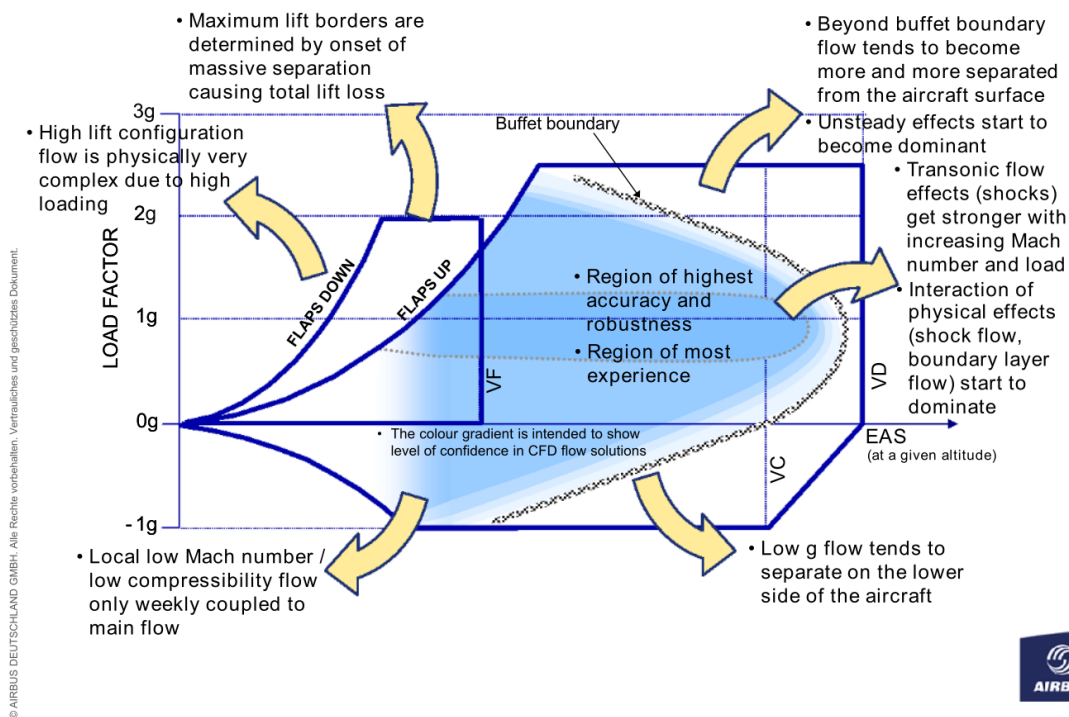


Figure 1.1 – Aircraft flight envelope limit (taken from Abbas-Bayoumi and Becker (2011))

The general objective of this thesis is to increase the physical understanding of the stall and buffet phenomena. More precisely this document focuses on the shift from two-dimensional to three-dimensional flow topology in these two flight regimes. This chapter will first introduce the field of computational fluid dynamics to support the discussion about numerical models throughout the thesis. Then the literature pertaining to the stall and transonic buffet phenomena is presented. This chapter ends with the presentation of the specific objectives and the outline of the thesis.

## 1.2 Computational Fluid Dynamics

Computational Fluid Dynamics (CFD) simulations are now an important tool in the design of modern aircraft. However, their use is limited by both the level of resolution required and the CPU time of the simulations, within the availability of High Performance Computing (HPC) resources. This section is intended to provide an overview of the available CFD methods with their limitations. These methods extend from potential methods which rely on inviscid, incompressible and irrotational assumptions to Direct Numerical Simulations (DNS), for which all the flow turbulent scales are resolved. An overview of some methods used in CFD is shown in Figure 1.4. The methods which will be part of this thesis methodology are

shown in blue. Methods in red are those which are still too expensive for this project. As a general reference, an overview of the applications and challenges of CFD for aircraft design is presented by Spalart and Venkatakrisnan (2016). This section focusses on compressible flows, since buffet occurs in the compressible regime. Note that subsonic stall, although often studied at low Mach number (0.15-0.3) can have pockets of compressible and even transonic flow caused by the acceleration of the flow on the suction side of the airfoil.

### 1.2.1 Numerical simulation of steady and unsteady flow

Potential methods include a variety of techniques using singularities to solve the Laplace equation and model the flow over a geometry. For instance, panel methods (Hess and Smith, 1967; Maskew, 1987) have been developed by disposing sinks and sources on panels representing the geometry. Other potential methods include Vortex Lattice Methods (Katz and Plotkin, 2001) where the wing is modeled by a set of thin surfaces of vortex rings. These methods are restricted to inviscid, incompressible and irrotational flows. Recently potential equations have been solved using Finite-Element methods (Galbraith *et al.*, 2017). To include viscous and compressibility effects, coupling techniques like the Non-Linear Vortex Lattice Method (Chattot, 2004; van Dam, 2002; Gallay and Laurendeau, 2015; Parenteau and Laurendeau, 2018; Hosangadi and Gopalathnam, 2020) have been developed over the last few years. Compressible flows can also be modeled using full potential theory (Jameson, 1983; Galbraith *et al.*, 2017) or transonic small disturbances (Murman and Cole, 1971; Kafyeke *et al.*, 1988) equations. Potential methods have also been coupled to boundary layer codes to provide viscous-inviscid coupling strategies (Cebeci *et al.*, 2005; Le Balleur and Girodoux-Lavigne, 1989; Edwards, 1993). These methods have a low computational cost. However, they can be classified as low to medium fidelity methods.

Simplification of the Navier-Stokes equations can be obtained by neglecting the viscosity. This results in the Euler equations which model an inviscid compressible fluid. A large body of work in the field of CFD has been devoted to these equations since great care must be taken in the discretization of the convective terms. Many numerical schemes have been developed for this purpose. To maintain stability, one can use upwind schemes for which the differential operator is biased in the upwind direction. Hence, flux-vector splitting schemes like the Van Leer's (van Leer, 1982), AUSM (Liou, 1996) and CUSP (Tatsumi *et al.*, 1995) schemes and flux-difference splitting schemes like the Roe scheme (Roe, 1981) have been developed. Another approach is to use a central operator with added numerical dissipation. Popular schemes of this family include the Jameson-Schmidt-Turkel (JST) (Jameson *et al.*,

1981) and matrix dissipation schemes (Swanson and Turkel, 1992).

When considering the Navier-Stokes equations, the largest difficulty arises from the resolution of turbulence (Spalart *et al.*, 1997), which involves small structures in space and high frequencies. This implies excessively refined grids and time steps in the case of a Direct Numerical Simulation (DNS). Such simulations are prohibitive for high Reynolds number flow. Since the early 2000's, the Reynolds Averaged Navier-Stokes (RANS) approach has been widely used for aerodynamic design in the aerospace industry. This method averages the turbulent fluctuations and uses a model for the resulting Reynolds stress tensor. The most widely used models are linear and rely on the Boussinesq assumption. This approach allows to model the effect of the turbulence as an added viscosity term which is computed with various algebraic (Baldwin and Lomax, 1978) or transport equations models which can have one (Spalart and Allmaras, 1992), two (Menter, 1994) or more equations (Rumsey, 2017). These Eddy Viscosity Models (EVM) account for the bulk of the high fidelity simulations used in the aerospace industry since they provide affordable and accurate solutions of turbulent flows at high Reynolds numbers, and in nominal flight conditions. Reynolds Stress Models (RSM) can also be used. Spalart (2015) presents his view on the development of turbulence models.

Since Euler and RANS simulations admit steady solutions, one can use a wide range of acceleration techniques which sacrifice the time accuracy to gain in convergence rate. For instance, most of the simulations are done using a local time step for every cell of the computational domain. This technique can be seen as a scalar preconditioner (Pierce and Giles, 1997) and following the same concept, matricial preconditioner like the point-implicit block-Jacobi one can be used (Allmaras, 1993). Popular acceleration techniques also include geometrical multigrid (Martinelli, 1987; Mavriplis, 1998), implicit schemes (Jameson and Yoon, 1987; Yoon and Jameson, 1988) and implicit residual smoothing (Jameson and Baker, 1983). Pierce and Giles (1997) presented a complete analysis of the combination of time integration scheme, geometrical multigrid, preconditioner and numerical dissipation scheme to optimize the convergence rate of Euler and RANS solver. However, one of the issue arising in the solution of the RANS equations is the possibility of multiple solutions. For example, Kamenetskiy *et al.* (2014) showed that multiple fully converged solutions of the RANS equations exist for a single flow problem, and that the combination of the numerical scheme, numerical algorithm and acceleration techniques may lead the solution towards one of the possible solutions.



The RANS method can be used for time accurate simulations resulting in the Unsteady Reynolds Averaged Navier-Stokes (URANS) approach. This method is only relevant for flows where the unsteadiness occurs at a low frequency which is far from the time scale of the turbulent fluctuations. A trivial way to compute unsteady flows is to use an explicit scheme with a global time step (Blazek, 2015). However, this implies using a very small time step to maintain the stability of the numerical scheme. To maintain the time accuracy of RANS simulations, one can use the Dual Time Stepping (DTS) method (Jameson, 1991) in which the time derivative is discretized with a finite difference approach between a set of time steps. A pseudo-time derivative is used for the convergence of the time steps, allowing to use all the acceleration techniques developed for steady flow solvers. Such a method allows to use physical time steps of the scale of the flow unsteadiness rather than a time step prescribed by the stability limit of the time integration scheme. For an overall presentation of the components of a CFD solver for Euler and RANS equations, one can look at the article of Witherden *et al.* (2017) or the book of Blazek (2015).

URANS equations can also be solved with frequency domain methods such as Time Spectral (Gopinath and Jameson, 2005), Non-Linear Frequency Domain (McMullen *et al.*, 2001, 2002) or Harmonic Balance (Hall *et al.*, 2002, 2013). These methods use Fourier transforms to discretize the time derivatives of the conservative variables for periodic flow problems. This Fourier series is limited to a selected number of harmonics, leading to a fixed number of time samples over a period. In these methods, the viscous and convective fluxes are evaluated in the time domain to avoid the complexity imposed by the transformation in the frequency domain of the Navier-Stokes equations. This method is efficient for time-periodic flows since it directly targets the saturated periodic regime without computing the transient.

The issue with RANS simulations is their accuracy for off-design conditions, where separation take place (Deck *et al.*, 2014). Stall and transonic buffet imply separation. In such cases, the choice of the turbulence model can have a large impact on the solution and flow models with a higher resolution are required. To obtain higher fidelity methods, one must add the resolution of turbulent scales to the simulations. This means that the simulations must be three-dimensional and unsteady. In the most complete way, Direct Numerical Simulations (DNS), resolves all the turbulent scales. These simulations provide first principle solutions. However, they are prohibitive for high Reynolds number flows since the grid and time resolution must be at the scale of the turbulent fluctuations. For instance, Spalart (2000a) evaluates the number of grid points for a DNS of a full aircraft in the order of  $10^{16}$  points whereas in the order of  $10^7$  points are required for a (U)RANS simulation.

To reduce the cost of turbulent scale resolved simulations, one can use the Large Eddy Simulation (LES) approach in which a subgrid-scale model is used to model the turbulent fluctuations which are too small for the grid and resolves the fluctuations up to the size of the mesh cells. LES can be classified as Wall Resolved LES (WRLES) or Wall Modeled LES (WMLES) depending on the fact that LES is used in the entire boundary layer or not. In the case of WMLES a model is used in the lower part of the boundary layer, resulting in a great reduction of the number of grid points and a larger time step. Rather than using a subgrid scale model, one can rely on the intrinsic dissipation of the numerical scheme to take into account the unresolved turbulent scale. This is often called Implicit Large-Eddy Simulation (ILES) or Quasi Direct Numerical Simulation (QDNS). Nevertheless, many comments have been made on the feasibility of LES for large problems (Spalart *et al.*, 1997). For instance, Spalart (2000a) evaluates the cost of a pure LES of an aircraft to the order of  $10^{11}$  grid points and  $10^7$  time steps, which will probably still not be affordable in the coming decades, leading to the development of more affordable methods. As such, only a handful of simulations with a span relevant for a 2D case are published for applications like the transonic buffet.

Hybrid RANS/LES methods have been proposed as a lower cost alternative to LES. A recent review on this type of method is presented by Chaouat (2017). Typically, RANS is used in regions of attached boundary layer, where it is the most accurate, and LES is used for separated flow regions. This type of method was introduced with the Detached Eddy Simulation (DES97) of Spalart *et al.* (1997) which modifies the reference length scale of the Spalart-Allmaras turbulence model to switch between a RANS model and a subgrid-scale LES model. This concept is in some way reminiscent of WMLES. However, the RANS model is here used in the complete thickness of the attached boundary layer. Many developments have been made in the field of Detached Eddy Simulations, some of which are reported by Spalart (2009). These developments have aimed at solving some flaws of the original DES97, like the Modeled-Stress Depletion (MSD) and Grid-Induced Separation (GIS). MSD occurs when a grid is fine enough to activate the limiter inhibiting the eddy-viscosity of the RANS model, but too coarse to produce LES content. Hence, the turbulence is not modeled nor resolved. MSD can cause GIS. Delayed Detached Eddy Simulation (Spalart *et al.*, 2006) was developed to solve the issue of GIS by extending the RANS region with a history effect. Improved Delayed Detached Eddy Simulation (IDDES) (Shur *et al.*, 2008) was also proposed to fix problems with the original DES97.

Classic Detached Eddy Simulation relies on a single formulation over the entire computational domain. In opposition, Deck (2005a,b) proposed the Zonal Detached Eddy Simulation (ZDES). The main difference in this method is the selection by the user of regions of pure RANS and regions of DES. In its recent versions (Deck, 2012), three variants of the ZDES can be used depending on whether the separation is induced by the geometry (mode 1), by a pressure gradient (mode 2) or by history of the boundary layer (mode 3/WMLES). A representation of these modes is shown in Figure 1.2. These modes and (U)RANS (mode 0) can be combined in the same computation. This method has the disadvantage of requiring additional inputs from the user and a knowledge of the flow topology to select the appropriate mode. The advantage of the method is that it provides a sure way to prevent MSD and GIS. Deck *et al.* (2014) presented their view on the perspectives of ZDES and, by extension, of hybrid RANS/LES methods. Some of these applications are shown in Figure 1.3. One can see that transonic buffet is one of them and that every application includes flow separation.

In his review of Hybrid RANS/LES methods, Chaouat (2017) defines zonal methods as methods which rely on two models, a RANS model and a subgrid-scale model. Hence, DES and its variant are classified as zonal. Non-zonal approaches include Very Large Eddy Simulations (VLES), Partially Averaged Navier-Stokes (PANS) and Partially Integrated Transport Model (PITM). One should note that this definition of zonal differs from the distinction between DES and ZDES. As one can see, a large number of methods exist in the field of hybrid RANS/LES and discussions are still ongoing, justifying the Hybrid RANS/LES Symposiums occurring every two years since 2005 (Hoarau *et al.*, 2018).

Another approach gaining interest for the simulation of high Reynolds flows is the Lattice Boltzmann approach (Chen and Doolen, 1998; Aidun and Clausen, 2010). This method

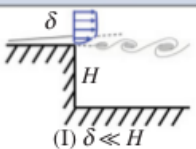
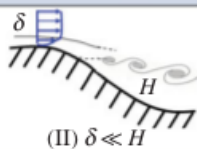
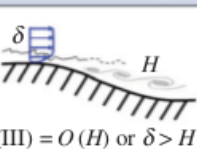
zonal detached eddy simulation (ZDES)			
	mode 1	mode 2	mode 3
flow category	 (I) $\delta \ll H$	 (II) $\delta \ll H$	 (III) $= O(H)$ or $\delta > H$
applications	base flow, free shear flows, spoilers, steps, slat/flap cove, etc.	buffet, flaps, duct flows, nacelle intake, etc.	corner flows, turbulent boundary layer, separation onset on high-lift devices, shallow separations, etc.

Figure 1.2 – Classification of typical flow problems, associated ZDES modes and examples of applications (taken from Deck *et al.* (2014))

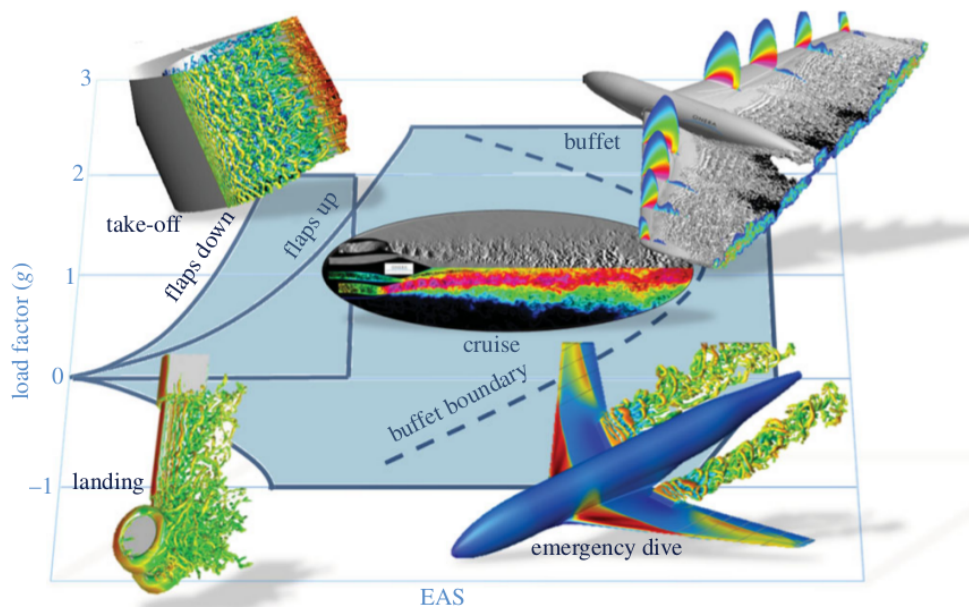


Figure 1.3 – Application of hybrid RANS/LES at flight conditions (taken from Deck *et al.* (2014))

is based on particle interactions rather than a continuous approach like the Navier-Stokes equations. Lattice Boltzmann is mentioned here since it is gaining attention from the CFD community and numerical solutions of buffet and stall have been published.

### 1.2.2 Modal analyses

Recently, methods to carry out modal analysis of a fluid flow (Sipp *et al.*, 2010; Theofilis, 2003, 2011; Taira *et al.*, 2017) have made their way from canonical cases to industrially relevant applications. Taira *et al.* (2017) provided an overview of modal analyses covering data-based methods (ex.: Proper Orthogonal Decomposition (POD)) and operator-based techniques (ex.: linear stability analysis). In this thesis we focus on the latter. These analyses rely on a linearization of the Navier-Stokes equations around a base-flow to model the growth or decay of perturbations around this base-flow. They can be classified as local or global. Local analyses are applicable to parallel base-flows (i.e. flows that are non-periodic in only one direction). Global stability analyses are applicable to base-flow without spatial periodicity (TriGlobal analysis (Theofilis, 2011)). One can also assume periodicity of the perturbation in one spatial direction leading to what is called BiGlobal analysis. This thesis will focus on BiGlobal and TriGlobal analyses since the parallel flow assumption of the local analysis does not apply to airfoils in stall and buffet conditions. These analyses proceed by computing the linear operator associated with the Navier-Stokes equations (i.e. the Jacobian). Then,

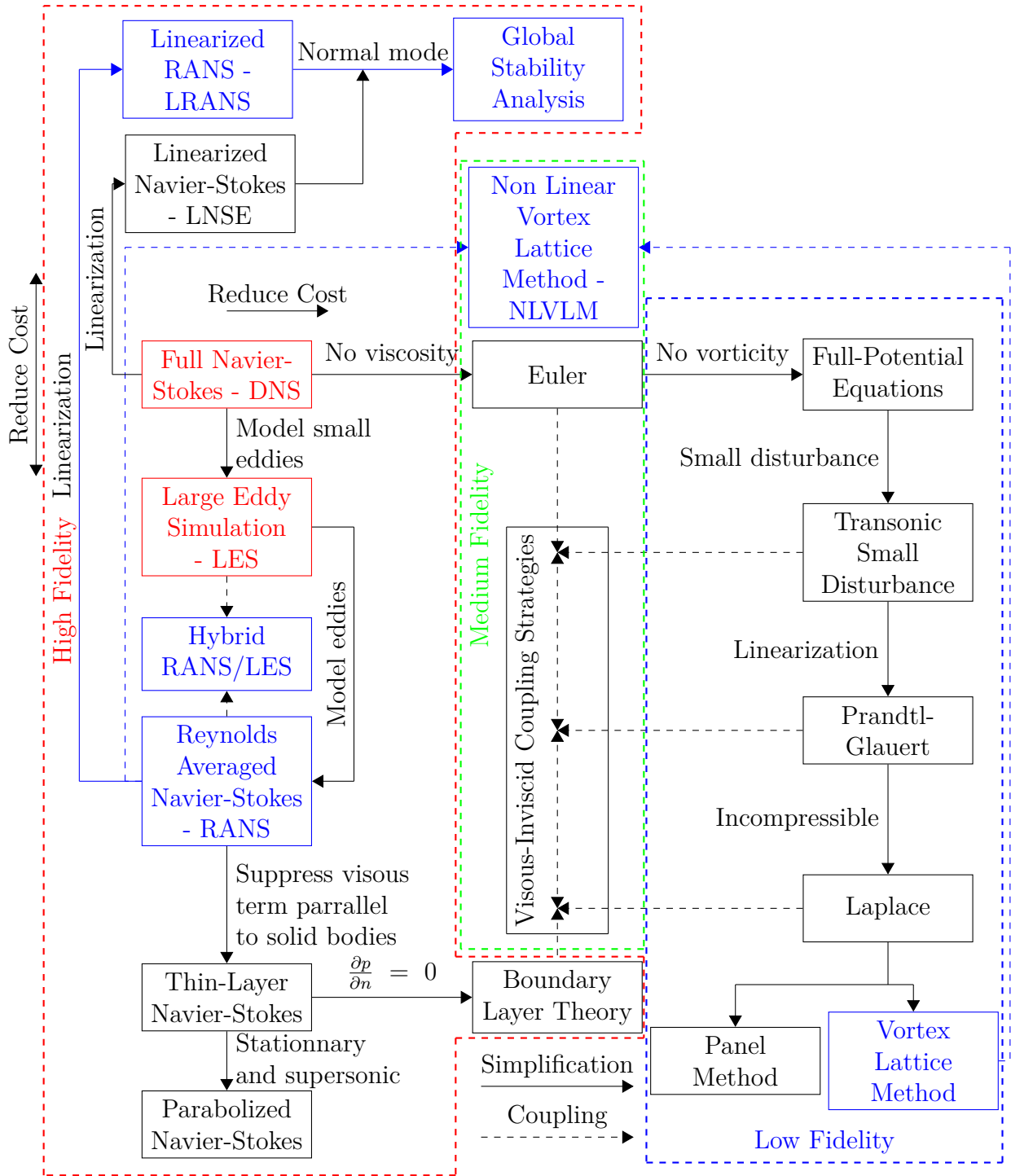


Figure 1.4 – Computational Fluid Dynamics models (adapted from Gallay (2016))

one can assume that small amplitude perturbations around the base-flow take the form of normal modes. Introducing this assumption, the problem reduces to an eigenvalue problem in which the eigenvectors are the shape of the modes and the eigenvalues describe the temporal evolution of the modes. This approach has often been used for laminar flows where steady solutions of the Navier-Stokes equations can be obtained. It has also been applied to the RANS equations, which admit steady-state solutions.

To obtain the linear operator, one can linearize the equations before the discretization. This has often been done for incompressible laminar flows. However, in the case of the complex flow problems resulting from the compressible RANS equations, which include numerical dissipation and turbulence model, this can imply complex mathematical derivations. This approach is used in combination with a finite volume solver by Crouch *et al.* (2007, 2008, 2009). One can also discretize the equations before the linearization. This approach was presented by Mettot *et al.* (2014). They solved the base-flow using a compressible finite volume RANS flow solver and then linearized the equation around this base-flow. To do so, they applied a small perturbation to every degree of freedom of the discretized problem and evaluated the elements of the Jacobian matrix with a finite difference approach. This method has the advantage of using the flow solver as a black box, making it portable between flow solvers. This method also presents the advantage of being compatible with any numerical scheme and turbulence model combinations. This method can easily be applied to a finite volume solver and the number of residual evaluations is limited when compact stencils are used.

Most of the global stability studies involve the resolution of large eigenvalue problems. In fact, the linearized Navier-Stokes operator is a square matrix of the size of the number of degrees of freedom of the discretized flow problem. Thus, this matrix has a large number of eigenvalues. Theofilis (2011) briefly presents the methods for the computation of the eigen-spectrum. An option is to solve the complete eigenvalue problem. This has been done for some problems but is prohibitive for large ones. Generally, only a few eigenvalues are related to physical modes of interest. Those modes are often the ones with the largest real parts (leading modes i.e. the most unstable modes). This led to the development of algorithms to extract a part of the spectrum. A classic approach to solve eigenvalue problems is the Arnoldi algorithm (Arnoldi, 1951) provided in numerical libraries like ARPACK (Lehoucq *et al.*, 1998). This method targets the eigenvalues with the largest magnitudes. These eigenvalues might not be the ones of interest. Hence, this method is often used in combination with a spectral transformation (Theofilis, 2011) like the shift-and-invert transforma-

tion (Christodoulou and Scriven, 1988) which modifies the problem in order to search the eigenvalues around a prescribed value. This allows to target eigenvalues based on the user knowledge. The drawback of this method is the need to invert a matrix of the size of the linearized Navier-Stokes operator. This can be done for the number of degrees of freedom involved in a solution of the 2D RANS equations with a direct LU decomposition. Libraries developed for the factorization of sparse matrices like MUMPS (<http://mumps.enseeiht.fr/>) can be used. However, the memory cost of such decomposition becomes prohibitive for 3D cases. To avoid this issue, one can replace the direct linear solver by an iterative one like the Generalised Minimal Residual (GMRES) (Saad and Schultz, 1986). For instance, Timme and Thormann (2016) and Xu *et al.* (2015) used a restarted GMRES solver with an incomplete lower-upper (ILU) preconditioner. Preconditioners are required in such methods to help the convergence. This reduces the memory requirement but it can increase the computational time.

Another issue encountered in linear stability is the computation of the base-flow. The main idea of using stability analysis is to study unstable flows. Hence, a steady flow solver can fail to converge to a fixed point (of the steady equations). As an example, the laminar flow behind a circular cylinder admits a steady solution with two counter-rotating symmetric recirculation zones. This steady solution of the Navier-Stokes equations is unstable. Hence, the flow solver can fail to converge to this solution and go in the direction of an unsteady one. As shown by Kamenetskiy *et al.* (2014), varying numerical parameters such as the time stepping scheme, residual smoothing, multigrid, etc. can force the algorithm towards one of the possible flow solutions. However, this may lack robustness and techniques have been developed to force the convergence of the flow solver to steady solutions. One of these is the Selective Frequency Damping (SFD) method proposed by Åkervik *et al.* (2006). This method adds a proportional forcing term to drive the solution towards the steady state. An approximation of the solution is necessary and is taken as a low-pass filtered version of the solution history available in the time marching scheme. The SFD method requires extensive modifications to a baseline flow solver. For this reason, Jordi *et al.* (2014) proposed an encapsulated version of the SFD to be implemented around a flow solver treated as a black box. One of the drawbacks of the SFD is the necessity to fix two parameters, namely the gain of the proportional controller and the width of the low-pass filter. Methods to find the optimal parameters were proposed by Jordi *et al.* (2015) and Cunha *et al.* (2015). The SFD has been applied to the laminar vortex shedding of a cylinder (Jordi *et al.*, 2014, 2015; Haas *et al.*, 2017), to high angle of attack airfoils (Richez *et al.*, 2016; Zhang and Samtaney, 2016), to the separated flow over a shallow bump (Cunha *et al.*, 2015) and stratified-Poiseuille flow (Cunha *et al.*, 2015). One

interesting feature of the SFD is the fact that it can also act as an acceleration technique similar to the multigrid for steady flows (Plante and Laurendeau, 2018). Another approach is to use a Newton iteration to converge to the steady state (Kamenetskiy *et al.*, 2014; Busquet *et al.*, 2017; Wales *et al.*, 2012). However, such techniques might lack robustness. Hence, one must carefully choose the starting point of the iterative methods. Finally, the *Boostconv* algorithm of Citro *et al.* (2017) has been proposed as an alternative to the SFD.

### 1.3 Subsonic stall

This section presents a review of the literature concerning wing stall. This review will present studies of various types of stall, but will focus on experimental and numerical studies involving the presence of three-dimensional cellular patterns (i.e. stall cells).

#### 1.3.1 Two-dimensional stall classification

Three principal types of stall are observed on two-dimensional airfoils. This classification is the one proposed by McCullough and Gault (1951). Figure 1.5 provides support for this section. The studied geometries are the NACA63-009, NACA63<sub>1</sub>-012, NACA63<sub>3</sub>-018, NACA64A006 and a double wedge airfoil. These airfoils are symmetrical and cover a wide range of thickness to chord ratios. The first stall type, trailing edge stall, is usually observed for thick airfoils. In this case the flow separates from the rear part of the airfoil and the separation line progresses towards the leading edge when the angle of attack is increased. Stall occurs when the loss of lift caused by the separation is no longer balanced by the attached portion of the flow field. This type of stall is usually smooth since the slope of a lift versus angle of attack curve will decrease over a large range of angles of attack. This type of stall is represented by the NACA63<sub>3</sub>-018, which is the thickest airfoil considered. NACA63<sub>1</sub>-012 and NACA63-009 exhibit a leading edge type stall. One can see that the lift versus angle of attack curve increases linearly up to the maximum lift angle of attack. At this angle of attack, an abrupt reduction of the lift coefficient occurs. This means that the flow stays attached up to the stall and separates abruptly from the leading edge. In the experiments of McCullough and Gault (1951) the flow was separated over the entire suction side at stall. The last stall type observed by McCullough and Gault (1951) is the thin airfoil stall. This type of stall is observed for sharp leading edge (double wedge) and thin airfoil. In this case, a laminar separation happens near the leading edge and the flow reattaches downstream. The reattachment point moves downstream with increasing angle of attack, leading to the plateau in the lift coefficient curves (Figure 1.5). This classification is a simple representation of stall phenomenon and combinations of these phenomena can happen simultaneously.



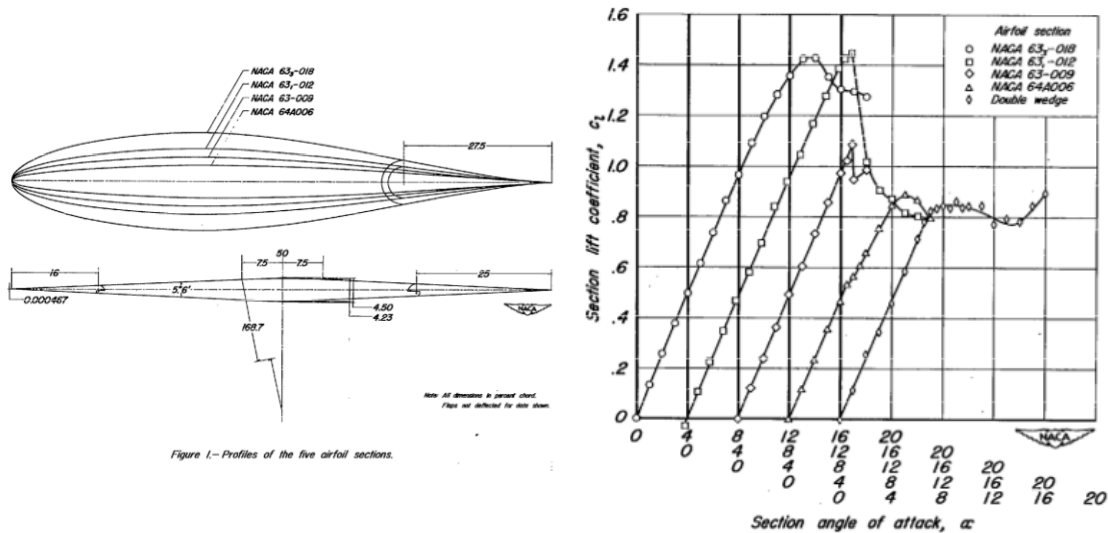


Figure 1.5 – Stall types:  $C_L - \alpha$  curves for 5 airfoils geometries (taken from McCullough and Gault (1951))

### 1.3.2 Stall cells

#### Experimental studies

Multiple experimental studies exhibit the presence of three-dimensional flow structures known as stall cells, owl faces or mushrooms on configurations which are essentially two-dimensional. Experimental results for stall cells are summarized in Table 1.1. In most cases the wavelength of the stall cells is approximated based on available flow visualization and the stall cells can be irregular. These flow structures have been observed since the 1970's (Moss and Murdin, 1971; Gregory *et al.*, 1971) for wings spanning the entire wind tunnel width. At the time, the possibility of an origin of the stall cells caused by the presence of side walls was not excluded and one or two cells were observed depending on the span of the wing. The experimental results of Winkelmann and Barlow (1980) (Figure 1.6) exclude the sidewalls as a cause for the appearance of the stall cells. They tested rectangular wings based on a Clark Y airfoil with aspect ratios from 3 to 12 and free tips. Their results show an increase in the number of cells with the aspect ratio.

Schewe (2001) studied the effect of the Reynolds number on the formation of stall cells for the FX77W270 airfoil, a circular cylinder and a trapezoidal shape. He observed the formation of three-dimensional structures on wings of aspect ratio 4 (2 cells) and 6 (4 cells). Since the number of cells increases with the aspect ratio and there is no zone of two-dimensional flow

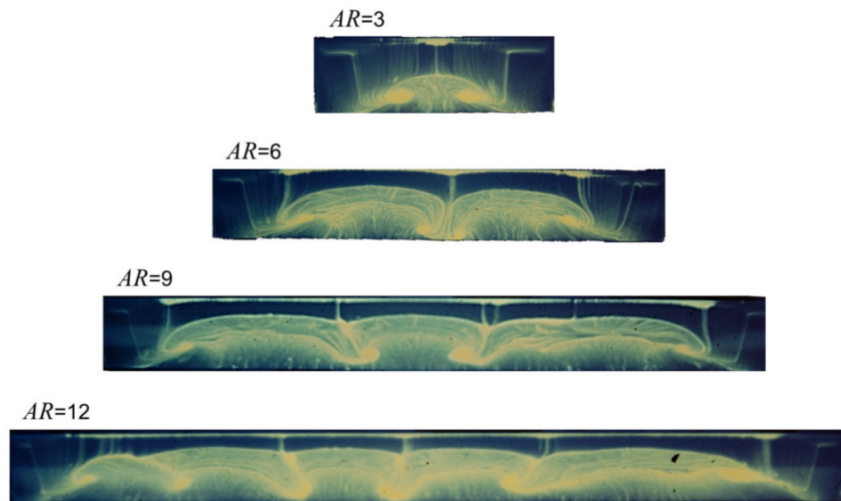


Figure 1.6 – Stall cells for various aspect ratio (reproduction of Winkelmann and Barlow (1980), taken from Disotell and Gregory (2015))

over the wing once the cells appear, he concluded that the stall cells will still be present for an infinite wing. This study tends to further eliminate the wind tunnel walls as a cause for the three-dimensional flow.

Broeren and Bragg (2001) studied 5 airfoils with 4 different stall behaviors. The Ultra Sport airfoil exhibits a trailing edge stall, the NACA2414 a leading edge stall and NACA64A010 a thin-airfoil stall. The last two airfoils (LRN-1007 and E374) showed a combination of thin airfoil and trailing edge stall. This paper relies on previous observations of stall conditions exhibiting low frequency two-dimensional unsteady flows or three-dimensional features. They concluded that there is a fundamental difference between the two phenomena. In particular, they observed the presence of steady 3D flows over a range of angles of attack near the maximum lift for the NACA2414 and Ultra Sport airfoils. For the other airfoils the flow was two-dimensional and a low frequency oscillation in the range of  $St = \frac{f c \sin \alpha}{V_\infty} = 0.02$  was observed. Since most of the studies on stall cells are carried out for airfoils with trailing edge stall behavior, this seems to confirm a relation between the stall type and the occurrence of stall cells. The two airfoils which exhibit stall cells have a portion of the  $C_L - \alpha$  curve where the slope is slightly negative or flat. This is characteristic of a trailing edge stall behavior, even though it is reported that the NACA2414 has a leading edge type of stall.

The low-frequency oscillations have been investigated in several studies (Bragg *et al.*, 1993, 1996; Broeren and Bragg, 1999; Zaman *et al.*, 1987, 1989). The particularity of this phe-

nomenon is its Strouhal number of 0.02 to 0.04 instead of the well-known vortex shedding frequency which has a Strouhal number of 0.2. Bragg *et al.* (1993) presented results for a LRN(1)-1007 airfoil at a Reynolds number of  $3 \times 10^5$  and subsonic flow conditions. They observed oscillations at a Strouhal number of 0.02 for angle of attack of  $14^\circ$  and  $15^\circ$  and the classic vortex shedding Strouhal number of 0.173 for an angle of attack over  $25^\circ$ . This study also shows that this low frequency is present for Reynolds numbers up to 1.36 million. Bragg *et al.* (1996) observed this low frequency over a range of angles of attack from 14.4 degrees to 16.6 degrees and a range of Reynolds number from 0.3 to 1.25 million. Their results show that the frequency slightly increases with both the Reynolds number and the angle of attack. They also associated this frequency to the presence of a leading edge separation bubble. This was confirmed by the elimination of the unsteadiness when a zigzag tape was used to suppress the separation bubble. These studies provide further evidences that this low frequency oscillation is not linked to the stall cells. This oscillation seems to be linked to a leading edge separation bubble, while the stall cells are related to a trailing edge separation. Busquet *et al.* (2017); Busquet (2020) observed a very low frequency unstable mode using global stability analysis about a two-dimensional converged flow solution in the post stall regime. Thus suggesting a link between this unsteadiness and a global unstable mode.

Yon and Katz (1998) reported stall cells for a narrow range of angles of attack spanning  $2^\circ$  to  $3^\circ$  centered around  $17^\circ$ . The experiment was conducted for a NACA0015 airfoil at a Reynolds number of  $6.2 \times 10^5$ . The boundary layer was not tripped, but the investigators assumed a turbulent boundary layer on the suction side of the airfoil. They reported high frequency arbitrary motion of the cells, as well as their momentaneous merging. They also reported stable patterns with two cells for aspect ratio between 3.5 and 4.5. This suggests that the stall cells have a preferential aspect ratio. When this aspect ratio is not supported by the span of the wing, a transition between multiple flow patterns happens. They measured high amplitude, low frequency pressure fluctuations inside the stall cells. This low frequency is around a Strouhal number of 0.04. However, their analysis leads them to think that there is no link between stall cells and this low frequency phenomenon, similar to the one observed by Zaman *et al.* (1989).

Elimelech *et al.* (2012) presented the experimental study of two airfoils at Reynolds numbers between 10 000 and 20 000 using Constant Temperature Anemometry (CTA). Two aspect ratios were investigated with models having different chord lengths. They observed the presence of 2 and 4 cellular flow patterns for aspect ratio of 2.5 and 5 respectively. A comparison between a converged 2D CFD simulation and the velocity profiles in the middle

and outside of a cell shows that the flow outside the cell behave like a 2D flow. Also, since the cells have been observed across a wide range of Reynolds numbers by many authors, Elimelech *et al.* (2012) suggested that the cellular patterns are caused by inviscid effects.

Manolesos and Voutsinas (2013, 2015) and Manolesos *et al.* (2014) conducted experimental investigations on a wind turbine airfoil with trailing edge stall. They tried to induce local or full span disturbances with zigzag tapes. Without disturbances, various patterns of stall cells were reported. The presence of 1, 1.5 or 2 cells was reported and the pattern changed in time. Using a zigzag tape to trip the boundary layer along the full span did not change the flow behavior. Placing the disturbance on the tips of the wing induced two half cells near the wind tunnel walls. Most of their results were produced with a local disturbance of 10% span on the center of the wing to induce a single stable stall cell.

Dell’Orso *et al.* (2016) and Dell’Orso and Amitay (2018) studied a NACA0015 airfoil and found that the stall cells only appear for specific combinations of Reynolds numbers and angles of attack. They observed eight different surface oil flow patterns (from a 2D separation to fully formed stall cells) depending on the angle of attack and the Reynolds number. Similarly to Manolesos *et al.* (2014), they induced the formation of stall cells using zigzag tape. Sarlak *et al.* (2018) studied a S826 airfoil at several Reynolds numbers. They observed an effect of the Reynolds number on the formation of stall cells. For low Reynolds numbers, no stall cells were found. This result is similar to the observation of Dell’Orso and Amitay (2018). They also reported that more distinct vortex pairs were obtained when a surface roughness was added.

## Numerical studies

Many authors investigated the stall cells with numerical simulations. Table 1.2 compiles some of these results. For instance, Bertagnolio *et al.* (2005) encountered these flow structures in the URANS simulation of a 3D wind turbine blade. They might be present in their DES simulation as well. However, no detailed results of the 3D flow structure were presented. Zarutskaya and Arieli (2005) presented solutions of the steady RANS equations obtained with the Fluent Solver on a wing based on the NACA0012 airfoil at an intermediate ( $390000$ ) and a high ( $4.6 \times 10^6$ ) Reynolds number, and a wing based on the NASA SC2 airfoil at a high Reynolds number of 4.6 million. Simulations were carried out on a half wing with a symmetry condition at one end and a free wing tip at the other. For these three configurations, two stall cells are reported over a range of angle of attack of two to three degree in

Table 1.1 – Experimental studies of stall cells

	Profile	AR	$Re_c(10^6)$	nb. cells	$\frac{\lambda}{c}$	Sidewall	Flow Visualization
Moss and Mordin (1971)	NACA0012	3.75	0.84, 1.68	1	$\sim 2.5$	Tunnel walls	Oil surface flow
Gregory <i>et al.</i> (1971)	NACA0012	1.42	1.7	1	$\sim 1.2$	Tunnel walls	Oil surface flow
	NPL9619	3.29	0.85, 3.14	1, 2	$\sim 2.5$ , $\sim 1.6$	Tunnel walls/End-plates	
Winkelmann and Barlow (1980)	Clark Y	3.59	2.88	2	$\sim 1.2$	Free tips	Oil surface flow
		3.5	0.245	1	$\sim 3$		
		3		2	$\sim 1$		
		6		2	$\sim 2.3$		
		9		3	$\sim 2.4$		
Yon and Katz (1998)	NACA0015	12		5	$\sim 1.9$	End-plates	Tufts
		3	0.62	1.4	2.1		
		3.5		2.0	1.8		
		4		2.0	2.0		
		4.5		2.0	2.25		
		5		2.5	2		
Broeren and Bragg (2001)	Ultra Sport NACA2414	2.8	0.3	1.5	1.8	Tunnel walls	Tufts
	Schewe (2001) FX-77-W270	4	0.12	2	$\sim 1.25$	Tunnel walls	Oil surface flow
Elimelech <i>et al.</i> (2012)	NACA0009	6	0.74	4	$\sim 1.25$	Tunnel walls	CTA
		2.5	0.01-0.018	2	1.25	Tunnel walls	
Manolesos and Voutsinas (2013)	NTUA t18	5	0.01-0.018	4	1.25	Tunnel walls	
		1.5, 2.0	0.5-1.5	1	1.5-2.0	Endplates	Tufts
Dell’Orso <i>et al.</i> (2016)	NACA0015	4	0.209-0.481	0-2	$\infty - 2$	Tunnel walls	Oil surface flow
Dell’Orso and Amitay (2018)	NACA0015	4	0.299-0.447	0-2	$\infty - 2$	Tunnel walls	Oil surface flow
Sarlak <i>et al.</i> (2018)	S826	5	0.16	2	$\sim 1.5$	Tunnel walls	Oil surface flow

the post-stall regime. However, from the flow visualization shown in the article, there seems to be one and a half cells, with the half cell cut by the symmetry plane. Moreover, the stall cells do not extend up to the wing tip. Hence, one can estimate the stall cells to have a wavelength of 2 chords. A similar number of cells were observed experimentally for the wing at a Reynolds number of 390 000. It should be noted that the two airfoils exhibit a trailing edge type stall behavior.

Table 1.2 – Numerical studies of stall cells

	Profile	$Re_C(10^6)$	$\alpha[^\circ]$	AR	$\frac{\Delta z}{c}$	Model	Turbulence Model	Sidewalls	$\frac{\lambda}{c}$
Bertagnolio <i>et al.</i> (2005)	RISØ-B1-18	1.6	15.9	2.56	0.02	URANS	$k - \omega$ SST	periodicity	$\sim 1.28$
Zarutskaya and Arieli (2005)	NACA0012	0.39	17.0	8		RANS	SA	symmetry, free tip	$\sim 2.0$
	NACA0012	4.6	20.0						$\sim 2.0$
Gross and Fasel (2011)	NASA SC2	4.6	16.0						$\sim 2.0$
	NACA64 <sub>3</sub> -618	0.322	13.2	0.4	0.00625	Hybrid RANS/LES		periodicity	N/A
Kamenetskiy <i>et al.</i> (2014)	NACA0012	2.63	23	4	0.015625	URANS	$k - \omega$	symmetry	
		5	18	1	Unstructured RANS	SA, $k - \omega$ SST	slip wall	1	
Manolesos <i>et al.</i> (2014)	NTUA t18	1	7 - 16	2	0.0248 - 0.0646	URANS	SA	symmetry, slip wall	0.2-1.0
Manni <i>et al.</i> (2016)	NACA0012	1	17 - 19	10	0.5-0.05	URANS	$k - \omega$ SST	periodicity	1.4-1.8
					0.05	DDES	$k - \omega$ SST		

Gross and Fasel (2011) carried-out URANS, hybrid RANS/LES simulations and under-resolved DNS (Implicit Large Eddy Simulation) simulations of airfoils at stall. However, the simulations with LES content were carried out on a domain too small to be relevant for stall cells analysis. Nevertheless, the 3D URANS results showed a curved separation line, but without the clear stall cells observed in other studies. However, a large reduction of the lift coefficient is reported between a three-dimensional and a two-dimensional simulation. Manolesos *et al.* (2014) performed URANS simulations in support to their wind tunnel campaign. Since a zigzag tape was used to perturb the flow on a portion of the wing they used the BAY model (Bender *et al.*, 1999) to perturb the flow in the numerical simulations. Their comparison to experiments showed that the CFD qualitatively reproduced the stall cell behavior. They reported stall cells width from 20% of the chord length to one chord length.

Manni *et al.* (2016) presented the simulations of a stalled wing with a high aspect ratio of 10 and with periodic boundary conditions. The computations were carried out with the SIMPLE algorithm in Fluent with URANS and DDES modeling. For this wing, they carried out a grid refinement study using up to 200 cells in the spanwise direction. In URANS they observed stall cells with an aspect ratio between 1.4 and 1.7. As in other studies, the lift coefficient with stall cells is lower than the one of a two-dimensional flow. Their DDES simulations resulted in a more complex flow field. However, they asserted that similar structures were present in the DDES simulations. From their grid refinement study in URANS they concluded that the spanwise grid spacing should at least be lower than 0.2 chord. This number seems coherent for URANS simulations. However, they reported a chordwise spacing  $\Delta x^+$  of 200 and a spanwise spacing  $\Delta z^+$  of 2100. It is recommended to have a similar grid spacing in the three directions in the LES regions of a DES type simulation (Spalart, 2001). The grid used in this paper for DDES does not respect this criterion.

Flow structures similar to the stall cells were observed by Kamenetskiy *et al.* (2014) using RANS computations. This paper explored the possibility of multiple solutions of the discretized RANS equations, even when the flow solver is converged to machine accuracy. These multiple solutions were obtained by using various numerical setups for the same physical conditions. Some of these solutions exhibited flow patterns reminiscent of stall cells. In particular, the simulation of a wing of an aspect ratio of one and closed by free slip walls shows the presence of the mushroom shape pattern of the stall cells. A lower lift coefficient is also obtained when compared to a purely two-dimensional simulation. The wavelength of the stall cell is one chord length. However, this is constrained by the span of the computational domain. Two flow visualizations are shown, one with the stall cell centered in the

computational domain and the other with the center of the cell aligned with the free slip boundary conditions. Hence, these multiple solutions could be a translation of each other and be essentially the same. Nevertheless, it is possible that the stall cells are one of the possible solutions of the Navier-Stokes equations. Finally, a large number of significantly different fully converged steady solutions were found for simulations over the Trap wing (Rumsey *et al.*, 2011).

## Stall cell models

Recently, Spalart (2014) presented a model for the appearance of stall cells based on the lifting line theory. A similar approach was used by Gross *et al.* (2015) to relate the wavelength of the stall cells to the slope of the lift versus angle of attack curve ( $\frac{\partial C_L}{\partial \alpha}$ ). Based on these two studies, a negative slope of the  $C_L - \alpha$  curve is a necessary condition for the appearance of stall cells and no impact of the type of stall is embedded in the model. These models are consistent with the observation of stall cells by Gallay and Laurendeau (2015) with a Non-Linear Vortex Lattice Method and Paul and Gopalarathnam (2014) with an iterative decambering approach. Both methods couple potential flow theory with viscous lift curves. A previous model for the occurrence of stall cells was proposed by Weihs and Katz (1983) based on the Crow instability (Crow, 1970). The latter is an instability of two infinite parallel vortex lines, usually observed for the wingtip vortices. The model of Weihs and Katz (1983) relies on the presence of a spanwise vortex line on the suction side of the airfoil. By supposing the action of the airfoil surface as the one of a symmetry plane, a counter-rotating vortex can be imagined at equal distance of the pressure side of the airfoil, leading to a situation similar to the one necessary for the Crow instability. It is then possible to deduce a criterion for the wavelength of the cells based on the characteristic length of the Crow instability,  $\lambda = 2h \times 8.6$  with  $h$  the distance between the vortex core and the surface. The models developed for the length of the stall cells are in fair agreement with experimental and numerical results. Gross *et al.* (2015) compared his model to the experiments of Yon and Katz (1998) with a good agreement. Manni *et al.* (2016) also found his URANS computations to be in good agreement with the criterion of Gross *et al.* (2015). Gross and Fasel (2011) tried to compare their URANS results with the criterion of Weihs and Katz (1983), but a great discrepancy is obtained. Weihs and Katz (1983) model's is in good agreement with the wind tunnel results of Winkelmann and Barlow (1980). Finally, Katz (1982) proposed a vortex-lattice model for flow structures similar to stall cells in a locally separated flow. Generally speaking, these results suggest an explanation to the stall cells with inviscid theories. However, the parameters strongly differ between the models.

The origin of the stall cells has been explained by an unstable global mode of the flow separation over an airfoil in laminar regime by Rodríguez and Theofilis (2011). This mode causes the two-dimensional flow over an airfoil to become three-dimensional by inducing a spanwise modulation of the flow. These analyses were carried out for the case of a Joukowski airfoil, similar to the geometry of a NACA0015 airfoil, at a Reynolds number of 200 and an angle of attack of 18 deg. Previously Kitsios *et al.* (2009) observed a similar non-oscillatory mode with a spanwise wavenumber  $\beta = 2\pi/\lambda_z = 1.0$  for an ellipse and a NACA0015 airfoil at a Reynolds number of 200. He *et al.* (2017) carried out the same analysis, but did not find an unstable global mode. Zhang and Samtaney (2016) carried out stability analysis of a NACA0012 at a Reynolds number of 400 to 1000. They found unstable non-oscillatory three-dimensional modes with  $\beta = 2$  and 4 for Reynolds numbers of 800 to 1000.

### 1.3.3 Partial conclusion

The literature on stall cells shows that they occur over a narrow range of angles of attack in the post-stall regime. The phenomenon seems to be linked to the type of stall and is most of the time observed for trailing edge type stall. However, it has also been observed for an airfoil which was stated as having a leading edge stall (Broeren and Bragg, 2001). The experiments show stall cells with a width of 1.0 to 3.0 chord lengths. Numerical results report stall cells with a wavelength between 1.2 and 2.0 chord lengths, with the exception of the study of Manolesos *et al.* (2014). From the literature, the cells seem to be steady. However, the superposition of various flow unsteadiness can be observed, or a transition between various stall cells patterns. The latter could probably be attributed to a preferential stall cell size. One of the issues for this thesis is the low Reynolds numbers used in the experiments, since the laminar to turbulent transition remains one of the great challenges of CFD. Most of the studies did not use a boundary layer trip to force the transition. Numerical solutions with (U)RANS modeling allow for the representation of stall cells. Limited comparison between experiences and computations are available. This might be caused by the fact that most of the experimental studies do not impose the transition to turbulence. DES type simulations could be useful to get a better modeling of the separated flow. However, the results in the literature seem to use grids that are too coarse in the spanwise direction. Finally, multiple models based on inviscid theories have been proposed with a fair agreement to the wavelength of the stall cells observed both numerically and experimentally.



## 1.4 Transonic buffet

Transonic buffet results from a strong interaction between the shock wave and the separated boundary layer over a wing or an airfoil. An extensive literature review on transonic buffet has been recently published by Giannelis *et al.* (2017). Typically, buffet is separated into two types. The first one occurs at zero angle of attack on symmetric airfoils with the presence of a shock wave on both the upper and lower surfaces. In this case, the interaction of the shock waves and the boundary layers is locked. This yields a cycle of back and forth movement of the shock on both sides of the airfoil with a phase shift of  $180^\circ$ . The second type of buffet involves oscillations of the shock position on the suction side of the airfoil, with a periodic separation and reattachment of the boundary layer. A large, and the most recent, body of work is devoted to the second buffet type since it is encountered on non-symmetric airfoils in conditions near the operating regime of modern aircraft. Hence, this thesis will focus on this type of buffet.

### 1.4.1 Two-dimensional buffet

#### Experimental studies

Two-dimensional buffet has been experimentally investigated by McDevitt and Okuno (1985) on a NACA0012 airfoil. This database has been used as a reference for the prediction of the buffet onset in many studies, since a large number of angles of attack and Mach numbers are presented. Benoit and Legrain (1987) studied the transonic buffet over a RA16SC1 airfoil and a wing typical of transport aircraft. Jacquin *et al.* (2009) presented the results of a wind tunnel campaign on the OAT15A airfoil. This experimental database has been used as validation data for many numerical studies carried out in the past decade. More precisely, the results for an angle of attack of  $3.5^\circ$ , a Mach number of 0.73 and a Reynolds number of 3 million have been widely used for code comparison (see Figure 1.7). Recently, Brion *et al.* (2017) presented an experimental campaign aiming at studying the transonic buffet over a laminar airfoil. This type of airfoil presents an increasing interest in order to reduce drag and fuel consumption of civil aircraft. The ONERA OALT25 airfoil was used. The experiments have been carried out with a boundary layer tripped, to force the transition to the turbulent regime, at 7% and 40% chord as well as free transition. In the latter, the laminar to turbulent transition happens near the shock foot. The observations with a tripped boundary layer are similar to those over other airfoils. Table 1.3 summarizes the buffet frequencies in these studies. One can observe that the buffet frequencies are all included in a range of Strouhal numbers from 0.06 to 0.09. The exception is the result of Brion *et al.* (2017), on the

laminar airfoil with free laminar to turbulent transition, for which the frequency is an order of magnitude higher. In this case the transition to turbulence happens at the shock foot, resulting in a different buffet mechanism. This physics has been studied by Bonne (2018) and by Dandois *et al.* (2018). This also suggests that the buffet mechanism is the same for every airfoil, provided that the laminar to turbulent transition occurs upstream of the shock foot.

## Numerical studies

A non-exhaustive summary of the results obtained by many researchers for the simulation of the 2D transonic buffet is presented in Table 1.4. The numerical methods used for buffet simulation span from viscous-inviscid strategies to LES and LBM. This section comments on the difficulty arising from the numerical simulation of buffet and the physics modeled by such computations.

In an early attempt to simulate the transonic buffet, Le Balleur and Girodoux-Lavigne (1989) used a viscous-inviscid coupling and Edwards (1993) used an Interactive Boundary Layer Coupling Method. Since the turbulent boundary layer is modeled in these methods, the results suggest that transonic buffet is related to large features of the flow field and not the small-scale unsteadiness of the turbulence. For this reason, the bulk of the transonic buffet simulations have been produced with URANS simulations.

The effect of the numerical scheme has been investigated by Goncalves and Houdeville (2004). They used different discretizations of the convective fluxes, namely the Roe scheme (Roe, 1981), the AUSM+ scheme (Liou, 2001), the Jameson Schmidt and Turkel (JST) scheme (Jameson *et al.*, 1981) and a modified version of the JST scheme. The MUSCL extrapolation is used in the case of the Roe and AUSM schemes. The k- $\omega$  Menter SST model is used for closure of the URANS equations. Transonic buffet onset is captured with all

Table 1.3 – Experimental studies of two-dimensional buffet

	Profile	Mach	$Re_c$ (million)	$\alpha$ ( $^\circ$ )	$St$	
McDevitt and Okuno (1985)	NACA0012	0.75	10.0	4.0	0.075	
		0.77			0.070	
		0.80			0.060	
		0.72			6.0	0.088
Benoit and Legrain (1987)	RA16SC1	0.73	4.1	3.0	0.067	
				4.5	0.083	
				3.25	0.066	
Jacquin <i>et al.</i> (2009)	OAT15A	0.73	3.0	3.5	0.066	
					3.9	0.066
					3.5	0.062
					3.5	0.073
					3.5	0.070
Brion <i>et al.</i> (2017)	OALT25	0.735	3.0 tripped 7% 3.0 laminar		1.0	

Table 1.4 – Numerical studies of two-dimensional buffet

	Profile	Model	Turbulence Model	Convective scheme	Mach	$Re_c$ (million)	$\alpha$ (°)	$St$	$\Delta C_L$
Le Balleur and Girodoux-Lavigne (1989)	RA16SC1 NACA0012	Viscous-inviscid	NA	N/A	0.723	4.2	4.0		
					0.775	10.0	4.0	0.055	$\sim 0.34$
Edwards (1993)	NACA0012	Viscous-inviscid	N/A	N/A	0.725	10.0	4.0	0.051	
					0.750		3.5	0.041	
							4.0	0.073	
					0.775		2.5	0.048	
							4.0	0.080	$\sim 0.25$
					0.8		1.75	0.029	
Goncalves and Houdeville (2004)	RA16SC1	URANS	SA	JST	0.835	4.2	3.0	0.063	0.0146
			$k-l$ SST		0.642		0.061	0.0084	
			$k-\epsilon$ Durbin				0.066	0.012	
			$k-\omega$ SST				0.069	0.11	
			Menter						
			SA				4.0	0.070	0.325
			$k-l$ SST					0.075	0.296
			$k-\epsilon$					0.073	0.17
			$k-\epsilon$ SST					0.073	0.48
			$k-\epsilon$ Durbin					0.072	0.437
			$k-\omega$ SST					0.074	0.33
			Menter						
			$k-\omega$ Kok					0.073	0.26
			$k-\omega$ Kok SST					0.073	0.26
			$k-\omega$ Kok					0.073	0.26
			Durbin						
			SA				5.0	0.077	0.55
			$k-l$ SST					0.078	0.53
			$k-\epsilon$					0.075	0.43
			$k-\epsilon$ SST					0.078	0.67
$k-\epsilon$ Durbin			0.078	0.67					
$k-\omega$ Kok			0.074	0.48					
$k-\omega$ Kok SST			0.074	0.445					
$k-\omega$ Kok			0.074	0.45					
Durbin									
$k-\omega$ SST		Roe MUSCL		3.0	0.069	0.014			
Menter									
							0.069	0.018	
				AUSM+ MUSCL			4.0	0.077	0.3
				Roe MUSCL				0.076	0.307
				AUSM+ MUSCL					
				AUSM+P	0.73	3.0	4.5	0.066	
Deck (2005a)	OAT15A	URANS	SA				3.5		
		ZDES	SA				6.97	0.05	$\sim 0.65$
Xiao <i>et al.</i> (2006)	BGK 1	URANS	$k-\omega$ with lag model	Roe	0.71	20.0			
Thiery and Coustols (2006)	OAT15A	URANS	$k-kl$	JST	0.73	3.0	3.5	$\sim 0.065$	0.22
			$k-\epsilon$ SST				$\sim 0.075$	0.14	
			SA confined				$\sim 0.075$	0.21	
			$k-kl$ confined				$\sim 0.063$	0.42	
			$k-\epsilon$ SST confined				$\sim 0.069$	0.36	
Garnier and Deck (2010)	OAT15A	LES	N/A	modified Roe	0.73	3.0	3.5	0.069	
Iovnovich and Raveh (2012)	NACA0012	URANS	SA	HLLC	0.75	10.0	4.0	0.062	0.1
					0.77		4.0	0.064	0.23
					0.72		6.0	0.080	0.46
					0.732		4.0	0.068	0.4
					0.75		5.5	0.054	0.2
Huang <i>et al.</i> (2012)	OAT15A	IDDES	$k-\omega$ SST	STVD	0.73	3.0	3.5	0.074	$\sim 0.33$
Grossi <i>et al.</i> (2014)	OAT15A	URANS	EDW+CC	Roe MUSCL	0.73	3.0	3.5	0.070	$\sim 0.3$
			DDES					0.077	$\sim 0.3$
			EDW+CC						
Ishida <i>et al.</i> (2016)	OAT15A	ZDES	SA-RC	SLAU	0.73	3.0	3.5	$\sim 0.066$	
	OAT15A	IDDES						$\sim 0.057$	
Ribeiro <i>et al.</i> (2017)	OAT15A	LBM	modified $k-\epsilon$	N/A	0.73	3.0	1.5 to 3.9		
Bonnifet (2018)	OAT15A	PANS	GLVY-RSM	WENO	0.73	3.0	3.9	0.067	
					0.75	3.0	5.0	0.073	
					0.743	3.0	4.3	0.073	
					0.735	3.0	3.9	0.072	
					0.73	3.0	3.5	0.069	0.16
Giannelis <i>et al.</i> (2018)	OAT15A	URANS	$k-\omega$ SST, reduced $a_1$	Roe MUSCL	0.73	3.0	3.0	0.069	0.16
					0.72		3.5	$\sim 0.064$	
					0.74		3.5	$\sim 0.074$	
					0.68		5	$\sim 0.050$	$\sim 0.31$
					0.68		6	$\sim 0.067$	$\sim 0.58$
					0.68		7	$\sim 0.087$	$\sim 0.48$
					0.60		6.5	$\sim 0.052$	$\sim 0.18$
					0.66		6.5	$\sim 0.066$	$\sim 0.54$
					0.71		6.5	$\sim 0.083$	$\sim 0.51$
								0.0715	0.33
								$\sim 0.066$	
					Fukushima and Kawai (2018)		OAT15A	WMLES	SORSM
Deck and Renard (2020)	OAT15A	ZDES	SA		0.73	3.0	3.5	0.065	$\sim 0.34$

these schemes. However, the buffet amplitude is higher with the JST scheme, resulting in an amplitude closer to the experiments for the angle of attack of  $3^\circ$  and an overestimation of the amplitude at  $4^\circ$ . For all cases, the frequency stays close to the experimental results.

Thiery and Coustols (2006) pointed out the effect of the turbulence model and the effect of the wind tunnel test sections. They tested the Spalart-Allmaras (SA) (Spalart and Allmaras, 1992),  $k-kl$ ,  $k-\omega$  and  $k-\omega$  SST models (Menter, 1994). For a classic 2D simulation with far field conditions, only the  $k-kl$  and  $k-\omega$  SST models developed a self-sustained lift oscillation at the conditions of the experiments. They observed that an increase of one degree of the angle of attack was required to capture the transonic buffet with the SA model. A similar observation was made by Deck (2005a) in his URANS simulation. By taking into account the confinement of the wind tunnel walls, the SA model also produced an unsteady behavior at the conditions of the experiments. Their results also showed a weak dependency of the frequency to the turbulence model and far field conditions, but the amplitude and time-averaged value of the lift oscillation is strongly impacted by the numerical setup. The effect of the turbulence model on the simulation of the transonic buffet has also been investigated by Goncalves and Houdeville (2004). They used an extensive selection of turbulence models, with a wall law approach. For brevity, Table 1.4 only reports combinations of parameters for which the flow is unsteady and some turbulence models failed to compute an unsteady behavior. For the case presented by Goncalves and Houdeville (2004) the experimental results show a Strouhal number of 0.067 and 0.077 for an angle of attack of  $3^\circ$  and  $4^\circ$  respectively. Hence, the numerical frequencies are similar to the experiments with a maximum error of 9.0% when the unsteadiness is captured. However, the amplitude of the lift oscillation exhibits a large discrepancy from one model to the other and the angle of attack of  $5^\circ$  is out of the buffet regime in the experiments, while some simulations still produce buffet.

Recently, Giannelis *et al.* (2018) carried out an extensive survey of the effect of the Mach number and the angle of attack on the transonic buffet over the OAT15A airfoil with URANS simulations. This study used ANSYS Fluent R18.0 with the Menter SST turbulence model, modified to reduce the  $a_1$  coefficient. This once again stresses out the sensitivity of transonic buffet computations to turbulence modeling. Computations with a Reynolds Stress Model (SORSM) and the Spalart-Allmaras model with curvature correction (SA-RC) were also presented. The SA-RC model failed to predict unsteadiness at the experimental conditions and the SORSM over-predicted the buffet amplitude. This study shows that the behavior of the flow changes from periodic to pseudo-periodic between the buffet onset and buffet offset when increasing the angle of attack. The idea of simulating buffet from onset to offset has

also been investigated for a smaller number of conditions by Iovnovich and Raveh (2012). They studied the buffet over three airfoil geometries and suggested that buffet onset occurs in conditions for which the shock is near, yet aft, of the maximum curvature location of the airfoil suction side.

The effects of numerical scheme and turbulence model have motivated the use of higher fidelity numerical methods such as hybrid RANS/LES. These methods reduce the impact of the choice of turbulence model since LES is used in the separated flow regions, where the turbulence model is the most inaccurate. Most of these studies are carried out for the OAT15A airfoil at Mach 0.73, Reynolds 3 million and an angle of attack of  $3.5^\circ$  (wind tunnel tests of Jacquin *et al.* (2009)). Deck (2005a) used the ZDES and DES methods, to compute the transonic buffet. To reduce the number of grid points, the RANS region was treated as a 2D flow and a 2D/3D coupling strategy was used to connect with the ZDES regions. RANS was imposed on most of the pressure side and on the first part of the suction side of the airfoil, to use DES only in regions where the flow separates. They found that an angle of attack higher than the experimental one was required to compute unsteady buffet with URANS and DES. However, ZDES predicted unsteadiness at the experimental angle of attack with an averaged shock position slightly upstream of the experiments. Grossi *et al.* (2014) carried out URANS and DDES simulations of the OAT15A airfoil. They compared a selection of RANS turbulence models. The addition of the compressibility correction (Spalart, 2000b) and the Edwards-Chandra modification (Edwards and Chandra, 1996) to the Spalart-Allmaras model resulted in a buffet amplitude close to the experimental one. Other studies used a similar model (Crouch *et al.*, 2007; Plante *et al.*, 2017). This model is used in the DDES implementation of Grossi *et al.* (2014). For the same test case, Ishida *et al.* (2016) used IDDES and ZDES. In their ZDES computations, a RANS region is imposed in the near wall region with a thickness based on the boundary layer thickness at the shock foot, taken from a steady RANS case. The thickness of this RANS region had a great impact on their results. If it is too small, the shock position moved towards the leading edge and the amplitude of the buffet is smaller. However, this thickness must be limited in order to activate the LES model.

Going to a higher resolution, Garnier and Deck (2010) presented LES computations of the OAT15A airfoil and Fukushima and Kawai (2018) used Wall-Modeled LES (WMLES). Ribeiro *et al.* (2017) used the commercial LBM solver PowerFLOW to compute LBM-VLES simulations. This method includes the use of a RANS type turbulence model and the resolution of a part of the turbulent fluctuations. These simulations produced accurate, yet expensive

numerical simulations. For the case of the laminar transonic buffet of the OALT25, a LES simulation has been carried out by Dandois *et al.* (2018) with very good agreement to the experiments for both the frequency and time-averaged pressure distribution. However, the physical mechanisms involved in this flow are different and the Strouhal number is around 1.2 rather than 0.06-0.07 for turbulent buffet. Memmolo *et al.* (2018) studied the two-dimensional buffet of a V2C supercritical laminar airfoil with URANS, DDES and ILES. However, they compared URANS and DDES with an incoming turbulent boundary layer to a ILES without a boundary layer trip to force the turbulence in the boundary layer. They found a similar buffet onset boundary with URANS and DDES, but a different lift signal and time-averaged pressure distribution. From the provided lift and drag signals, one can compute a dominant Strouhal number around 0.08 in the URANS and DDES simulations, which is to be expected for the two-dimensional buffet. The authors report a Strouhal number of 0.1 (close to the turbulent buffet Strouhal number) and a Strouhal number of 1.0, which they state is related to the boundary layer separation, for the ILES. The higher frequency is similar to the laminar buffet frequency found by Dandois *et al.* (2018). However, Memmolo *et al.* (2018) associate it to a different mechanism, even though the small concavity characteristic of a laminar separation bubble is observed upstream of the shock wave in the time-averaged pressure distribution. For this reason, one can question their interpretation of the results.

Figure 1.7 compiles the time-averaged pressure coefficients of studies cited in the previous paragraphs and the number of grid cells as a metric for the computational cost. One can observe the characteristic pressure distribution of a supercritical airfoil, with a pressure plateau before the shock. However, the time averaging of the buffet oscillation results in a smeared transition between the plateau and the recompression zone. In the DES type results reported here, the pressure coefficient is over-predicted near the trailing edge. The pressure plateau is also too low. This is not the case with the URANS simulation of Grossi *et al.* (2014) where the plateau and the trailing edge pressures agree with the experiments and only the time-averaged shock wave position is slightly shifted. However, this result is obtained with a turbulence model specifically selected to match the experiment and the literature shows a great variation of the results depending on the turbulence model. A recent simulation by Deck and Renard (2020) shows a correct prediction of the supersonic plateau and trailing edge pressure with a new version of the ZDES mode 2. However, the shape of the time-averaged shock is different than the experimental one. Moreover, the number of points in the simulation is in the range of the one used in older LES simulations. The LES results are in good agreement with the experiments, with the only discrepancy being the position of the shock. This is interesting since the LES reduces to the maximum the

effect of turbulence modeling. It is hard to identify the cause of the discrepancies between hybrid RANS/LES and LES or URANS results from these results, since the number of grid points vary significantly between computations. However, they suggest that the transition between LES and RANS must be carefully treated since URANS and LES alone provide results in fair agreement with the experiments. The over predicted pressure coefficient near the trailing edge might be attributed to the quality of the grid, since most of these studies used similar grids. Also, the difference between RANS and Hybrid RANS/LES upstream of the shock is unexpected since the RANS behavior should be maintained in this part of the domain. The LBM-VLES method (Ribeiro *et al.*, 2017) gives a solution which is close to the LES results. Partially-Averaged Navier-Stokes simulations have also been successfully carried-out (Bonnifet, 2018; Bonnifet *et al.*, 2017).

An alternative to the classic URANS approach has been tested by the author (Plante *et al.*, 2017) using a time spectral approach to solve the transonic buffet over the OAT15A airfoil. This method assumes a periodic flow of known frequency to discretize the time derivative with a pseudo-spectral operator. Hence, an iterative method (McMullen, 2003; Hall *et al.*, 2013) was used to converge the frequency as an unknown of the problem and fed to the frequency domain solver. This method proves to be able to reproduce the dual time stepping solution of the URANS equations with as few as 3 or 5 modes (7 or 11 time samples over a buffet period). This result confirms that the 2D buffet occurs at a well-defined frequency since the Time Spectral approach only takes into account harmonics of the dominant frequency. It also provides evidence that URANS is able to model the main features of buffet since the temporal sampling is very coarse. Nevertheless, the method has an exponential convergence in number of modes and yields accurate solutions.

## Partial conclusion

Two-dimensional transonic buffet is generally described as a high amplitude oscillation of the shock position associated with a detachment/reattachment of the boundary layer thus inducing large oscillations of the aerodynamic forces. This phenomenon occurs at a well-defined frequency in a range of Strouhal numbers from 0.06 to 0.1 in turbulent regime. From a numerical point of view, URANS simulations manage to reproduce experimental results. However, the combination of numerical schemes and turbulence model must be carefully chosen. This point is emphasized by the capacity of a frequency domain solver to produce accurate solutions. The studies carried out with hybrid RANS/LES methods can be less sensitive to such parameters. Nevertheless, some discrepancies are present between the

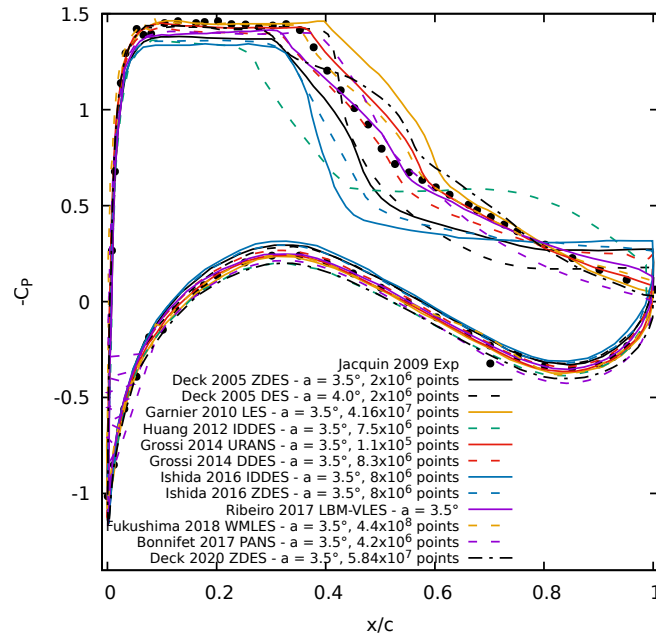


Figure 1.7 – Time-averaged pressure coefficient over the OAT15A airfoil

numerical results and the experimental ones. Such discrepancies are not observed for LES simulations. This suggests that great care must be taken in the coupling of RANS models with LES simulations.

### 1.4.2 Three-dimensional buffet

This section presents numerical and experimental studies on the three-dimensional buffet. Tables 1.5 and 1.6 respectively compile numerical and experimental results of 3D buffet. This review focuses on the frequency content of the buffet and the presence of cellular patterns.

#### Numerical studies

Sartor and Timme carried out several studies of the three-dimensional transonic buffet on a half wing-body configuration representative of modern transport aircraft (RBC12). They (Sartor and Timme, 2015) presented URANS computations with various turbulence models. As it can be expected, the turbulence model has an effect on the buffet onset and amplitude. They also carried out an extensive study of the effects of the Mach number and the angle of attack (Sartor and Timme, 2016), which is not common for three-dimensional buffet due to



Table 1.5 – Numerical studies of three-dimensional buffet

	Configuration	Sweep ( $^{\circ}$ )	Mach	$Re_{MAC}$ (million)	$\alpha$ ( $^{\circ}$ )	Model	$St$ or $f$
Brunet and Deck (2008)	CAT3D		0.82	2.8	4.2	ZDES	100-200 Hz
Sartor and Timme (2016)	RBC12	25	0.74-0.84	3.75	0.0-5.6	URANS	0.1-0.4
Sartor and Timme (2017)	RBC12	25	0.8	3.75	3.8	DDES	0.15-0.3
Ohmichi <i>et al.</i> (2018)	CRM	35	0.85	1.5	4.87	ZDES	0.2-0.6
Ribeiro <i>et al.</i> (2017)	CRM	35	0.85	1.5	4.87	LBM	
			0.85		5.92		
			0.84		6.58		
Hashimoto <i>et al.</i> (2018)	CRM	35	0.85	1.5	4.87	ZDES	500-1000 Hz
Masini <i>et al.</i> (2020a)	RBC12		0.801	3.75	3.1	DDES	0.22 and 0.27(broadband)

the large computational resources required for unsteady simulations. They report broadband frequencies in the order of 100 to 400  $Hz$  for Strouhal numbers in a range from 0.1 to 0.4. One should note that the Strouhal number is based on a characteristic dimension which is usually taken as the MAC for half wing-body configurations. Hence, the Strouhal numbers based on local dimensions could vary. Also, the flow unsteadiness was mainly located on the outer part of the wing. They concluded that (U)RANS is able to model the main features of the transonic buffet. The same authors studied the effect of vortex generator on the transonic buffet of a 3D wing (Timme and Sartor, 2015) and computed DDES simulations (Sartor and Timme, 2017). Figure 1.8 shows a snapshot of the URANS and DDES skin pressure. One can observe what the buffet cells look like. These figures also show the ratio of the eddy viscosity over the laminar viscosity. The scale is not the same for the two figures. Hence, one can observe that the eddy viscosity is at least an order of magnitude smaller for the DDES because the resolved turbulence replaces the modeled one. In their paper, they compared the use of a first order Roe scheme with a second order one for the convective terms of the SA turbulence model. It should be noted that first order fluxes are often used in the turbulence models. They concluded that the unsteadiness causing buffeting is better captured by the first order scheme. This is related to a lower level of eddy viscosity in the boundary layer and wake. This effect also shows the strong impact of the turbulence modeling on the transonic buffet. All these studies indicate that URANS simulations can model the main features of three-dimensional buffet. However, the results are strongly dependent on various numerical parameters, as it was observed for 2D results.

In the same way that hybrid RANS/LES methods are popular for 2D computations, many authors have presented 3D solutions of transonic buffet with LES content. Sartor and Timme (2017) used DDES, whereas Brunet and Deck (2008), Ishida *et al.* (2017) and Hashimoto *et al.* (2018) used ZDES. Brunet and Deck (2008) imposed a RANS region with a thickness equal to the boundary layer thickness at the foot of the shock to prevent grid induced separation. Pressure coefficients in the separated regions are in good agreement with the experiments, and the spectra are broadband and have the same shape as the experimental ones. How-

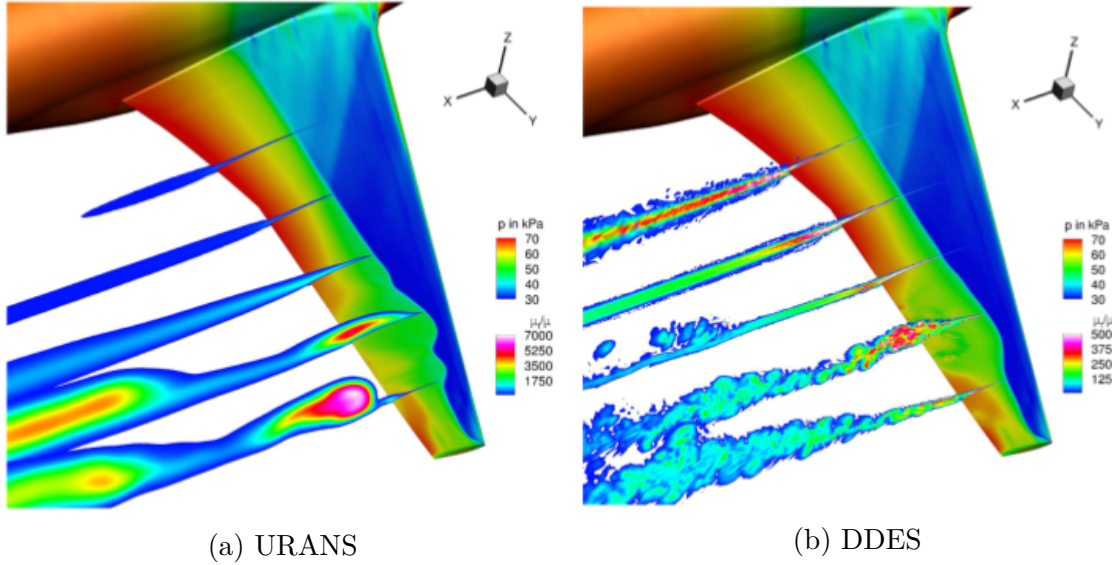


Figure 1.8 – Numerical solutions of RBC12 configuration in buffet conditions (taken from Sartor and Timme (2017))

ever, the pressure fluctuations are overestimated. A similar computational strategy was used by Ishida *et al.* (2017) for the NASA Common Research Model (CRM). The same research group (Ohmichi *et al.*, 2018) presented an analysis of this configuration using Proper Orthogonal Decomposition (POD) and Dynamic Mode Decomposition (DMD) to identify the dominant flow structures. Using these techniques, they identified a mode at  $St = 0.42$  which is associated to buffet cells and a mode at  $St = 0.055$  which is coherent with two-dimensional buffet. Hashimoto *et al.* (2018) used a ZDES with a wall function model and obtained a good prediction of the time-averaged shock position. We can conclude that ZDES simulations can produce accurate solutions of three-dimensional transonic buffet. However, the boundary layers must be protected either with a RANS region or a wall model. In a very different approach, Ribeiro *et al.* (2017) used the Lattice-Boltzmann approach (LBM-VLES) on the NASA CRM and reported the movement of large three-dimensional structures along the span.

Recently, Masini *et al.* (2020a) compared results of a DDES simulation over the RBC12 configuration to high-quality experimental data (Masini *et al.*, 2020b). They used two formulations of the subgrid length scale, the classic formulation of the DES97 method and a vorticity-sensitive filter. The latter was found to produce results in closer agreement to the experiments. These formulations produced dominant frequencies centered around 0.22 and 0.27 respectively and data-based modal analysis (POD and DMD) found an outboard run-

ning mode consistent with buffet cells at these frequencies. However, the experimental data showed a second dominant mode at a Strouhal number around 0.07 associated with very long wavelength structures running in the inboard direction. This mode is not identified in the numerical data. Finally, a mode similar to the Kelvin-Helmholtz instability was also identified in the DDES data.

A particular study by Iovnovich and Raveh (2015) presented URANS simulations over what they called infinite swept wings. These wings are generated by extruding a RA16SC1 airfoil without taper ratio nor twist. The wing is ended by symmetric/extrapolation or symmetric/cut-collapse boundary conditions. The first one is referred to as infinite swept wing because the wing tip effect is removed. However, the symmetric ending is in fact a three-dimensional boundary condition which induces the presence of a  $\lambda$  shock. Their results on these configurations show the appearance of buffet cells, which are convected in the spanwise direction, and an effect of the sweep angle on the buffet frequency and amplitude. The frequency observed for an unswept wing was in the range of the two-dimensional buffet frequency, even though spanwise variation of the shock wave position was observed. For swept wing, the frequency increased with the sweep angle. The authors suggested that the generation of pressure perturbations at the  $\lambda$  shock was linked to the buffet cells phenomenon. A similar study was carried out by the author (Plante *et al.*, 2017), with similar observations.

## Experimental studies

This section is a summary of the experimental campaigns on transonic buffet. All these studies have been carried out on half wing-body configurations in order to further the understanding of the transonic buffet for cases relevant to the aerospace industry. For this reason the wings are all swept at an angle higher than 25 degrees. Moreover, these wings have complex geometries and quantities like the Strouhal numbers can vary in both the chordwise and the spanwise direction. Hence, the articles cited in this section contains large quantities of data. Table 1.6 is intended to summarize a set of relevant quantities to describe the buffet phenomenon.

Roos (1985) studied a high-aspect ratio wing typical of transport aircraft with sweep and taper. In heavy buffeting conditions, a large bump is observed in the power spectral density of pressure between a Strouhal of 0.2 and 0.6. Data are provided for the chordwise convection speed of pressure fluctuations and spanwise coherence of the sectional lift. Greatest coherence is observed in a range of Strouhal from 0.25 to 0.35 for the two inboard spanwise sections

Table 1.6 – Experimental studies of three-dimensional buffet

	Configuration	Sweep(°)	Mach	$Re_{MAC}$ ( $10^6$ )	$\alpha$ (°)	$St_{MAC}$
Roos (1985)	N/A	39	0.826	4.5	10.5	0.2 - 0.6
Molton <i>et al.</i> (2013)	CAT3D	30	0.82	2.5	3.5	0.2-0.6
Dandois (2016)	S3Ch	30	0.82	2.5	3.5	0.2 - 0.6
	AVERT	30	0.82	2.83	3.5	0.1 - 0.5
					3.0	0.02-0.2
					4.25	0.2 -0.5
Sugioka <i>et al.</i> (2018)	CRM	35	0.85	1.54	4.68	0.3-0.5
Koike <i>et al.</i> (2016)	CRM	35	0.84	1.54	6.58	0.3
	CRM	35	0.84	0.947	6.58	
Masini <i>et al.</i> (2017)	RBC12	25	0.8	2.8 to 3.9	2.73	0.05 - 0.15
					3.30	0.05 - 0.43
Paladini <i>et al.</i> (2019a)	BUFFET'N Co	30	0.82	2.5	3.5	0.27
	AVERT	30	0.82	N/A	3.5	0.26
	DTP	27.9	0.8	N/A	4.3	0.3
	FLIRET	30	0.85	N/A	3.37	0.48
Masini <i>et al.</i> (2020b)	RCB12	25	0.8	3.6	3.3	0.22 - 0.44

( $\eta = \frac{z}{b} = 0.42$  and  $0.64$ ). These results suggest a convection of flow structures at frequencies in the order of what is observed in the numerical results.

Molton *et al.* (2013) carried out an experimental study on the control of three-dimensional transonic buffet. For the uncontrolled configuration, they measured a broadband spectrum in the range of Strouhal number from 0.2 to 0.6 at 60% of the model span. They tested mechanical and fluidic vortex generators and found that both devices are effective to reduce flow separation and postpone buffet.

The half wing-body configuration studied by Sartor and Timme (2017) (RBC12) has also been analyzed by Lawson *et al.* (2016). The wing instrumentation includes static pressure taps, Kulite pressure transducers, accelerometers and a root Strain gage. Dynamic Pressure-Sensitive Paint (DPSP) is also used. The accuracy of the DPSP is verified by comparison to static pressure measurements and frequency spectra measured by the Kulite below and above the buffet onset. Multiple experimental buffet onset indicators are also tested. Masini *et al.* (2017) also studied the RBC12 wind tunnel model, focusing on the control of buffet with vortex generators (VGs). Two controlled configurations are studied. The full VG configuration used 30 VGs while the second one used one out of 4 VGs (8 in total). The VGs are located at 32% chord from 63 to 91% span. Based on the analysis of the root strain gages signal, the full and partially controlled configurations delay the buffet onset by  $0.4^\circ$  and  $0.2^\circ$  respectively. At buffet onset, a broadband frequency content in the range of Strouhal from 0.05 to 0.15 based on the MAC is obtained for the clean configuration. These frequencies are lower than the one usually observed for 3D buffet. However, when scaled by the local chord length instead of the MAC, the dominant Strouhal stays around 0.05 which is close to 2D buffet frequency. Moreover, at angles of attack slightly higher than  $3.30^\circ$ , a wider broadband spectrum is observed. An interesting point of the controlled configurations is the suppression

of the higher frequency content. The authors also reported the presence of waves traveling towards the root of the wing for angles of attack below and near the buffet onset. At higher angles of attack, the nature of this convection changes towards the tip.

Lepage *et al.* (2017) presented the state of the experimentation conducted at ONERA on the subject of transonic buffet and its control, and Dandois (2016) analyzed two wind tunnel test campaigns on two wing body configurations in ONERA S3Ch and S2MA wind tunnels respectively. It should be noted that both configurations are based on the OAT15A supercritical airfoil. He observed the characteristic three-dimensional buffet phenomenon as well as the Kelvin-Helmholtz instability, with a frequency higher than the buffet one. Broadband spectra centered around a Strouhal of 0.3 are found in multiple flow conditions. A convection speed of perturbations towards the tip of the wing of around 61 m/s ( $0.2 V_\infty$ ) is associated to the dominant Strouhal number of 0.26. Analysis of the results of Roos (1985) shows a convection speed of  $0.4 V_\infty$ . These results suggest that the higher buffet frequency is caused by the convection of flow structures at a high velocity and he computed a wavelength  $\lambda/c = \frac{V_c/V_\infty}{St} = 1.0$  for these structures. He also observed a low Strouhal number around 0.04 which is associated with a convection velocity of  $0.21 V_\infty$  in the inboard direction. The wavelength of this flow structure is larger than the span of the wing.

Paladini *et al.* (2019a) analysed four experimental databases of transonic buffet over half wing-body configurations. Two of these databases were produced in the BUFET'N Co and AVERT wind tunnel campaign, also studied by Dandois (2016). These wings have a leading edge sweep angle of 30 degrees, no Yehudi break, and a taper ratio of 0.83 and 0.5 respectively. The third one is the *DTP Tremblement model* which has a double sweep leading edge. The sweep angle of the outboard part of the wing can be evaluated around 27.9 degrees from the wing planform provided in the article and a taper ratio of 0.3. The last one, the FLIRET model, has a geometry typical of transport aircraft with a leading edge sweep angle of 30 degrees, a Yehudi break and a low taper ratio of 0.21. Hence, these databases cover a wide range of taper ratios but the sweep angles are similar from one model to the other. Convection speeds in a range from 0.23 to 0.26 are reported and a comparison of Strouhal numbers based on several reference length is presented. An interesting point is the fact that the Strouhal number based on the MAC varies between 0.26 to 0.48 when comparing the four models, with the highest Strouhal number being observed on the most tapered wings (0.3 for the *DTP Tremblement model* and 0.48 for the FLIRET model). However, when the frequencies are normalized by the local chord the Strouhal number is similar from one model to the other (0.22 to 0.27). For the two wings with variation of sweep angle along the

span (*DTP Tremblement model* and FLIRET), Strouhal numbers based on the MAC of the outboard part of the wing are reported. This shows the reference length used in most of the studies (the MAC) might not be the best choice to allow the comparison between the buffet frequencies. It should also be noted that the frequency spectra presented in the article are broadband, an observation made in most of the experimental studies on transonic buffet.

Results of an experimental investigation of the RBC12 configuration including unsteady Pressure Sensitive Paint (PSP), which provides a high resolution pressure measurement in space and time, has been presented by Masini *et al.* (2020b). They identified two phenomena. The first one has a low Strouhal number in the range 0.05 to 0.15 based on the MAC. This frequency is associated with inboard running waves with a long wavelength (in the order of 80% of the semi-span, the span being the distance between the wingtips of a full aircraft). The convective velocity is around  $0.26 V_\infty$ . The second one has a broadband frequency content in the range of Strouhal number between 0.22 and 0.44. This mode is associated with an outboard propagation of perturbations with a wavelength of 0.6 to 1.2 MAC at a dimensionless velocity of  $0.26 V_\infty$ . These two dominant flow features are identified using proper orthogonal decomposition (POD) and dynamic mode decomposition (DMD).

Sugioka *et al.* (2016, 2018) presented results of fast response PSP over the NASA-CRM in buffet conditions. Figure 1.9 shows time samples of the PSP measurements. One can observe three-dimensional structures similar to the one shown in Figure 1.8, with the presence of buffet cells. Sugioka *et al.* (2018) reported broadband Strouhal numbers between 0.3 and 0.5 for intermediate angles of attack between 4.68 and 6 degrees. For higher angles of attack, another low Strouhal number around 0.1 is measured. Koike *et al.* (2016) also studied the transonic buffet on the CRM configuration. They observed a bump in the spectrum around a Strouhal number of 0.3 for angles of attack from 3 to 5.5 degrees, and a broadband low frequency spectrum for higher angles of attack. The frequency of  $St = 0.3$  is associated with a propagation of perturbations in the spanwise direction at a speed of  $110m/s$ . From the total temperature and Mach number, the free stream velocity is approximately  $300m/s$ , meaning a ratio  $\frac{V_c}{V_\infty} = 0.37$ . This result is very close to the observations of Dandois (2016).

## Partial conclusion

Three-dimensional buffet is characterized by a frequency significantly higher than the one of the 2D buffet. The frequency content is broadband for half wing-body configurations and cellular patterns are observed. The three-dimensional buffet Strouhal number is 3 to

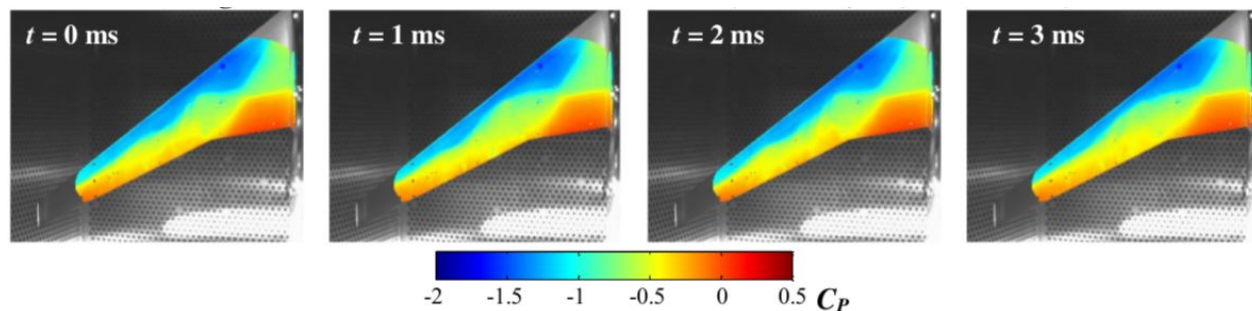


Figure 1.9 – Pressure coefficient time history measured with unsteady pressure sensitive paint (taken from Sugioka *et al.* (2016))

10 times larger than the two-dimensional one. Also, three-dimensional buffet is associated with a spanwise propagation of buffet cells. This propagation speed is evaluated between  $0.26$  and  $0.4 V_\infty$  for civil aircraft configurations with sweep angles in a range from  $25^\circ$  to  $35^\circ$ . The exception is the study of Iovnovich and Raveh (2015) who studied several sweep angles. However, the set of boundary conditions might not allow the phenomenon to be fully developed, because of the low wing aspect ratio studied. Hence, there is a place for simulations on even more simplified geometries to allow a better insight into the physics involved in 3D buffet. The results of Iovnovich and Raveh (2015) show an effect of the sweep angle on the buffet frequency. Hence, we can expect that the similitude of buffet frequencies reported in the literature is caused by similar sweep angles ( $25^\circ$  to  $35^\circ$ ). Results from the literature shows that both URANS and Hybrid RANS/LES can be used to study the phenomenon. As it can be seen, a large number of articles on the three-dimensional buffet have been published in the past 5 years, showing that this field of research gathers significant attention.

### 1.4.3 Buffet models

Many attempts to achieve a model for the origin of transonic buffet are presented in the literature. Of those, the model presented by Lee (2001) describes the buffet phenomenon as a feedback loop between the shock and acoustic wave generated at the trailing edge. Jacquin *et al.* (2009) attempted to model the buffet frequency based on this model by estimating the convection speed of pressure waves traveling on the upper and lower side of the airfoil. Results were in the same order of magnitude as the experimental frequency and discrepancies could be attributed to the difficulty of getting accurate estimation of the convection speeds. They also observed waves traveling along the pressure side of the airfoil, suggesting an alternative path for the feedback loop. A good agreement to Lee's model was also found in the numerical

work of Xiao *et al.* (2006). On the other hand, Garnier and Deck (2010) observed Lee’s model is not in agreement with the buffet period in their LES simulation. Memmolo *et al.* (2018) compared several paths for the upstream traveling acoustic waves and found the best agreement between the model and the numerical frequencies if the acoustic wave travels around the shock tip. Feldhusen-Hoffmann *et al.* (2018) and Hartmann *et al.* (2013a) carried out experimental studies of a DRA 2303 airfoil. They investigated the effect on the transonic buffet of adding an artificial noise. Hartmann *et al.* (2013a) used a frequency of 1030 Hz. The latter was selected to be at the frequency of the natural trailing-edge noise with a modulation at a frequency near the transonic buffet phenomenon. They found that the dominant frequency aligns itself with this modulation frequency. These studies conclude that the acoustic waves have a strong impact on the shock oscillation, which tends to confirm Lee’s model. Hartmann *et al.* (2013b) experimentally investigated the effect of a forced pitch and heave motion on the buffet instability and reported a lock-in phenomenon between the motion and the shock oscillation. A similar effect was observed numerically by Raveh and Dowell (2011) and Thomas and Dowell (2015). In the latter, this phenomenon is used as an indicator of a buffet condition in a shape optimization process intended to delay the buffet onset. Paladini *et al.* (2019b) investigated the origin of transonic buffet with several approaches. The first part of this study used methods to localize the regions of the flow which are the most active for a given unstable global mode. The second part used the Selective Frequency Damping (SFD) (Åkervik *et al.*, 2006) on specific regions of the computational domain to damp unsteady fluctuations. Their results show that the regions of importance in the buffet mechanism are the shock wave and the separated boundary layer. On the opposite, the pressure side of the airfoil, the wake and the region above the separated boundary layer do not contribute to the instability. This seems to exclude the generation of acoustic waves traveling from the trailing edge to the shock wave above the boundary layer or through the pressure side as a physical mechanism for transonic buffet. Memmolo *et al.* (2018) also ruled out propagation of waves on the pressure side by using a sponge area where the numerical fluxes were forced at zero. However, Paladini *et al.* (2019b) also excluded the propagation of perturbations in the paths proposed by Memmolo *et al.* (2018). As such, they conclude that the proper model for transonic buffet should be a feedback mechanism inside the separated boundary layer.

Using global stability analysis Crouch *et al.* (2007, 2008, 2009), described the 2D buffet phenomenon as a global mode instability. This method was also used by Sartor *et al.* (2015) and Iorio *et al.* (2014). Furthermore, Sartor *et al.* (2015) carried out an analysis of the adjoint global mode to show the region of the flow which is receptive to harmonic forcing. They also



carried out resolvent analysis to study the receptivity of the flow to external forcing. The global stability method has also been applied to three-dimensional buffet in the past three years, in parallel to the current research project. Crouch *et al.* (2018, 2019) applied the method to infinite unswept and swept wings by including an assumption of periodicity in the spanwise direction (BiGlobal analysis). They observed a mode coherent with the two-dimensional buffet, which is to be expected since this mode exists for purely two-dimensional cases, and a mode consistent with the convection of the buffet cells in the spanwise direction. Such conclusions were also obtained using fully three-dimensional (TriGlobal) analyses of infinite swept wing (Paladini, 2018; He and Timme, 2020a,b). Finally, Timme (2018, 2019, 2020) studied configurations representative of modern transport aircraft. Their analyses of the NASA CRM show unstable modes consistent with the formation of buffet cells and their convection in the spanwise direction. More recently He and Timme (2020a), carried out the resolvent analysis of infinite swept and unswept wings. They found optimal forcing and response similar to the results of Sartor *et al.* (2015) for 2D airfoil. Responses in line with the transonic buffet and the Kelvin-Helmholtz instability were found. However, in the three-dimensional wing case, another optimal forcing is observed. The latter is at a very low frequency for the unswept wing and in the range of Strouhal number from 0.1 to 1.0 for the wing swept at 20 deg. The optimal responses to these forcings exhibit spanwise variations consistent with results of the linear stability analyses.

## 1.5 Research objectives

From the literature review one can notice there is a limited number of numerical studies on the stall cells. With the exception of the computations of Manni *et al.* (2016), computations were made on low aspect ratio wings. Moreover, no computations on swept wings are available, even though in the application transport aircraft wings are swept. On the side of the models for the occurrence of stall cells, lifting line methods predict stall cells but an extension to a lifting surface method would be interesting for applications to complex wings and aircraft design. Stability analyses are also identified as proper avenues to explain the phenomenon. However, these analyses were all done for low Reynolds number laminar base-flows while the experiments are all done at moderate to high Reynolds numbers where turbulence cannot be neglected. Hence, some gaps are still present in the understanding of the stall cells and addressing them will help to elucidate the complexity of stall dynamics.

On the side of the transonic buffet, Iovnovich and Raveh (2015) presented a very useful attempt to study the three-dimensional buffet on a simple geometry and provide insight on the

basic physical behaviors involved. However, these wings were not the simplest configurations possible. The simplest case would be infinite unswept/swept wings analogous to the stall cells computations available in the literature. Such simulations would provide information about the most basic features of the transonic buffet. Another point which lacks comprehension is the origin of the buffet cells. Explanation for the origin of the two-dimensional transonic buffet is provided by global linear stability analysis. However, the first applications of this method to the three-dimensional buffet were published during this Ph.D. project (Crouch *et al.* (2018); Timme (2018)).

As of now, the connection between stall cells and buffet cells was never proposed. However, the fact that both phenomena consist in a bifurcation from a spanwise invariant solution to a complex three-dimensional flow leads to the following assumption to guide this research project:

**The stall cells and the buffet cells are the same flow instability in two different flow regimes.**

To support this claim two sub-objectives will be assessed in this thesis. The first one is to characterize the stall cells and buffet cells on infinite swept wings. The second one is to propose a model to explain the occurrence of both phenomena. By doing so, the thesis will also propose numerical tools towards an application in aircraft design.

The methodology used to assess these objectives is to first use URANS numerical simulations of infinite swept wings to investigate the effect of the sweep angle on the stall cells and the buffet cells. Two main metrics are analyzed. The wavelength of the cells and the frequency of the flow. The literature review shows that URANS models produce stall cells and buffet cells and its computational cost sufficiently low to enable parametric studies. Then a single ZDES simulation is used to investigate the buffet cells, since the cost of this simulation is prohibitive. The second part of the study uses global stability analyses about spanwise invariant steady flows. These studies allow to investigate the wavelength and frequency of unstable modes. At last a non-linear lifting surface model is proposed for the stall cells and, by extension, for the buffet cells.

## 1.6 Outline

The main part of this thesis consists of three research articles (chapters 2, 4 and 5). Hence, the beginning of each of these chapters presents a summary of these research articles and

introduce them with respect to the objectives of the project. Chapters 2 and 3 target the first sub-objective by characterizing the stall cells and buffet cells, first using RANS/URANS simulation and then ZDES simulations. Supplementary analyses are provided in the appendix C. Chapter 4 explains these two phenomena as a global instability and chapter 5 proposes an explanation based on a potential flow method. As such these two chapters aims the second sub-objective of the thesis. Finally, a discussion and a global conclusion on the objectives and the research assumption are presented.

## CHAPTER 2    ARTICLE 1 : SIMILARITIES BETWEEN CELLULAR PATTERNS OCCURRING IN TRANSONIC BUFFET AND SUBSONIC STALL

*The first article characterizes the saturated regime of the unsteady flow over infinite swept wings in transonic buffet and subsonic stall using Unsteady-Reynolds Averaged Navier-Stokes simulations (URANS). The infinite swept wing is modeled by extruding a two-dimensional airfoil over a finite span in the third dimension. This results in a three-dimensional grid and periodicity conditions are imposed between the two boundaries in the third dimension. A limitation of this approach is the fact that this boundary condition imposes a constraint on the size of the flow structures within the computational domain. Thus a parametric study of the span of the three-dimensional grid is carried out. A parametric study on the wing sweep angle is also carried out while keeping the flow conditions constant in the plane normal to the leading-edge.*

*Using this methodology, the case of the transonic buffet over the OALT25 airfoil at a Mach number of 0.7352, a Reynolds number of 3 million and an angle of attack of 4 degrees is investigated. For every sweep angle, buffet cells are obtained and an unsteady flow is observed. For an unswept wing, a single dominant frequency is obtained and this frequency can be associated with a two-dimensional buffet phenomenon. For swept wings, two dominant frequencies are obtained. The first one is constant with respect to the sweep angle and is associated with a two-dimensional phenomenon. The second one increases with a proportionality relation to the sweep angle.*

*For the subsonic stall case, a NACA4412 airfoil at a Mach number of 0.2, a Reynolds number of 350 000 and an angle of attack of 15 degrees is analyzed. For every sweep angle stall cells are present. However, the flow is only unsteady for swept wings and in this case the frequency increases with the sweep angle.*

*These results show the similarities between the stall cells and the buffet cells. Both phenomena occur when the slope  $C_L - \alpha$  curve of steady flow solutions is negative. Their frequency is also proportional to the sweep angle for both flow conditions. This unsteady behavior is due to the convection of buffet cells in the cross-flow direction. This supports the working assumption that the buffet cells and the stall cells are the same phenomenon.*

PLANTE, F., DANDOIS, J., LAURENDEAU, É., "Similarities Between Cellular Patterns Occurring in Transonic Buffet and Subsonic Stall", *AIAA Journal*, vol. 58 no. 1, pp. 71-84, 19 Sep. 2019, doi: 10.2514/1.J058555.

This paper studies the similarities between the 3D cellular patterns which appear in conditions of transonic buffet and subsonic stall, using RANS/URANS simulations. The geometries are obtained from the extrusion of a 2D airfoil with an added sweep angle with periodic boundary conditions imposed at both ends. Firstly, numerical simulations of transonic buffet are performed. Numerical solutions exhibit three-dimensional cellular flow patterns, forming what has been named buffet cells. The latter are convected in the spanwise direction when a sweep angle is added, leading to the superposition of two frequencies. The first one is independent of the sweep angle and is characteristic of the two-dimensional buffet. The second one increases with the sweep angle and is related to the convection of the buffet cells. These cells are reminiscent of the stall cells which are well-known for low-speed flow conditions. Secondly, solutions of the (U)RANS equations for infinite swept wings in stall conditions at low-speed are computed, showing the same convection of the cellular patterns. These results indicate that the discrepancies between 2D and 3D buffet are caused by the appearance of stall cells, which are the same as buffet cells.

## 2.1 Introduction

Transonic buffet has been extensively studied owing to its physical complexity and industrial relevance. This phenomenon results from the interaction between a shock wave and a boundary layer which induces a separation. This causes a chordwise oscillation of the shock wave position and variations of the aerodynamic loads. This phenomenon is self-sustained on fixed wings, and can cause vibrations since it can occur at frequencies near the structural ones. Hence, transonic buffet constitutes a flight envelope boundary of transport aircraft. An extensive review of the literature on this topic was presented by Giannelis *et al.* (2017). At low-speed, subsonic stall is another boundary of an aircraft flight envelope. This phenomenon also involves complex physics and is a challenge for numerical aerodynamics, thus justifying studies like the high-lift prediction workshops (Rumsey *et al.*, 2018). Moreover, complex three-dimensional flow topologies named stall cells have been experimentally observed on unswept wings created from the extrusion of 2D airfoils (Winkelmann and Barlow, 1980). Such configurations are usually considered to be two-dimensional but the appearance of these stall cells lead to three-dimensional flow structures.

Several researchers have carried out two-dimensional buffet wind tunnel campaigns. McDevitt and Okuno (1985) results have been used as a reference for many numerical studies because of the large range of Mach numbers and angles of attack available for a NACA0012 airfoil. In these cases, the buffet Strouhal number ( $St = f c / v_\infty$ ) ranges from 0.06 to 0.09. Benoit and Legrain (1987) investigated transonic buffet over a RA16SC1 airfoil and obtained similar frequencies. For the past decade, the experimental study of an OAT15A airfoil by Jacquin *et al.* (2009) has been extensively used to validate numerical simulations of transonic buffet, owing to the detailed data available. The reported frequencies stay in a range of Strouhal numbers from 0.062 to 0.073. More recently, Brion *et al.* (2017) studied transonic buffet on the OALT25 airfoil, which is designed to promote laminar flow. Data are available with a boundary layer tripped at 7% and 40% chord as well as free transition. The results with forced transition exhibit a similar behavior as other experiments in turbulent regime with a Strouhal number of 0.07. However the buffet frequency is larger by an order of magnitude ( $St \approx 1.0$ ) for the free transition, for which the transition occurs at the shock foot. This case was also studied using Large Eddy Simulation (Dandois *et al.*, 2018). Hence, two-dimensional transonic buffet occurs within a well-defined range of frequencies when the boundary layer upstream of the shock is turbulent.

Numerical studies have been carried out to assess the predictive capability of Computational Fluid Dynamics (CFD). Early works by Le Balleur and Girodoux-Lavigne (1989) and Edwards (1993) used viscous-inviscid coupling strategies to predict transonic buffet. Accurate solutions have been obtained using Unsteady Reynolds Averaged Navier-Stokes (URANS) simulations. Thiery and Coustols (2006) studied the effect of the turbulence model and confinement of the wind tunnel walls for the OAT15A airfoil. They showed a strong variation of the buffet prediction depending on both parameters. Similar observations were made by Goncalves and Houdeville (2004) when considering several turbulence models for the RA16SC1 airfoil. They also studied the effect of the discretization of the convective fluxes. These results showed that the numerical schemes and the turbulence model have a strong effect on the predicted buffet onset angle of attack and amplitude but not on the frequency of the buffet. For instance, the Strouhal numbers stayed in the range 0.073 to 0.078 for a Mach number of 0.642, a Reynolds number of 4.2 million and an angle of attack of 5 deg. The experimental result (Benoit and Legrain, 1987) is a Strouhal number of 0.083. Grossi *et al.* (2014) used Delayed Detached Eddy Simulations (DDES) (Spalart, 2009) and URANS simulations. They also reported a strong effect of the turbulence model on the simulation of transonic buffet. The Edwards-Chandra modification of the Spalart-Allmaras model with compressibility correction was used in their implementation of the DDES. Deck (2005a) used

URANS, Detached Eddy Simulation (DES) (Spalart *et al.*, 1997) and Zonal Detached Eddy Simulation (ZDES) (Deck, 2005b, 2012). As observed by other authors, URANS with the Spalart-Allmaras turbulence model required to increase the angle of attack in comparison to the experiment to obtain an unsteady flow. Similar observations were made with DES, but the ZDES predicted the buffet onset at the same angle of attack as the experiment. Large Eddy Simulations (LES) have been carried out by Garnier and Deck (2010) and Fukushima and Kawai (2018). These simulations are in good agreement with the experiments, but are computationally very expensive. In summary, URANS simulations are able to reproduce the main features of the two-dimensional buffet, but scale-resolving simulations might be required to reduce the sensitivity of the simulations to the turbulence model. The turbulent transonic buffet frequencies predicted by CFD are in good agreement with experimental results.

Concerning three-dimensional buffet, most of the experimental studies have been carried out for half wing-body configurations, representative of modern transport aircraft. Roos (1985) reported a broadband frequency content with Strouhal numbers ranging from 0.2 to 0.6. Dandois (2016) and Paladini *et al.* (2019a) presented the analysis of several wind tunnel campaigns over 3D half-wing body configurations. The characteristic bump in the pressure spectra is observed at frequencies 4 to 7 times higher than the two-dimensional buffet frequency. Two physical phenomena with different characteristic frequencies are present : transonic buffet with the convection of buffet cells towards the wing tip and the Kelvin-Helmholtz instability in the shear layer. Spanwise flow structures, buffet cells, can also be observed on the pressure-sensitive paint (PSP) measurements of Sugioka *et al.* (2018).

Iovnovich and Raveh (2015) studied infinite swept configurations based on the RA16SC1 airfoil. These configurations were obtained from a swept extrusion of the airfoil and various boundary conditions were used to close the computational domain at the wing tips. In all cases a symmetric boundary condition was imposed at the root. Results showed the occurrence of what they named buffet cells and an effect of the sweep angle on both the amplitude and the frequency of transonic buffet. Sartor and Timme (2016, 2017, 2015) and Timme and Sartor (2015) carried out an extensive study of the RBC12 configuration with (U)RANS and DDES. They obtained an unsteady shock motion with various turbulence models and observed an effect on the buffet onset angle of attack (Sartor and Timme, 2015). They reported Strouhal numbers in the range 0.1 to 0.4 with unsteadiness mostly located on the outer part of the wing. Their results also exhibited buffet cells. Brunet and Deck (2008) carried out a ZDES simulation of the CAT3D model and Ishida *et al.* (2017) presented ZDES results for the NASA CRM. ZDES results on this configuration were analyzed using Dynamic

Mode Decomposition (DMD) and Proper Orthogonal Decomposition (POD) by Ohmichi *et al.* (2017, 2018). Using these methods they identified a mode at  $St \approx 0.2 - 0.6$  associated with the buffet cells and a mode at  $St \approx 0.06$  which is coherent with two-dimensional buffet.

Two-dimensional transonic buffet was explained as a global instability by Crouch *et al.* (2007, 2008, 2009) and Sartor *et al.* (2015). Recently, this concept was extended to three-dimensional buffet (Crouch *et al.*, 2018; Paladini, 2018) on infinite swept wings. These analyses were carried out on a quasi-three-dimensional flow with the assumption that perturbations in the spanwise direction are periodic. An unstable mode with a spatial wavelength of the order of one chord length is observed. The frequency of the latter is null for unswept wings and increases when a sweep angle is added. Three-dimensional stability analysis of a half wing-body configuration has been carried out by Timme and Thormann (2016); Timme (2018), showing a three-dimensional unstable mode coherent with experimental observations.

Concerning low-speed flow conditions, stall cells have been observed in the post-stall regime since the 1970's (Moss and Murdin, 1971; Gregory *et al.*, 1971). Since then, many experimental and numerical studies have been carried out. The cells observed experimentally have a wavelength between one (Manolesos and Voutsinas, 2013; Manolesos *et al.*, 2014) and three chord lengths (Winkelmann and Barlow, 1980) and their behavior can be steady or unsteady. For instance, Dell'Orso and Amitay (2018) observed transition between one and two stall cells. The observation of steady or unsteady patterns might depend on the visualization technique used and the aspect ratio of the wing (Yon and Katz, 1998). Also, the stall cells seem to only be present for a narrow range of angles of attack in the post-stall regime (Yon and Katz, 1998). Most of the study agree that the number of cells depends on the span of the wing (Winkelmann and Barlow, 1980; Schewe, 2001). Based on this observation Schewe (2001) concluded that the cells are not caused by the effect of the tunnel walls in the experiments. Recently Dell'Orso and Amitay (2018) carried out a parametric experimental study of the stall cells on a NACA0015. They observed the transition between a two-dimensional flow separation and fully developed stall cells by increasing the Reynolds number. Broeren and Bragg (2001) studied multiple airfoils and concluded that trailing edge separation is necessary to observe stall cells, which were generally steady. To the author's knowledge, the phenomenon was only reported for a trailing edge type stall.

Stall cells were computed by Bertagnolio *et al.* (2005) in the context of wind turbine design. Kamenetskiy *et al.* (2014) also encountered this type of flow topology while investigating the possibility to obtain multiple fully converged solutions of the discretized RANS



equations. Manni *et al.* (2016) presented results of stall cells using URANS and DDES simulations. Recent studies point towards an inviscid source for the stall cells. Solutions using viscous-inviscid coupling methods exhibit structures reminiscent of stall cells (Gallay and Laurendeau, 2015; Paul and Gopalarathnam, 2014). Moreover, Spalart (2014) proposed a model based on the lifting line theory with which he obtained what he called lift cells. Based on this model, stall cells result from a growing instability when the lift versus angle of attack curve slope is negative. Gross *et al.* (2015) proposed a model based on the lifting line theory for the wavelength of the cells with respect to the slope of the  $C_L - \alpha$  curve. Weihs and Katz (1983) tried to explain the stall cells based on the Crow instability (Crow, 1970) and Rodríguez and Theofilis (2011) linked stall cells to a global unstable mode.

Previous work by the authors (Plante *et al.*, 2017) studied a configuration similar to the one of Iovnovich and Raveh (2015). A symmetry plane was imposed at the root of the wing, inducing 3D effects in the form of a  $\lambda$  shock. For this reason the wavelength and amplitude of the cells varied in the spanwise direction. Thus, a very large span was required to get fully developed cells. In the present paper infinite swept configurations are studied. This means that periodicity conditions are imposed to allow the buffet cells to fully develop in the spanwise direction and remove any spanwise flow disturbances induced by the boundary conditions at the wing root. This paper presents simulations of buffet cells and stall cells. This study is novel since it examines three-dimensional buffet on infinite swept wings, which is the simplest configuration. At low-speed, the stall cells are also studied on swept wings. Together these results allow to identify similar behaviors between stall cells and buffet cells. The paper will start by presenting the numerical methodology. Numerical solutions of transonic buffet cells and subsonic stall cells will follow and the paper will end with a conclusion.

## 2.2 Numerical method

Computations are carried out for infinite swept wings obtained from the extrusion of a 2D airfoil. The meshes are generated by extruding a 2D grid with a shift in the  $x$ -direction to obtain a swept wing. The  $x$ -coordinates of this grid are modified by a factor  $1/\cos \delta$ , with  $\delta$  the sweep angle, to keep the baseline airfoil geometry in the plane normal to the leading edge. Fig. 2.1 shows the 3D mesh used for transonic buffet. For clarity only every fourth grid point is shown in all directions. One can observe the angle between the leading edge and the  $z$ -axis and the two parallel planes closing the domain at the tips of the wing. The baseline grid for transonic buffet is an O-type mesh of the OALT25 airfoil with 512 chordwise by 128 normal cells and a first cell wall spacing of  $8 \times 10^{-6}$  chord. Fig.2.2 shows the grid refinement

study based on the steady RANS solution at a Mach number of 0.7352, a Reynolds number of 3 million and an incidence of 4.0 deg., the buffet condition studied in this paper. One can observe that refining the grid in both directions does not change significantly the pressure coefficient. In this paper we use a constant spanwise grid spacing of 0.036 chord. For the subsonic stall conditions, the profile is the NACA4412 airfoil and the mesh is an O-type grid of 512 by 128 cells with a wall spacing of  $5 \times 10^{-5}$  chord. The grid convergence was verified for the stall case by comparing the 2D pressure coefficients obtained with a grid of 512 by 128 cells to a grid refined by a factor 2 in both directions. No significant difference was observed. The spanwise grid spacing is 0.054 chord. Multiple spans and leading edge sweep angles are analyzed.

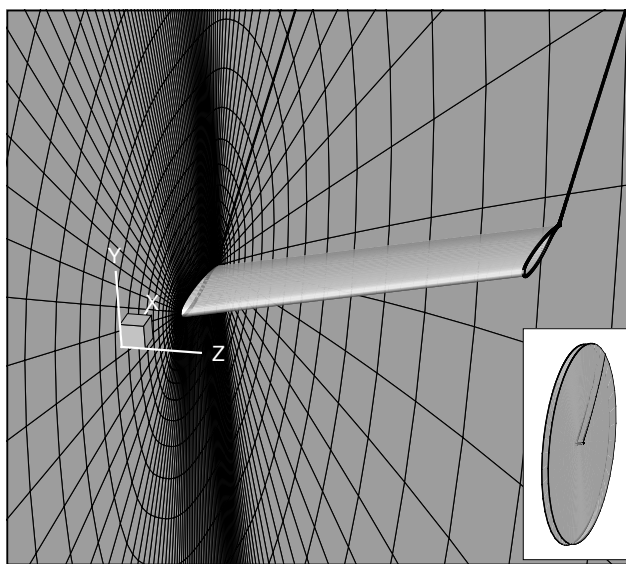


Figure 2.1 – Three-dimensional mesh obtained from the extrusion of a two-dimensional grid.

No slip boundary conditions are imposed on the airfoil surface and the domain is closed by periodicity conditions in the spanwise direction. Farfield conditions are imposed on the remaining boundaries. The farfield conditions are modified to maintain the similarity between the cases when considering values in the plane normal to the leading edge. To do so, the Mach number, Reynolds number and angle of attack are modified following equations 2.1. One should note that nondimensionalization of the results ( $C_p$  for example) is based on the quantity in the plane normal to the leading edge to allow comparison between cases with various sweep angle.

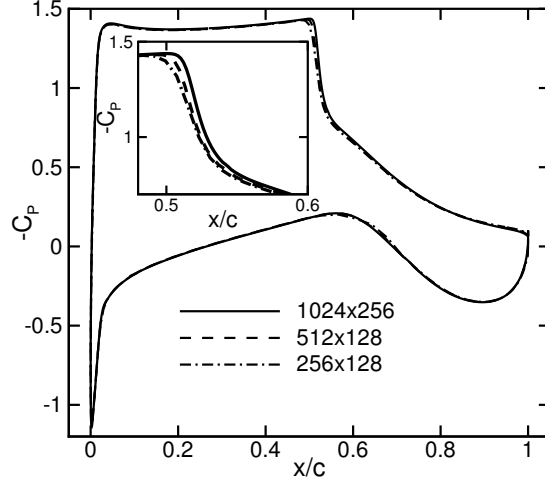


Figure 2.2 – OALT25 grid refinement study.

$$\begin{aligned}
 M_{3D} &= \frac{M_{2D}}{\cos(\delta)} \\
 \alpha_{3D} &= \arctan [\tan(\alpha_{2D}) \cos(\delta)] \\
 Re_{3D} &= \frac{Re_{2D}}{\cos(\delta)^2}
 \end{aligned} \tag{2.1}$$

Part of the results are computed with the 2.5D assumptions (Ghasemi *et al.*, 2014; Bourgault-Côté *et al.*, 2017; Franciolini *et al.*, 2018). These simulations are carried out on a grid with a single spanwise cell. Hence, all the derivatives in the spanwise direction are equal to zero, but not the velocity. This allows to include the effect of the sweep angle without the development of flow structures in the third dimension.

This study uses the ONERA-Airbus-SAFRAN elsA software (Cambier *et al.*, 2013) which is a structured finite volume solver. A second order cell-centered scheme with scalar numerical dissipation is used to discretize the convective fluxes. Convergence is accelerated using local time steps and geometrical multigrid. Pseudo-time integration is carried out with a LU-SSOR scheme and time-accurate solutions are computed with a dual time stepping approach. Selective frequency damping (SFD) (Åkervik *et al.*, 2006; Jordi *et al.*, 2014, 2015; Richez *et al.*, 2016; Plante and Laurendeau, 2018; Casacuberta *et al.*, 2018) is used in some cases to force the convergence to a steady state. For all cases the one equation Spalart-Allmaras turbulence model (Spalart and Allmaras, 1992) with Edwards-Chandra (Edwards

and Chandra, 1996) modification is used for closure of the (U)RANS equations. This correction produces less eddy viscosity and has been found to be helpful in the simulation of transonic buffet (Grossi *et al.*, 2014). Simulations are done in fully-turbulent mode and the farfield eddy viscosity ratio is set to 0.001.

## 2.3 Numerical results

### 2.3.1 Transonic buffet

In this section, numerical simulations of the transonic buffet over the OALT25 airfoil at a Mach number of 0.7352, an angle of attack of 4 deg. and a Reynolds number of 3 million are presented. As mentioned in the previous section, these conditions are kept constant in the plane normal to the leading edge for the swept wings. The dimensional time step of  $1 \times 10^{-5} s$  results in a nondimensional time step ( $\bar{t} = tV_{ref}/l_{ref}$ ) of 0.01, where  $l_{ref}$  and  $V_{ref}$  are respectively the chord and velocity in the plane normal to the leading edge.

First, 2.5D computations were carried out to study the effect of the sweep angle on transonic buffet. Fig. 2.3 shows the lift coefficient for various sweep angles. One can observe that the crossflow added by the sweep angle has no effect on the frequency. The non-dimensional time period is 13.4 for a Strouhal number of 0.075. Hence, 2.5D cases behave like 2D ones and the discrepancies between 2D and 3D buffet have to be attributed to fully three-dimensional phenomena. Fig. 2.4 compares the time-averaged surface pressure coefficients obtained with the two-dimensional ( $\delta = 0$  deg.) and 2.5D buffet computations to the experiments of Brion *et al.* (2017). One can observe that the pressure coefficients match the experiment, with the exception in the vicinity of the shock wave position. The URANS simulations produce a shock wave downstream of the experimental one. Fig. 2.5 shows the pressure fluctuations on the airfoil surface. The distribution is qualitatively similar to the experimental one, with a maximum obtained in the vicinity of the shock wave. Adding a sweep angle has the effect of reducing the pressure fluctuations. This is coherent with the lower lift oscillation amplitude for swept wings in fig 2.3. However, no scaling law between the buffet amplitude and the sweep angle was found. The 2.5D simulations also demonstrate that the similarity between the flow conditions is maintained by adjusting the farfield conditions to the sweep angle since the same pressure distribution is obtained, with the exception of the buffet amplitude.

Following simulations are computed on infinite three-dimensional swept wings. Fig. 2.6 shows the pressure coefficient and the skin friction lines for four time instances of the three-dimensional URANS simulation with an aspect ratio  $Lz/l_{ref} = 6$  and a sweep angle of 20 deg.

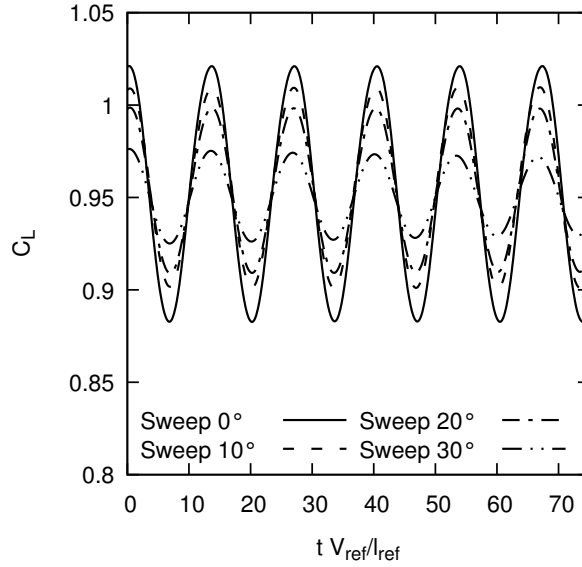


Figure 2.3 – Lift coefficient for the 2.5D cases.

One can observe a variation of the chordwise shock wave position along the span of the wings, forming what has been called buffet cells by Iovnovich and Raveh (2015). These structures appear naturally without the introduction of a spanwise perturbation. The amplitude of the buffet cells changes in time, and the maximum amplitude can be observed at the non-dimensional time  $\bar{t} = 8.4$ . This variation of the buffet cells amplitude is accompanied by large changes in the flow topology aft of the shock wave. A convection of the buffet cells in the spanwise direction is also observed.

Fig. 2.7 shows the instantaneous pressure coefficient and the skin friction lines on the suction side of the wing for sweep angles of 0, 10 and 30 deg. For the unswept case, the flow is unsteady but irregular. With a sweep angle, these cells are convected along the span of the wings and the flow is time periodic. Fig. 2.8 shows the pressure coefficient and the skin friction lines for various wing spans and a sweep angle of 20 deg. This allows to identify the evolution of the number of buffet cells with respect to the wing span. Tab. 2.1 and 2.2 compile the observed buffet cells wavelength. One should note that the  $Lz'/l_{ref}$  was chosen to be constant when changing the sweep angle. This causes the length of the leading edge  $Lz'$  to vary in  $1/\cos(\delta)$ , resulting in various buffet cells wavelengths. For  $Lz'/l_{ref}$  up to 4.52, only one buffet cell is present. From  $Lz'/l_{ref} = 5.32$  to 6.39 there are 2 cells and we observe 3 cells for  $Lz'/l_{ref}$  greater than 6.62 and at least lower than 8.51. Since the periodic boundary conditions force the number of cells to be an integer, a higher number of simulations would be required

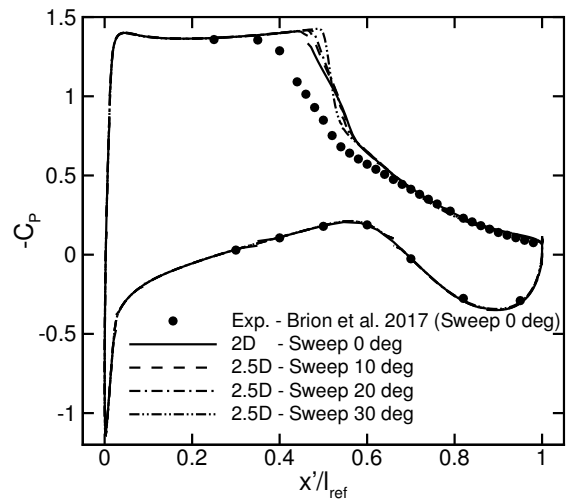


Figure 2.4 – Time-averaged surface pressure coefficient for 2.5D cases.

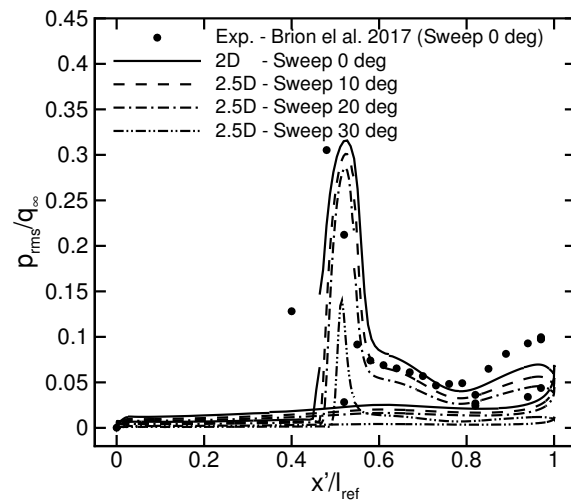


Figure 2.5 – RMS of the surface pressure fluctuations for 2.5D cases.

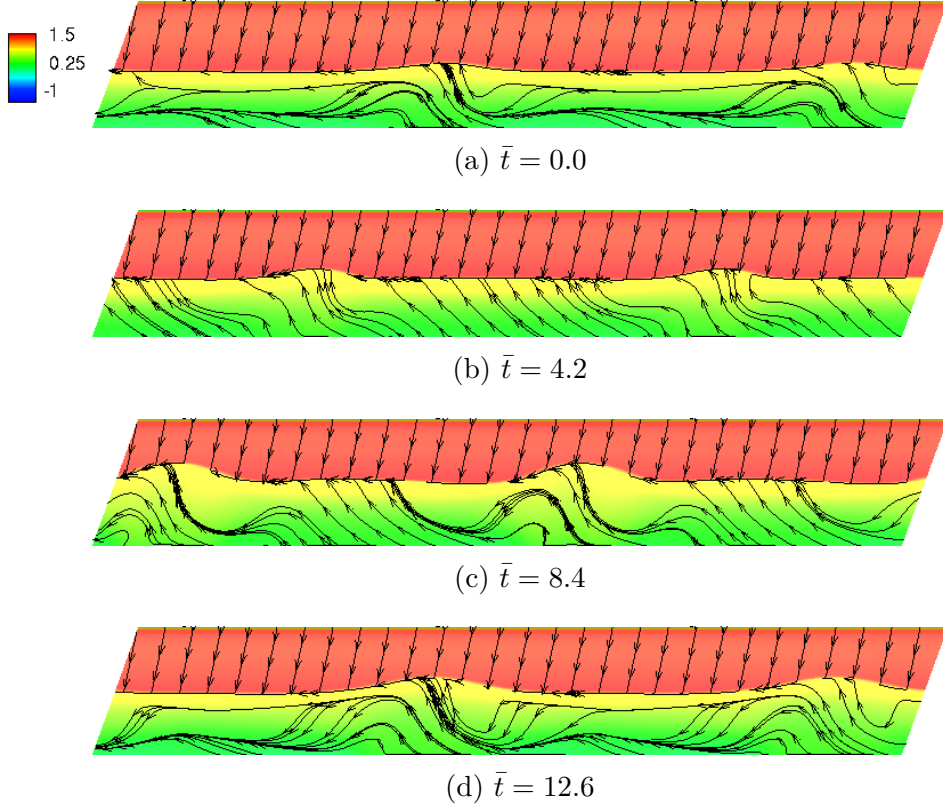


Figure 2.6 – Time evolution of the pressure coefficient and skin friction lines for infinite swept wings ( $\delta = 20$  deg.).

to get a more accurate result. However, this gives a good insight that the number of cells is mostly related to the span since the ratio between the number of cells and  $Lz'$  is the same when  $Lz'$  is increased alone or by increasing the sweep angle.

A model can be proposed for the frequency associated with the convection of the buffet cells with respect to their aspect ratio  $\lambda_z$  and their convection speed  $V_C$  (see fig.2.9). For convenience, we define a coordinate system  $(x', y', z')$  with  $z'$  aligned with the leading edge of the wing. We suppose that the convection speed is proportional to the free stream tangential speed  $V'_z$ . Since the velocities are constant in the plane normal to the leading edge, this velocity only depends on the sweep angle  $\delta$ .

Fig. 2.10 shows a  $(z', t)$  diagram of the time evolution of the pressure coefficient along a line parallel to the leading edge. For brevity this analysis is only shown for a sweep angle of 20 deg. and  $Lz'/l_{ref} = 6$ . For most of the points in this chart, the pressure is constant and is the one associated with the pressure plateau upstream of the shock wave.

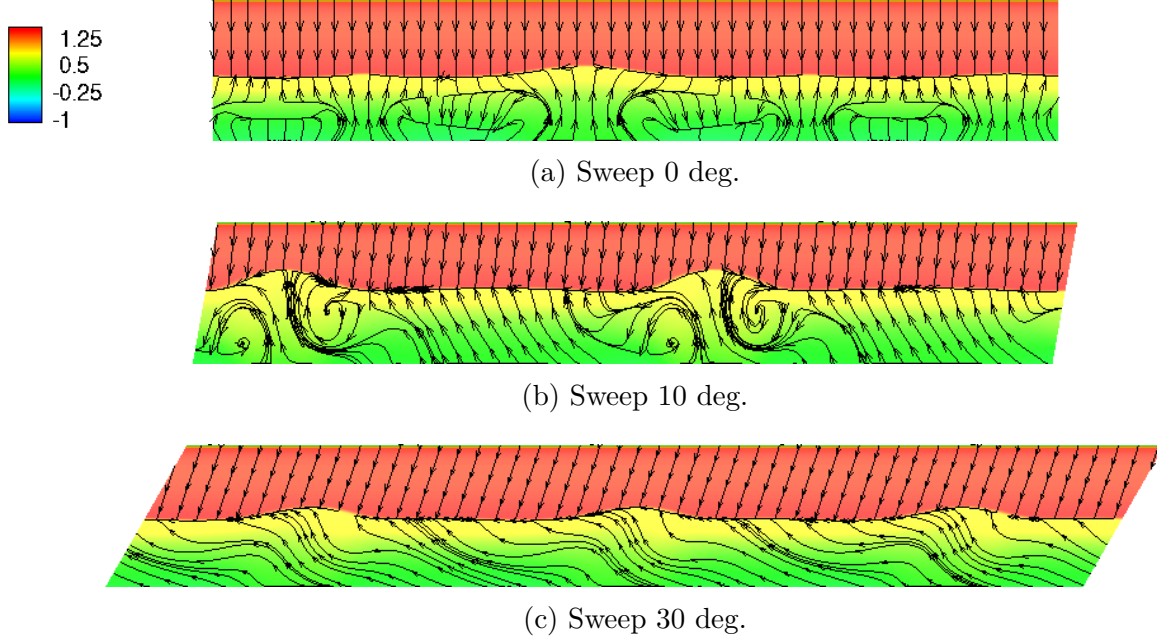


Figure 2.7 – Effect of the sweep angle on the pressure coefficient and skin friction lines for infinite swept wings.

One can observe the periodic variation of the buffet cells amplitude by the discontinuities in these lower pressure zones. These cells are in phase since the two cells appear on the extraction line at the same time samples. The time between two appearances of the buffet cells corresponds to a Strouhal number around 0.06, which is in the range of values normally associated with two-dimensional buffet. This frequency is observed for every simulation. The non-dimensional convection speed can be read as the slope of the iso-pressure contours. This convection speed  $V_C/V_{ref}$  is equal to 0.26 for a sweep angle of 20 deg. In this case the length  $Lz'$  of the wing is 6.39 and there are two cells, so their non-dimensional wavelength  $\lambda_z/l_{ref}$  is equal to 3.2. Hence the Strouhal number associated with the convection of the buffet cells is  $(V_C l_{ref})/(V_{ref} \lambda_z) = 0.081$ . Results of this analysis for all the sweep angles and aspect ratios are compiled in tab. 2.1 and 2.2 respectively.

The convection speed increases with the sweep angle. This was expected since the tangential free stream velocity  $V'_z$  also increases with the sweep angle. Fig. 2.11 shows the evolution of the convection speed with respect to the sweep angle. The tentative model of fig. 2.9 gives an accurate representation of the convection speed with a constant multiplier around 0.7 ( $V_C/V_{ref} \approx 0.7 \tan(\delta)$ ). Also, the convection speed is constant for various wing spans at a constant sweep angle of 20 deg., giving more evidence that the convection speed is mostly



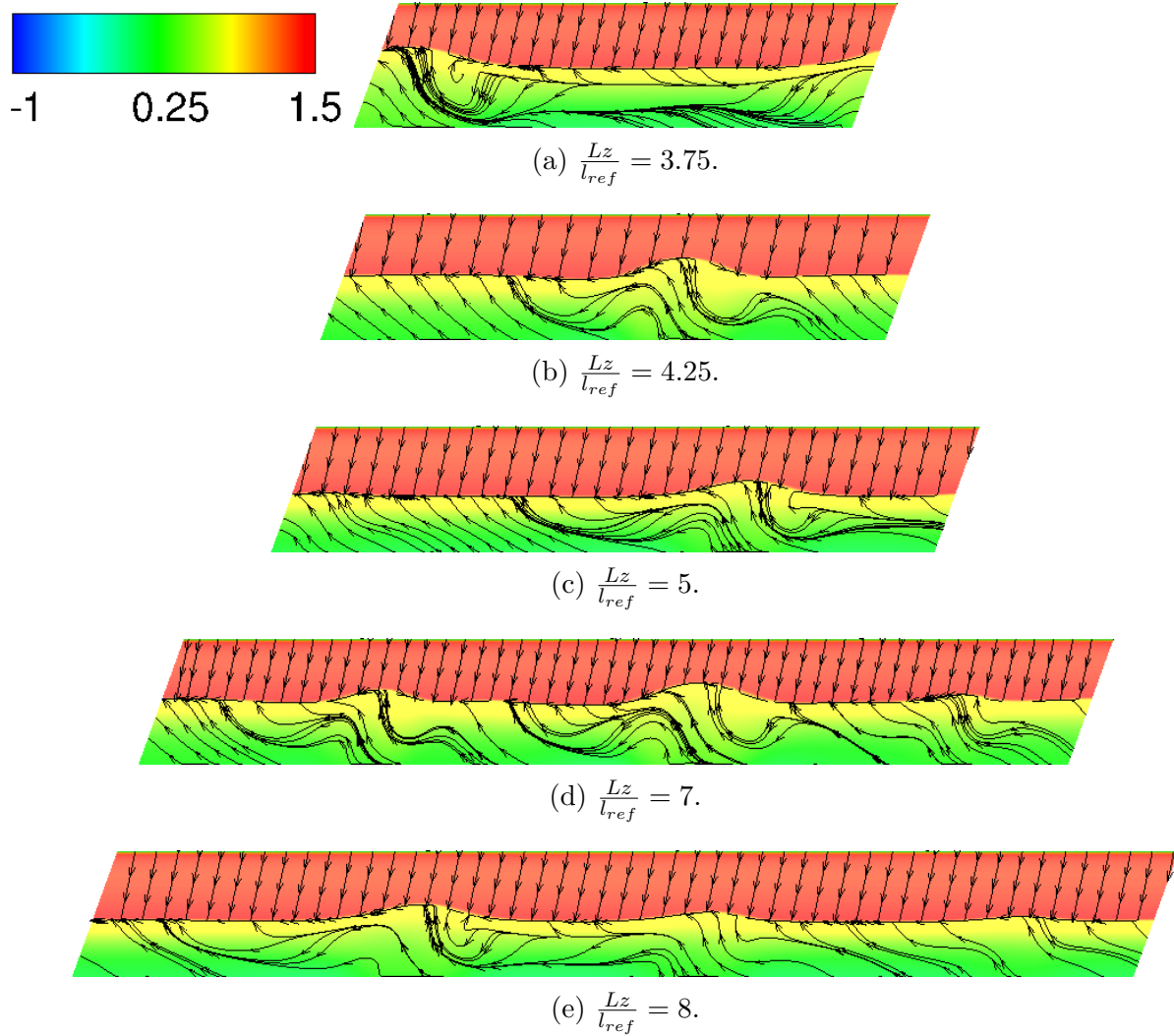


Figure 2.8 – Wing span effect on the number of buffet cells for a sweep angle of 20 deg.

related to the tangential speed.

The Strouhal number associated with the convection of buffet cells also increases with the sweep angle. However the wavelength of the buffet cells is constrained by the periodic boundary conditions. Hence, the wavelength increases with the length  $Lz'$  and the Strouhal number decreases up to the point where the span allows the formation of another cell. At this point the wavelength  $\lambda_z$  is sharply reduced, and the Strouhal number increases. Hence for the computations in this paper the convection speed is constant for a given sweep angle, but not the Strouhal number.

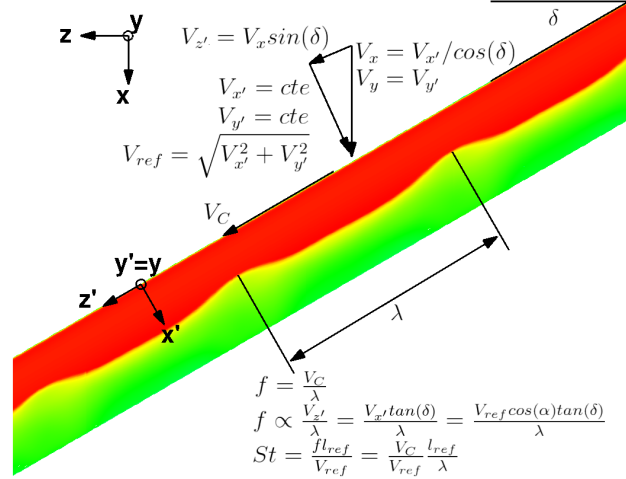


Figure 2.9 – Tentative model for the convection speed and buffet cells frequency.

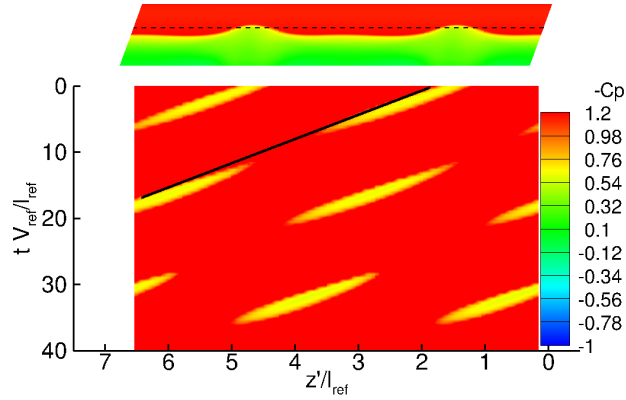
Figure 2.10 – Extraction of the pressure on a line parallel to the leading edge near  $x'/l_{ref} = 0.4$ .

Table 2.1 – Effect of the sweep angle.

$\delta$ (deg.)	$Lz/l_{ref}$	$Lz'/l_{ref}$	$N_{cells}$	$\lambda_z/l_{ref}$	$V_C/V_{ref}$	$St$
5	6.00	6.02	2	3.01	0.07	0.024
10	6.00	6.09	2	3.05	0.13	0.042
15	6.00	6.21	2	3.11	0.20	0.064
20	6.00	6.39	2	3.19	0.26	0.081
25	6.00	6.62	3	2.21	0.32	0.144
30	6.00	6.93	3	2.31	0.40	0.172

A Fourier decomposition is used to extract the contribution of several frequencies to the pressure distribution. Fig. 2.12 shows the contribution of the time-averaged mode ( $St = 0.0$ ), the 2D buffet mode ( $St \approx 0.063$ ) and the buffet cells convection mode ( $St \approx 0.083$ ) and its first harmonic ( $St = 0.166$ ) for a sweep angle of 20 deg. As expected, the time-averaged

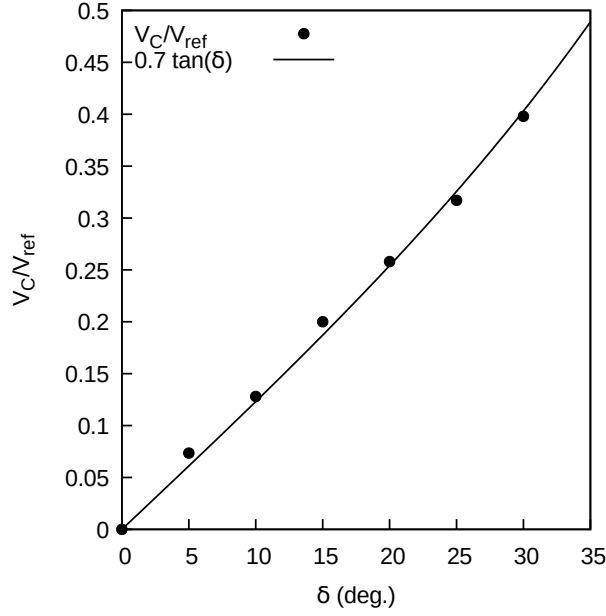


Figure 2.11 – Buffet cells convection speed model.

Table 2.2 – Effect of the span.

$Lz/l_{ref}$	$\delta$ (deg.)	$Lz'/l_{ref}$	$N_{cells}$	$\lambda_z/l_{ref}$	$V_C/V_{ref}$	$St$
3.75	20	4.00	1	4.00	0.27	0.066
4.25	20	4.52	1	4.52	0.27	0.060
5.00	20	5.32	2	2.66	0.26	0.097
6.00	20	6.39	2	3.19	0.26	0.081
7.00	20	7.45	3	2.48	0.26	0.104
8.00	20	8.51	3	2.84	0.26	0.091

pressure coefficient has no modulation in the spanwise direction. The mode at a Strouhal number of 0.063 is essentially two-dimensional and is characterized by an oscillation of the shockwave position in the chordwise direction. The mode associated with a Strouhal number of 0.083 is characterized by a strong modulation in the spanwise direction. The shape of this mode corresponds to a variation of the shock wave position along the span. Subfig. 2.12d shows a mode with 4 cells, which is a harmonic of the mode at  $St = 0.083$ . Higher harmonics could also be identified. Hence, the Fourier decomposition allows to separate flow features associated with the two-dimensional buffet phenomenon and the buffet cell one.

Fig. 2.13 shows the power spectral density of the lift coefficient extracted for a selected spanwise section for sweep angles from 0 deg. to 30 deg. One can observe a peak in the spectra around a Strouhal number of 0.06 for every sweep angle. In each spectrum, a second frequency

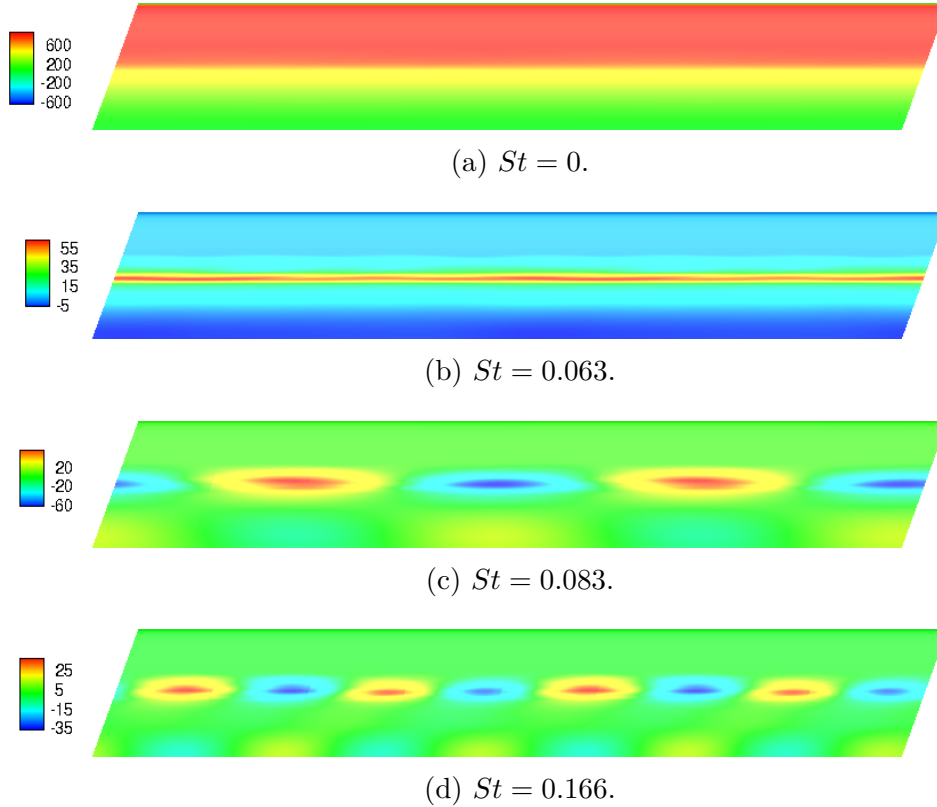


Figure 2.12 – Fourier coefficients of the pressure coefficient of four Fourier modes.

coincides with the buffet cells convection frequency identified by the  $(z', t)$  diagrams. For comparison, the global lift coefficient (for the entire wing) spectra are plotted in fig. 2.14. One can observe the peak at a Strouhal number of 0.06 is still present. However, the buffet cells convection frequency is not distinguishable in these spectra. This means that the effect of the buffet cells is canceled out on quantities integrated along the span. This is another indication that the 2D buffet and the 3D buffet cells are two different flow features. Fig. 2.15 shows the sectional power spectral density for several wings of sweep 20 deg. and increasing span. In every case the frequency of the two-dimensional buffet and buffet cells convection is noticeable.

All 3D simulations were computed using a spanwise spacing of 0.036 chord. Several spanwise spacings from 0.071 to 0.027 chord were computed for a sweep angle of 30 deg. In all cases the flows remain qualitatively similar and Fig.2.16 shows the power spectral density of the lift coefficient extracted on a slice. The two dominant frequencies are the same for all meshes thus demonstrating appropriate grid convergence.

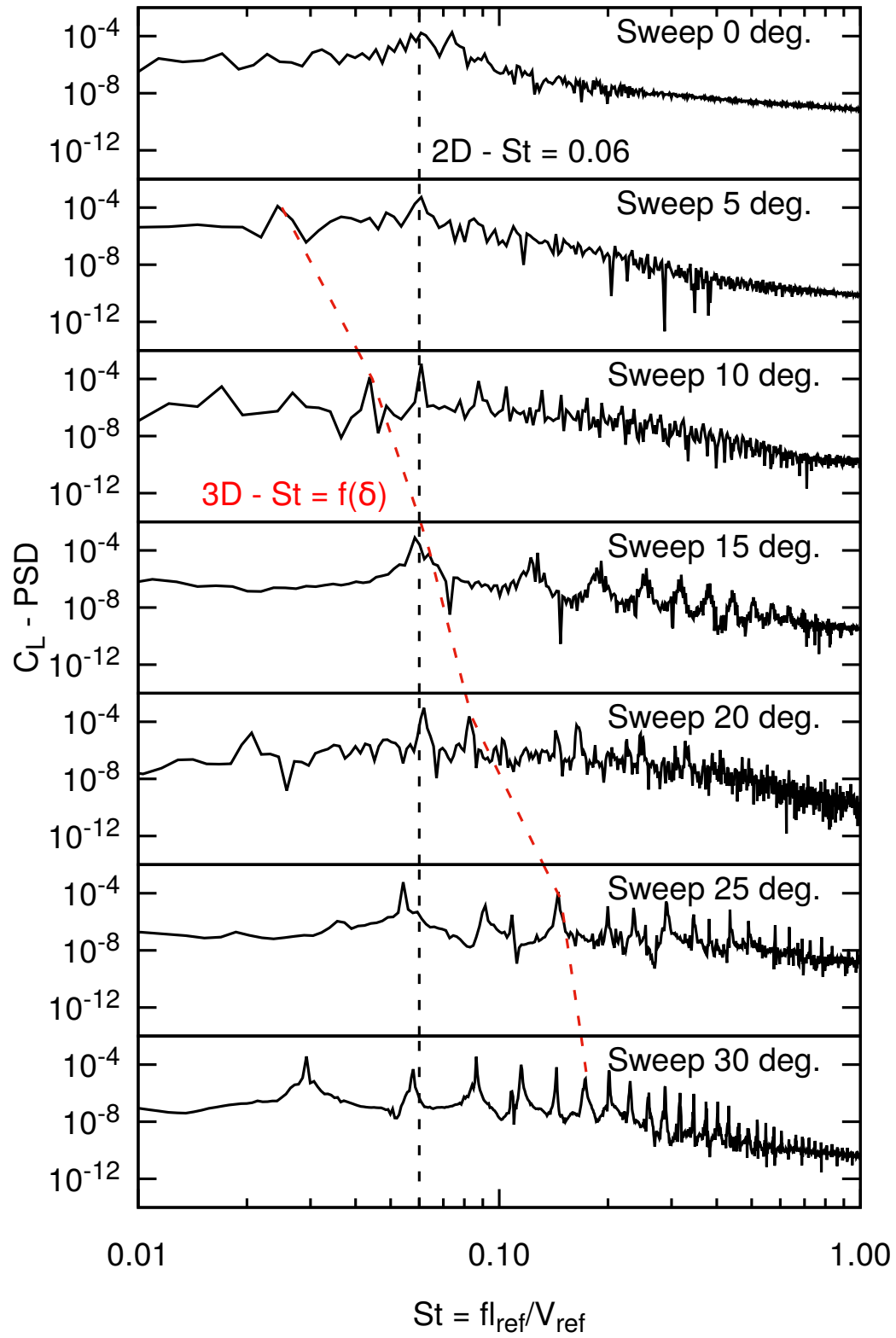


Figure 2.13 – Effect of the sweep angle on the sectional lift coefficient power spectral density

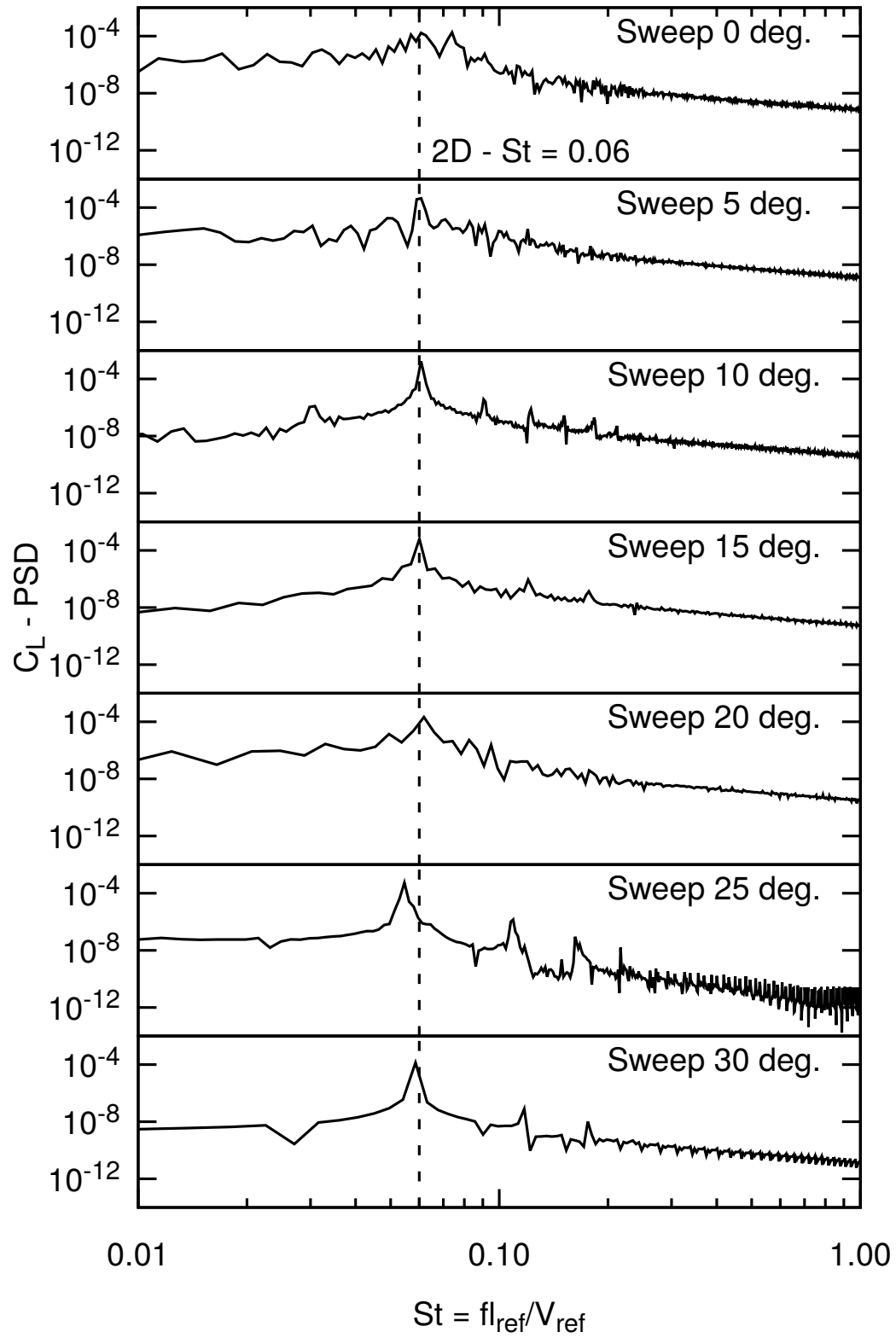


Figure 2.14 – Global lift coefficient power spectral density

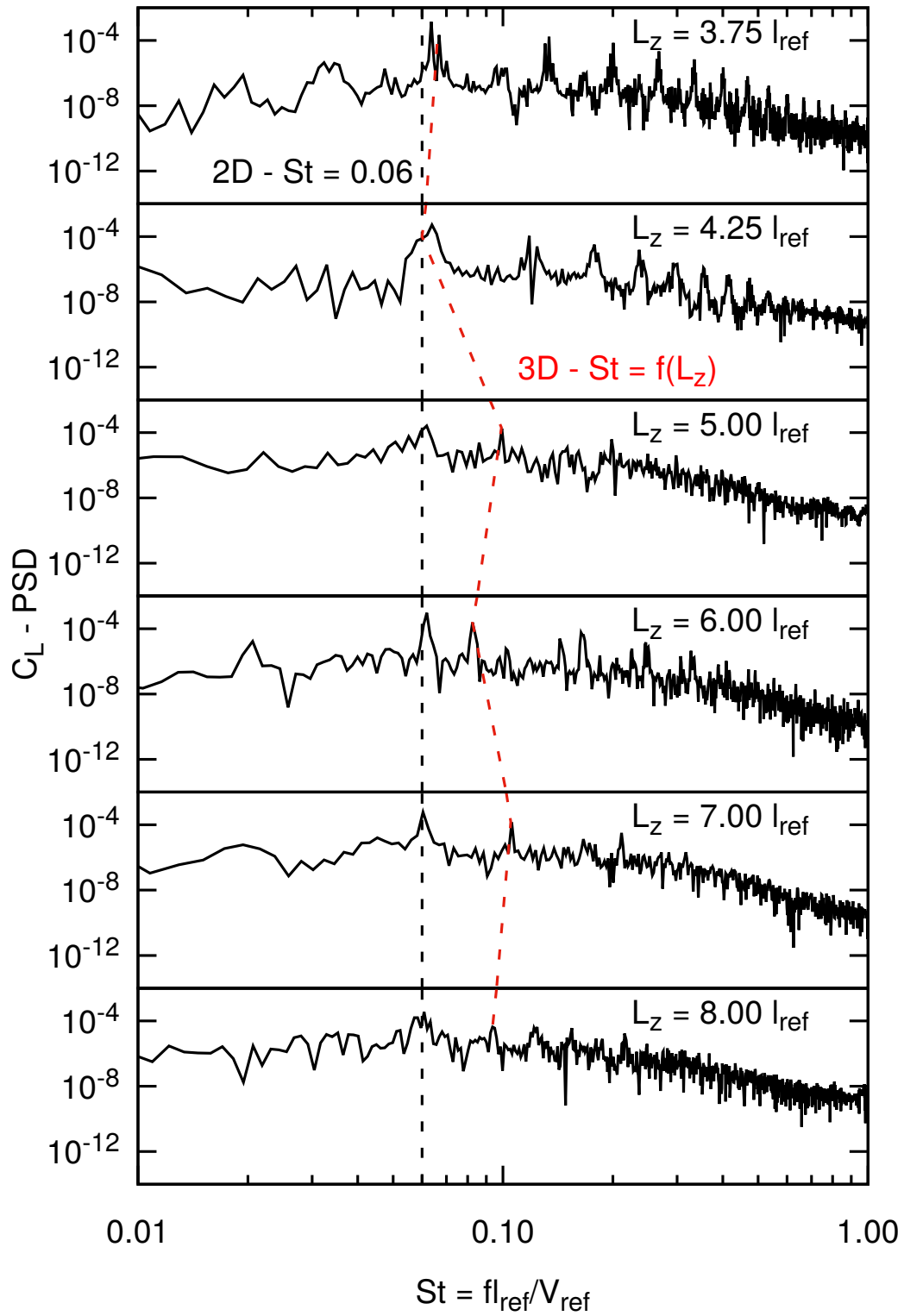


Figure 2.15 – Effect of the span on the sectional lift coefficient power spectral density

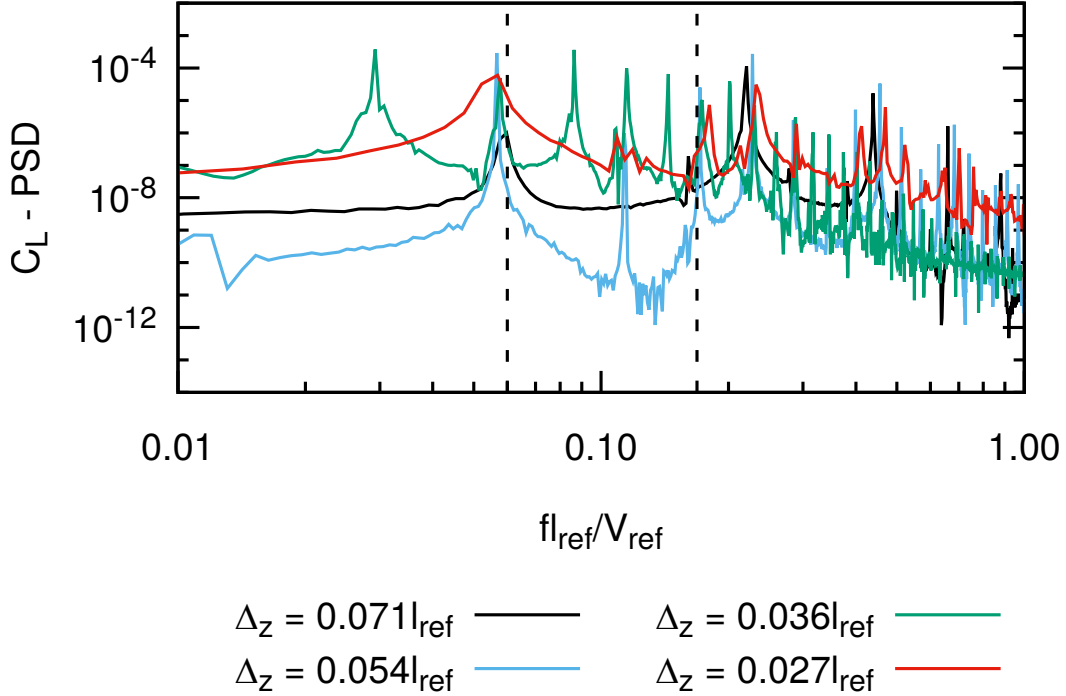


Figure 2.16 – Spanwise grid refinement for a sweep angle of 30 deg.

In summary, the superposition of two phenomena is observed: the classic 2D buffet phenomenon and the convection of buffet cells. The frequency of the first one is independent of the sweep angle whereas the frequency of the other increases with the sweep angle. This seems to indicate that the main reason for the higher buffet frequency in three dimensions than in two dimensions is the buffet cell phenomenon. The present results show that for small sweep angles the frequency induced by the convection of buffet cells is lower than the 2D buffet frequency. Most of the studies of three-dimensional buffet were made on configuration representative of transport aircraft, with sweep angles in the range 25 deg. to 35 deg. For this reason, the convection of buffet cells resulted in a higher frequency. For example, Dandois (2016) reports a convection speed of  $103m.s^{-1}$  or  $0.37 V_\infty$  for a sweep angle of 30 deg. When normalized by the speed normal to the leading edge  $V_{ref}$ , the convection speed is  $0.427 V_{ref}$ . This value is slightly higher than the trend derived in fig. 2.11. Also, the spectra presented here have sharp peaks instead of the broadband bump reported in the literature. Hence, this feature of the buffet on 3D wings could be related to geometrical parameters like the twist, the taper and the kink (Yehudi break), or to turbulence (small variation of the frequency in time). While the source of the transonic buffet has been identified as an interaction between the shock wave and the boundary layer, the buffet cells remain unexplained. However, there is a similarity to the stall cells observed in subsonic stall. This phenomenon is studied in the



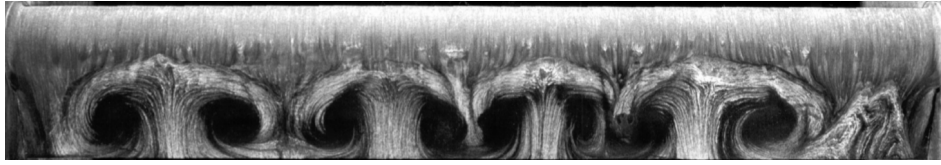
next section.

### 2.3.2 Subsonic stall

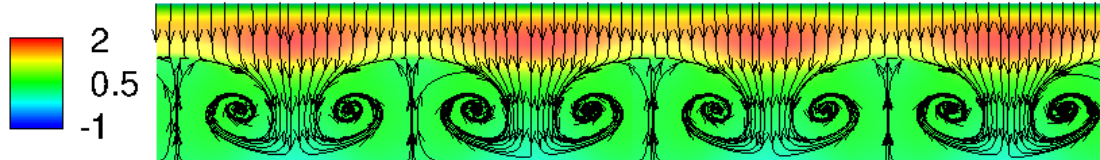
Many experimental campaigns have been carried out to investigate stall cells. However, most of them were done for relatively low Reynolds number and without boundary layer trip. This complicates the reproduction of these experiments with CFD simulations due to possible laminar to turbulent transition effects. Also, there are few experiments over large aspect ratio wings, where a large number of stall cells could be observed. An experiment with visualization of stall cells is the one of Schewe (2001) over a GROWIAN 27% thick airfoil. Fig. 2.17a is taken from this article. This oil flow visualization shows four stall cells for a wing with an aspect ratio of 6, and a Reynolds number of  $7.4 \times 10^5$ . The pressure coefficient and skin friction lines computed over a three-dimensional wing based on the FX77W270s airfoil at the same Reynolds number is shown in fig.2.17b. Four stall cells are obtained and the flow is qualitatively similar to the experimental result. However, the experiments present wall effects (corner flow separations) which are not modeled in the computation with periodic conditions.

Fig. 2.18 provides validation of the numerical setup by comparing the pressure coefficient on a NACA4412 airfoil obtained at a Reynolds of 1.52 million and an angle of attack of 13.87 deg. to the experiments (Coles and Wadcock, 1979) and the solution of the CFL3D solver, provided on the NASA Turbulence Modeling Resource website (Rumsey, 2017). It should be noted that the wall spacing was reduced to  $5 \times 10^{-6}$  chord to account for the Reynolds number. ElsA's solution matches the solution of CFL3D with a small discrepancy around the trailing edge.

The following simulations are carried out at a Reynolds number of 350 000 and a Mach number of 0.2 to neglect the compressibility effects. The wall spacing is  $5 \times 10^{-5}$  chord since the Reynolds number is smaller. For simplicity, fully turbulent RANS simulations are carried out. Fig. 2.19 shows the lift coefficient polar. The maximum lift coefficient of 1.57 occurs at an angle of attack around 14.0 deg. This curve is characteristic of a trailing edge type of stall, where the flow separation progresses from the trailing edge towards the leading edge when the angle of attack is increased. For angles of attack up to 13 deg., the steady-state solver converges. Above this angle, the lift coefficient oscillates when local time steps are used, but converges to a steady value with a time-accurate method. Solutions converged within machine accuracy are obtained with this procedure. Hence these solutions of the URANS



(a) Oil flow visualization of the suction side ( $L/c = 6$ ,  $\alpha = 12$  deg.). (From Schewe (2001) with permission)



(b) FX77W270s Surface pressure coefficient and skin friction lines.

Figure 2.17 – Stall cells flow topology

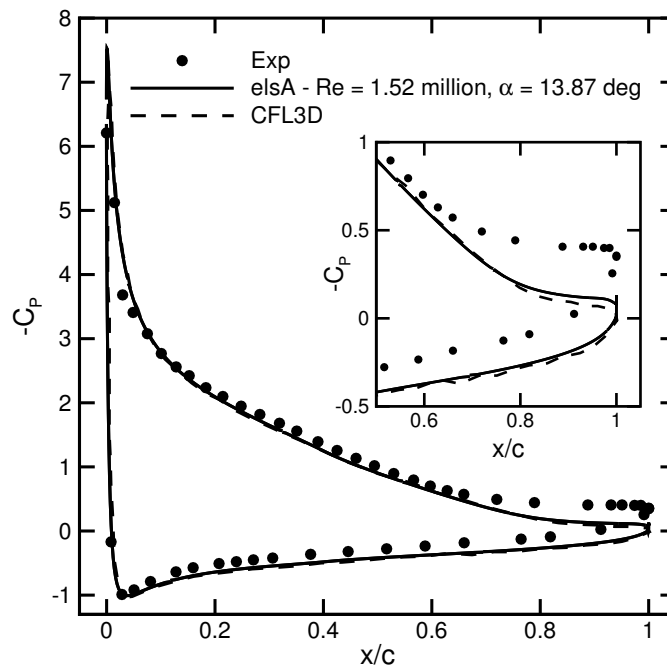


Figure 2.18 – Pressure coefficient over the NACA4412 airfoil.

equations are also solutions of the RANS equations. For angles of attack above 16.0 deg., the lift coefficient does not converge to a steady value and a Strouhal number around 0.2, based on the wake width, is observed. This corresponds to the well-known bluff body vortex shedding frequency. The boundaries of the lift oscillation are shown in fig. 2.19. These RANS and URANS simulations were all computed with the free stream flow conditions as initial solution. Simulations using the SFD method to force the convergence to a steady state are also shown in this figure. These simulations were carried out in sequence by restarting the solution from the previous angle of attack. Solutions between 20.5 deg. on the increasing part of the hysteresis and 18 deg. on the decreasing part do not converge. Nevertheless, two branches of converged flows are found for angles of attack between 16.8 and 18.0 deg. The machine accurate converged flow solutions of the upper and lower branches for an angle of attack of 18 deg. are shown in fig. 2.20. The upper branch solution exhibits a flow separation around 30% of the chord, while the lower branch flow separates from the leading edge. These results are similar to the one of Busquet *et al.* (2017) where a Newton solver was used to converge multiple solutions. Following these results three-dimensional infinite swept wings are computed in the post stall regime.

Fig. 2.21 shows the surface pressure coefficient and skin friction lines obtained for the infinite unswept wing with an aspect ratio equal to 6.0 at an angle of attack of 15 deg. One can observe four spanwise structures ( $\lambda_z/c = 1.5$ ). This computation does not converge to a steady solution, but a stationary solution is obtained when the simulation is carried out with URANS modeling. This is coherent with the two-dimensional simulation at the same angle of attack. The solution can also be converged to a steady state when the SFD technique is used. The left part of fig. 2.21 shows the result with a spanwise grid size refined by a factor 2 (a spacing of  $0.027c$  instead of  $0.054c$ ). Very similar flow topologies are obtained with both meshes and the global lift coefficient is 1.497 in both cases. Hence, all the simulations are computed with 112 spanwise cells to reduce the computational cost. Fig. 2.22 shows the same case with a span of  $12c$ . The same flow topology is observed. Since the number of cells can only be an integer, the preferential wavelength could also be 1.71 or 1.33 with 7 and 9 stall cells instead of 8. Hence the relative error is estimated to be  $14\%$  ( $\frac{1.71-1.5}{1.5} = 0.14$ ), and a very large domain would be required to obtain more accuracy.

Fig. 2.23 shows the two-dimensional pressure coefficient at the angle of attack of 15.0 deg. and the extraction of the pressure coefficient on two sections of the three-dimensional wing (identified on fig. 2.21). Section 1 is between two stall cells, where the flow separation occurs at the most downstream position. Section 2 is extracted at the middle of a stall cell, where

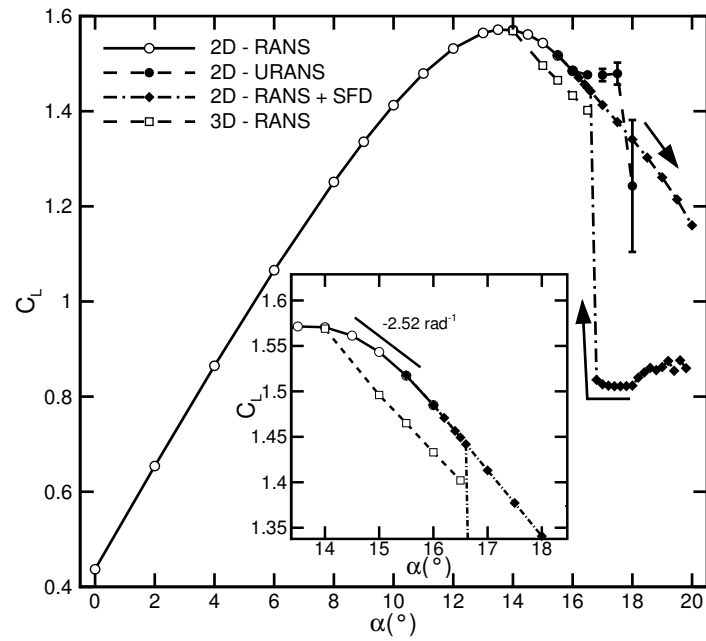
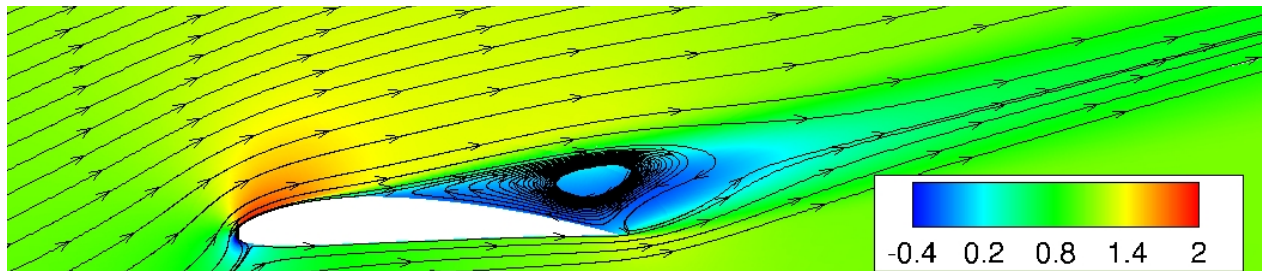
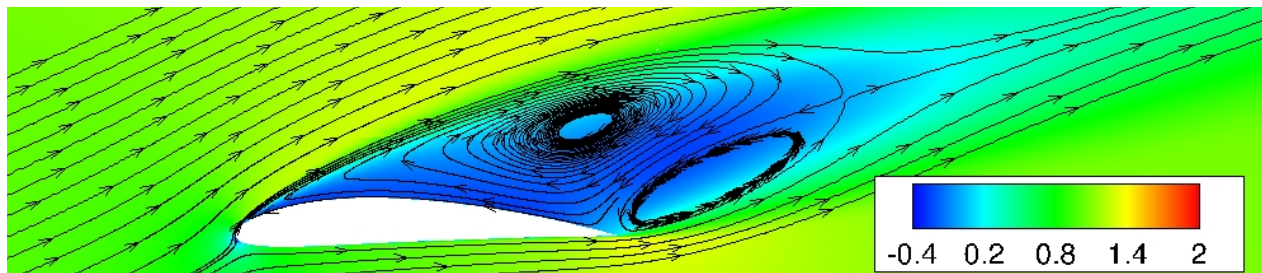


Figure 2.19 – Lift coefficient of the NACA4412 airfoil.



(a)  $\alpha = 18$  deg., upper branch



(b)  $\alpha = 18$  deg., lower branch

Figure 2.20 – Contour of  $u/v_{ref}$  and streamtraces.

the separation is maximal. As it can be seen, the two-dimensional pressure coefficient is between the two extreme pressure coefficients. The squares in fig.2.19 show the global 3D lift coefficients. For cases with stall cells, the lift coefficient is lower than the two-dimensional one at the same angle of attack.

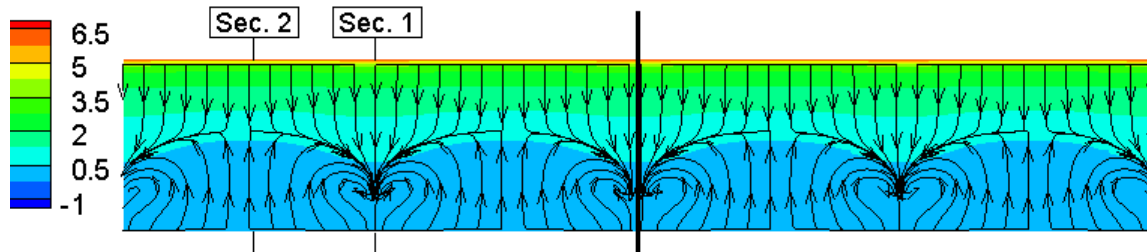


Figure 2.21 – Surface pressure coefficient and skin friction lines with 224 (left) and 112 (right) spanwise cells ( $\alpha = 15.0$  deg.).

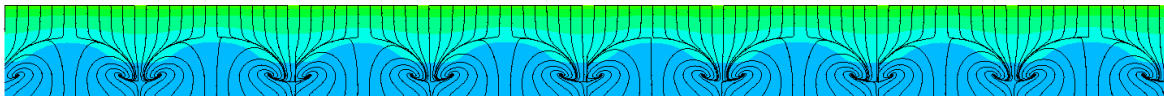


Figure 2.22 – Surface pressure coefficient and skin friction lines for a wing of aspect ratio 12.

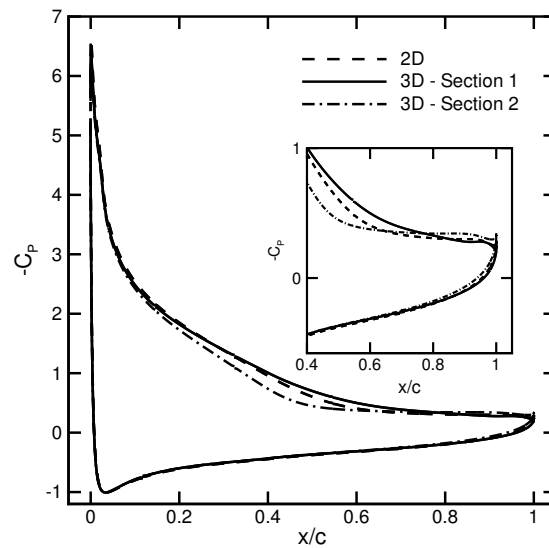


Figure 2.23 – Two-dimensional and three-dimensional sectional surface pressure coefficient.

Computations were carried out for other angles of attack past the maximum lift coefficient. For an angle of 14 deg., the flow remains two-dimensional. The bifurcation towards a three-dimensional flow with stall cells is obtained for an angle of attack of 14.25 deg. For  $\alpha = 18$  deg., it is necessary to use the SFD method to converge the flow and the latter is two-dimensional. The flow separates at the leading edge at this angle of attack and the lift coefficient is equal to the one of the lower branch lift hysteresis. This seems to indicate that the solution locked on the lower branch of the post stall hysteresis. Hence, the stall cells are observed over a narrow range of angles of attack between 14 deg. and 18 deg. More investigations are necessary to determine if the stall cells could be computed for a broader range of angles of attack on the upper branch of the hysteresis.

Spalart (2014) and Gross *et al.* (2015) asserted that a negative slope of the lift versus angle of attack curve is a necessary condition for the presence of stall cells. The simulations presented in this paper tend to confirm this criterion since the stall cells are only observed in the post-stall regime. Moreover, the slope of the  $C_L - \alpha$  curve is flat on the lower branch at an angle of 18 deg., where no stall cells are observed. Gross *et al.* (2015) proposed two criteria for the wavelength of the stall cells. The discrete model state that  $\frac{\lambda_z}{c} = -\frac{1}{2} \frac{\partial C_L}{\partial \alpha}$  and the continuous model is  $\frac{\lambda}{c} = -\frac{\pi}{4} \frac{\partial C_L}{\partial \alpha}$ . For an angle of attack of 15 deg., these equations give a wavelength  $\lambda_z$  of  $1.26c$  for the discrete model and  $1.97c$  for the continuous model. Hence, the computed wavelength of  $1.5c$  falls between the two models.

Fig. 2.24 shows the pressure coefficient and the skin friction lines on the surface of wings swept at 10 deg., 20 deg. and 30 deg. One can observe that the stall cell patterns still have 4 cells in the spanwise direction. The flow topology changes with the sweep angle and the skin friction lines are now aligned in the spanwise direction, especially for 30 deg. Foci are still observed for 10 deg. and 20 deg., but not for the sweep angle of 30 deg. These flow structures are also convected in the spanwise direction. Hence, the flow topology with stall cells is very similar to the one observed in transonic buffet. However, at an angle of attack of 15 deg., the flow unsteadiness is fully driven by the convection of the stall cells. A vortex shedding could possibly be observed at higher angles of attack. Fig. 2.25 shows the history of the sectional lift coefficient for the three sweep angles. The lift coefficient computed on the wing sections is periodic because of the traveling stall cells. The frequency of the latter significantly increases with the sweep angle. On the other hand, the lift coefficient of the entire wing is constant in time. This is due to the fact that the stall cells are very regular, thus they compensate each other when averaged along the span.

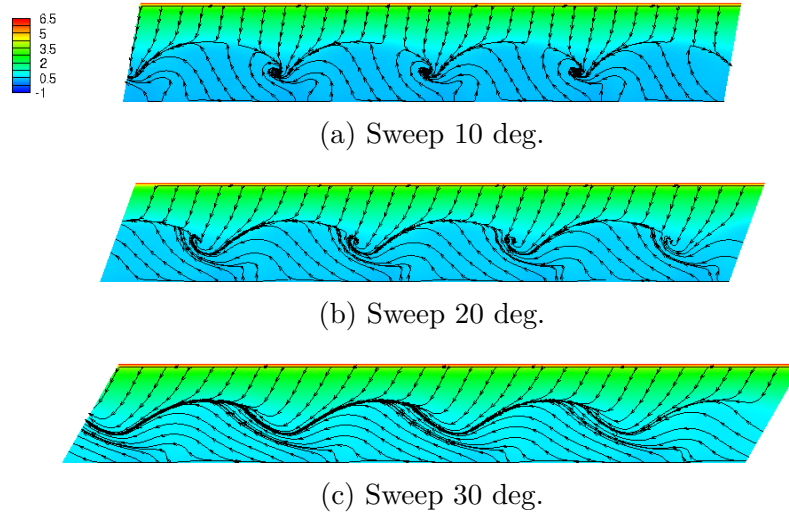


Figure 2.24 – Effect of the sweep angle on the surface pressure coefficient and skin friction lines.

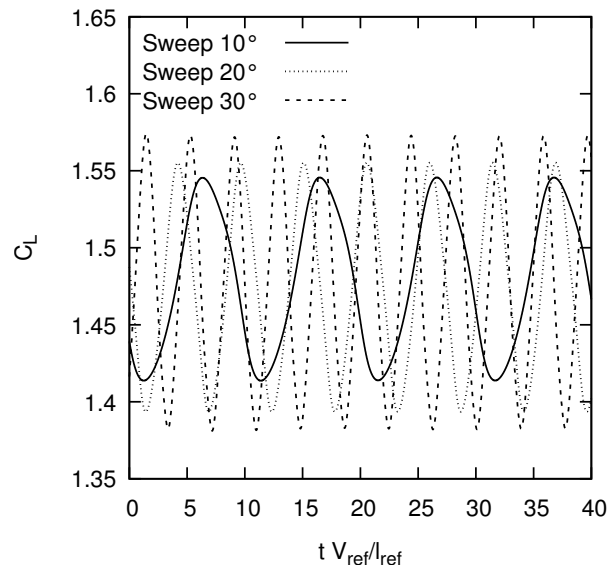


Figure 2.25 – Sectional lift coefficient.

Since the behavior of the stall cells is very similar to the one of the buffet cells, we can try to apply the model presented in fig. 2.9. Fig. 2.26 shows the time history of the pressure coefficient extracted on a line parallel to the leading edge for a sweep angle of 30 deg. One can observe a series of parallel iso-contour of pressure. As it was the case for buffet cells, this corresponds to the convection of stall cells. Here the iso-contours are continuous since

the only major unsteadiness is the convection of the stall cells. Hence, the extraction line always crosses the stall cells, which was not the case for transonic buffet. Also, the variation of pressure coefficient is smaller than for buffet since the stall cells are not bounded by a shock wave. The convection speed of the stall cells is extracted from such graphs. Fig. 2.27 shows the evolution of the convection speed of the buffet cells and the stall cells. One can see that the evolution of the convection speed is proportional to the crossflow component of the free stream velocity with a coefficient 0.8 close to the one found for the buffet cells (0.7). This further emphasizes the similarities between buffet cells and stall cells.

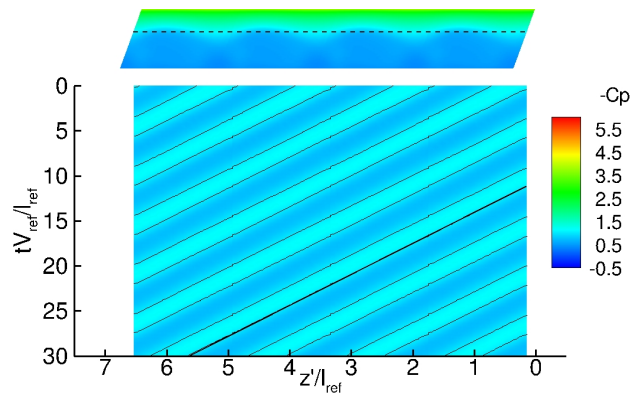


Figure 2.26 – Extraction of the pressure on a line parallel to the leading edge near  $x'/l_{ref} = 0.4$  for a sweep angle of 20 deg.

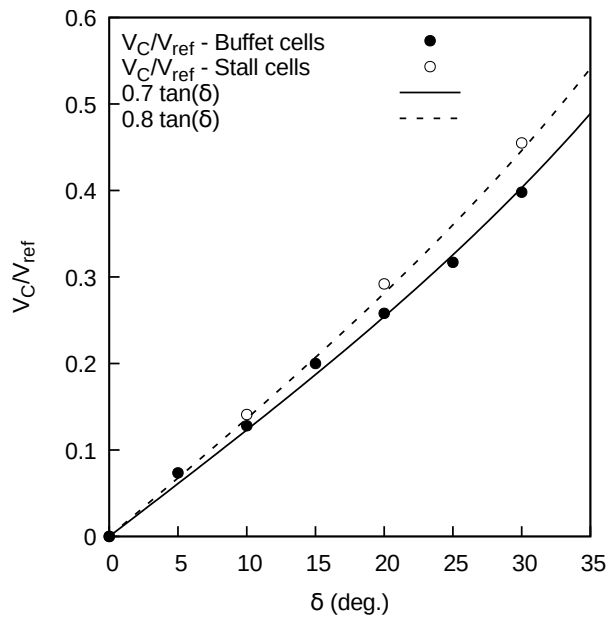


Figure 2.27 – Convection speed model for buffet cells and stall cells.



## 2.4 Conclusion

Numerical simulations of transonic buffet over infinite swept wings have been performed. These simulations were carried out on infinite swept wings to exclude any three-dimensionality from the boundary conditions or geometry. The 2.5D solutions showed that without development of 3D structures, the buffet phenomenon remains very similar to the two-dimensional buffet. The analysis of the frequency content of three-dimensional buffet over infinite swept wings showed the superposition of two phenomena: the 2D buffet, and the convection of the buffet cells. The latter results in a varying frequency with respect to the sweep angle. Contrary to the results over aircraft wings, the frequency associated with the convection of the cells is well-defined. Hence, the effects responsible for the broadband spectra observed in the experiments and other computations are not encountered in URANS simulations of infinite swept wings. The frequency of the unsteadiness caused by buffet cells is related to the size of the buffet cells and their convection speed. The latter is proportional to the spanwise component of the free stream velocity. Hence, the missing element for explaining the frequency of transonic buffet is a model for the occurrence and size of the buffet cells.

Computations of infinite swept wings in subsonic regime with trailing edge separation showed the appearance of stall cells. The topology of those cells compares well with the topology of the buffet cells. Also, for swept wings, the cells are convected in the spanwise direction resulting in an unsteady flow very similar to the three-dimensional buffet. In contrast to transonic buffet, the unsteadiness is only associated with the convection of the stall cells. Hence, without sweep the flow is steady. These observations suggest that the flow physics of the stall cells and the buffet cells are related. With regards to the literature this means that the buffet cells could be explained by inviscid theories and thus provide a better understanding of the complex transonic buffet phenomenon.

## Acknowledgments

This work is supported by the Natural Sciences and Engineering Research Council of Canada/Conseil de recherches en sciences naturelles et en génie du Canada. Part of this work made use of the GENCI CINES facilities (Grant DARI No.A0042A10423).

## CHAPTER 3 ZONAL DETACHED EDDY SIMULATIONS

The previous chapters used the solver elsA developed by Airbus, Safran and ONERA, which is a general purpose flow solver with state of the art convergence acceleration techniques like geometrical multigrid for the steady state RANS equations. In this section the solver FastS, which is a recent structured flow solver optimized to reduce the time per iteration and maximize parallel computing performance is used. These properties make it suitable for resolved turbulent scale simulations like DNS, LES and Hybrid RANS/LES simulations. For this reason, it was used to carry out ZDES simulations of the OALT25 airfoil in buffet conditions.

### 3.1 Numerical methods

The numerical setup is the same as the one used in the previous chapter with the extrusion of a baseline 2D grid to obtain the 3D one. The sweep angle is introduced by adding a side-slip component to the farfield conditions (see Figure 4.1). This type of grid is preferable to the one used in chapter 2, when the mesh was swept and no cross-flow components were added since FastS uses the uniform grid direction to simplify the computation of the fluxes and reduce the computational cost. As it is the case throughout the thesis, a Mach number of 0.7352, a Reynolds number of 3 million and an angle of attack of 4 degrees are retrieved in the plane normal to the leading edge. For comparison between the URANS simulation and the ZDES of FastS, two grids are used. The first one is the O-type grid used in chapters 2 and 4. The second one is designed to be finer in regions where a separated flow is expected. This C-H type grid is shown in Figure 3.1 and has 166 800 grid cells with a  $\Delta x^+$  of 200 in the region where the flow separates. The grid is extruded in the third dimension to have a  $\Delta z^+$  around 200. A small span of 0.25 chord is used to investigate the two-dimensional buffet and a larger span of 4 chord lengths is considered for the three-dimensional buffet case.

In the FastS flow solver, the AUSM+P scheme is used for the convective fluxes discretization. Time-accurate solutions are obtained with the second-order Gear scheme. A time step smaller than the one used in the URANS simulations of  $7 \times 10^{-5} V_\infty / c$  is used since turbulent scales must be resolved. This numerical setup is also used for a 2D URANS computation. In this case, the Spalart-Allmaras turbulence model with the compressibility correction is used. For the ZDES simulations, the computational domain is separated into three main regions. The first one around the leading edge and the pressure side is coarsely meshed and is treated

as a URANS zone. The zones on the trailing edge and the suction side are treated with ZDES type 1 or 2 depending on the case (see Figure 3.1). A layer with a thickness of 0.007 chord over the entire surface is computed in URANS mode in every case. This thickness is the boundary layer thickness observed when the shock is at its average position in a 2D computation.

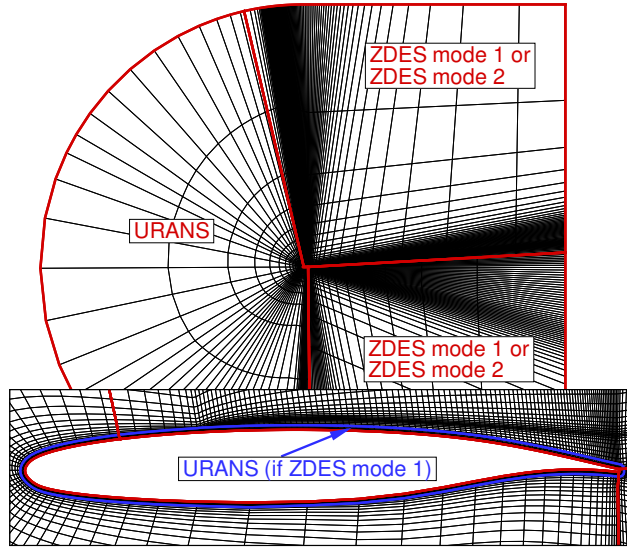


Figure 3.1 – C-H type grid with repartition of the model type (only one point out of four shown)

### 3.2 Two-dimensional buffet

First, the URANS solutions of FastS can be compared to the URANS simulations of elsA. One should note that the grid is not the same between the two computations. The elsA simulation is the unswept 2D case presented in chapters 2 and 4, while the FastS simulation is done on the grid designed for the ZDES simulations. Moreover, the numerical method is different (spatial scheme, time integration and turbulence model). The two simulations produce similar results for the pressure distribution (Figure 3.2a). The pressure on the pressure side and supersonic plateau are the same. However, the shock wave position in the elsA simulation is slightly downstream of the FastS one. Additionally, one can observe that the shock excursion amplitude is larger in the FastS simulation by looking at the pressure fluctuations (Figure 3.2b). Such results were expected since the main difference between URANS simulations with various numerical methods and turbulence models from the literature is the shock wave position and its excursion.

Then one can look at the results of three different numerical setups for the ZDES computations over a small span. In every case, the shock wave position is upstream of the experiment and the URANS simulations. The pressure near the trailing edge is also too low and the pressure of the supersonic plateau is too high. These discrepancies between the ZDES and the URANS are in line with the results presented in the literature (Figure 1.7). One should note that there is an issue with the protection of the boundary layers in the ZDES mode 2 and the DDES for fine grids. Since the computations presented in this thesis have been carried out, a new protection function has been proposed by Deck and Renard (2020) with improved results for the transonic buffet case over an OAT15A airfoil. In this thesis, using the ZDES mode 1 allows to better protect the boundary layer.

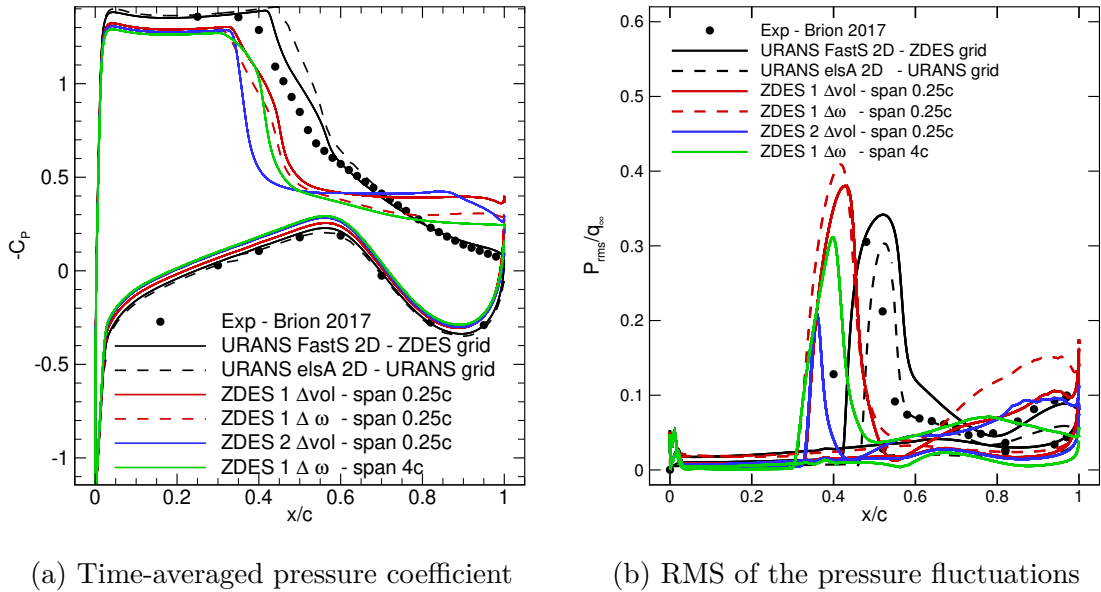


Figure 3.2 – Pressure distribution of the 2D URANS ZDES simulations.

### 3.3 Three-dimensional buffet

The ZDES mode 1 with the  $\Delta_\omega$  formulation is used for a computation with a span of 4 chord lengths and a sweep angle of 20 deg. A layer of 0.007 chord length is treated in URANS near the wall. In this case, the grid has 320 million cells which is close to the number used in recent LES simulations of the two-dimensional buffet at a similar Reynolds number (in the order of 400 million in the computation of Fukushima and Kawai (2018) and Dandois *et al.* (2018)). The ZDES modeling allows to reduce the number of points and compute a larger span.

The pressure coefficient averaged in time and in the spanwise direction is shown in Figure 3.2a. One can observe this pressure distribution is slightly different from the one obtained in the small span case. The upper part of the time-averaged pressure coefficient near the shock is rounder and the pressure at the trailing edge differs. Fig. 3.3 shows a comparison between the time-averaged pressure coefficient of the ZDES and URANS simulations with a span of six chord lengths (which are further analyzed in chapter 4). The differences between the ZDES and the URANS results are still observed (pressure plateau too low, shock too upstream and pressure too low at the trailing edge). However, one can notice the particular shape of the upstream portion of the time-averaged shockwave which is rounder than in the small span and two-dimensional cases. This feature is an indication of the presence of buffet cells which modify the position of the shock at these chordwise positions. Figure 3.4 shows the iso-surface of the  $Q$ -criterion and the density on the wing surface. One can observe two buffet cells in the form of a shockwave position closer to the leading edge. These buffet cells are associated with two regions where the  $Q$ -criterion shows turbulent structures. Otherwise, these turbulent structures are only observed near the trailing edge. These structures are associated with regions of flow separation. As it is the case in the URANS simulations, the buffet cells are convected in the spanwise direction.

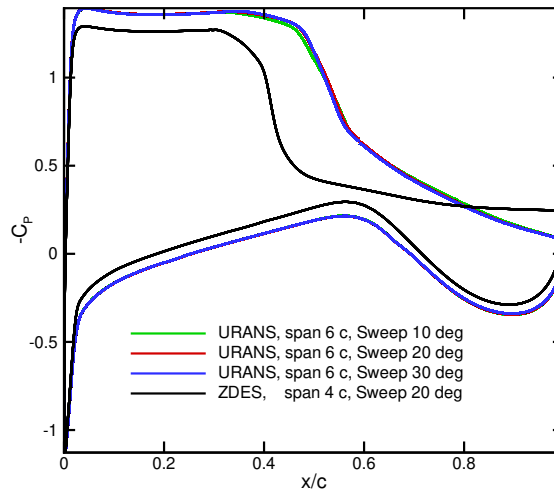


Figure 3.3 – Time-averaged pressure distribution of three-dimensional buffet on swept wings.

To enable a finer analysis of the ZDES simulation, a set of probes are used to extract the pressure signal in time. Fig. 3.5 shows the location of these probes. They are located on the wall and in the field along the boundary of the separation zone. Of course this zone changes in time. The probes are distributed in the X-Y plane and are duplicated eight times along

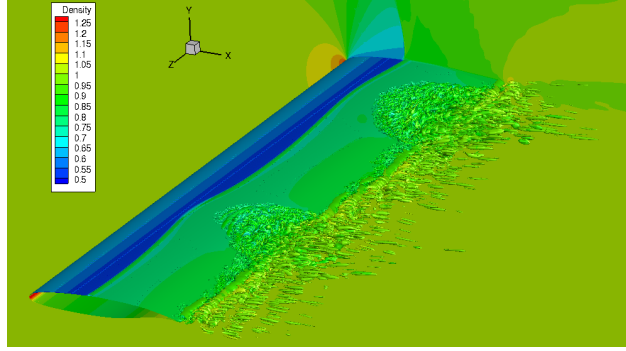


Figure 3.4 – Q-criterion iso-surface of level 60.0 colored by density and density contour on the plane  $z/c = 4$  and the wing surface.

the span with a spacing of 0.5 chord. The power spectral density of the pressure signals is evaluated using Welch’s method with 50% overlap between the blocks. In total, the signal length is 368 time units ( $\bar{t} = tV_{ref}/c$ ) and 3 blocks are used. This yields a Strouhal number resolution of 0.0054. The power spectral density for the probes at one spanwise section on the wall and in the field are shown in Figure 3.6. Two dominant frequencies at Strouhal numbers around 0.09 and 0.175 can be identified in these spectra. These frequencies are harmonics of one another. Another frequency at a larger Strouhal number of 4.86 is also present in the spectrum extracted near the trailing edge. This frequency is probably associated with a Kelvin-Helmholtz instability. Finally, a small peak is observed near  $St = 0.07$ . Some of the probes (i.e.  $x/c = 0.15$ ) are located upstream of the shock at every moment. These probes do not monitor strong unsteady behavior. The probes aft of the shock position record the peaks between  $St = 0.07$  and 0.175. The high Strouhal number of 4.86 is only observed for the probes near the trailing edge. One should note that the frequency resolution is not optimal. This is limited by the computational cost of the ZDES simulation. The time step of the ZDES simulation must be selected to resolve the high frequency of the turbulence. However, the transonic buffet (even the three-dimensional one) has a relatively low frequency. Hence, a time step that is orders of magnitude smaller than the one used in URANS simulations must be used. This combined with the large number of grid cells to resolve the turbulence results in a large computational cost. For this reason, the length of the simulation is limited.

The cross-spectrum analysis for the probes Field002 (see Figure 3.5 for the location) along the span is shown in Figure 3.7. For this analysis, 5 blocks are used in Welch’s method to reduce the noise in the spectra. One can observe bands of higher coherence (Figure 3.7a) between the probes aligned in the spanwise direction near the dominant frequencies of 0.09 and 0.175. Another band is observed near 0.07. Following this, the phase (Figure 3.7b)

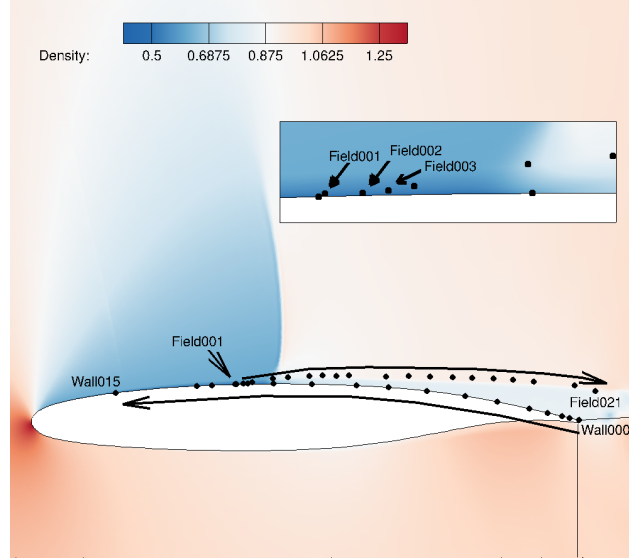
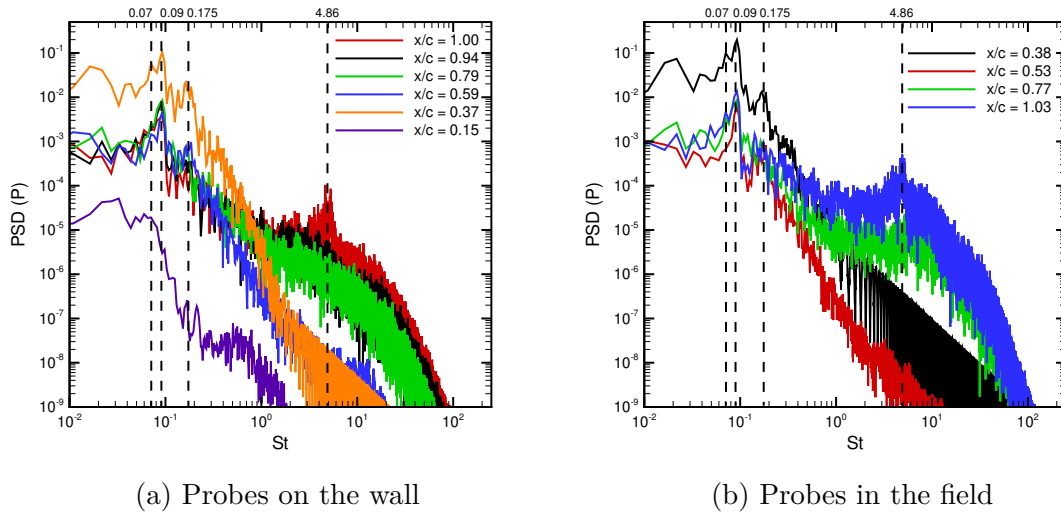


Figure 3.5 – In X-Y plane location of the probes for the ZDES simulation.



(a) Probes on the wall

(b) Probes in the field

Figure 3.6 – Power spectral density of the pressure in the large span ZDES simulation.

between these sensors is analyzed. From this quantity, one can compute the convection speed:

$$\frac{V_C}{V_{ref}} = 2\pi \frac{f}{V_{ref}} \frac{\Delta z}{\Delta \phi} \quad (3.1)$$

Where  $\frac{\Delta z}{\Delta \phi}$  is the variation of the phase along the span. From this we find a null convection speed associated with a Strouhal number of 0.07, a normalized convection speed of 0.18 (0.26 in the URANS simulations) associated with the Strouhal number of 0.09 and of 0.36 associated with the Strouhal number of 0.175. These two frequencies are consistent with the convection of buffet cells with a wavelength of  $2.0c$  ( $\lambda/c = (V_C/V_{ref})/St = 0.36/0.175 = 0.18/0.09 \approx 2$ ). This result is expected for the Strouhal number of 0.09. However, if the Strouhal of 0.175 is associated with a harmonic of the convection of the buffet cells, one should expect the convection speed to be  $0.18V_{ref}$  and the wavelength to be of the order of the chord length. Instead, the convection speed is twice the one of the buffet cells convection. This result is more consistent with the nonlinear interaction between a two-dimensional mode, as analyzed in the appendix C (which presents a detailed analysis of the URANS simulations). The equations C.2 to C.3 show that a mode which has a frequency equal to the difference or the addition of a two-dimensional frequency and a three-dimensional one ( $\omega_3 = \omega_1 + \omega_2$ ) will yield a convection speed equal to  $V_{C,3} = V_{C,2}\omega_3/\omega_2$  with  $V_{C,3}$  the new convection speed. Since the convection speed is twice the one of the buffet cell convection mode, one should expect the frequency of the two-dimensional mode to be  $St = 0.09$ . However, we found the mode without convection to be at a Strouhal of 0.07. This discrepancy might be explained by an insufficient frequency resolution. The fact that the buffet cell convection frequency and the two-dimensional mode frequency are close might also impair the capacity to separate the phenomena involved in this ZDES simulation. One can also look at the inverse Fourier mode of the pressure on the wing surface for the dominant frequencies, shown in figure 3.8. The mode at a Strouhal number of 0.07 is essentially two-dimensional and will cause the shock wave to oscillate in the chordwise direction. The mode at a Strouhal number of 0.09 clearly shows a modulation with a wavelength of 2 chords in the spanwise direction. This mode is consistent with the presence of buffet cells. The mode associated with a Strouhal number of 0.175 is more difficult to analyze. This mode shows a modulation in the spanwise direction, but the wavelength is not clearly equal to 2 chord, which should be expected for the interaction between the two-dimensional mode and the convection mode. This might be explained by the fact that this frequency is close to the harmonic of the buffet cells convection and this Fourier mode might not be associated with a single mechanism.



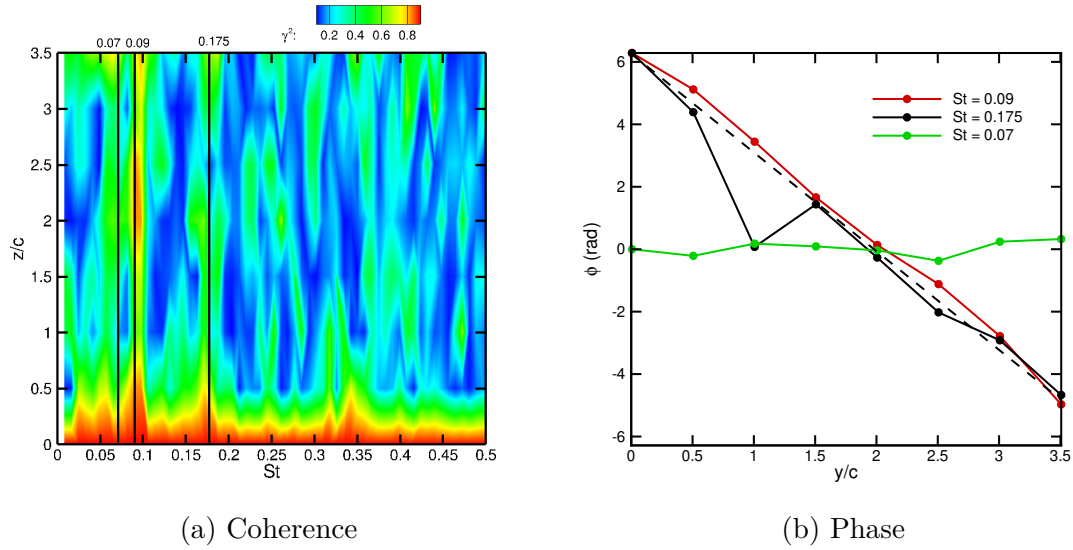


Figure 3.7 – Cross-spectrum analysis in the spanwise direction for the Field002 probes.

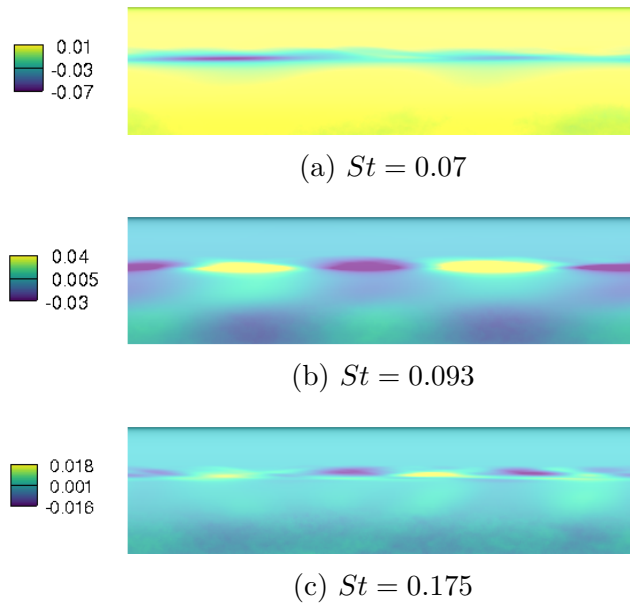


Figure 3.8 – Inverse Fourier modes.

### 3.4 Conclusion

In conclusion, the solution of the ZDES and URANS simulations are in qualitative agreement. The two-dimensional buffet is observed on the small span ZDES simulations. However, the shock wave position is upstream of the experimental and URANS ones. Significant dis-

crepancies are also observed in the pressure distribution. The same observations hold for the large span ZDES simulation. In this simulation, the flow visualization clearly shows the presence of 2 buffet cells. The frequency associated with the latter is found to be  $St = 0.09$  by looking at the Fourier decomposition of the wall pressure evolution in time. Furthermore, this mode is associated with a convection speed  $0.18V_{ref}$ , which is lower than the one observed in the URANS simulation. A two-dimensional oscillation of the shock wave position is also observed. The spectra (Figure 3.7) do not exhibit the broadband buffet frequency normally observed for the three-dimensional buffet. Hence, even with the addition of turbulent fluctuations, a narrow band frequency can be associated with the convection of the buffet cells and another cause for the broadband frequencies observed on complex geometries must be sought. However, a longer simulation time would have been necessary to increase the precision of the analyses and the selection of another sweep angle would have been suitable to increase the separation between the two-dimensional buffet frequency and the buffet cell convection one. Another possible explanation for the narrow band frequency is the fact that there are no turbulent fluctuations in the shock foot area since the simulation uses a RANS model upstream of the flow separation. To address this point a ZDES mode 3 would be required or a LES simulation. However, such a simulation would be more costly than the simulation presented in this chapter.

## CHAPTER 4    ARTICLE 2 : LINK BETWEEN SUBSONIC STALL AND TRANSONIC BUFFET ON SWEPT AND UNSWEPT WINGS: FROM GLOBAL STABILITY ANALYSIS TO NONLINEAR DYNAMICS

*The second article builds on the results of the first one (chapter 2) by carrying out global stability analyses on the same test cases. Results of URANS simulations like the ones presented in chapter 2 are recalled for the completeness of the article. To simplify the interpretation, URANS simulations have been carried out on an unswept wing with a sideslip angle added to the free stream. In chapter 2 the wings were swept and the free stream had no sideslip. Both flow configurations represent the same flow problem. However, it has been noticed that adding the sideslip angle results in faster convergence. This can be explained by a better quality grid since the cells are not skewed in the third dimension. The selected URANS results in the article lead to the same conclusions as those of the first article.*

*Then, global stability analyses of these flows are carried out. Carrying fully three-dimensional stability analyses would be prohibitive and limit the range of values in the parametric analyses. For this reason, an approach where the perturbation around a two-dimensional base-flow is assumed to be periodic in the spanwise direction is used. This allows to reduce the size of the eigenvalue problem involved in the stability analysis to the size of a two-dimensional problem which can be solved on a desktop computer or, in this case, a single node (24 cores) of a computer server. This allowed to carry extensive parametric studies on the sweep angle and angle of attack. A downside of the proposed methodology is the fact that the wavenumber of the flow perturbation must be provided. Hence, a new parameter is added to the analysis and the problem must be solved for several wavenumbers and one can speculate that the wavenumber for which the mode has the strongest growth rate will develop in the real three-dimensional case. Nevertheless this also presents the advantage of allowing to separate the modes at different wavenumbers, including the two-dimensional one at  $\beta = 2\pi/\lambda_z \rightarrow \infty$ .*

*Using these simulations, the presence of an unstable mode associated with two-dimensional buffet is found as well as a three-dimensional one. A proportionality relation between the convection speed of the buffet/stall cells and the sweep angle is found and the latter is coherent with the one found using the URANS simulations, both in the subsonic and the transonic case. The wavelengths predicted by the global stability analyses are also in line with the wavelengths of the stall cells in the URANS simulations of the NACA4412 airfoil. However, for the OALT25 there is a discrepancy between the wavelengths in the stability analysis and*

the URANS simulations. Since the global stability is a linear model and the previous URANS simulations were carried out to solve the non-linear regime (starting from an unconverged solution), the next step is to study the transition between the linear and the saturated non-linear regime. Hence, simulations are started from the steady-state base-flows used for the stability analyses and run up to the point where periodic regimes are found. In the case of the subsonic stall the flow diverges from the base-flow with the number of stall cells predicted by the stability analysis and settled at a solution with the same number of cells. In the case of the transonic buffet, the flow actually diverges following the behavior predicted in the stability analysis but transition to longer buffet cells before reaching the steady state. Also, the buffet cells are superimposed to a chordwise oscillation of the shockwave position.

The final part of this article uses the stability analysis to show that a three-dimensional unstable mode akin to stall/buffet cells can be found for Mach numbers from the subsonic to the transonic range. This mode is found for every Mach number from 0.2 to 0.73 even though the base-flow topology changes. For Mach numbers lower than 0.5 the flow separates with a trailing edge stall behavior. However, at a Mach number of 0.4 and 0.5 a small shock induced separation occurs near the leading edge. Nevertheless the three-dimensional mode is located at the foot of the larger trailing edge separation. For Mach number greater than 0.5, a strong shock wave is present and the three-dimensional mode is located at the shock foot. Moreover, the relations between the convection speed of the buffet/stall cells and the sweep angle also hold for this new test case. A scaling of the wavelength by the separation height is also proposed to unify the wavelength of the buffet cells and stall cells. These results emphasize the similarities between the buffet and stall cells. Thus this article supports the hypothesis that buffet cells and stall cells are the same instability and propose a model for their appearance, the one of a global unstable mode.

The appendix and supplementary material are in the appendix A. The appendix B presents results for the continuous branch of base-flows between the upper and lower branches of the polar of the NACA4412 airfoil, using a Newton continuation technique. These results show a continuous evolution from the onset of the three-dimensional mode to its offset by following a path of fully converged base-flows in between the two initially found branches. The appendix C expands on the URANS results by presenting extraction of the pressure in space and time (like in Figure 4.10) for several extraction lines and sweep angles for the transonic buffet case. This appendix also presents cross-spectrum analyses of the signals of pressure probes at the surface of the wings. This allows to extract the convection speed associated with specific frequencies and to identify the source of the peaks in the spectra in Figure 4.9.

PLANTE, F., DANDOIS, J., BENEDDINE, S., LAURENDEAU, É., and SIPP, D., "Link between subsonic stall and transonic buffet on swept and unswept wings: from global stability analysis to nonlinear dynamics", *Journal of Fluid Mechanics*, vol. 908, published online 4 Dec. 2020, doi: 10.1017/jfm.2020.848.

This paper examines the three-dimensional cellular patterns appearing on wings in subsonic stall and transonic buffet conditions. Unsteady Reynolds-Averaged Navier-Stokes simulations are carried out for three-dimensional infinite swept configurations closed by periodic boundary conditions in the spanwise direction. In both flow conditions the occurrence of stall/buffet cells is observed, as well as their convection at a speed proportional to the sweep angle. In transonic buffet conditions, this phenomenon is superimposed to the well-documented two-dimensional buffet instability. These results indicate that the discrepancies between two-dimensional and three-dimensional buffet are caused by the occurrence of buffet cells and that this phenomenon is similar to the one observed at low speed. These phenomena are then studied using global linear stability analysis with the assumption of a periodic flow in the spanwise direction. From these analyses a mode coherent with the two-dimensional buffet is obtained, as well as a mode coherent with two-dimensional vortex shedding in stall conditions. In addition, in both flow conditions an unstable mode reminiscent of stall/buffet cells is observed.

#### 4.1 Introduction

Transonic buffet and subsonic stall are two boundaries of the flight envelope of civil aircraft. Transonic buffet is an oscillation of the shock wave position over a wing caused by an interaction between a separated boundary layer and the shock wave. This oscillation induces variation of the aerodynamic forces which can be detrimental to aircraft handling. A thorough review of the state of knowledge about transonic buffet is presented by Giannelis *et al.* (2017). On the other hand, subsonic stall occurs when flow separation causes a reduction of the lift forces as the wing angle of attack is increased. These phenomena involve complex physics, part of which is the occurrence of three-dimensional flow features which are named buffet cells and stall cells respectively. The stall cells are identified as a spanwise variation of the flow separation, while the buffet cells are a spanwise variation of the shock wave position, and thus of the shock induced flow separation.

Stall cells were observed experimentally (Moss and Murdin (1971); Gregory *et al.* (1971)) since the 1970's. Most of these studies were carried out for wing which spans the entire

wind tunnel width, a setup which is often considered as "two-dimensional". However, the flow becomes strongly three-dimensional when stall cells are present. Early studies suggested that the phenomenon might be caused by the side walls. However, the experimental results of Winkelmann and Barlow (1980) contradict this conclusion since the stall cells are observed over the entire span of wings of aspect ratios up to twelve and with free tips. They reported that the number of cells is proportional to the aspect ratio. Schewe (2001) also reports the effect of the aspect ratio on the number of stall cells. Experiments by Broeren and Bragg (2001) of aerofoil with trailing edge, leading edge and thin aerofoil type of stall suggest that trailing edge separation is a necessary condition for the occurrence of stall cells. Yon and Katz (1998) obtained stall cells over a narrow range of angles of attack and discussed the unsteady nature of the stall cells. More recently, Dell'Orso and Amitay (2018) carried out a parametric study of the effect of the angle of attack ( $\alpha$ ) and the Reynolds number ( $Re = \frac{\rho_\infty V_\infty c}{\mu_\infty}$ ). They identified eight types of flow topologies from a full span separation (2-D) to the presence of one or two stall cells. From these results, the stall cells are observed above a given critical Reynolds number and angle of attack. They also observed conditions for which the topology oscillates in time between two types of flow topology. This might explain the fact that steady and unsteady stall cells are reported in the literature. Hence, the stall cells seem to be very sensitive to the flow conditions and are observed in the presence of a trailing edge separation. The stall cells can be steady or unsteady depending on the experiments. However, the measurement methods might also have a time-averaging effect and impact the visualisation of an unsteady behaviour.

Stall cells were computed by Bertagnolio *et al.* (2005) for a wind turbine aerofoil with Reynolds-Averaged Navier-Stokes (RANS) and Unsteady Reynolds-Averaged Navier-Stokes (URANS) simulations. Manni *et al.* (2016) studied the stall cells over a wing with an aspect ratio equal to ten at a Reynolds number of one million with Unsteady RANS (URANS) and Delayed Detached Eddy Simulation. Their URANS results showed stall cells with spanwise spacing of 1.4 to 1.8 chord length over a narrow range of angles of attack. Liu and Nishino (2018) studied the unsteady behaviour of stall cells over a NACA0012 at a Reynolds number of  $1.35 \times 10^5$  and  $1 \times 10^6$ . Previous work by the authors (Plante *et al.* (2019a)), based on URANS simulations of a NACA4412 aerofoil at Reynolds 350 000, showed the convection of the stall cells in the spanwise direction when the wing is swept. To the authors' knowledge this is the first analysis of the stall cells phenomenon on swept wings.

Multiple models have been proposed for the origin of the phenomenon. Analyses based on the lifting line theory by Spalart (2014) and Gross *et al.* (2015) suggest that a negative slope

of the lift versus the angle of attack is necessary to observe the stall cells. Analyses with lifting surface models (Vortex Lattice Method) coupled with RANS data by Gallay and Laurendeau (2015) and Paul and Gopalarathnam (2014) exhibits similar lift distributions. Kitsios *et al.* (2009) studied an ellipse and a NACA0015 aerofoil in stall conditions at a Reynolds number of 200 with global linear stability analyses. They found a non-oscillatory unstable mode with a spanwise wavenumber  $\beta = 2\pi/\lambda_z = 1.0$ . Rodríguez and Theofilis (2011) linked this non-oscillating unstable global mode to the stall cells phenomenon. However, the existence of this mode has then been questioned by the later work of He *et al.* (2017), who were unable to recover the unstable global modes, and this with two different numerical approaches. Zhang and Samtaney (2016) carried out similar stability analyses on a NACA0012 aerofoil at Reynolds numbers in a range from 400 to 1000. Besides the classical oscillatory modes, they identified an unstable non-oscillatory three-dimensional ( $\beta = 2$  and 4) mode on an aerofoil in laminar regime but for slightly higher Reynolds numbers (between 800 and 1000). They associated this mode to a centrifugal instability of the recirculation bubble, present when the backflow velocity is larger than 20% of the inflow velocity. In these articles, flows with a low Reynolds number of a few hundreds to a thousand were studied. As such, the literature lacks a proper relation between stall cells and a global instability for high Reynolds turbulent flows. The present paper has the purpose of providing this link using RANS models. This is done by carrying out three-dimensional URANS simulations and global stability analyses.

Similar flow instabilities are reported for separation bubbles at low Reynolds numbers on various geometries. Separation bubbles on flat plates were analysed by Theofilis *et al.* (2000) and Rodríguez and Theofilis (2010). In the latter study a link to the structure of stall cells was proposed in relation with the above mentioned questionable computations in Rodríguez and Theofilis (2011). Barkley *et al.* (2002) investigated a backward facing step and found a three-dimensional instability. They studied flows at Reynolds numbers within a range between 450 to 1050 based on the height of the step, and associated the three-dimensional unstable mode to a centrifugal instability thanks to the criterion of Bayly *et al.* (1988). Gallaire *et al.* (2007) studied the flow over a bump at a Reynolds number of 400. They found a non-oscillatory mode causing the flow to become three-dimensional. A similar instability was found by Marquet *et al.* (2009) for an S-shaped duct and by Picella *et al.* (2018) in open-cavity flows. Finally, a three-dimensional non-oscillatory unstable mode was found for a shockwave boundary layer interaction by Robinet (2007). These studies show that three-dimensional instabilities such as those found on aerofoils at low Reynolds numbers are also found on other configurations displaying recirculation bubbles.

Concerning transonic buffet, the two-dimensional phenomenon was investigated for a NACA0012 aerofoil by McDevitt and Okuno (1985) for a wide range of Mach number and angle of attacks at a Reynolds number of 10 million. Strouhal numbers ( $St = \frac{fc}{V_\infty}$ ) in a range from 0.06 to 0.07 were identified, and the buffet onset boundary in the Mach number - angle of attack plane was identified. Similar buffet frequencies were obtained by Benoit and Legrain (1987) for a RA16SC1 aerofoil and Jacquin *et al.* (2009) for the OAT15A aerofoil. The latter study is now widely used to validate numerical models. Recently, Brion *et al.* (2017) studied the OALT25, an aerofoil designed to promote laminar flow, with free transition and tripped boundary layer. They obtained Strouhal numbers of the order of 0.07 in the turbulent boundary layer case. From these experiments, turbulent transonic buffet is identified as a large amplitude oscillation of the shock position with a well-identified Strouhal number around 0.07.

Many numerical studies of two-dimensional transonic buffet have been carried out. Le Balleur and Girodoux-Lavigne (1989) and Edwards (1993) used viscous-inviscid coupling strategies. However, the bulk of the numerical simulations reported in the literature is carried out with Unsteady Reynolds Averaged Navier-Stokes models (URANS) (Goncalves and Houdeville (2004); Thierry and Coustols (2006); Iovnovich and Raveh (2012); Giannelis *et al.* (2018); Grossi *et al.* (2014); Plante and Laurendeau (2019)). These simulations identified frequencies in the range of those obtained experimentally. However, the simulations are found to be very sensitive to the numerical scheme and turbulence model. Large Eddy Simulations (LES) were carried out by Garnier and Deck (2010) and Fukushima and Kawai (2018) with excellent agreement to the experiment of Jacquin *et al.* (2009). However, such simulations are computationally very expensive. Hence, hybrid RANS-LES simulations were attempted (Deck (2005a); Huang *et al.* (2012); Grossi *et al.* (2014); Ishida *et al.* (2016); Deck and Renard (2020)) and Ribeiro *et al.* (2017) used the Lattice Boltzmann Method. These simulations predicted transonic buffet, but discrepancies to the experimental pressure distributions were found. Hence, URANS simulations reproduce the main feature of transonic buffet. However, the turbulence modelling has a strong effect on the quantitative results.

Three-dimensional transonic buffet is more complex. Most of the studies were carried out on half-wing body aircraft configuration. A broadband frequency content with a dominant frequency higher than the one of two-dimensional buffet was found experimentally (Roos (1985), Dandois (2016), Paladini *et al.* (2019a), Masini *et al.* (2020b), Koike *et al.* (2016)). On such configurations, the convection of flow perturbations towards the wing tip was observed and buffet cells can be seen in the pressure-sensitive paint measurements of Sugioka *et al.*



(2018). Numerical simulations of such configurations were carried out with URANS (Sartor and Timme (2016)) and hybrid RANS-LES simulations (Brunet and Deck (2008), Sartor and Timme (2017), Ishida *et al.* (2017)). Ohmichi *et al.* (2018) used Dynamic Mode Decomposition and Proper Orthogonal Decomposition to identify two dominant modes. One high-frequency mode ( $St \approx 0.2 - 0.6$ ) associated to buffet cells and one at  $St \approx 0.06$ , coherent with two-dimensional buffet. Iovnovich and Raveh (2015) studied simplified swept wings closed by a symmetry plane and an extrapolation boundary condition to emulate an infinite swept wing. They observed buffet cells and an effect of the sweep angle on the buffet amplitude and frequency. Previous work by the authors (Plante *et al.* (2019a)) investigated infinite swept wings closed by periodic boundary conditions. Such simulations produced much more regular buffet cells and showed that buffet cells occur without any three-dimensional disturbance from the physical setup, thus making this phenomenon a candidate for an explanation based on global stability analysis.

Transonic buffet was described as a feedback loop between the shock wave motion and acoustic waves generated near the trailing edge by Lee (1990). The description of the transonic buffet as a globally unstable mode was introduced by Crouch *et al.* (2009) and further investigated by Iorio *et al.* (2014) and Sartor *et al.* (2015). Such analyses produce an accurate prediction of the buffet frequency and onset angle of attack angle. Three-dimensional global stability analyses were attempted by Iorio *et al.* (2014), but an unstable mode specific to three-dimensional buffet was not found. Recently, global stability analysis was applied to infinite swept wings using a spanwise periodicity assumption (Crouch *et al.* (2018), Crouch *et al.* (2019); Paladini *et al.* (2019c); Plante *et al.* (2019b)) and fully three-dimensional analyses (Paladini (2018); He and Timme (2020b)). Stability analysis has also been applied to the NASA Common Research Model by Timme (2018, 2019, 2020). These analyses exhibit unstable modes coherent with the occurrence of buffet cells, thus emphasising the phenomenological differences between two-dimensional and three-dimensional buffet.

This paper aims at showing that the buffet cell phenomenon occurring in transonic flow has the same origin as the stall cell one occurring during stall at low speed. In particular, we will show that a similar unstable global mode is at the origin of both phenomena and highlight discrepancies between linear dynamics predictions provided by global stability analyses and saturated nonlinear dynamics given by URANS simulations. In addition, the unstable global mode corresponding to the buffet/stall cell phenomenon is followed from low speed to transonic conditions to establish a close link between these two phenomena. First, the numerical methods are presented. Then, numerical solutions for low-speed stall and tran-

sonic buffet conditions are analysed. Linear global stability analyses around steady base-flow are presented and the transition from the linear to the nonlinear dynamic is investigated. Finally, the link between the two flow regimes is discussed.

## 4.2 Physical and numerical set-up

This section first describes the physical setup studied in this paper. Then the governing equations and the numerical methods used to solve them are presented.

### 4.2.1 Configurations

In this study, infinite swept wings are considered. Fig. 4.1 shows the numerical setup. Usually, aerodynamic analyses are carried out in a referential  $(x, y, z)$  where the span of the wing is defined as the length  $L_z$  along the  $z$  direction, and the sweep angle  $\delta$  is the angle between the  $z$ -axis and the leading edge of the wing. With these definitions, the velocity in the  $z$  direction is null and the free-stream velocity is defined by its norm  $V_{\infty,3D}$  and the angle of attack  $\alpha_{3D}$  (see fig. 4.1). However, it is convenient for the present analysis to define another referential  $(x', y', z')$  with  $x'$  normal to the leading edge,  $y' = y$  and  $z'$  aligned with the leading edge. In this referential, the sweep angle becomes a sideslip angle applied to the free-stream velocity  $V_{\infty,3D}$ .

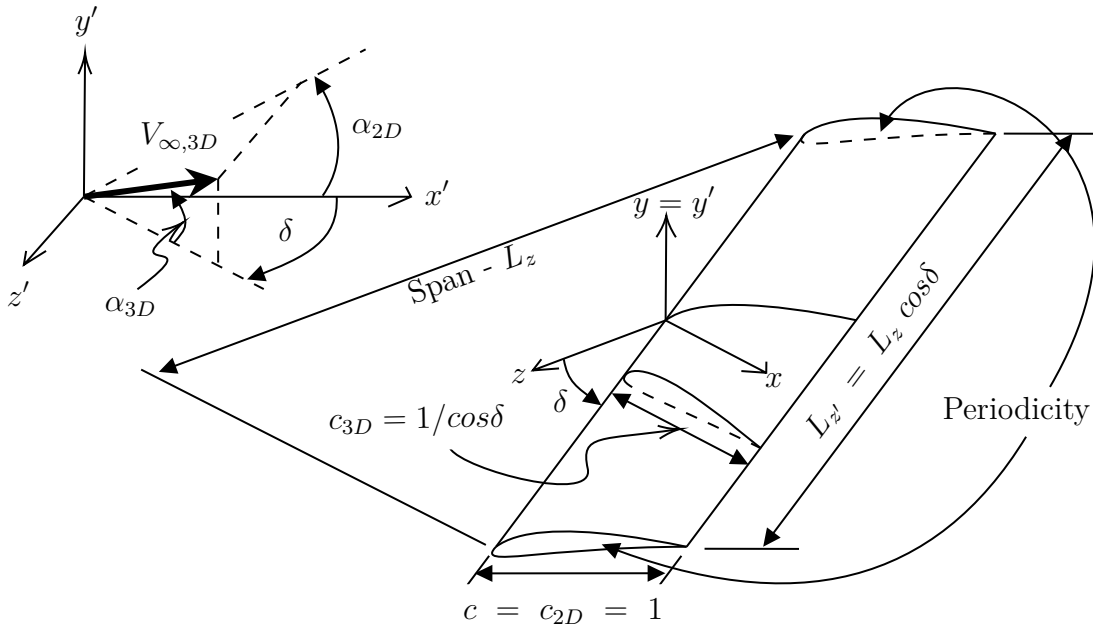


Figure 4.1 – Infinite swept wing configuration

Since the sweep angle will be changed in this article, we define the 2-D flow quantities as the conditions in the plane normal to the leading edge i.e. in the plane  $(x', y')$ . Hence we get the relations

$$M_{3D} = \frac{V_{\infty,3D}}{\sqrt{\gamma P_{\infty}/\rho_{\infty}}} = \frac{M_{2D}}{\cos(\delta)} \quad (4.1)$$

$$\alpha_{3D} = \arctan [\tan(\alpha_{2D}) \cos(\delta)] \quad (4.2)$$

$$Re_{2D} = \frac{\rho_{\infty} V_{\infty,2D} c_{2D}}{\mu_{\infty}} \quad (4.3)$$

$$Re_{3D} = \frac{\rho_{\infty} V_{\infty,3D} c_{3D}}{\mu_{\infty}} = \frac{Re_{2D}}{\cos(\delta)^2} \quad (4.4)$$

For this study, the 2-D flow conditions are kept constant when the sweep angle changes to maintain the similarity. This means that the Mach number  $M_{2D}$ , the Reynolds number  $Re_{2D}$  and the angle of attack  $\alpha_{2D}$  are kept constant. For convenience the 2-D subscripts are dropped (in the following  $M = M_{2D}$ ,  $Re = Re_{2D}$ ,  $\alpha = \alpha_{2D}$ , etc.) and the reference quantities are defined as  $V_{\infty} = V_{\infty,2D} = 1.0$ ,  $c = c_{2D} = 1.0$ . For example, the Strouhal number is defined as  $St = \frac{f c_{2D}}{V_{\infty,2D}} = f$ . This is done to help the comparison of non-dimensional quantities based on these reference quantities when the sweep angle varies. The aspect ratio  $AR$  is defined as  $AR = \frac{L_{z'}}{c_{2D}} = L_{z'}$  and it should be noted that the baseline aerofoil is always retrieved in the plane  $(x', y')$ . The  $(x', y', z')$  referential is more adapted for the present study, and therefore, it will be the only referential used throughout this paper. As such, the prime symbol is dropped for the sake of conciseness.

The present paper focuses on two regimes: the subsonic stall regime and the transonic buffet regime. The subsonic study is based on the NACA4412 aerofoil at a Reynolds number  $Re = 350\,000$  and a Mach number  $M = 0.2$  such that compressibility effects are negligible. This case is selected because it exhibits a trailing edge type of stall. The transonic case focuses on the ONERA OALT25 aerofoil at  $M = 0.7352$  and  $Re = 3 \times 10^6$ , such that the experimental 2-D results of Brion *et al.* (2017) can be used for comparison. This aerofoil was designed to promote laminarity and has been studied experimentally both with free transition and a boundary layer tripped at 7% on both sides. With the tripped boundary layer, the buffet instability is similar to that of other turbulent aerofoils. In the present study, the laminar

region is neglected and simulations are carried out in fully turbulent conditions. Hence, the experimental data with a tripped boundary layer are used to validate the numerical set up for two-dimensional buffet computations. The final part of the paper is dedicated to a third aerofoil, the NACA0012, at a Reynolds number  $Re = 1 \times 10^7$  and various Mach numbers and angles of attack. This aerofoil is used to link the results from the two previous cases, since it allows to track phenomena from the low-Mach stall regime to the transonic buffet regime. This particular test case is selected since the experiments of McDevitt and Okuno (1985) showed the transonic buffet in the high Mach range and this aerofoil is suitable to have a trailing edge type stall behaviour in the low Mach range. This makes it suitable to observe both the stall cells and the buffet cells. The aerofoils considered in this paper have a trailing edge thickness of 0.0025, 0.005 and 0.0025 chord units for the NACA4412, OALT25 and NACA0012 aerofoils respectively.

## 4.2.2 Governing equations

### Non-linear model

In this study, the Reynolds-Averaged Navier-Stokes (RANS) equations are used to model the fluid flow. The one-equation Spalart-Allmaras turbulence model with the Edwards-Chandra modification is used to close the RANS equations system. This system reads in integral form

$$\mathbf{V} \frac{\partial \mathbf{W}}{\partial t} + \mathbf{R}(\mathbf{W}) = 0 \quad (4.5)$$

where  $\mathbf{W} = [\rho, \rho u, \rho v, \rho w, \rho e, \rho \tilde{v}]^t$  is the conservative variables vector,  $\mathbf{V}$  is a diagonal matrix whose non-zero coefficients are the mesh cells volume and  $\mathbf{R}$  is the summation of the convective and viscous fluxes, and the source terms. In this article,  $z$ -invariant solutions (all the derivatives of the flow variables with respect to  $z$  are null) with  $w = 0$  will be referred to as a 2-D solution, while  $z$ -invariant solutions with  $w \neq 0$  will be referred to as 2.5-D solutions (Ghasemi *et al.* (2014); Bourgault-Côté *et al.* (2017)).

### Linear model

Steady solutions  $\mathbf{W}_0$  of equation (4.5), also known as base-flows, are computed to carry out global linear stability analyses (Sipp *et al.* (2010); Theofilis (2011); Taira *et al.* (2017)). By definition, they satisfy  $\mathbf{R}(\mathbf{W}_0) = 0$ , and under a first-order approximation, infinitesimal perturbations  $\mathbf{W}'$  about a base-flow  $\mathbf{W}_0$  are governed by the linearisation of equation (4.5),

which reads

$$\frac{\partial \mathbf{W}'}{\partial t} = \mathbf{A} \mathbf{W}' = -\mathbf{V}^{-1} \left. \frac{\partial \mathbf{R}}{\partial \mathbf{W}} \right|_{\mathbf{W}_0} \mathbf{W}' \quad (4.6)$$

where  $\left. \frac{\partial \mathbf{R}}{\partial \mathbf{W}} \right|_{\mathbf{W}_0}$  is the Jacobian of the discretised RANS equations evaluated about the base-flow, including the turbulence model. Solutions in the form of normal modes are sought.

$$\mathbf{W}' = e^{\lambda t} \hat{\mathbf{W}}, \quad (4.7)$$

such that eq. 4.6 reduces to the eigenproblem

$$\mathbf{A} \hat{\mathbf{W}} = \lambda \hat{\mathbf{W}}. \quad (4.8)$$

Thus, the stability problem consists in computing eigenpairs of the Jacobian operator. The eigenvectors  $\hat{\mathbf{W}}$  describe the spatial structure of the global modes and the eigenvalues  $\lambda = \sigma + i\omega$  describe their time behaviour ( $i = \sqrt{-1}$ ). For each mode, the real part  $\sigma$  is its growth rate and  $\omega$  is its angular frequency.

### 4.2.3 Numerical discretisation and algorithms

#### Computational grids

Three-dimensional grids are obtained from the extrusion of baseline 2-D grids. Structured grids with an O-type topology are used. Table 4.1 reports the number of points on the aerofoil surface ( $n_i$ ), in the direction normal to the aerofoil surface ( $n_j$ ), on the pressures side ( $n_{p.s.}$ ), on the suction side ( $n_{s.s.}$ ), on the trailing edge ( $n_{t.e.}$ ), the wall spacing ( $\Delta y_w$ ), the distance from the aerofoil surface to the farfield boundary condition ( $\Delta y_{f.f.}$ ) and the spacing across the shockwave ( $\Delta x_{s.f.}$ ).

#### Solution of the non-linear model

In this paper, the ONERA-Airbus-Safran elsA (Cambier *et al.* (2013)) software is used to solve the (U)RANS equations. For this study, a cell-centred structured finite volume

Table 4.1 – Characteristics of the grids.

Aerofoil	$n_i$	$n_j$	$n_{p.s.}$	$n_{s.s.}$	$n_{t.e.}$	$\Delta y_w$	$\Delta y_{f.f.}$	$\Delta x_{s.f.}$
NACA4412	512	128	143	353	16	$5 \times 10^{-5}$	100	N/A
OALT25	512	128	133	355	24	$8 \times 10^{-6}$	100	0.004
NACA0012	512	128	170	318	24	$2 \times 10^{-6}$	100	0.004

method is used. A second order cell-centred scheme with scalar numerical dissipation is used for the discretisation of the convective fluxes. Convergence towards steady-state solutions is accelerated using local time steps and geometrical multigrid with a LU-SSOR pseudo-time integration scheme. In some case, Selective Frequency Damping (SFD) (Åkervik *et al.* (2006); Jordi *et al.* (2014, 2015); Richez *et al.* (2016)) or a Newton solver (Busquet *et al.* (2017), Wales *et al.* (2012)) is used to force the convergence to a steady state. Time-accurate solutions are obtained by using a second order dual time stepping approach.

### Solution of the linear model

This study involves three-dimensional geometries for which  $\mathbf{A}$  has a high dimension and a large bandwidth. Therefore, solving the eigenproblem is often too costly. But in our cases, the base-flows are always homogeneous in the spanwise direction, such that the method proposed by Schmid *et al.* (2017) and used by Paladini *et al.* (2019c) and Plante *et al.* (2019b) for  $n$ -periodic arrays of fluid systems may be used to significantly reduce the cost of the eigenvalues computation. This method exploits the block-circulant structure of matrix  $\mathbf{A}$ , which takes the form

$$\mathbf{A} = \begin{bmatrix} \mathbf{A}_0 & \mathbf{A}_1 & \mathbf{A}_2 & \dots & \mathbf{A}_{n-1} \\ \mathbf{A}_{n-1} & \mathbf{A}_0 & \mathbf{A}_1 & \dots & \mathbf{A}_{n-2} \\ \mathbf{A}_{n-2} & \mathbf{A}_{n-1} & \mathbf{A}_0 & \dots & \mathbf{A}_{n-3} \\ \vdots & \vdots & \vdots & \ddots & \vdots \\ \mathbf{A}_1 & \mathbf{A}_2 & \mathbf{A}_3 & \dots & \mathbf{A}_0 \end{bmatrix} \quad (4.9)$$

when the degrees of freedom are properly indexed. As shown by Schmid *et al.* (2017),  $\mathbf{A}$  can be transformed into a block diagonal matrix

$$\hat{\mathbf{A}} = \begin{bmatrix} \hat{\mathbf{A}}_0 & 0 & \dots & 0 \\ 0 & \hat{\mathbf{A}}_1 & \ddots & \vdots \\ \vdots & \ddots & \ddots & 0 \\ 0 & \dots & 0 & \hat{\mathbf{A}}_{n-1} \end{bmatrix} \quad (4.10)$$

with

$$\hat{\mathbf{A}}_j = \sum_{k=0}^{n-1} \rho_j^k \mathbf{A}_k \quad (4.11)$$

and

$$\rho_j = e^{ij\frac{2\pi}{n}} \quad (4.12)$$

Eigenvalues of  $\hat{\mathbf{A}}$  are also eigenvalues of  $\mathbf{A}$  and each block matrix  $\hat{\mathbf{A}}_j$  can be treated separately, resulting in  $n$  separated eigenproblems of the size of a two-dimensional problem

$$\hat{\mathbf{A}}_j \mathbf{v}_j = \lambda_j \mathbf{v}_j. \quad (4.13)$$

The eigenvectors of  $\mathbf{A}$  are then retrieved as

$$\hat{\mathbf{W}} = [\mathbf{v}_j, \rho_j \mathbf{v}_j, \rho_j^2 \mathbf{v}_j, \dots, \rho_j^{n-1} \mathbf{v}_j]^t \quad (4.14)$$

This method implies to solve the eigenproblem for all the  $\hat{\mathbf{A}}_j$  matrices to get the stability result for all the  $n$  possible wavenumbers. However, the only difference between each  $\hat{\mathbf{A}}_j$  matrix is the coefficients  $\rho_j$  such that changing the value of  $j$  or  $n$  has the effect of changing the wavenumber. Hence, solving for the matrix  $\hat{\mathbf{A}}_2$  is equivalent to solving  $\hat{\mathbf{A}}_1$  with  $n$  divided by two. Therefore, in this study, the problem is only solved for the matrix  $\hat{\mathbf{A}}_1$  with various values of  $n$ . This allows to get the results over a continuous range of wavenumbers.

This analysis yields results similar to the biGlobal stability analysis carried out by Crouch *et al.* (2019) and He *et al.* (2017). However, this approach presents several advantages. In particular, it does not require tedious mathematical developments to include the periodicity assumption in the Jacobian matrix. This makes this approach suitable for the use of a black box CFD solver, in this case elsA.

The linear operator  $\mathbf{A}$  is obtained with the fully discrete approach proposed by Mettot *et al.* (2014). This Jacobian is extracted with a second-order finite difference scheme as

$$\mathbf{A} \mathbf{u} \approx \frac{1}{2\epsilon} (\mathbf{R}(\mathbf{W}_0 + \epsilon \mathbf{u}) - \mathbf{R}(\mathbf{W}_0 - \epsilon \mathbf{u})) \quad (4.15)$$

where  $\epsilon$  is a small parameter and  $\mathbf{u}$  are vectors chosen to efficiently compute every non-zero coefficient of the Jacobian matrix (see Beneddine (2017) for details). For the second-order finite volume scheme used in this study, the numerical stencils have a width of five grid cells. Hence,  $\mathbf{A}_3 = \mathbf{A}_4 = \dots = \mathbf{A}_{n-3} = 0$ , and all the non-zero block matrices  $\mathbf{A}_j$  (eq. 4.9) can be retrieved from a three-dimensional grid with only five grid cells in the spanwise direction (see Paladini *et al.* (2019c); Plante *et al.* (2019b)). Hence, the base-flows are computed as two-dimensional solutions and the grid is extruded to get the three-dimensional mesh for the extraction of the 3-D Jacobian  $\mathbf{A}$ . The spanwise spacing  $\Delta z$  must be imposed. Refinement study of this parameter will be presented, but no extra computational cost is associated with change in  $\Delta z$ , which can therefore be chosen arbitrarily small. This Jacobian matrix is then

reduced as  $\hat{\mathbf{A}}_1$  by assuming a given wavenumber in eq. (4.11). The eigenproblems are then solved with the Arnoldi iteration method (Sorensen, 1992) coupled with a shift-and-invert strategy (Christodoulou and Scriven, 1988) to extract inner eigenvalues.

### 4.3 Unsteady Reynolds-Averaged simulations

This section presents the results of URANS simulations for the low-speed and transonic cases. These simulations are carried out to observe stall and buffet cells as well as the superposition between the 2-D transonic buffet mode and the buffet cells.

#### 4.3.1 Subsonic stall

In this section the 2-D and 3-D simulations of the NACA4412 aerofoil at a Reynolds number of 350 000 are compared. Then the simulations of swept wings are presented.

##### Unswep $\delta = 0^\circ$ case

Let us first focus on the flow over an unswep wing in the post-stall regime. Fig. 4.2 shows the lift polar in the unswep case ( $\delta = 0^\circ$ ) for two kinds of simulations: two-dimensional solutions and three-dimensional ones with an aspect ratio  $AR = 6$  and 113 spanwise grid points. The maximum lift coefficient of 1.57 is obtained for an angle of attack around  $\alpha = 14^\circ$  in both cases. For angles of attack higher than  $16^\circ$  the flow solver failed to converge. This is caused by the occurrence of an instability linked to a vortex shedding. This is further discussed in section 4.4.1. In order to obtain steady-state two-dimensional solutions in this regime, the SFD method presented by Richez *et al.* (2016) and the Newton algorithm have been used. The SFD is used with a local time-stepping algorithm and the cut-off frequency and damping coefficient were based on a parametric study to obtain solutions converged within machine accuracy. A value of the filter width  $\Delta = 1/74$  and the proportional controller coefficient  $\chi = 50$  allowed the solution to converge and the CFL is set to 50 to compute the local timestep in the LU-SSOR implicit scheme. To ensure consistency, it has been checked that both methods provide the same solution for several cases. Successive solutions are obtained by initialising each computation from the previous angle of attack. The lower branch of the lift polar is obtained by increasing the angle of attack up to values for which a converged solution could no longer be obtained. Then, by decreasing the angle of attack starting from these unconverged flow solution, the solution method is able to converge on the lower branch of the lift curve. Every solution has been converged within machine accuracy. Two distinct solutions are found for some angles of attack. Such hysteresis phenomena of



the discretised RANS equations were obtained by Wales *et al.* (2012) and Busquet *et al.* (2017) for the NACA0012 and the OA209 aerofoils, respectively. Grid convergence has been ensured by carrying out a two-dimensional simulation at an angle of attack of  $15^\circ$  with a grid refined by a factor 2 in both directions (1024 by 256 grid cells), resulting in non-significant differences in the pressure distribution.

For angles of attack over  $14^\circ$  the three-dimensional lift coefficient is lower than the two-dimensional one. These solutions are obtained using a global time step and the SFD technique. The lower lift coefficient is associated with the presence of stall cells, as seen in fig. 4.3 for an angle of attack of  $15^\circ$ . Four steady stall cells are observed and the skin friction lines exhibit the "owl-face" shape reported in the literature. The left part of this figure shows the result with a spanwise mesh refinement of a factor 2. No significant change in the result is noticeable, ensuring the grid convergence of the results. In this simulation, the wavenumber of the stall cell is 4.2. However, the periodic boundary conditions constrain the possible wavenumbers since the number of cells must be an integer. Hence, the only possible wavenumbers that may appear in the simulation are necessarily multiples of  $\beta_0 = 2\pi/6$ . There might therefore exist a discrepancy with respect to a truly infinite configuration, with  $AR = \infty$ . A more accurate estimation of the most amplified wavenumber may be obtained by considering a larger aspect ratio. For this reason, a simulation with  $AR = 12$  has also been run and 8 stall cells were obtained. Therefore, the most amplified wavenumber is narrowed down to a value between  $14\pi/12 \approx 3.7$  and  $18\pi/12 \approx 4.7$ . This range will be compared to the result of linear stability analyses in section 4.4.1.

Since the 2-D solutions are particular cases where every derivative in the spanwise direction are null, they are also solutions of the three-dimensional discretised RANS equations. Hence these results demonstrate the existence of multiple solutions, the two-dimensional and the three-dimensional ones, for a given flow conditions. Such results are in agreement with those from Kamenetskiy *et al.* (2014).

### Swept cases $\delta > 0^\circ$ , $\alpha = 15^\circ$

A fixed value  $\alpha = 15^\circ$  is now considered and a sweep angle is added. In these conditions, the flow is unsteady and time-accurate simulations with a non-dimensional time step of 0.008 are carried out. Fig. 4.4 shows the instantaneous pressure coefficient and the skin friction lines over wings swept at  $10^\circ$ ,  $20^\circ$  and  $30^\circ$ . Four stall cells are observed and the wavenumber is the same as for the unswept wing ( $\beta = 4.2$ ). The topology of the stall cells also changes with

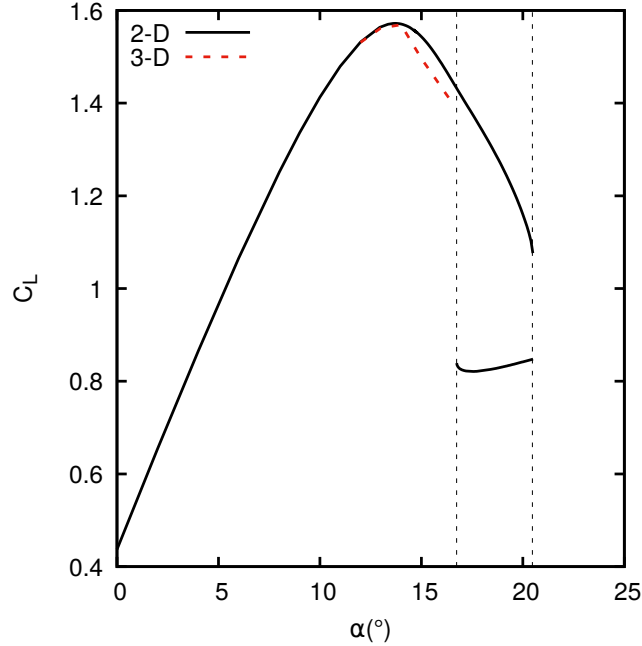


Figure 4.2 – Lift curve for the 2-D and 3-D steady solutions (NACA4412,  $Re = 350\,000$ ,  $M = 0.2$ ,  $\delta = 0^\circ$ ).

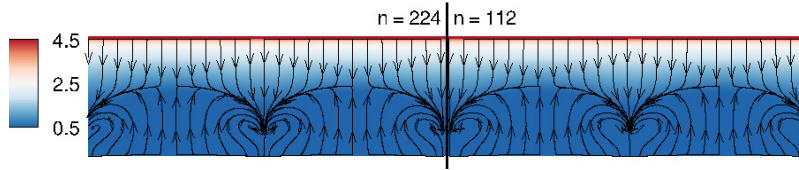


Figure 4.3 – Surface pressure coefficient and skin friction lines of 3-D steady solution with 224 (left) and 112 (right) spanwise grid cells (NACA4412,  $M = 0.2$ ,  $Re = 350\,000$ ,  $\alpha = 15^\circ$ ,  $\delta = 0^\circ$ ,  $L_z = 6$ ).

the sweep angle, and the skin friction lines are now aligned in the cross-flow direction. This is associated with a spanwise convection of the stall cells. This induces a frequency proportional to the wavelength of the cells and their convection speed ( $St = v_c/\lambda_z$ ). Table 4.2 summarises all the wavelength and convection speed obtained for sweep angles of  $0^\circ$ ,  $10^\circ$ ,  $20^\circ$  and  $30^\circ$ . Fig. 4.5 shows the definition of these quantities. For the simulations at a constant aspect ratio, the wavenumber is always 4.2. These results suggest that the sweep angle has no effect on the wavelength of the stall cells. However, as mentioned previously, this result is constrained by the wing aspect ratio. Finally, the convection speed observed in the URANS results is proportional to the sweep angle, as shown in fig. 4.11. These phenomena are also analysed using stability analyses in section 4.4.1.

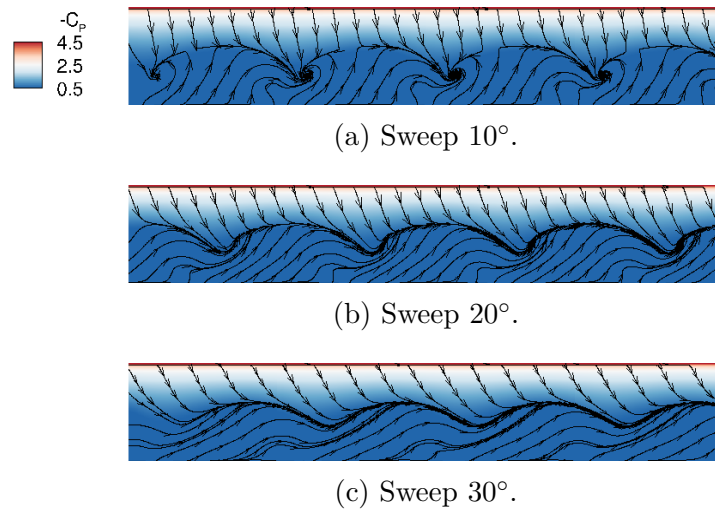


Figure 4.4 – Instantaneous surface pressure coefficient and skin friction lines over a swept wing (NACA4412,  $M = 0.2$ ,  $Re = 350\,000$ ,  $\alpha = 15^\circ$ ,  $L_z = 6$ ).

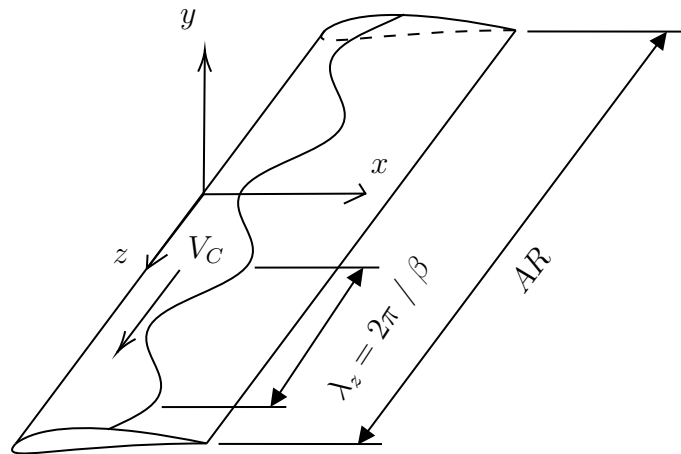


Figure 4.5 – Stall and buffet cells convection model.

### 4.3.2 Transonic buffet

This section analyses the transonic buffet on wings based on the OALT25 aerofoil at a Reynolds number  $Re = 3 \times 10^6$ , a Mach number of 0.7352 and an angle of attack of  $4^\circ$ . The non-dimensional time step is set to 0.0105. Simulations with the 2.5-D assumptions are first analysed. Then URANS results for 3-D infinite swept wings are presented.

Table 4.2 – Stall cells convection frequency for several wing spans and sweep angles (NACA4412,  $M = 0.2$ ,  $Re = 350\,000$ ,  $\alpha = 15^\circ$ ).

$\delta$ ( $^\circ$ )	$AR$	$N_{cells}$	$\lambda_z$	$\beta$	$V_C$	$St$
0	6.00	4	1.50	4.20	0.00	0.000
0	12.00	8	1.50	4.20	0.00	0.000
10	6.00	4	1.50	4.20	0.14	0.093
20	6.00	4	1.50	4.20	0.29	0.193
30	6.00	4	1.50	4.2	0.46	0.307

### Spanwise invariant solutions (2.5-D)

Fig. 4.6 shows the time-averaged wall pressure coefficient of 2-D and 2.5-D simulations. The pressure coefficient on the pressure side and the trailing edge agree with the experiments of Brion *et al.* (2017) and the pressure of the supersonic plateau is also the same. This indicates that the Mach number and angle of attack are the same between the experiments and the simulations. However, the shock wave of the simulations is located further downstream compared to the experimental field. It is seen that the pressure distribution is the same for every sweep angle, except in the shock wave region. This shows that the flowfields in the  $(x, y)$  plane remain close due to the fact that the upstream normal inflow conditions are kept constant when changing the sweep angle. The time evolution of the lift coefficient yields a Strouhal number of 0.075. The shock wave motion amplitude can be evaluated from the slope of the time-averaged pressure coefficient in the vicinity of the shock wave position. The largest buffet amplitude is observed for the unswept case and the buffet amplitude decreases as the sweep angle is increased. This relation between the sweep angle and the buffet amplitude is investigated with global stability analyses in section 4.4.2.

### Superposition between 2-D buffet mode and 3-D buffet cells

Fig. 4.7 shows the instantaneous pressure coefficient and skin friction lines on swept wings of aspect ratio  $AR = 6$  meshed with 168 spanwise grid cells. For the unswept wing and the wing swept at  $30^\circ$ , a variation of the shock wave position is observed, forming the so-called buffet cells. For the unswept wing ( $\delta = 0^\circ$ ), spanwise structures are observed. However, the amplitude of the buffet cells is irregular and the number of buffet cells varies in time. As such, the wavenumber varies in time and the buffet cells appear and disappear at random spanwise location since there is no convection. This results in a flow that can seem chaotic but a dominant Strouhal number of 0.06 is observed. This is related to the frequency of a chordwise variation of the shock wave position and a variation of the buffet cells amplitude.

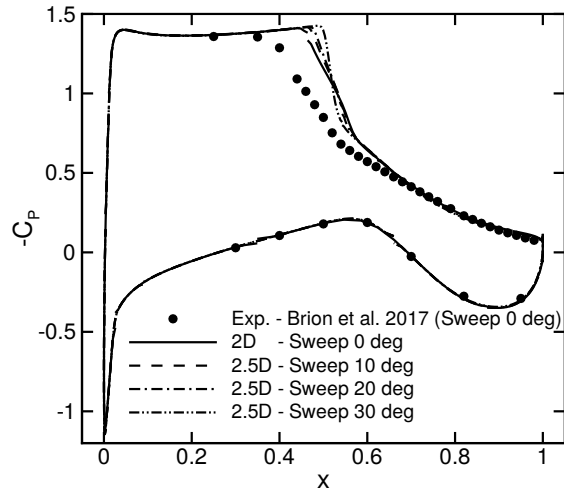
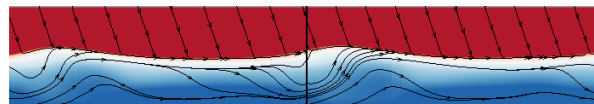


Figure 4.6 – Time-averaged wall pressure coefficient for spanwise invariant solution with several sweep angle (OALT25,  $M = 0.7352$ ,  $Re = 3 \times 10^6$ ,  $\alpha = 4^\circ$ ).

The same frequency is observed for swept wings ( $\delta > 0^\circ$ ). However, in these cases the number of buffet cells is constant and they are convected in the spanwise direction. Two cells are observed for a sweep angle of  $\delta = 30^\circ$ . This result is compared to the stability analysis results in section 4.4.2. Fig. 4.7 also shows the instantaneous solution with 112 and 168 spanwise grid cells. The comparison of the two fields shows that the grid spacing is sufficient for this case since no significant differences are noticeable in the skin friction lines and the pressure coefficient.



(a)  $\delta = 0^\circ$ .



(b)  $\delta = 30^\circ$  (right 112 spanwise grid cells, left 168 spanwise grid cells).

Figure 4.7 – Instantaneous surface pressure coefficient and skin friction lines for URANS simulations of infinite swept wings with two sweep angles (OALT25,  $M = 0.7352$ ,  $Re = 3 \times 10^6$ ,  $\alpha = 4^\circ$ ,  $L_z = 6$ ).

Fig. 4.8 shows the power spectral density of the sectional lift coefficient with 112, 168 and 224 spanwise grid cells. The sectional lift coefficient is extracted on a given chordwise wing section, the choice of this section has no effect since the buffet cells are convected in the spanwise direction. The sectional lift coefficient is sampled at every time-step (0.0105 nondimensional time-unit) over a time frame of 630 nondimensional time-units. A periodogram with boxcar window and a single block is used to estimate the power spectral density, which yields a Strouhal number resolution of 0.00158. This method is used since the signals for the grid refinement study are too short to use a sufficient number of averaging blocks. This yields noisier spectra and estimation errors on the amplitude. Nevertheless, one can observe that the peak frequencies are the same. A dashed line is added to indicate the Strouhal number around 0.06 (the frequency observed for every sweep angle) and a dashed-dotted line indicates the Strouhal number of 0.135. The latter is associated with the convection of buffet cells, as it will be shown in this section. Another peak at a frequency of 0.135 could correspond to the nonlinear interaction between the two dominant modes ( $St = 0.135 + 0.055 = 0.19$ ).

Fig. 4.9 shows the power spectral density of the sectional and global lift coefficient with sweep angles of  $10^\circ$ ,  $20^\circ$  and  $30^\circ$ . These spectra are evaluated using the Welch method with a Hann window and a 50% overlap between the blocks. The signal length is of 1260 non-dimensional time-units and nine blocks are used. The Welch method is used since the time series is longer than in the mesh refinement study. The sampling is done at every time step (0.0105 nondimensional time-units) for the sectional lift and every ten time step for the global lift. This yields a Strouhal number resolution of 0.0039. One can notice the frequency between  $St = 0.055$  and 0.06 indicated by a dashed line for every sweep angle in the global and sectional lift signals. Some harmonics of this frequency are also observed. This frequency is associated with a chordwise oscillation of the shock wave position which modulates the buffet cells amplitude (2-D oscillation). However, a second dominant frequency is observed in the sectional lift coefficient. The latter increases with the sweep angle and is due to the buffet cells convection in the spanwise direction. This second frequency is not observed in the spectrum of the global lift coefficient since the number of buffet cells is constant. For this reason, the variations of the lift coefficient associated with the convection are cancelled out when the lift coefficient is averaged along the span. Like in fig. 4.8, the dashed line indicates the 2D shock oscillation phenomenon while the dashed-dot lines indicates the buffet cells convection phenomenon. These two frequencies are further discussed in the next paragraph. Some harmonics of the buffet cells convection frequency are also observed. For instance the convection Strouhal number of 0.045 for a sweep angle of  $10^\circ$  has a harmonic at 0.09, which is also the convection frequency for a sweep angle of  $20^\circ$ .

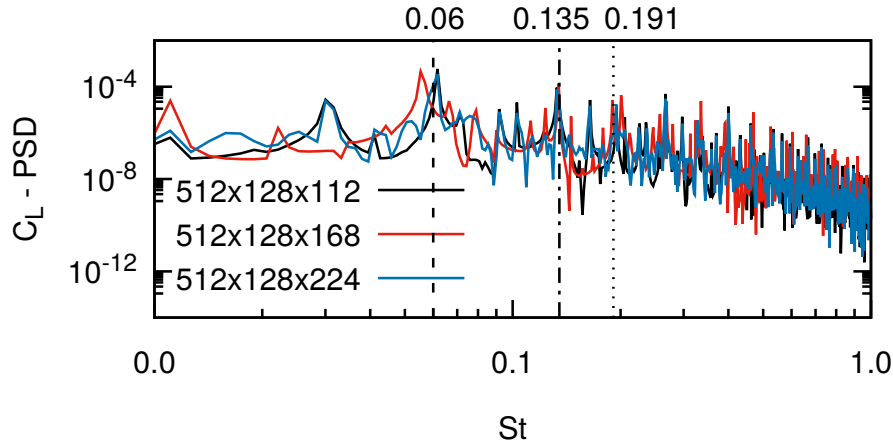


Figure 4.8 – Sectional lift coefficient power spectral density (OALT25,  $M = 0.7352$ ,  $Re = 3 \times 10^6$ ,  $\alpha = 4^\circ$ ,  $\delta = 30^\circ$ ).

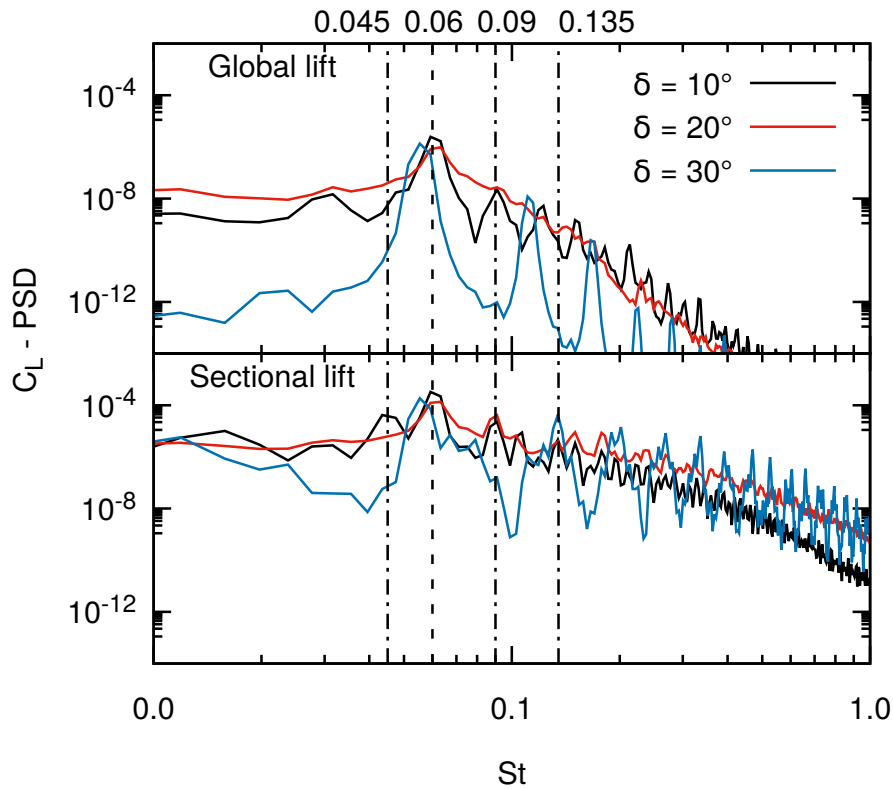


Figure 4.9 – Effect of the sweep angle on the global and sectional lift coefficient power spectral density (OALT25,  $M = 0.7352$ ,  $Re = 3 \times 10^6$ ,  $\alpha = 4^\circ$ ).

To visualize the unsteady behaviour of the flow, the pressure has been extracted along a line parallel to the leading edge. Fig. 4.10 is a  $(z, t)$  diagram showing this extraction of the pressure coefficient near  $x'/c = 0.43$  for the sweep angle of  $30^\circ$ . Most of the time, the pressure is equal to the one on the supersonic plateau. However two buffet cells periodically

cross the extraction line because the amplitude of the cells changes in time. This occurs with a period  $T = 18.0$ . This results in a Strouhal number equal to 0.055 (around the Strouhal number of 0.06 shown in fig. 4.9). A Strouhal number of this order is observed for every sweep angle, as previously shown, thus suggesting that the variation of the buffet cells amplitude relates to a two-dimensional buffet mode. In addition, this figure allows to follow the spanwise location of the buffet cells in time. Hence, the convection speed of the buffet cells can be extracted as the slope of an iso-contour of pressure on this pressure map (here  $V_C = 0.4$ ) and the associated frequency can be computed with the wavelength of the buffet cells ( $St = V_C/\lambda_z$ ). These quantities are schematised in fig. 4.5 and reported for multiple sweep angles in Table 4.3. Fig. 4.11 shows the relation between the sweep angle and the convection speed. The cross-flow velocity varies in  $\tan \delta$ , meaning that the convection speed is proportional to the far field velocity projected along the leading edge. This proportionality is true for low-speed flow conditions as well. A fit coefficient of 0.7 is found for the buffet cells and 0.8 for the stall cells. More details are provided in Plante *et al.* (2019a). This relation between the sweep angle and the convection speed of the buffet cells is further analysed using stability analyses in section 4.4 for the stall and buffet conditions.

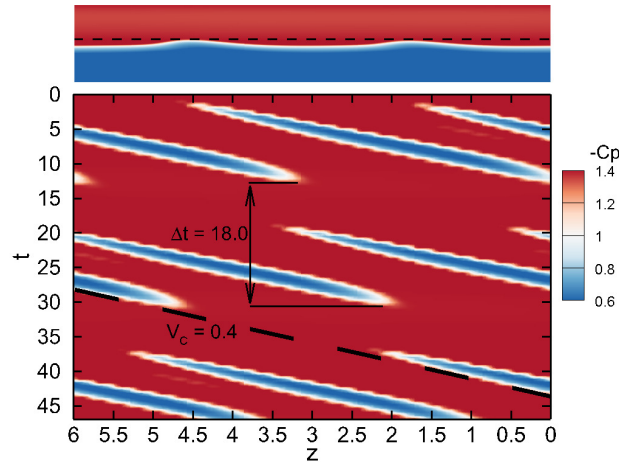


Figure 4.10 – Extraction of the pressure on a line parallel to the leading edge near  $x'/c = 0.43$  (OALT25,  $M = 0.7352$ ,  $Re = 3 \times 10^6$ ,  $\alpha = 4^\circ$ ,  $\delta = 30^\circ$ ).

### 4.3.3 Partial conclusion

Three-dimensional flow features in the form of stall cells and buffet cells are observed with URANS modelling, in the low-speed stall regime and in the high-speed buffet regime respectively. These phenomena can be obtained with a numerical setup in which no disturbances are imposed by the initial conditions and the boundary conditions. This suggests that there



Table 4.3 – Buffet cells convection frequency for several sweep angles (OALT25,  $M = 0.7352$ ,  $Re = 3 \times 10^6$ ,  $\alpha = 4^\circ$ ).

$\delta$ ( $^\circ$ )	$AR$	$N_{cells}$	$\lambda_z$	$\beta$	$V_C$	$St$
10	6.00	2	3.00	2.09	0.13	0.043
20	6.00	2	3.00	2.09	0.26	0.086
30	6.00	2	3.00	2.09	0.40	0.133

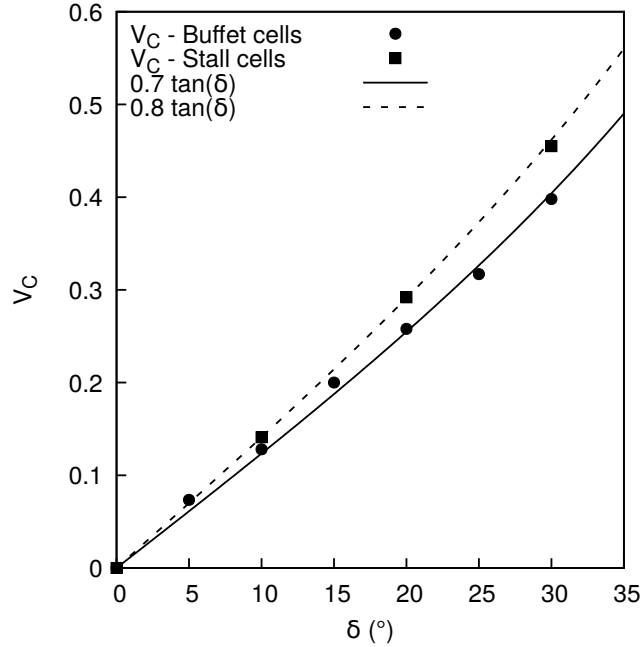


Figure 4.11 – Convection speed of stall (NACA4412,  $M = 0.2$ ,  $Re = 350\,000$ ,  $\alpha = 15^\circ$ ) and buffet (OALT25,  $M = 0.7352$ ,  $Re = 3 \times 10^6$ ,  $\alpha = 4^\circ$ ) cells.

is an instability inherent to these flow conditions. Moreover, the spanwise length of the cells remains approximately unchanged when the aspect ratio is increased. This suggests that there is a preferential wavenumber for these flow structures. However, finding a very accurate estimation of this wavenumber with URANS simulations would be computationally expensive since the aspect ratio constrains the number of cells which can be represented, and  $AR$  needs to be increased to reduce the uncertainty with respect to the most amplified wavelength. As it will be shown in the next section, stability analyses are a more appropriate tool to address this point. Finally, both types of cells are convected with a velocity proportional to the free stream cross-flow velocity. This causes an unsteady behaviour which is superimposed to a two-dimensional unsteadiness in the case of the transonic buffet simulations. These flow behaviours are analysed with global linear stability analyses in the next section.

## 4.4 Global stability analyses

The second part of this study uses global stability analyses to identify linearly unstable modes which could explain the stall cells and buffet cells observed in section 4.3. Results for the low-speed and transonic flow conditions are presented and discussed. Parameters characterising the size and intensity of the recirculation zones in the base-flows are provided as supplementary material to this article.

### 4.4.1 Subsonic stall

Steady 2.5-D and 2-D solutions of the NACA4412 aerofoil at a Reynolds number of 350 000, a Mach number of 0.2, and multiple angles of attack and sweep angles are converged within machine accuracy. These solutions are used as base-flows for the stability analyses. For consistency with the previous section, most of the analyses are carried out for an angle of attack of  $15^\circ$ .

#### Case $\delta = 0^\circ$ and $\alpha = 15^\circ$

The following focuses on the case  $\delta = 0^\circ$  and  $\alpha = 15^\circ$ . Fig. 4.12 presents the eigenvalues spectra obtained for two values of  $\beta$ . For both values, there is an unstable eigenvalue (positive real part) located along the real axis. This is a non-oscillatory unstable mode. A mode similar to this one has been observed by Zhang and Samtaney (2016) for low-Reynolds laminar flow. But in the present case this mode is observed at an intermediate Reynolds number with the use of a steady RANS base-flow. This figure also shows the radius covered by the shift-invert Arnoldi strategy. Different shifts with various imaginary parts are used in the shift-and-invert strategy to ensure that modes with non-zero imaginary part are not missed. Fig. 4.13 shows the growth rate of the steady unstable mode for a range of wavenumbers  $\beta$ . Multiple values of  $\Delta_z$  used in the extrusion of the grid are plotted to ensure that the grid is sufficiently refined. These results can be considered converged for every  $\beta$  with  $\Delta_z = 0.002$ . One can observe that the grid convergence is poorer in the high  $\beta$  range associated with small structures. This indicates that a finer grid is required to compute small flow structures, as expected. The grid spacing used in the URANS simulations ( $\Delta_z = 0.054$ ) is well converged up to  $\beta = 6$ , covering the case with the maximum growth rate and the wavenumbers obtained in the URANS simulations. This is consistent with the grid convergence shown in fig. 4.3.

The maximum growth rate is obtained for a spanwise structure with  $\beta \approx 4.4$ . This corresponds to a wavelength  $\lambda_z \approx 1.43$ , which is consistent with the value observed in the URANS

simulations ( $\beta = 4.2$ ). Indeed, in the simulations, the periodic boundary conditions constrained the possible wavenumbers to multiples of  $\beta_0 = 2\pi/AR$ . Therefore, the wavelength of the URANS simulation is as close as possible to that predicted by the stability analysis, showing that this unstable mode is responsible for the formation of stall cells. Fig. 4.14 shows the base-flow and the real part of the eigenvector  $\hat{\rho}e$  reconstructed in three dimensions with eq. 4.14, and extracted on the aerofoil surface and the plane  $z = 0$ . The instability is located in the shear layer and upstream of the separation line. The shape of this mode is consistent with the structure of the stall cells.

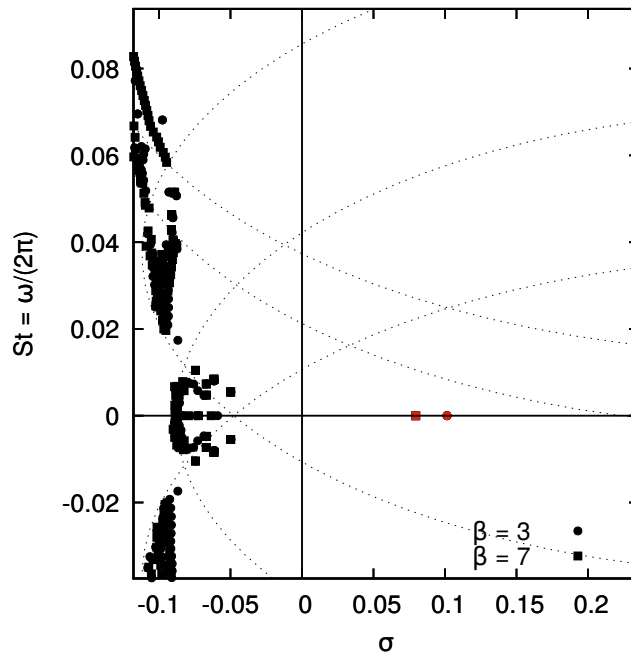


Figure 4.12 – Eigenspectrum (NACA4412,  $M = 0.2$ ,  $Re = 350\,000$ ,  $\alpha = 15.0^\circ$ ,  $\delta = 0.0^\circ$ ).

#### Case $\delta = 0^\circ$ and varying $\alpha$ .

These stability analyses are carried out for several angles of attack for which a solution converged to machine accuracy can be obtained (fig. 4.2). The three-dimensional unstable mode can be identified on the upper and lower branch of the lift polar hysteresis. Fig. 4.15 shows the growth rate of this mode for the most amplified wavenumber of the two branches. The mode is unstable from an angle of attack of  $14.15^\circ$  (the maximum lift) up to  $20.5^\circ$  (the last converged base-flow). On the lower branch, the growth rates are higher than for the upper one, but the mode is only unstable for angles of attack lower than  $16.9^\circ$ . Above this angle, the mode becomes stable again, even though the flow is massively separated. Fig. 4.16 shows the shape of the modes on the upper and lower branches. One can observe that the

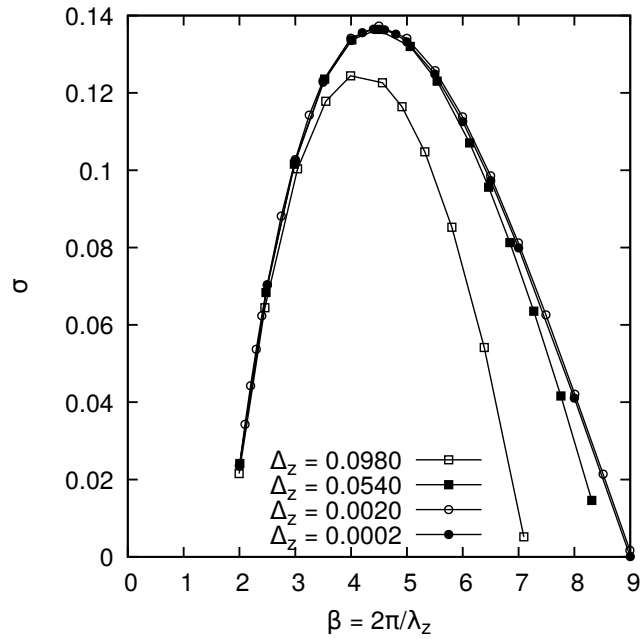
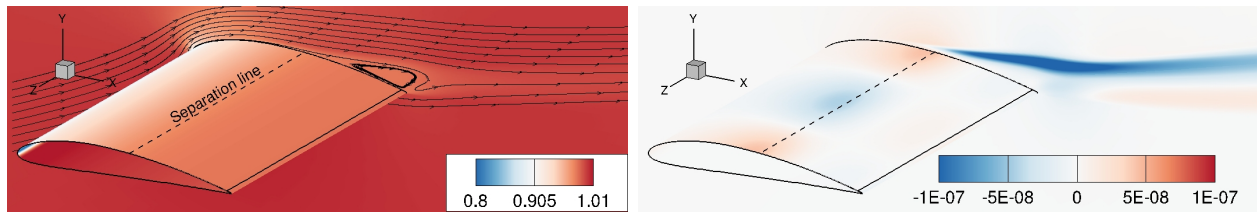


Figure 4.13 – Effect of spanwise grid density and the wavenumber on the growth rate of the unstable mode (NACA4412,  $M = 0.2$ ,  $Re = 350\,000$ ,  $\alpha = 15.0^\circ$ ,  $\delta = 0.0^\circ$ ).



(a)  $\rho^e/\rho_{e\infty}$  base-flow.

(b) Real part of the  $\hat{\rho}^e/\rho_{e\infty}$  eigenmode ( $\beta = 4.4$ ) -  $St = 0.0$ .

Figure 4.14 – Flow visualisation of the (a): base-flow and (b): 3-D unstable mode (NACA4412,  $M = 0.2$ ,  $Re = 350\,000$ ,  $\alpha = 15.0^\circ$ ,  $\delta = 0.0^\circ$ ).

unstable mode is located around the region where the flow separates. For  $\alpha = 18^\circ$  the flow separates far from the leading edge. However, for the other angles of attack the separation is close to the leading edge. Hence, it is possible that the mode is no longer unstable past  $\alpha = 16.9^\circ$  on the lower branch because the flow separation becomes fixed on the leading edge. This tends to validate the idea that stall cells are only observed with a trailing edge type of stall.

Works based on the lifting line theory by Spalart (2014) and Gross *et al.* (2015) suggested that a negative slope of the  $C_L - \alpha$  curve is a necessary condition for the occurrence of

stall cells. Fig. 4.15 shows the growth rate obtained in these flow conditions for different values of  $\alpha$ , and for the upper branch of the lift hysteresis, the most unstable eigenvalue crosses the imaginary axis at an angle of attack slightly below  $14.15^\circ$ . This coincides with the maximum lift angle of attack in fig. 4.2, which is therefore consistent with the negative  $C_L - \alpha$  slope criterion. However, the stability analysis of the lower branch of the lift hysteresis shows that the stall cell modes are stable for  $\alpha > 16.9^\circ$ , while the slope of the  $C_L - \alpha$  curve is negative between  $17.0$  and  $17.4^\circ$  (see fig. 4.2), which contradicts this criterion. Another conclusion of the analysis of Gross *et al.* (2015) is that the wavelength of the cells should be  $\lambda_z = -0.5 \partial C_L / \partial \alpha$  with a discrete model or  $\lambda_z = -\pi/4 \partial C_L / \partial \alpha$  with a continuous model. Since the linear instability occurs around the two-dimensional solution,  $\partial C_L / \partial \alpha$  is taken as the slope of the two-dimensional lift polar around an angle of attack of  $15.0^\circ$  ( $-2.52 \text{rad}^{-1}$ ). With this slope, the wavelength should be 1.26 or 1.98 ( $\beta = 3.2$  and  $5.0$  respectively). The values computed with the URANS ( $\beta = 4.2$ ) simulations and the stability ( $\beta = 4.4$ ) analyses fall between the values predicted with this model. However, the  $C_L - \alpha$  slope varies in the range of angles of attack studied with the global stability analysis and the values of  $\beta$  for which the flow is the most unstable does not vary significantly. This is in contradiction with the model proposed by Gross *et al.* (2015).

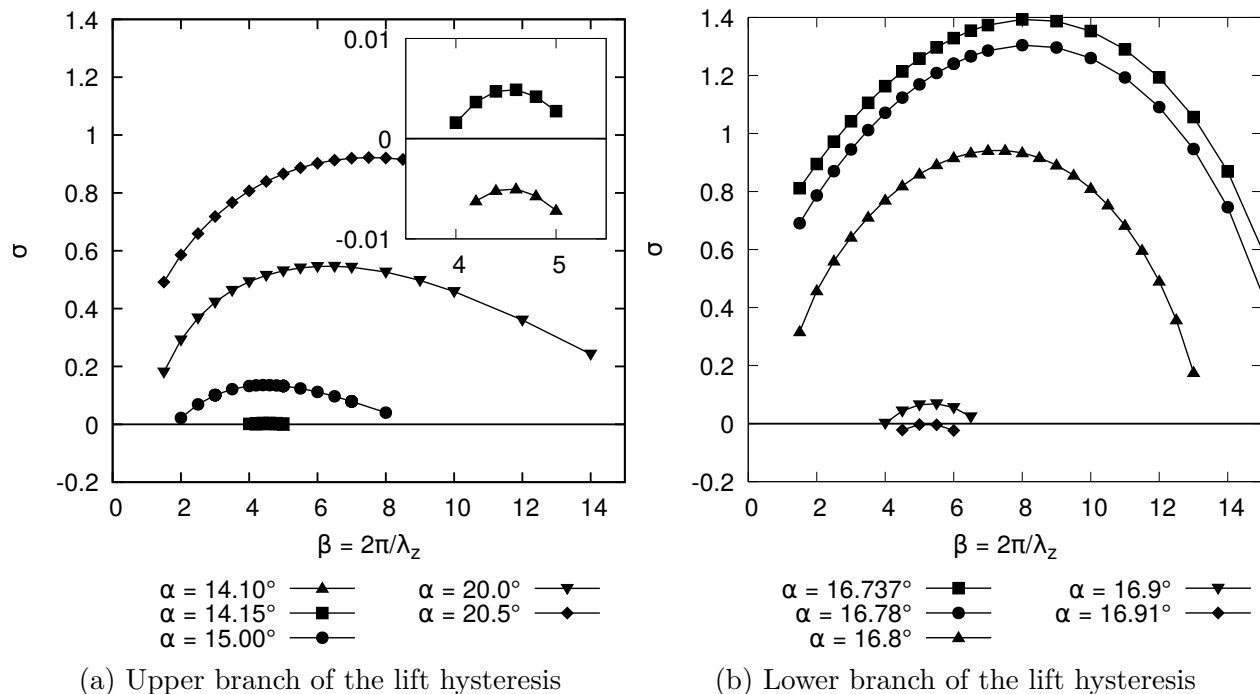


Figure 4.15 – Effect of the angle of attack on the growth rate of the unstable mode (NACA4412,  $M = 0.2$ ,  $Re = 350\,000$ ,  $\delta = 0.0^\circ$ ).

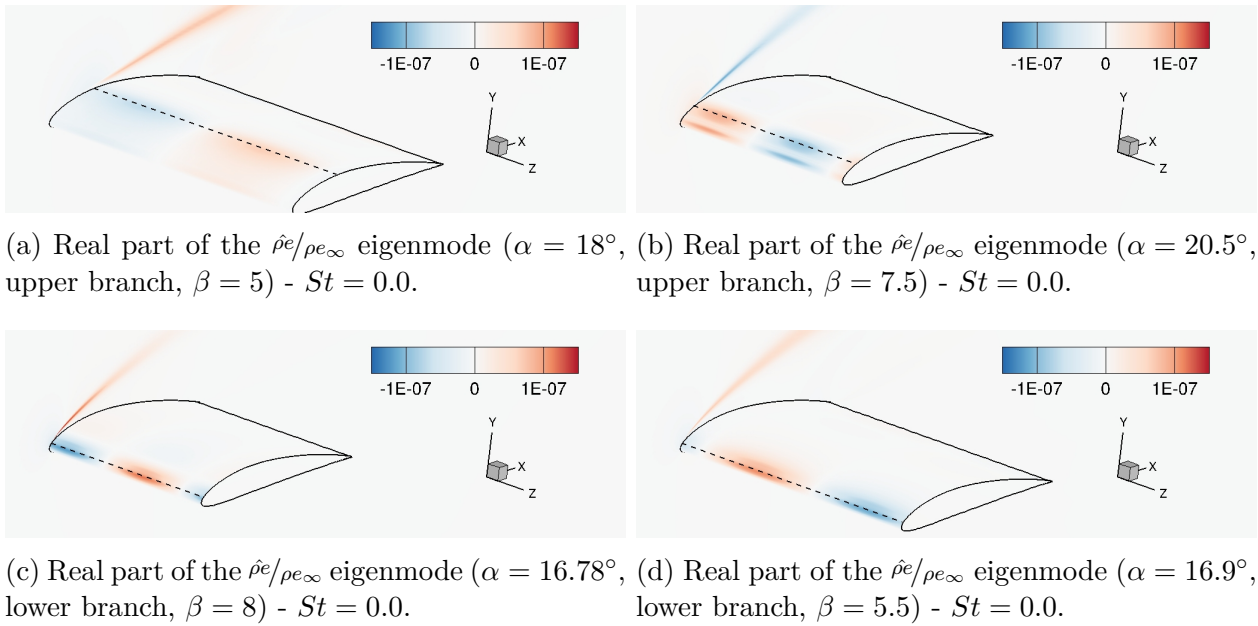


Figure 4.16 – Flow visualisation of the 3-D unstable mode for several angle of attack on the two branches of the lift hysteresis (NACA4412,  $M = 0.2$ ,  $Re = 350\,000$ ,  $\delta = 0.0^\circ$ ).

### Effect of sweep at $\alpha = 15^\circ$

The approach followed to carry out stability analyses also enables to study base-flow with  $\delta \neq 0$ . Figs. 4.17a and 4.17b show the growth rate and frequency of the unstable mode with sweep angles of  $0^\circ$ ,  $10^\circ$ ,  $20^\circ$ ,  $30^\circ$  and  $40^\circ$ . With these curves, it is possible to track the displacement of the most unstable eigenvalue with respect to the sweep angle. The frequency of the mode increases with the sweep and its growth rate decreases. For a sweep angle between  $40^\circ$  and  $50^\circ$ , the mode becomes stable. The value of  $\beta$  for which the growth rate is maximum also slightly decreases as the sweep angle increases. The stability results are consistent with the URANS simulations from section 4.3. For example, the wavenumber observed in fig. 4.3 in the unswept case is 4.2 with 4 stall cells. By accounting for the numerical constraint on the wavenumber (the domain size imposes the possible values of  $\beta$ ), the actual wavenumber on an infinite domain is expected to be between 3.7 and 4.7. The modes with the maximum growth rate have  $\beta$  between 4.0 and 4.4, hence within the expected range.

Fig. 4.17b also shows the frequency obtained with URANS simulations (red points) and the frequency extrapolated from the trend of the convection speed (see fig. 4.11) and the wavenumber (red lines). The frequencies observed in the URANS computations are well aligned with the frequency obtained with the global linear stability analysis. Hence, the

linear stability analyses predict the behaviour of the stall cells.

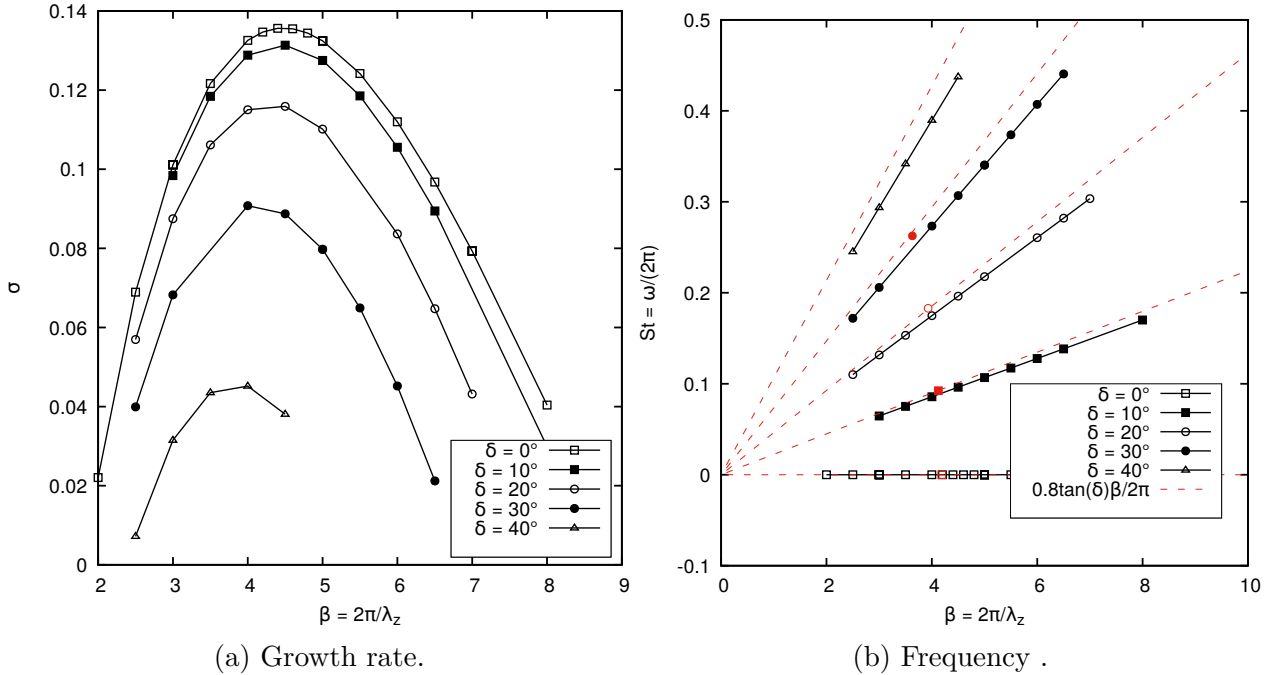


Figure 4.17 – Effect of the sweep angle on the growth rate and frequency of the 3-D unstable mode (NACA4412,  $M = 0.2$ ,  $Re = 350\,000$ ,  $\alpha = 15.0^\circ$ , black: stability analysis, red: URANS simulations).

### Two-dimensional wake instability mode.

These analyses are now carried for  $\beta = 0$ , which corresponds to two-dimensional analyses. Such analyses are performed for several angles of attack. Fig. 4.18 shows the part of the spectra where unstable modes are found. The mode becomes unstable for an angle of attack between  $16^\circ$  and  $17^\circ$  for the upper branch (UB) of the lift hysteresis, and is unstable for the entire lower branch (LB). This is consistent with the need to use the SFD technique or a Newton solver to converge the base-flow for angles of attack above  $16^\circ$ , where it was observed that the local time stepping technique failed to converge. Fig. 4.19 shows the eigenmodes for the upper and lower branch of the lift hysteresis at an angle of attack of  $18^\circ$ . The shape of these modes corresponds to a meandering of the wake which would lead to shedding of vortices in the nonlinear regime. The wavelength of this mode is larger for the lower branch, where the size of the separation is larger. As the angle of attack increases, the size of the separation region becomes larger and the Strouhal number based on the chord length ( $St_c$ ) decreases. However, the Strouhal number based on the frontal height of the

separation zone ( $St_l = St_{cl} = St_c(x_r - x_s) \sin \alpha$ ) stays constant around 0.2. This Strouhal number definition based on the separation height is inspired from the one of Yon and Katz (1998) and Zaman *et al.* (1989), but adapted to the case where the separation point  $x_s$  is not located at the leading edge but somewhere between the leading and the trailing edge. Here the flow re-attaches at the trailing edge ( $x_r = 1.0$ ). This shows that the Strouhal number based on the separation height is the correct one and its value is close to the expected one for vortex shedding (Chabert *et al.* (2016)). Hence, for  $\alpha \gtrsim 16.5^\circ$ , the three-dimensional non-oscillating mode coexists with a two-dimensional wake instability mode, such that an unsteady behaviour should be observed in the URANS simulations. On the other hand, the case  $\alpha = 15^\circ$  was analysed in section 4.3.1, and consistently with the stability results (only the three-dimensional steady mode is unstable for this value of  $\alpha$ ), the unsteady computation converges toward a steady state. Hence, once again, the results of section 4.3 are consistent with the stability analyses.

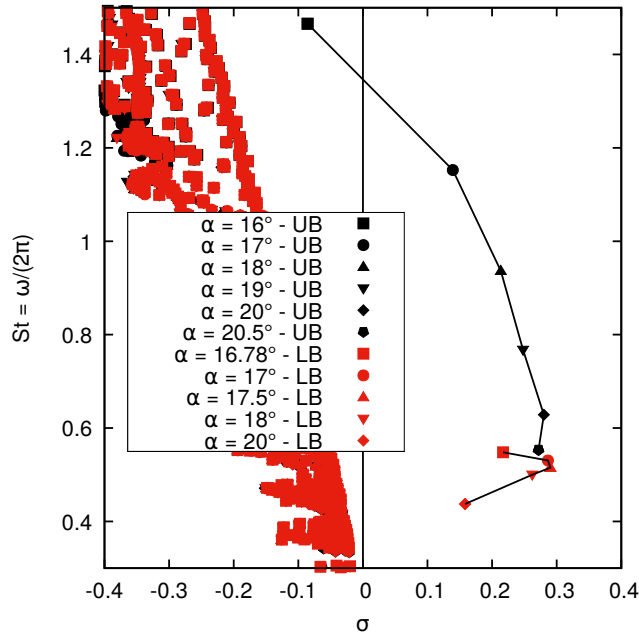
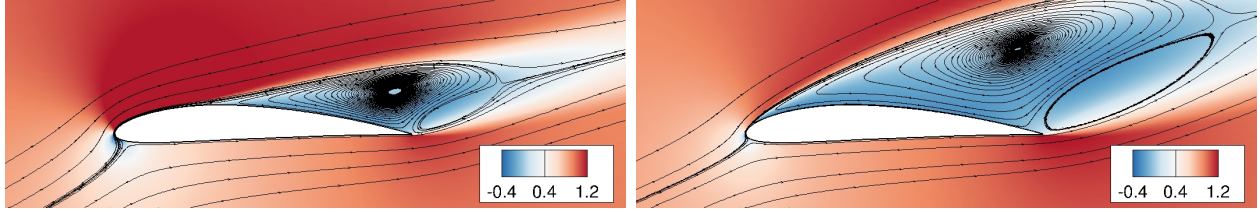


Figure 4.18 – Effect of the angle of attack on the spectra of the 2-D unstable mode (NACA4412,  $M = 0.2$ ,  $Re = 350\,000$ ,  $\delta = 0.0^\circ$ ,  $\beta = 0$ ).

### Effect of sweep angle on the 2-D wake instability mode

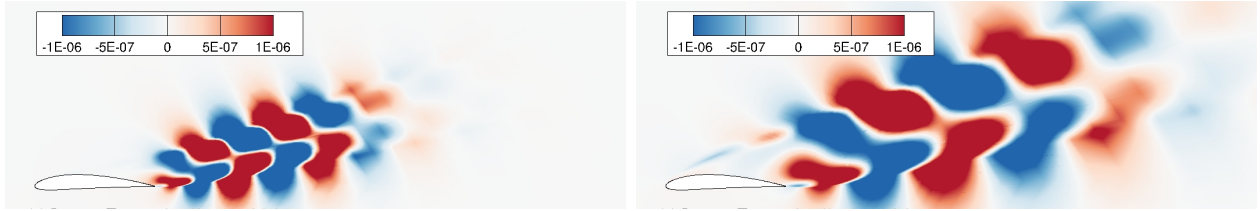
The same stability analyses are now carried out for sweep angles of  $0^\circ$ ,  $10^\circ$ ,  $20^\circ$  and  $30^\circ$  and an angle of attack of  $18^\circ$ . Fig. 4.20 shows the value of the growth rate and the Strouhal number of the wake instability mode for values of  $\beta$  around zero. This unstable mode exists for large wavenumbers  $\beta$ . In these figures, modes with a negative value of  $\beta$  are shown. These modes





(a)  $u$  base-flow. Upper branch of the lift hysteresis

(b)  $u$  base-flow. Lower branch of the lift hysteresis



(c) Real part of the  $\hat{\rho}u$  eigenmode. Upper branch of the lift hysteresis -  $St = 0.92$ .

(d) Real part of the  $\hat{\rho}u$  eigenmode. Lower branch of the lift hysteresis -  $St = 0.49$ .

Figure 4.19 – Flow visualisation of the (a,b): base-flow and (c,d): 2-D unstable mode on the two branches of the lift hysteresis (NACA4412,  $M = 0.2$ ,  $Re = 350\,000$ ,  $\alpha = 18.0^\circ$ ,  $\delta = 0.0^\circ$ ,  $\beta = 0.0$ ).

can also be seen as modes with positive  $\beta$  and a negative frequency. One can observe that, as expected, the spectrum is symmetric with respect to the imaginary axis when the sweep angle is null. In this case, the base-flow indeed exhibits a zero spanwise velocity and perturbations may equivalently propagate (in terms of phase, the phase-speed being  $v_\phi = \omega/\beta$ ) towards the inboard (negative  $z$ ,  $v_\phi < 0$ ) and outboard (positive  $z$ ,  $v_\phi > 0$ ) directions. If a positive sweep is considered, then a positive base-flow velocity in the  $z$  direction is added and the phase of the perturbation is generally preferentially advected in this direction (in the case of a constant  $W(x, y) = W$  base-flow velocity, one can show that the frequency  $\omega$  (resp. phase-speed  $v_\phi$ ) of a mode just shifts by an amount of  $\beta W$  (resp.  $W$ ), due to the Doppler-shift). Therefore, a positive sweep generally tends to increase the frequency of 3-D perturbations and their phase speed. For exactly two-dimensional oscillating perturbations (as obtained for the wake instability mode), the phase velocity is infinite (positive or negative), even if sweep is added. It is also seen that, if the perturbations become slightly 3-D ( $\beta \neq 0$ ), then the outboard propagating 3-D perturbations are slightly more unstable than the inboard propagating ones. Note that the discussion would have been different if the group velocity ( $v_g = d\omega/d\beta$ ) was considered, since the group velocity determines the speed of the envelope and fronts of a wave-packet and therefore better accounts for actual propagation of the perturbation: for this a convective/absolute stability analysis should be conducted following Huerre and Monkewitz

(1990). But this is outside the scope of this paper.

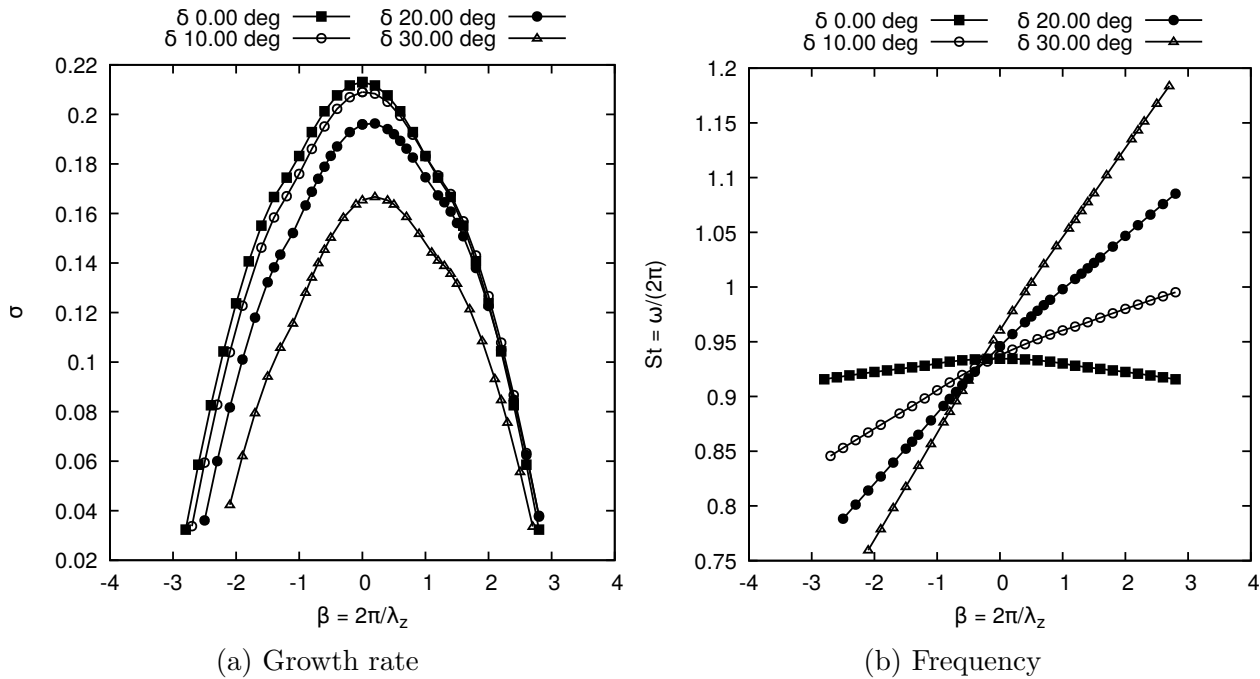


Figure 4.20 – Effect of the wavenumber on the 2-D wake instability mode (NACA4412,  $M = 0.2$ ,  $Re = 350\,000$ ,  $\alpha = 18.0^\circ$ ).

#### 4.4.2 Transonic buffet

The stability of base-flows obtained in the transonic regime for the OALT25 aerofoil at a Mach number of 0.7352 and a Reynolds number of 3 million is now studied. To begin with, the unswept case is analysed for several angles of attack. Then the effect of the sweep angle is analysed for a constant angle of attack of  $4^\circ$ . Finally, the two-dimensional case is analysed.

##### Effect of the angle of attack on the unswept case

Fig. 4.21 shows the spectra obtained for  $\beta = 2\pi$  and  $\beta = 0$  for an angle of attack of  $4^\circ$ , and a sweep angle of  $0^\circ$ . The cases where  $\beta$  tends to 0 are equivalent to the two-dimensional cases. As one can see, an unstable global mode is found at a Strouhal number of 0.075 when  $\beta = 0$  (unsteady two-dimensional) and a Strouhal number of zero when  $\beta = 2\pi$  (non-oscillating three-dimensional). Hence, two unstable eigenmodes are found for these flow conditions. This result is analogous to that at low speed where both a stall cells and a wake instability mode were observed. It should be noted that the spectra are symmetric with respect to the real axis, due to the symmetry of the problem in the non-swept case (a wave may propagate

in the positive and negative  $z$  directions). Thus, an unsteady mode with a negative frequency is also observed.

Following this analysis, fig. 4.22a shows the effect of the wavenumber  $\beta$  on the growth rate of the non-oscillating unstable mode for several angles of attack. All the analyses are done with a spanwise grid spacing of 0.002. An analysis similar to the one shown in fig. 4.13 has been carried out. It shows that refining the grid by a factor 100 does not change significantly the results for  $\beta$  up to 70 and for  $\alpha = 4.0$  and  $8.0$ . It should also be noted that the spanwise grid spacing used in the URANS simulations ( $\Delta_z = 0.035$ ) is properly converged for the range of unstable wavenumbers at an angle of attack of  $4^\circ$ .

As for the subsonic stall case, a bump in the growth rate is observed for a medium wavelength around  $\beta = 6.0$  for the low angle of attack. However, a second bump with a maximum growth rate at higher  $\beta$  is obtained as the angle of attack increases. For the particular angle of attack of  $4.25^\circ$ , the two bumps can clearly be distinguished. These results are similar to those obtained by Crouch *et al.* (2019) and Paladini *et al.* (2019c) on the OAT15A aerofoil, where an intermediate-wavelength mode and a short-wavelength one were reported. Crouch *et al.* (2019) suspected that the short-wavelength might be too small to be relevant to a RANS framework. Fig. 4.22b shows the spectra obtained for several  $\beta$  in between the intermediate-wavelength and short-wavelength bumps at an angle of attack of  $4.25^\circ$ . One can notice that there is only one unstable eigenvalue for each  $\beta$ . We do not observe a 2-mode switching, where the originally unstable mode would become stable while a previously stable mode would become unstable. This shows that these two bumps are in fact the same mode and not two separate modes which could have been both unstable for some angles of attack. Although this does not discard arguments on the physical relevance of the low-wavelength mode, the physical mechanism responsible for both these modes is the same.

Fig. 4.23 shows the  $C_L - \alpha$  curve of the steady base-flow of the OALT25. As it is the case for the NACA4412, the angles of attack for which the linear stability shows an unstable three-dimensional mode corresponds to angles of attack where the  $C_L - \alpha$  slope is negative, in agreement with Gross *et al.* (2015). However, the slope of this curve around  $\alpha = 4^\circ$  and the most unstable wavelength does not match the predictions of the model of Gross *et al.* (2015). If one takes the slope between  $5^\circ$  and  $9^\circ$ , wavenumbers of 6.5 and 4.13 are predicted with the discrete and continuous models respectively. The unstable mode has a wavenumber  $\beta = 6.0$ , which is in the predicted range. However, as it was the case for subsonic mode, changes in the  $C_L - \alpha$  slope are not associated with changes in the wavelength predicted by

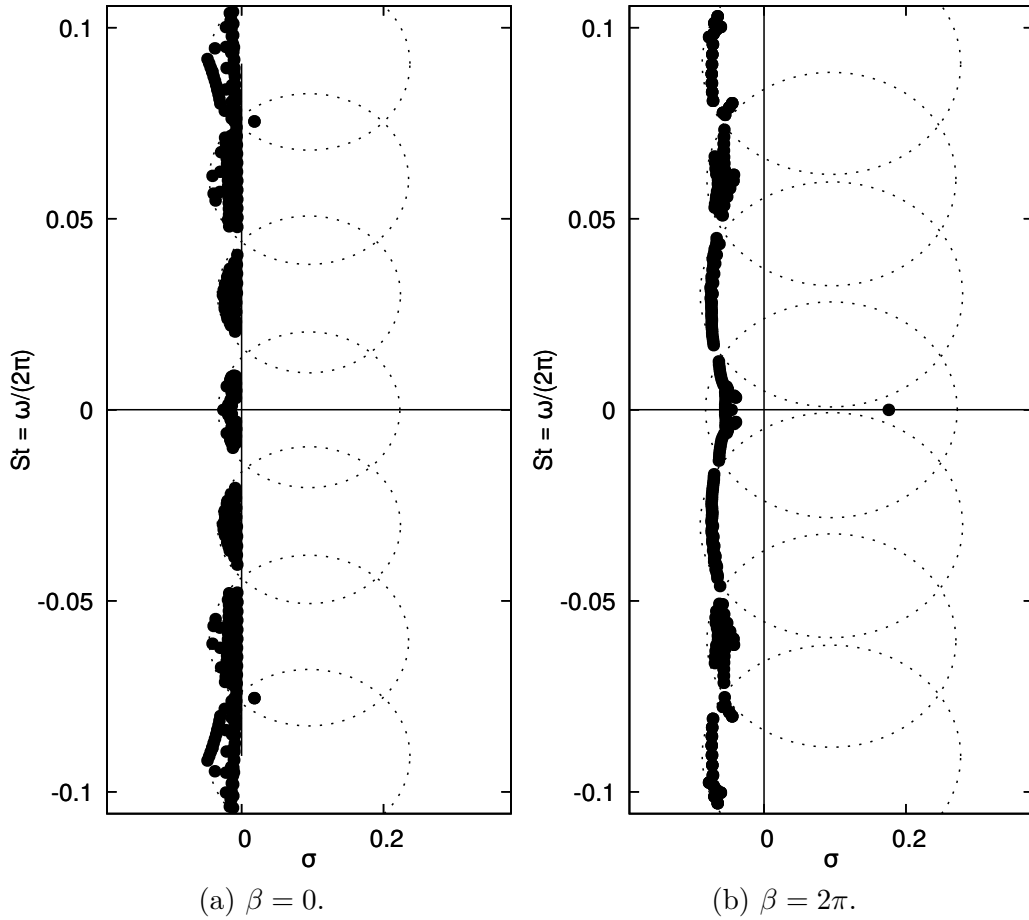


Figure 4.21 – Eigenspectrum in 2-D and 3-D (OALT25,  $M = 0.7352$ ,  $Re = 3 \times 10^6$ ,  $\alpha = 4.0^\circ$ ,  $\delta = 0.0^\circ$ ).

stability analyses.

### Sweep angle effect at $\alpha = 4^\circ$ .

Fig. 4.24a shows the effect of the sweep angle on the growth rate of the three-dimensional mode. As for the subsonic stall, the growth rate of the three-dimensional mode decreases as the sweep angle increases. From this trend, the mode becomes stable for a sweep angle slightly higher than  $40^\circ$  and is stable at  $50^\circ$ . Also, the wavenumber for which the mode is the most unstable slightly decreases when the sweep angle increases. However, the wavenumber obtained in the swept URANS ( $\beta = 2.09$ ) simulations is not unstable in the stability analysis. It will be shown in section 4.5 that this discrepancy is due to nonlinear effects.

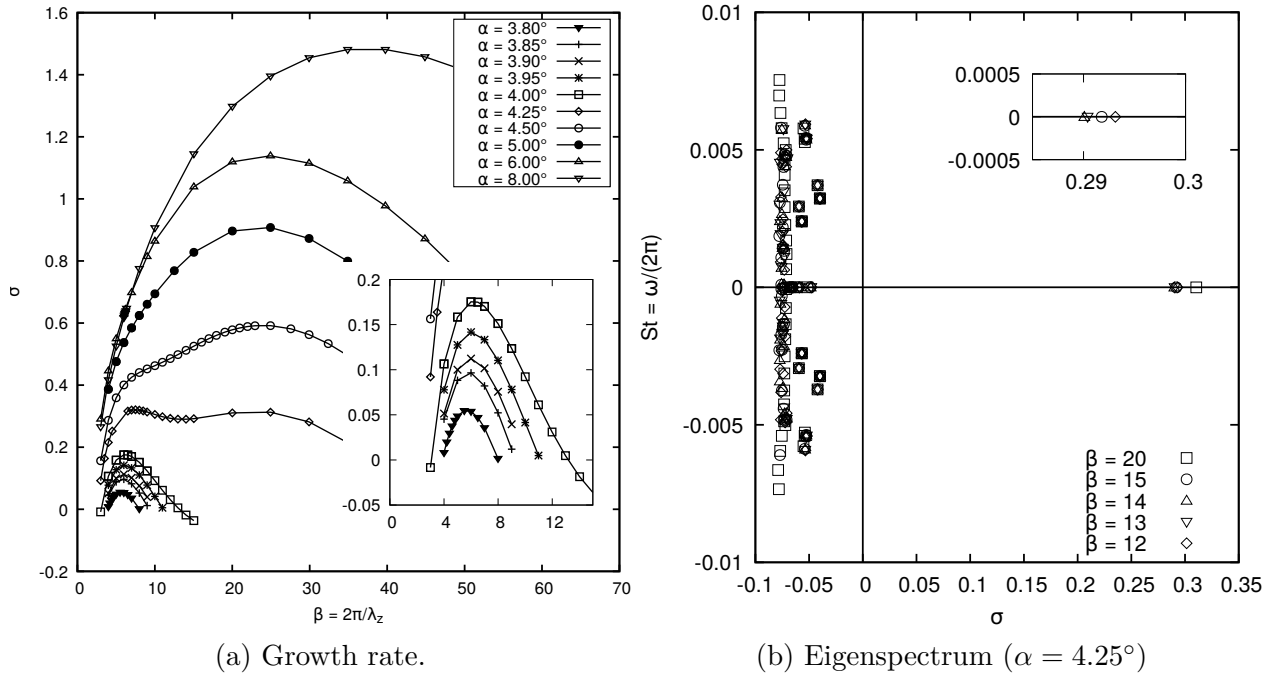


Figure 4.22 – Effect of the wavenumber  $\beta$  on the 3-D mode (OALT25,  $M = 0.7352$ ,  $Re = 3 \times 10^6$ ,  $\delta = 0.0^\circ$ )

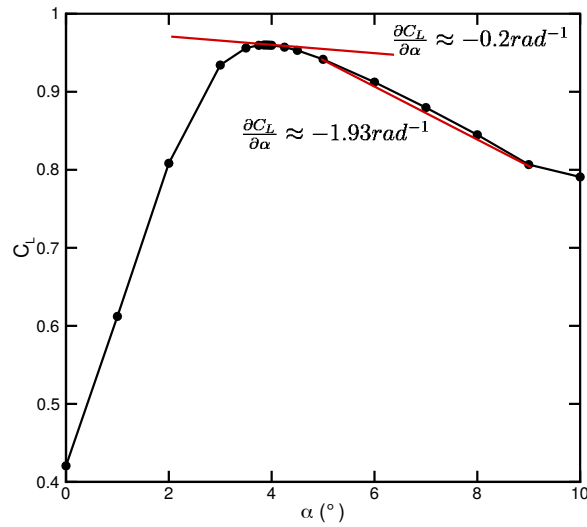


Figure 4.23 – Lift coefficient of the steady 2-D flow (OALT25,  $M = 0.7352$ ,  $Re = 3 \times 10^6$ ,  $\delta = 0.0^\circ$ ).

Fig. 4.24b shows the Strouhal number of the three-dimensional mode for sweep angles  $\delta$  of  $0^\circ$ ,  $10^\circ$ ,  $20^\circ$ ,  $30^\circ$  and  $40^\circ$  for a range of  $\beta$ . As expected, the frequency increases with  $\beta$  (smaller spanwise structures) and with the sweep angles (higher convection speed). The

URANS results (red points) and the frequencies extrapolated from the convection speed of the URANS simulations (red lines) are plotted on this graph as well. The frequencies obtained by Crouch *et al.* (2019) on the OAT15A aerofoil are also plotted. For the latter, the values have been corrected for the fact that the reference speed is taken as the speed normal to the leading edge instead of the free stream velocity. These curves match the stability results, even though the work of Crouch *et al.* (2019) was performed on a different aerofoil. Hence, the linear stability is able to predict the convection speed of the cells, but because of the discrepancy on the wavenumber with respect to the URANS simulations, the frequency of the simulations is incorrectly predicted by the stability analyses. This is due to nonlinear effects that shift the wavelength of the cells (see section 4.5).

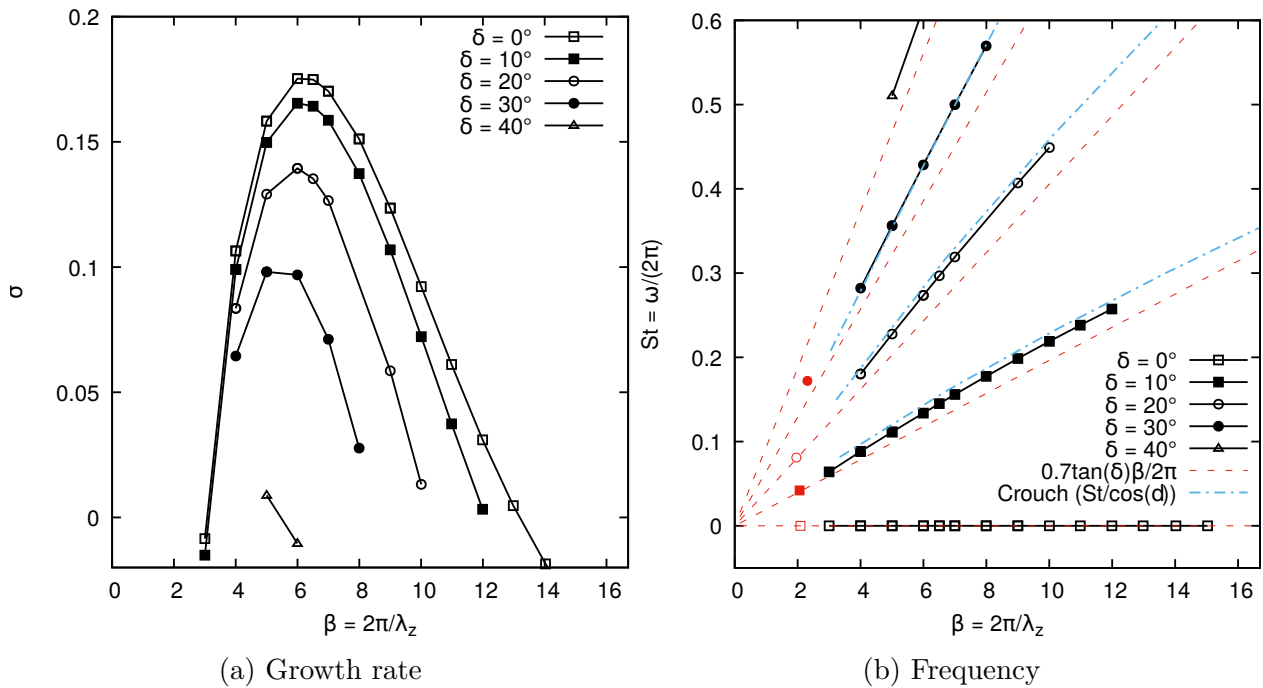


Figure 4.24 – Effect of the sweep angle on the 3-D mode (OALT25,  $M = 0.7352$ ,  $Re = 3 \times 10^6$ ,  $\alpha = 4.0^\circ$ , black: stability analysis, red: URANS simulations).

Fig. 4.25 shows the base-flow with a sweep angle of  $30^\circ$ , and the real part of the  $\hat{p}e$  two-dimensional and three-dimensional unstable modes. The two unstable modes are mostly located in the vicinity of the shock wave and in the shear layer. The two-dimensional mode displays the shape of the unstable mode reported in two-dimensional buffet studies of Crouch *et al.* (2009) and Sartor *et al.* (2015). The three-dimensional mode has spanwise fluctuations in the shock foot and trailing edge region. Those are regions of flow separation. The shape of this mode is in line with the observations of Crouch *et al.* (2019) and Paladini *et al.* (2019c).

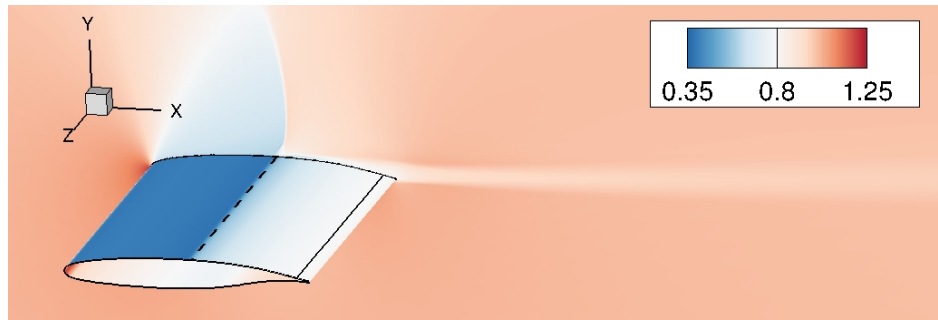
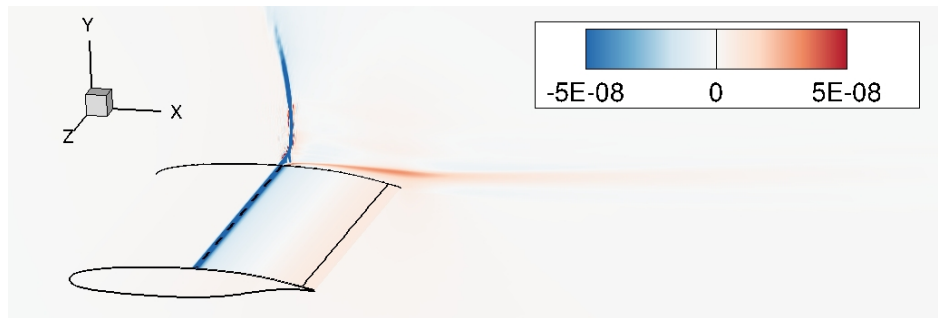
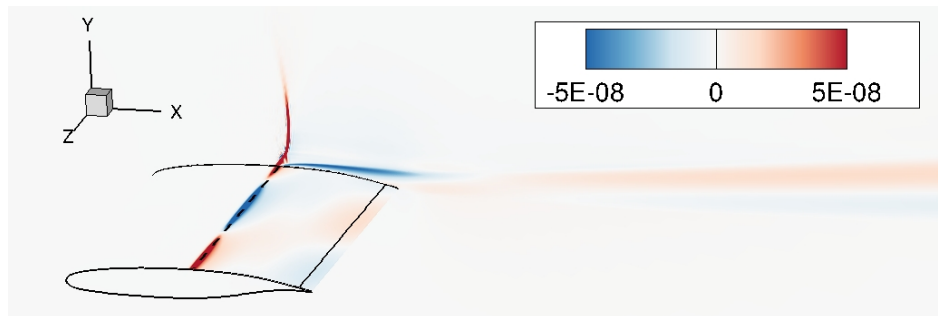
(a)  $\rho e / \rho e_\infty$  base-flow.(b) Real part of the 2-D  $\hat{\rho e} / \rho e_\infty$  eigenmode ( $\beta = 0.0$ ) -  $St = 0.075$ .(c) Real part of the 3-D  $\hat{\rho e} / \rho e_\infty$  eigenmode ( $\beta = 5.0$ ) -  $St = 0.356$ .

Figure 4.25 – Flow visualisation of the (a): base-flow, (b,c) 2-D and 3-D unstable modes (OALT25,  $M = 0.7352$ ,  $Re = 3 \times 10^6$ ,  $\alpha = 4.0^\circ$ ,  $\delta = 30^\circ$ ).

## 2-D buffet mode

Fig. 4.26 shows the portion of the spectrum where the unsteady two-dimensional mode is located. One interesting point is that the unstable unsteady mode (two-dimensional buffet) is only observed over a range of angles of attack between  $3.75^\circ$  and  $6.0^\circ$ . The three-dimensional buffet mode becomes unstable at an angle of attack around  $3.75^\circ$  as well. However, it does not become stable again at higher angles of attack in the range studied in this paper. Hence, this mode is observed for transonic stall conditions, where the two-dimensional buffet is stable.

Although this flow condition is an extreme one, which is not expected to be reached for a civil aircraft, this result suggests that the 3-D buffet can exist without the 2-D buffet phenomenon occurring. This is similar to the fact that the stall cells can be obtained without the wake instability mode.

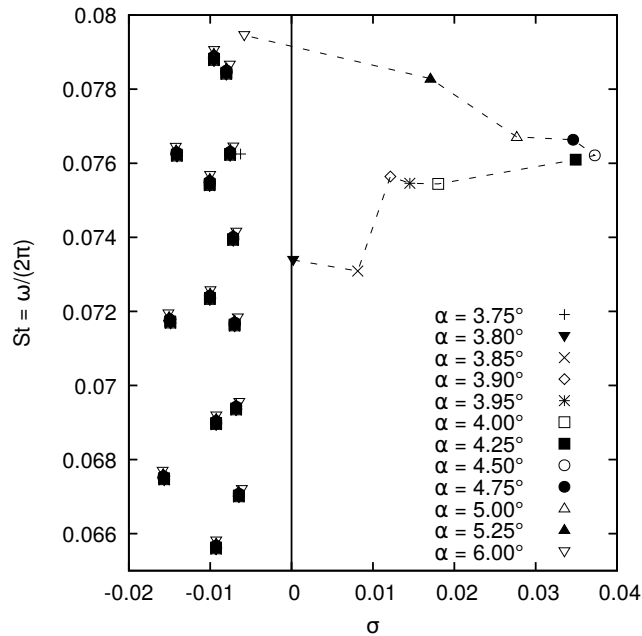


Figure 4.26 – Effect of the angle of attack on the 2-D unstable mode (OALT25,  $M = 0.7352$ ,  $Re = 3 \times 10^6$ ,  $\delta = 0.0^\circ$ ,  $\beta = 0.0$ ).

Finally, it is possible to analyse the effect of  $\beta$  on the two-dimensional buffet mode. Fig. 4.27 shows this effect on the growth rate and the frequency for several sweep angles. These are modes with very large wavelengths of at least 10 chord lengths. It should be noted that the spectrum is symmetric with respect to the real axis for  $\delta = 0^\circ$ . But it is not the case for swept wings. Hence, the effect of  $\beta$  on the growth rate and frequency is not the same for the positive and negative frequency. The two-dimensional buffet mode is more stable as the sweep angle increases. This is consistent with the fact that the buffet amplitude is lower when the sweep angle increases as shown in fig. 4.6. Also,  $\beta$  has an effect on the growth rate. Such results are similar to those of Crouch *et al.* (2019) for the OAT15A aerofoil. However, they did not report the peak in the growth rate between  $\beta = \pm 0.5$  and  $\beta = \pm 0.6$ . As verification, the case of Crouch *et al.* (2019) has been executed with the numerical setup of the present paper with similar results (see appendix A). Hence, these peaks are not caused by any problem related to the stability method or its implementation, and their existence remains unexplained for the OALT25 aerofoil. Also, the inboard propagating modes ( $\beta < 0$ ) are more unstable than



the inboard propagating modes when the wing is swept. This behaviour is opposite to the tendency of the wake instability mode (fig. 4.20).

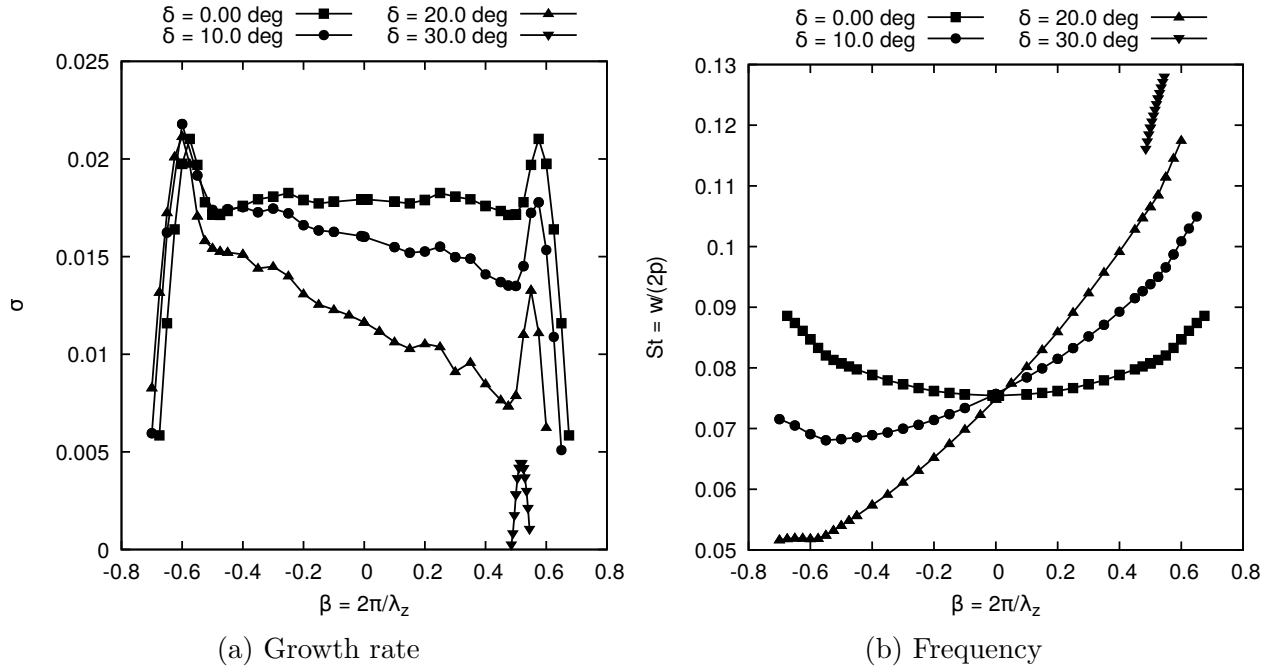


Figure 4.27 – Effect of the wavenumber on the 2-D buffet mode (OALT25,  $M = 0.7352$ ,  $Re = 3 \times 10^6$ ,  $\alpha = 4.0^\circ$ ).

#### 4.4.3 Partial conclusion

The global linear stability analyses predict two unstable modes in the subsonic stall conditions. One which can be related to the stall cells (3-D) and the other to the shedding of vortices (2-D). The wavenumber, convection speed and frequency of the 3-D mode are consistent with the URANS results presented in section 4.3.1. The 2-D mode has the expected frequency with a Strouhal number based on the separation height of 0.2. However, multiple frequency and size of the vortices are identified for some flow conditions since multiple steady-state base-flows are found.

Two unstable modes are also identified in the transonic buffet regime. The first one is associated to the 2-D buffet instability at a frequency around 0.07. The second one leads to spanwise flow structures which can be associated to buffet cells. There is a discrepancy between the wavenumber predicted by the stability analyses and the URANS simulations. However, the frequency of this mode is that of 3-D structures convected at the same speed as those in the URANS simulations.

For the case of the NACA4412, two solution branches have been analysed. Such multiple solutions have been observed in the literature before (Wales *et al.*, 2012; Busquet *et al.*, 2017). Multiple base-flows were not found for the OALT25 aerofoil, however, they cannot be ruled out. Nevertheless such multiple solutions do not seem to be related to the occurrence of stall cells since an unstable stall cell mode is found at angles of attack where only one base-flow is found.

## 4.5 From linear to non-linear regime

Section 4.3 analysed the non-linear saturated regime. This was done by starting the solution from a non-converged RANS solution. Section 4.4 studied the behaviour of the solution in the linear regime around a fully converged RANS solution. This section investigates the transient between the two regimes. To do so, the steady base-flows are extruded to get a three-dimensional initial condition, and the URANS solver is run from this initial solution.

### 4.5.1 NACA4412 at $\alpha = 15^\circ$ and $\delta = 0^\circ$

Fig. 4.28 shows how the solution diverges from the steady two-dimensional base-flow towards the solution shown in section 4.3. As one can see, the flow diverges with four regular stall cells and the flow topology converges to the one shown previously. This corresponds to a wavenumber  $\beta = 4.2$  which is the wavenumber with the maximum growth rate allowable on this grid (see fig. 4.17a), since the number of cells is constrained by the size of the domain. This result is consistent with the stability analysis.

### 4.5.2 OALT25 at $\alpha = 4^\circ$ and $\delta = 20^\circ$

Similar analyses can be done for the transonic buffet case. Fig. 4.29 shows three time samples of the URANS simulation with the extruded base-flow as the initial state and a sweep angle of  $20^\circ$ . One can observe that three-dimensionality occurs with the appearance of 6 buffet cells ( $\beta = 6.28$ ), in agreement with the largest growth rate allowable for this computational domain (see fig. 4.24a). However, the wavelength progressively increases toward the value observed in section 4.3. This shows that the stability analysis predicts the initial bifurcation from the base-flow to the presence of buffet cells. However, some non-linear effects are responsible for the shift of wavelength observed such that the saturated regime is different from the value predicted by the linear model.

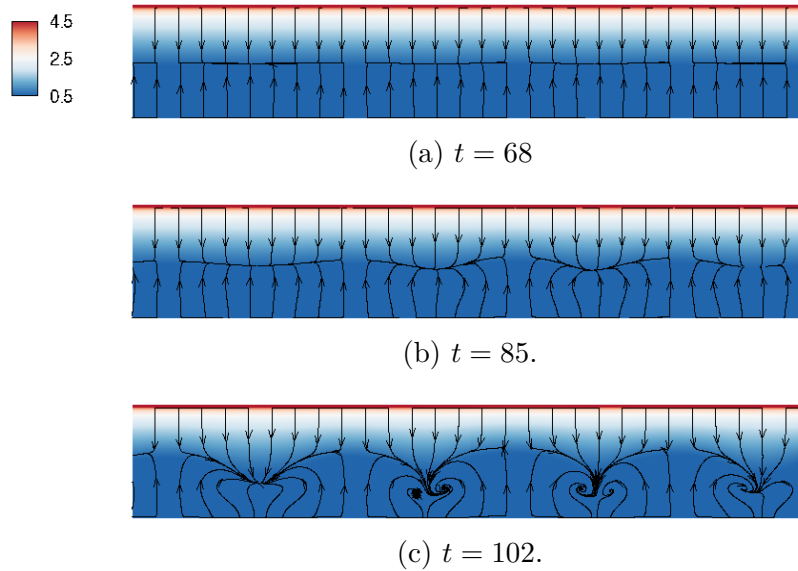


Figure 4.28 – Snapshots of the surface pressure coefficient and skin friction lines of the URANS simulations (NACA4412,  $M = 0.2$ ,  $Re = 350\,000$ ,  $\alpha = 15.0^\circ$ ,  $\delta = 0^\circ$ ,  $L_z = 6$ ).

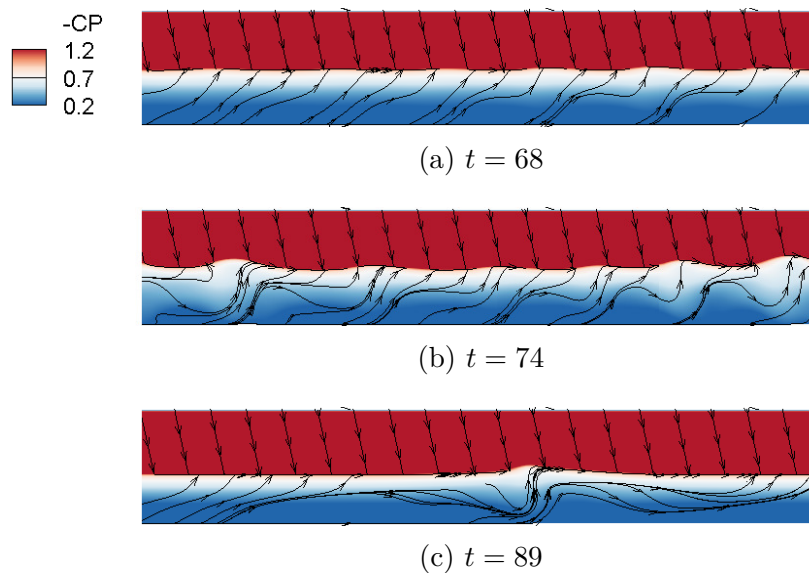


Figure 4.29 – Snapshots of the surface pressure coefficient and skin friction lines of the URANS simulations (OALT25,  $M = 0.7352$ ,  $Re = 3 \times 10^6$ ,  $\alpha = 4.0^\circ$ ,  $\delta = 20^\circ$ ,  $L_z = 6$ ).

#### 4.6 Link between stall and buffet cells

Previous solutions were obtained for two different aerofoils, at two Reynolds numbers. To clearly establish a link between buffet cells and stall cells, the stability analyses are now

carried out for a NACA0012 at a Reynolds number of 10 million and the unstable eigenvalues are tracked from the low-speed regime to the transonic one. The NACA0012 aerofoil at a high Reynolds number is selected since a trailing edge stall is expected at low Mach number and transonic buffet at higher speed (McDevitt and Okuno, 1985). As the Mach number increases, the angle of attack is decreased in order to recover the stall and buffet onset conditions. Fig. 4.30 shows the base-flow obtained for Mach numbers from 0.2 to 0.72. The flow topology at a Mach number of 0.2 is the one of a subsonic stall. Similar topology, but with a stronger flow acceleration and a weak shock wave near the leading edge are obtained for Mach numbers of 0.3 and 0.4. However, for Mach numbers higher than 0.5 the shock wave is stronger and flow separation occurs at the shock foot.

Fig. 4.31a shows the growth rate of the three-dimensional unstable mode. For the low-speed cases, the maximum growth rate is found for  $\beta$  around 4. This result is similar to the previous observations on the NACA4412 aerofoil, even though the Reynolds number is by far larger. For Mach numbers between 0.4 and 0.5, the flow topology changes significantly and so does the value of the most amplified  $\beta$ . In this case  $\beta$  is greater than 170. These are three-dimensional modes with a very small wavelength. As the Mach number increases, the value of  $\beta$  for which the three-dimensional mode is found decreases to reach a value of 100 for a Mach number of 0.6 and 50 for a Mach number of 0.72. This is consistent with the results of Crouch *et al.* (2018), who reported only a short-wavelength mode for the NACA0012 aerofoil and not the intermediate-wavelength like on the OAT15A and OALT25. One major difference between the NACA0012 and the OALT25 aerofoils is the fact that there is only a flow separation in the shock foot area for the NACA0012, while the flow over the OALT25 also separates at the trailing edge. Figs. 4.31(b) shows the growth rate of the three-dimensional mode normalized by the height of the separation  $h_s$ . By using this normalization, the maximum growth rates are located around  $\beta h_s \approx 0.25$  for every Mach number, which shows that this is the correct scaling length for this three-dimensional mode. The amplification factors are normalized by the same length scale. Two other scalings were attempted, namely a scaling by the separation length  $l_s$  and by the projection of the separation length in the direction normal to the inflow  $l$  (see supplementary material to this article). By using the separation length, a proper scaling is obtained for the subsonic and transonic cases separately. But this scaling does not hold between these two flow regimes.

Fig. 4.32 displays the eigenvectors at these flow conditions, indicating that the unstable modes are all located in the vicinity of the flow separation. For a Mach number larger than 0.5, a shock wave occurs in the base-flow. In these cases, the eigenmode reaches high values

at the separation point and further downstream, but it does not propagate in the supersonic region upstream of the shock wave, contrary to subsonic cases.

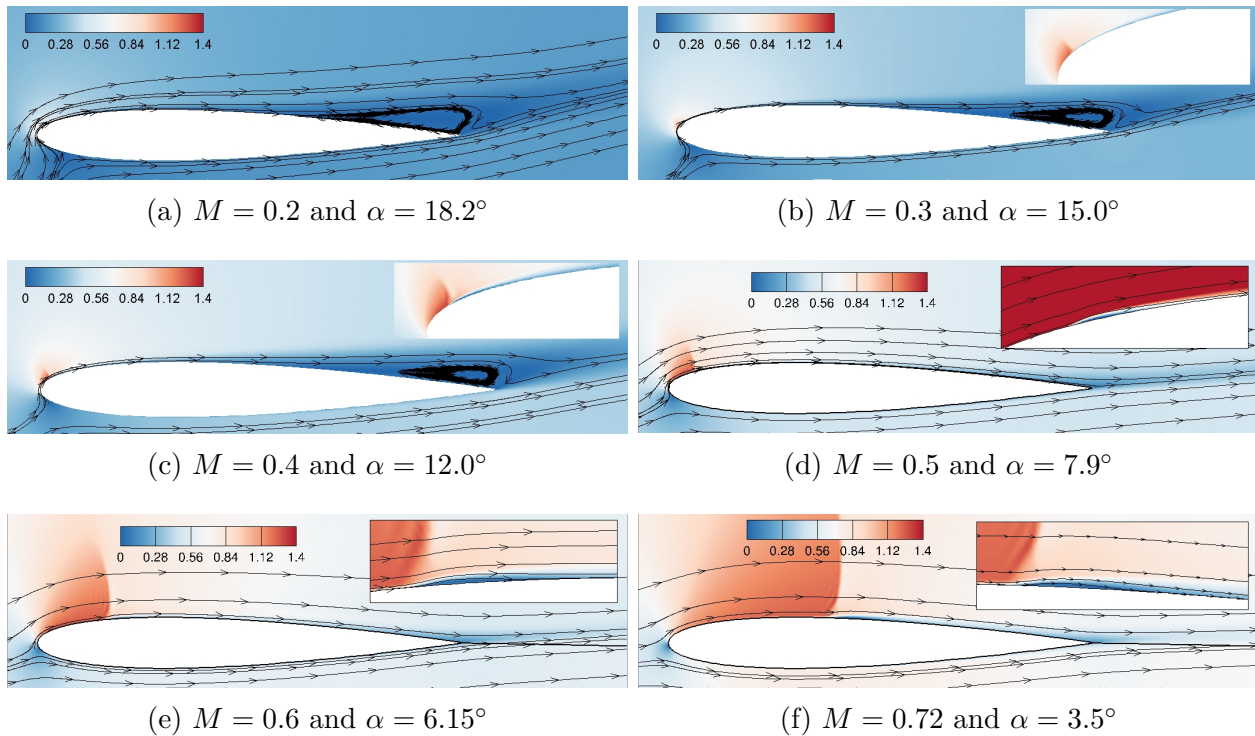


Figure 4.30 – Base-flow Mach number field at several Mach number and angle of attack (NACA0012,  $Re = 10^7$ ,  $\delta = 0^\circ$ )

In the case of the OALT25 aerofoil, the three-dimensional and two-dimensional modes become unstable around the same angle of attack. This may suggest that the two unstable modes are somewhat linked. For this reason, the angle of attack at which an unstable 2D buffet mode appears has been searched for the NACA0012 at  $M = 0.72$ . Fig. 4.33 shows the region of the spectra around which the unstable mode is expected. An unstable mode is present at an angle of attack of  $4.5^\circ$ , but this mode is stable for lower angles of attack. This indicates that the three-dimensional buffet mode can be unstable (see unstable branch at  $\alpha = 3.5^\circ$  in fig. 4.31) without an underlying two-dimensional mode (fig. 4.33).

As it is the case for the NACA4412 and the OALT25 aerofoils, 3-D modes with a non-zero frequency are obtained when a sweep angle is added. Fig. 4.34 shows the frequency of the 3-D modes with sweep angles of  $\delta = 0^\circ$ ,  $10^\circ$ ,  $20^\circ$  and  $30^\circ$ , and the scaling found previously. The angles of attack are slightly increased in comparison to previous results

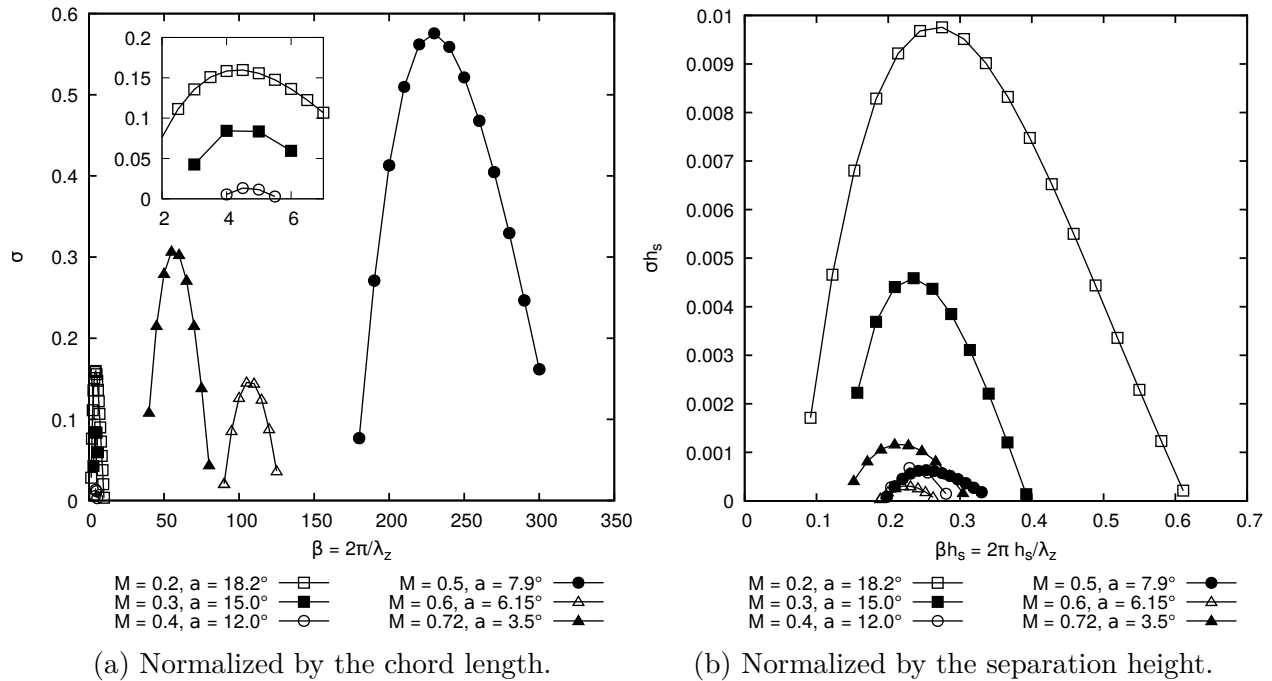


Figure 4.31 – Effect of the Mach number and angle of attack on the growth rate of the 3-D mode (NACA0012,  $Re = 10^7$ ,  $\delta = 0^\circ$ ).

on the NACA0012 because the sweep angle has a stabilizing effect. As one can see, the frequency of these unstable modes is still proportional to the spanwise velocity. Moreover, the proportionality coefficients found for the NACA4412 and the OALT25 still hold for the NACA0012 in subsonic and transonic regimes respectively.

Hence it is possible to follow a single and same unstable mode that represents stall cells in the subsonic regime and buffet cells in the transonic flow regime. This branch of modes exhibits the same features as those found separately for the NACA4412 and the OALT25 aerofoils. This also shows that the stall cell mode is present both at an intermediate (350 000) and high ( $10^7$ ) Reynolds number. Moreover, a scaling by the height of the separation bubble is proposed to link the size of the stall cells to that of the buffet cells.

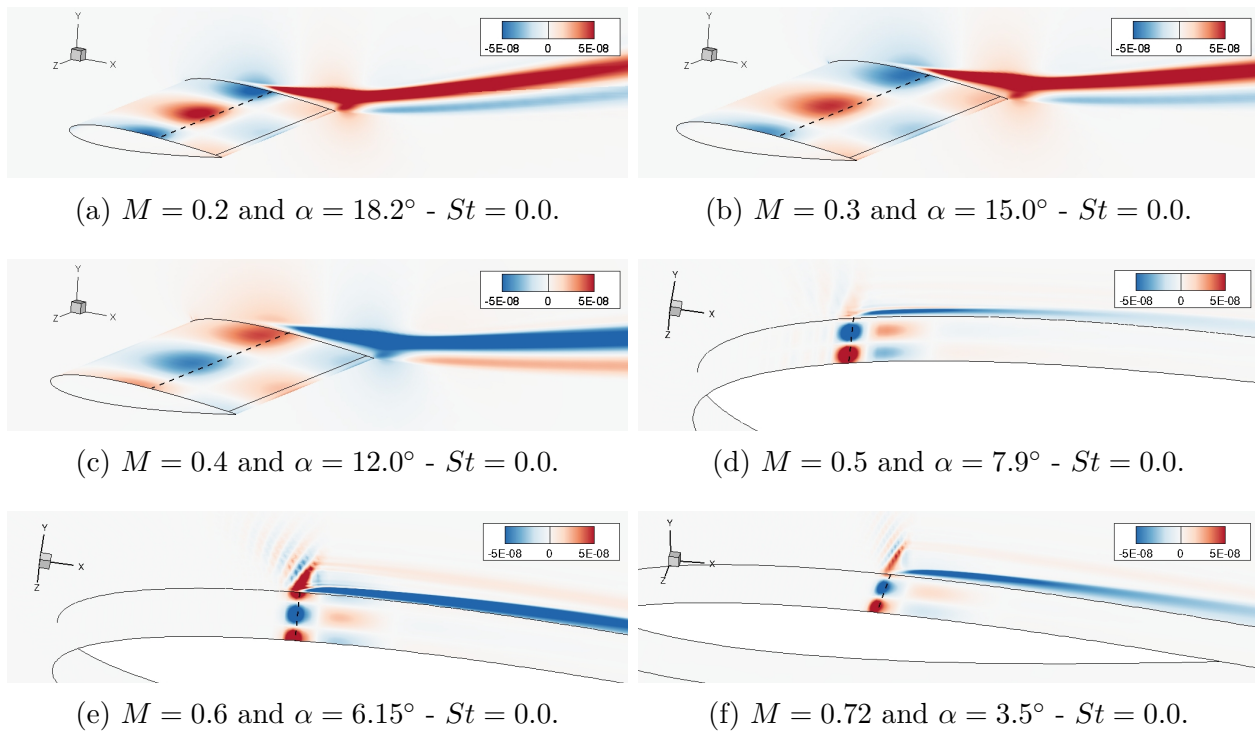


Figure 4.32 – Flow visualisation of the 3-D  $\hat{\rho}_e/\rho_{e\infty}$  unstable mode (NACA0012,  $Re = 10^7$ ,  $\delta = 0^\circ$ ).

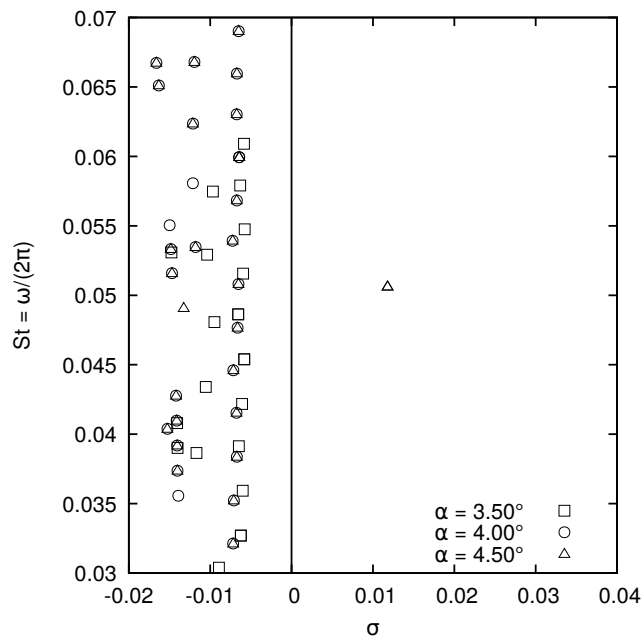
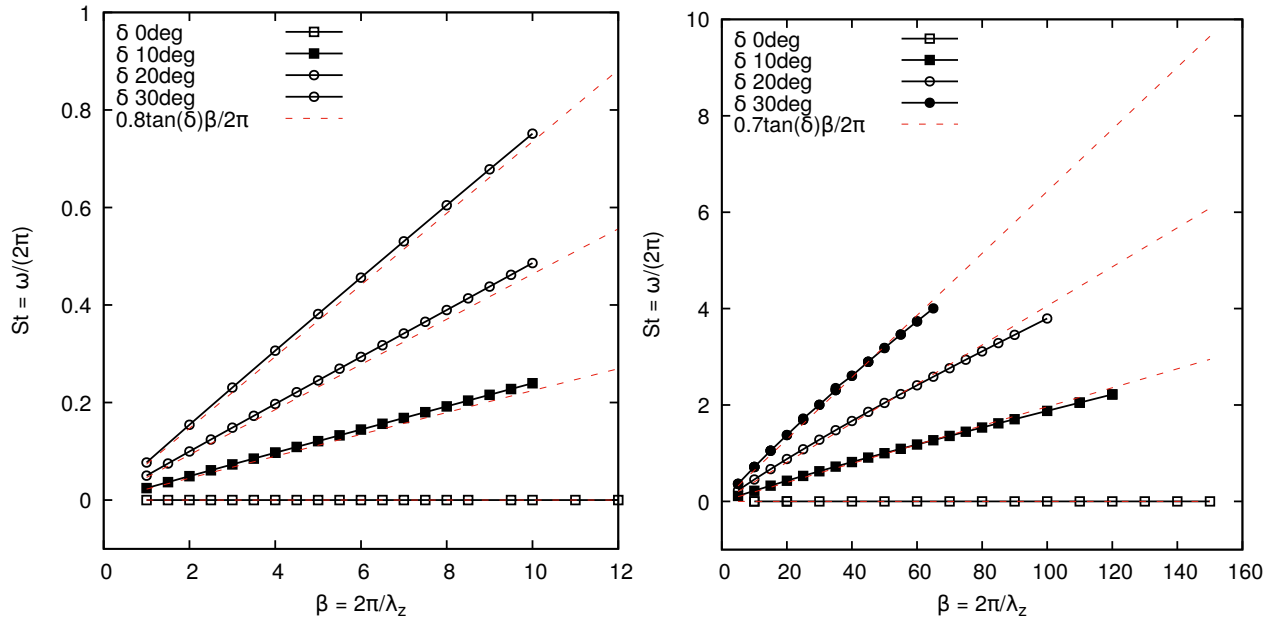


Figure 4.33 – Effect of the angle of attack on the 2-D unstable mode (NACA0012,  $M = 0.72$ ,  $Re = 10^7$ ,  $\delta = 0.0^\circ$ ,  $\beta = 0.0$ ).



(a) Subsonic (NACA0012,  $M = 0.2$ ,  $Re = 10^7$ ,  $\alpha = 18.5^\circ$ ), (b) Transonic (NACA0012,  $M = 0.72$ ,  $Re = 10^7$ ,  $\alpha = 4.5^\circ$ ).

Figure 4.34 – Effect of the sweep angle on the 3-D mode frequency.

## 4.7 Conclusion

Three-dimensional flows over infinite swept configurations were obtained using URANS simulations for low-speed stall and transonic buffet conditions. The observed stall/buffet cells are steady for unswept wings, and convected in the spanwise direction when the wing is swept. This induces a frequency which can be related to the distance between two cells and their convection speed. In the case of the subsonic stall, this unsteadiness dominates the flow. However, it is superimposed to the two-dimensional buffet phenomenon at high-speed.

Global linear stability analyses of 2.5-D base-flows were carried out for subsonic stall and transonic buffet. An unstable three-dimensional mode was observed in both flow conditions. The frequency of the latter is null for unswept wings and becomes unsteady as the sweep angle is increased. The frequencies and wavelength of stall cells obtained with stability analysis are in line with the observation of the URANS simulations. However, discrepancies between the wavelength of buffet cells and the global mode with the largest growth rate are observed. Nevertheless, the frequency of the unstable modes is consistent with that of structures convected at the convection speed observed in the URANS simulations. A mode consistent with a two-dimensional vortex-shedding in subsonic stall conditions was found, as



well as a two-dimensional buffet mode in transonic buffet conditions. The two-dimensional vortex shedding is not observed in the URANS simulations because the angle of attack is lower than the one for the onset of this unstable mode. A similar condition where the buffet cell mode is present but not the two-dimensional buffet mode might allow to obtain steady buffet cells on an unswept wing.

Nonlinear flow simulations starting from the base-flows effectively shows that the flows diverge following the shapes identified in the stability analyses. In the case of the subsonic stall, the number of cells predicted in the stability analyses stay constant in the nonlinear regime. However, the solution of transonic buffet over swept wings diverges towards buffet cells with a lower wavenumber after the appearance of spanwise flow structures of the length identified with the stability analyses, possibly because of non-linear effects.

Finally, results of the stability analyses allow to follow the angle of onset of a three-dimensional mode from the low-speed to the transonic flow regime. This study was done on a NACA0012 aerofoil at a Reynolds number of 10 million. Although the wavelength of this mode varies greatly with the Mach number, using the separation height as the reference length allows to centre the non-dimensional wavenumber around a value  $\beta h_s \approx 0.25$ . This result reinforces the conclusion that the two phenomena are the same and are related to the occurrence of flow separation. Also, the three-dimensional mode is identified at an angle of attack lower than the two-dimensional buffet onset angle. This shows that the buffet cells associated with three-dimensional buffet can be observed without the presence of the two-dimensional buffet.

Hence, this paper provides evidences that the buffet cells and the stall cells are in fact the same flow instability. Even though it is convenient to describe the three-dimensional mode in buffet condition as a three-dimensional buffet phenomenon in the context of applied aerodynamics, one can show that this mode is oscillatory only when the wings are swept. Moreover, the physical mechanisms involved in the two-dimensional buffet and the buffet cells are different. As such, one can question the accuracy of naming the so-called buffet cells as three-dimensional buffet and not just as stall cells.

## Acknowledgment

Parts of this paper were presented at the 54th 3AF International Conference AERO2019 Conference (FP63-AERO2019-plante). This work is supported by the Natural Sciences and

Engineering Research Council of Canada (NSERC). Part of this work made use of the GENCI CINES facilities (Grant DARI No.A0042A10423).

### **Declaration of interests**

The authors report no conflict of interest.

## CHAPTER 5    ARTICLE 3 : STALL CELL PREDICTION USING A LIFTING SURFACE MODEL

*The third article explores the topic of modeling stall cells using an inviscid model like the lifting line model used by Spalart (2014). This article uses the next level of approximation which is a lifting surface model. The proposed approach is a nonlinear Vortex Lattice Method (NL-VLM). With this method, viscous effects are modeled by adding an angle of attack correction to the section of the wing in the VLM. The system is converged when the sectional lift coefficient provided by the VLM method with the correction angle is equal to the lift coefficient interpolated in a lift versus angle of attack curve. This method allows to model the stall behavior in an inviscid model. A numerical artefact allowing to simulate an infinite wing with a periodicity assumption is also proposed. Another numerical parameter of the model is an artificial dissipation.*

*Results show that stall cells are obtained when a section of the wing sees an effective angle of attack for which the lift-curve slope is negative  $\frac{\partial C_L}{\partial \alpha} \leq 0$ . The canonical case of an elliptic wing is studied since this is a three-dimensional wing for which the effective angle is constant from one section to the other. Hence, all the sections of the wing stall simultaneously. However, the stall cell phenomenon causes some of the wing section to get into a deeper stall and other to see a lower angle of attack. Thus, stall cells are obtained. An interesting observation is the fact that no wing sections see an effective angle of attack for which  $\frac{\partial C_L}{\partial \alpha} \leq 0$  in the converged solution. Hence, the stall cells are composed of fully stalled sections and un-stalled sections. As such, it is observed that the lift curve slope cannot stay negative as the angle of attack goes to infinity if one seeks a steady-state solution. For this reason several lift curves are designed to study the effect of the lift polar on the solution of the model. The latter is found to have an impact on the wavelength of the stall cells. Adding a numerical dissipation helps to obtain smoother solutions, but does not qualitatively change the solutions.*

*Following these results an analysis of a rectangular wing is done in order to make a comparison with the experimental results of Winkelmann and Barlow (1980). Qualitative agreement is obtained. However, the post stall behavior of the two-dimensional polar has been extrapolated from an experimental reference. Finally, the infinite wing case is studied. As it is the case for the elliptical wing, the whole wing stalls simultaneously and the stall cells are observed when the geometrical angle of attack is in the stall regime. Hence this article provides a model for the occurrence of stall cells and addresses the last objective of the thesis.*

PLANTE, F., LAURENDEAU, É., DANDOIS, J., Stall cell prediction using a lifting-surface model, Accepted at the *AIAA SciTech 2021 conference*, Submitted to *AIAA Journal* 24 Aug. 2020.

This paper investigates the use of a lifting surface method towards the study of lift cells on wings, thereby extending the lifting-line model proposed by Spalart. In particular, calculations are made with a 3D Vortex-Lattice Method (VLM) coupled with two-dimensional sectional lift versus angle of attack polar to include viscous effects. This viscous coupling allows to capture pre- and post-stall regimes, making it a Non-Linear Vortex Lattice Method (NL-VLM). Canonical cases are examined, such as infinite span wings and wings with elliptical lift distributions coupled with manufactured lift-curves. To achieve these goals, numerical artefacts are developed. One is to enable solutions over infinite span wings, while the other has been traditionally used to stabilise the numerical scheme in the form of added numerical dissipation. Various parametric studies are performed using Spalart's model and our proposed NL-VLM model. This paper identifies the limitations of both models. It is found that Spalart's model suffers from robustness issues without the addition of a Gaussian filter, and that the number of cells increases with the numbers of modes. In contrast, the NL-VLM model converges with and without the use of artificial dissipation without affecting the number of stall cells.

## 5.1 Introduction

Three-dimensional flow features over wings in stall conditions have been experimentally observed since the 1970's. Experiments such as those of Moss and Murdin (1971) and Gregory *et al.* (1971) showed three-dimensional vortex structures on essentially two-dimensional wings spanning the entire wind tunnel width. This phenomenon was later studied by Winkelmann and Barlow (1980) on a wing based on the Clark Y airfoil with free tips. This experiment showed "mushroom" shaped flow structures over the entire span of the wing and an increasing number of these structures when the aspect ratio of the wing increases. This phenomenon is now often called stall cells. Observations similar to the one of Winkelmann and Barlow (1980) were made by Schewe (2001). The number of stall cells increases with the aspect ratio of the wings. Early studies speculated that the wind tunnel walls were responsible for these three-dimensional effects. However, the observation of stall cells over the full span of high aspect ratio wings and wings with free tips discarded the effect of the wind tunnel walls as the origin of stall cells. Experiments by Broeren and Bragg (2001) investigated the effect of the type of stall on the three-dimensional stall features. Their results suggest that a trailing edge

type of stall is a necessary condition for the appearance of these features. Other experiments by Dell’Orso and Amitay (2018) showed an effect of the Reynolds number on the stall cells and identified a transition between a two-dimensional stall to a three-dimensional one with increasing Reynolds number.

This phenomenon has been observed in multiple numerical studies. Manni *et al.* (2016) carried out Unsteady-Reynolds-Averaged Navier-Stokes (URANS) simulations and Delayed Detached Eddy simulations (DDES) of a wing of aspect ratio 10 at a Reynolds number of one million. Bertagnolio *et al.* (2005) obtained stall cells over a wind turbine airfoil with URANS simulations. A previous study by the authors (Plante *et al.*, 2019a) studied the stall cells over a NACA4412 airfoil at a Reynolds number of 350 000 and several sweep angles with URANS simulations, showing the convection of the stall cells on swept wings. All these numerical studies point out the occurrence of stall cells without the application of any three-dimensional disturbance from the geometry. This suggests that the stall cells are caused by an inherent flow instability and not the boundary conditions.

Explanation of the stall cells as a globally unstable mode was proposed by Kitsios *et al.* (2009), Rodríguez and Theofilis (2011), He *et al.* (2017) and Zhang and Samtaney (2016) for wings at a Reynolds number of a few hundreds to a thousand. A similar study was carried out by Plante *et al.* (2019b) for wings based on the NACA4412 airfoil at an intermediate Reynolds number of 350 000 with RANS modeling, for which a trailing edge stall behavior is observed. This study showed that the stall cells predicted with a global stability analysis closely matched the prediction of the non-linear URANS equations in (Plante *et al.*, 2019a).

An attempt to model the stall cells, or lift cells, was done by Spalart (2014) using the lifting line theory coupled with a manufactured sectional lift polar including a post-stall regime. This model will be further discussed in this paper. From this model the stall cells can be linked to a negative slope in the  $C_l(\alpha)$  curve. Such a conclusion was also reported in the work of Gross *et al.* (2015) where a criterion for the wavelength of the cells was proposed based on the lifting line theory. The model of Spalart (2014) included a free parameter in the form of a Gaussian filter width. This numerical element was required to prevent the model from producing very low wavenumber modes. This study (Spalart, 2014) suggests a simple inviscid model can be used to explain the stall cell phenomenon and Spalart (2014) proposed that a lifting surface model would be the next level of approximation. Filling this gap is one of the objectives of the present paper.

The lifting line model of Spalart (2014) can be described as a  $\Gamma$ -based coupling since it proceeds by assuming a circulation distribution allowing to compute the downwash for each wing station and the induced angle of attack. This induced angle of attack is used to get the viscous lift coefficient of the wing sections. Finally, a new circulation distribution is obtained with the Kutta-Joukowski theorem. This procedure is carried out until the solution reaches steady state. A method of this type was also presented by Chattot (2004).

Another approach is to use an  $\alpha$ -based method such as the one of van Dam (2002). This method solves the lifting line theory and the viscous effects are taken into account by a correction to the local angle of attack. Extension to this method was presented by Gallay and Laurendeau (2015) for an application as a preliminary design tool (Gallay and Laurendeau, 2016). Solution presenting features similar to stall cells were obtained by Gallay and Laurendeau (2015). Similar solutions have also been obtained with a coupling using a decambering approach by Paul and Gopalarathnam (2014).

This paper aims to provide the next level of approximation to the lifting line model of Spalart (2014), a lifting surface model. It also characterizes the post-stall solutions obtained with a lifting surface model coupled with a viscous database by an  $\alpha$ -based method. The paper first presents the numerical methods of the models used in this paper. The lifting line model of Spalart (2014) is recalled and the lifting surface model is introduced. A numerical procedure to include a periodicity condition in the lifting surface model is also proposed. Section 5.3 presents the verification of the models. Then, the analyses of post-stall cases with the lifting line and lifting surface models are presented. The case of an infinite wing, an elliptic wing and a rectangular wing are studied. Results for several aspect ratios and viscous lift polars are presented and the effect of adding a numerical dissipation proposed by Gallay and Laurendeau (2015) to the coupling is investigated.

## 5.2 Methodology

An inviscid, irrotational, and incompressible flow can be modeled by Laplace's equation :

$$\nabla^2\phi = 0 \tag{5.1}$$

with  $\phi$  the velocity potential. Since this equation is linear, solutions can be sought in the form of the superposition of elementary solutions (vortices, sinks, sources, doublets, etc.). A wide variety of methods were developed based on this concept, of which the lifting line and lifting surface models.

### 5.2.1 Non-linear lifting line model

Spalart (2014) proposed a model based on the lifting line theory for what he called lift cells. In the present study, numerical experiments with this model are carried out and a lifting surface model will be compared to it. Hence the model for an infinite wing is recalled here. The problem is formulated using a Fourier transform for the circulation  $\Gamma$  :

$$\Gamma(y) = cV_\infty \sum_{j=0}^{\infty} A_j \cos(jk_0y) + B_j \sin(jk_0y) \quad (5.2)$$

where  $y$  is the spanwise coordinate,  $k_0$  the wavenumber,  $c$  the wing chord and  $V_\infty$  the freestream velocity. The downwash velocity is :

$$w(y) = -\frac{k_0cV_\infty}{4} \sum_{j=0}^{\infty} jA_j \cos(jk_0y) + jB_j \sin(jk_0y) \quad (5.3)$$

The circulation is related to the lift coefficient using the Kutta-Joukowski relation :

$$\Gamma(y) = c \frac{V_\infty}{2} C_l(\alpha_{eff}) \quad (5.4)$$

and under the small angle hypothesis :

$$\alpha_{eff}(y) = \alpha + \frac{w(y)}{V_\infty} \quad (5.5)$$

To solve this model one can first assume a distribution for the Fourier coefficients  $A$  and  $B$ . This allows to compute the downwash distribution and the effective angle of attack. In return this gives the circulation by interpolating the lift coefficient  $C_l(\alpha_{eff})$  in a user given polar and applying the Kutta-Joukowski relation. Finally, the new  $A$  and  $B$  coefficients can be obtained by the inverse Fourier transform :

$$A_j = \frac{k_0}{\pi c V_\infty} \int_0^{2\pi/k_0} \Gamma(y) \cos(jk_0y) dy \quad (5.6)$$

$$B_j = \frac{k_0}{\pi c V_\infty} \int_0^{2\pi/k_0} \Gamma(y) \sin(jk_0y) dy \quad (5.7)$$

The model is then iterated up to the point where the solution reaches a steady state. Spalart proposed to apply a Gaussian filter to the inverse Fourier transform so that :

$$A_j = \frac{k_0}{\pi c V_\infty} e^{-(c_f c j k_0)^2} \int_0^{2\pi/k_0} \Gamma(y) \cos(j k_0 y) dy \quad (5.8)$$

$$B_j = \frac{k_0}{\pi c V_\infty} e^{-(c_f c j k_0)^2} \int_0^{2\pi/k_0} \Gamma(y) \sin(j k_0 y) dy \quad (5.9)$$

where  $c_f$  is the filter width. This filter reduces the amplitude of the high wavenumber and has the effect of smoothing out the distribution of the circulation. However, this also means that two values of the circulation and thus of the lift coefficient are obtained simultaneously. The first one is obtained from equation 5.4 with the lift coefficient interpolated in the lift polar and the other is the one obtained from equation 5.2. This will be analyzed in section 5.4.1.

### 5.2.2 Lifting surface model - Vortex Lattice Method

Another approach to solve the Laplace's equation is the vortex Lattice Method (VLM), which is a well-known lifting surface model. This method uses vortex ring elements (Katz and Plotkin, 2001) to model a lifting surface and the velocity induced at a point  $P$  by a segment of a vortex ring is given by the Biot-Savart equation :

$$\vec{q}_{1,2} = \frac{\Gamma}{4\pi} \frac{\vec{r}_1 \times \vec{r}_2}{|\vec{r}_1 \times \vec{r}_2|^2} r_0 \cdot \left( \frac{\vec{r}_1}{|\vec{r}_1|} - \frac{\vec{r}_2}{|\vec{r}_2|} \right) \quad (5.10)$$

The numerical setup is shown in fig. 5.1. The wing is meshed with a structured grid of  $n_i$  by  $n_j$  cells ( $N = n_i \times n_j$  cells) and every line segment of the grid is a vortex segment and the wake is meshed with a vortex ring of infinite length. The model is closed with a boundary condition to impose a velocity tangential to the lifting surface. This result in a linear system of equation of the form :

$$\begin{bmatrix} A_{1,1} & A_{1,2} & \dots & A_{1,N} \\ A_{2,1} & A_{2,2} & \dots & A_{2,N} \\ \vdots & \vdots & \ddots & \vdots \\ A_{N,1} & A_{N,2} & \dots & A_{N,N} \end{bmatrix} \begin{pmatrix} \Gamma_1 \\ \Gamma_2 \\ \vdots \\ \Gamma_N \end{pmatrix} = -\vec{V}_\infty \cdot \vec{n} \quad (5.11)$$

with  $A_{a,b}$  the influence coefficient for the velocity induced on the panel  $a$  by the panel  $b$ . This method is suitable for simulation of finite span wings. In order to eliminate the effect of the wing tip, one can carry the simulations on a very large aspect ratio wing. However, the stall cells have an aspect ratio of the order of the chord length. Hence, meshing a wing of a large aspect ratio with a small spanwise resolution results in a large number of mesh cells. Since the cost of the VLM simulation increases with the square of the number of mesh cells the cost



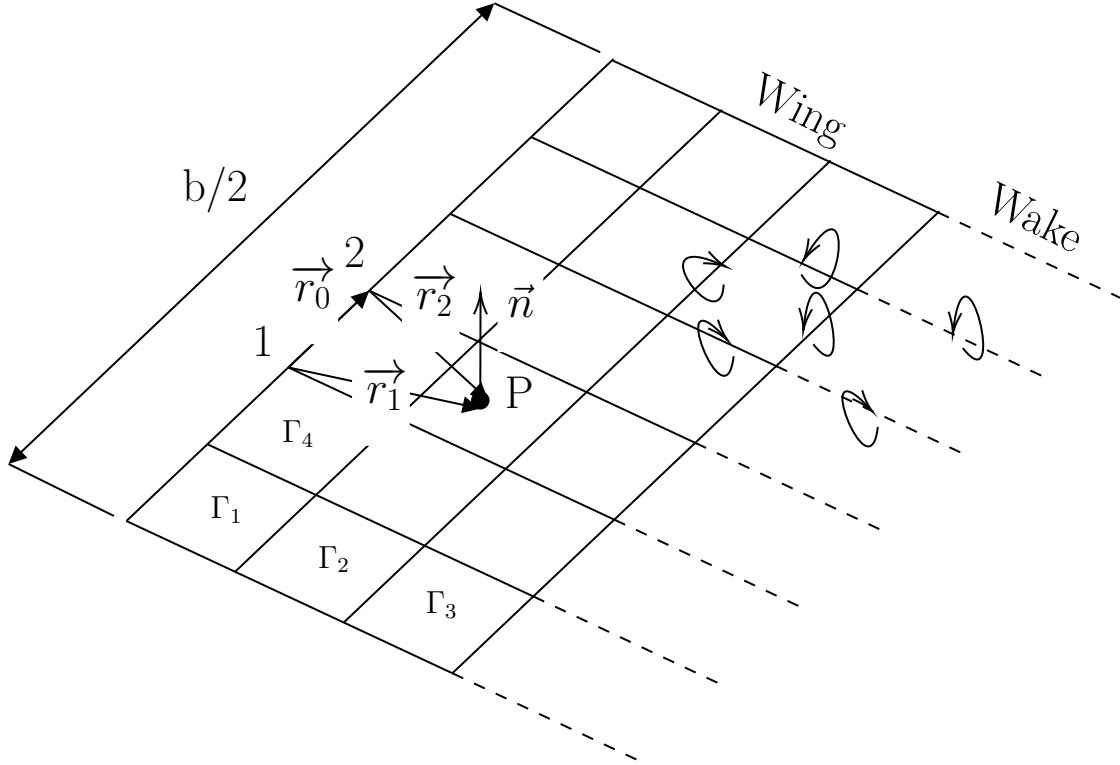


Figure 5.1 – VLM computational setup.

of such simulations can become computationally prohibitive. For this reason, an assumption of periodicity is proposed. To do so, a wing of very large aspect ratio is assumed and the values of  $\Gamma$  are taken to be periodic with a period  $T$  meshed with  $n_j$  spanwise panels. Hence :

$$\Gamma_{(kn_j+j)n_i+i} = \Gamma_{jn_i+i} \quad (5.12)$$

with  $k \in ]-\infty, \infty[$ . This is illustrated in fig. 5.2

Using these assumptions, a modified influence matrix  $\mathbf{A}'$  can be computed with the influence coefficient :

$$A'_{a,b} = \sum_{k=-\infty}^{\infty} A_{a,b+kN} \quad (5.13)$$

Since the influence coefficient is proportional to the inverse of the distance between two panels, in practice the values of  $k$  can be restricted to a finite number of panels. Finally, by assuming that the wing is infinite the  $(kn_j + j)n_i + i$  equations are identical. Hence the problem is restricted to  $N$  equations :

$$\begin{bmatrix} A'_{1,1} & A'_{1,2} & \dots & A'_{1,N} \\ A'_{2,1} & A'_{2,2} & \dots & A'_{2,N} \\ \vdots & \vdots & \ddots & \vdots \\ A'_{N,1} & A'_{N,2} & \dots & A'_{N,N} \end{bmatrix} \begin{pmatrix} \Gamma_1 \\ \Gamma_2 \\ \vdots \\ \Gamma_N \end{pmatrix} + \vec{V}_\infty \cdot \vec{n} = 0 \quad (5.14)$$

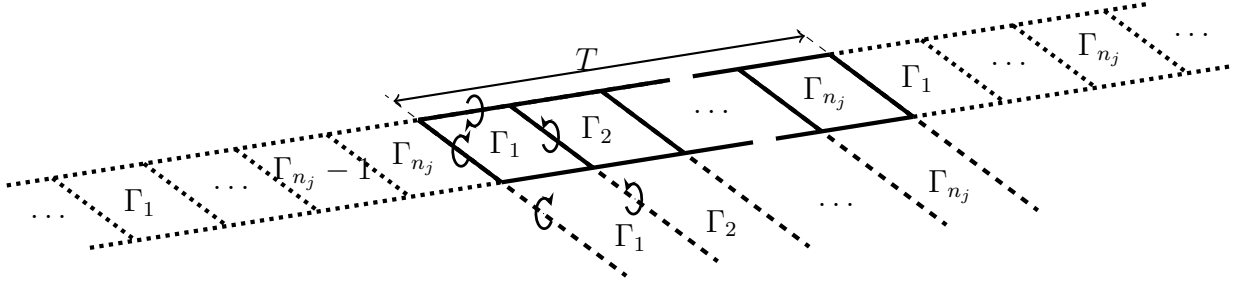


Figure 5.2 – Infinite wing Vortex Lattice Method with periodicity assumption.

To account for viscous and compressibility effects, the Non-Linear Vortex Lattice Method (NL-VLM) (Gallay and Laurendeau, 2015, 2016; Kontogiannis *et al.*, 2019; Parenteau *et al.*, 2018a,b) is used. This method applies a correction to the local angle of attack of the VLM sections in order to get a local lift coefficient  $C_{l_{inv}}$  equal to a two-dimensional lift coefficient  $C_{l_{vis}}$ , which is provided by Reynolds-Averaged Navier-Stokes (RANS), experimental data, or as in this paper by manufactured lift curves. They are called manufactured lift curves because they are given by an analytical formula chosen to present some specific features. The viscous correction concept is illustrated in fig. 5.3. Due to the thin airfoil theory the sectional lift coefficient of the VLM is :

$$C_{l_{inv}} = 2\pi\alpha_{inv} \quad (5.15)$$

$$\alpha_{inv} = \alpha_{3D} + \alpha_i + \Delta\alpha \quad (5.16)$$

with  $\alpha_{3D}$  the geometrical angle of attack,  $\alpha_i$  the induced angle of attack and  $\Delta\alpha$  the viscous correction. The viscous coupling is done for the spanwise grid section  $j$  as :

$$\alpha_{eff,j} = \frac{C_{l_{inv},j}}{2\pi} - \Delta\alpha_j \quad (5.17)$$

$$\Delta\alpha_j = \Delta\alpha_j + \omega \frac{C_{l_{vis}}(\alpha_{eff,j}) - C_{l_{inv},j}}{2\pi} - \mu(\Delta\alpha_{j-1} - 2\Delta\alpha_j + \Delta\alpha_{j+1}) \quad (5.18)$$

with  $\omega$  a relaxation factor and  $\mu$  a dissipation coefficient to smooth the solution.  $C_{l_{vis}}(\alpha_{eff,j})_j$  is the lift coefficient provided by a  $C_l(\alpha)$  curve to correct the VLM. This lift coefficient can vary from one spanwise section to the other. However, for this study, it is assumed to be constant. These two equations are coupled and result in a non-linear system of equations. Hence, the  $\Delta\alpha$  are first initialized at zero for the first solution of the VLM system to get the  $C_{l_{inv}}$  of each section. Then subiterations between the VLM and the coupling are carried out up to the point where  $|C_{l_{vis}} - C_{l_{inv}}| < \epsilon$  with  $\epsilon$  a given tolerance.  $\Delta\alpha$  is added to the VLM as a rotation of the vector  $\vec{n}$  normal to the panel. Thus only the right-hand side of the VLM system of equations is modified during subiterations and the influence matrix is inverted only once. The lift polar provided for the viscous coupling can include the post stall angle of attack, thus allowing to model three-dimensional wings in the post-stall regime.

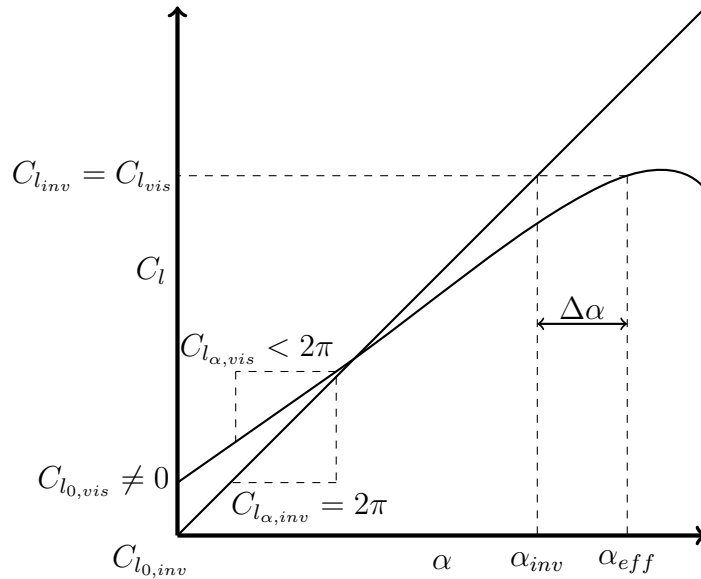


Figure 5.3 – Viscous coupling applied to the VLM model.

### 5.3 Numerical verification

This section provides numerical verification of the VLM method, in particular with respect to the periodicity assumption and the viscous coupling. A classic test case for a VLM code

is the verification that  $C_l = 2\pi\alpha$  for a wing of infinite aspect ratio, which is equivalent to a two-dimensional thin airfoil. The same case with the NL-VLM should return the lift of the user provided viscous lift curve. Hence, simulations are carried out for a wing of the aspect ratio  $1 \times 10^{12}$  with 100 panels in the spanwise direction and one panel in the chordwise direction. No artificial dissipation is used. Fig. 5.4 shows the solution of the VLM and the NL-VLM coupled to the manufactured lift polar proposed by Spalart (2014) :

$$C_l(\alpha) = 2\pi\alpha + 0.5(1.2 - 2\pi\alpha)(1 + \text{erf}((\alpha - 0.28)/0.02)) \quad (5.19)$$

One can observe that the linear VLM correctly reproduces the thin airfoil theory with  $C_l(\alpha) = 2\pi\alpha$ . When this VLM is coupled to a viscous polar, the two-dimensional lift coefficient prescribed by the polar is obtained. Note that the results are matching pre and post-stalls regions.

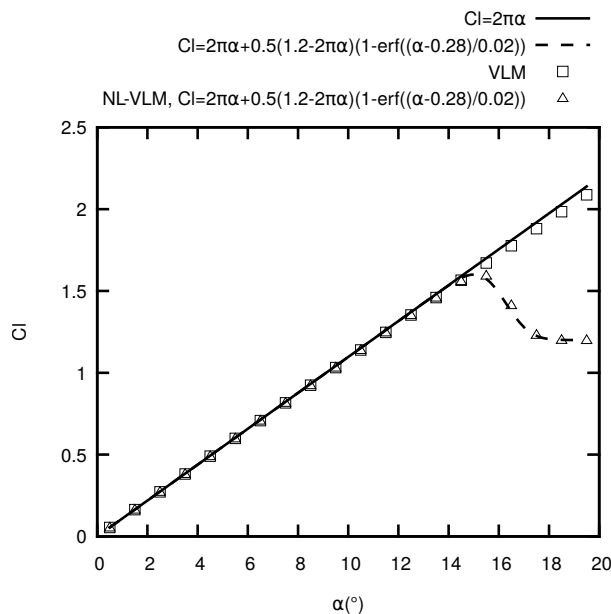


Figure 5.4 – Infinite wing solution of the NL-VLM

Now that the non-linear coupling is verified, the periodicity assumption should be verified, a nontrivial task. To do so, simulations are carried out on wings with a periodic twist distribution of the form :

$$\alpha_t(y) = \alpha_{t0} + \alpha_{t1}\cos(2\pi y/\lambda_t) \quad (5.20)$$

with  $\alpha_t$  the twist,  $\alpha_{t0}$  the mean twist,  $\alpha_{t1}$  the amplitude of the twist modulation and  $\lambda_t$  the twist period. Wings of large aspect ratio with 1 chordwise cell, a spanwise spacing  $\Delta y = 0.1$ ,  $\alpha = 5.0^\circ$ ,  $\alpha_{t0} = 0.0^\circ$ ,  $\alpha_{t1} = 10.0^\circ$  and  $\lambda_t = 5.0$  are computed. Fig. 5.5 shows the lift distribution for wings of aspect ratio 50, 100 and 200. As one can see the solution around  $y/c = 0.0$  is nearly periodic, thus it will be used to verify the computation with the periodicity assumption.

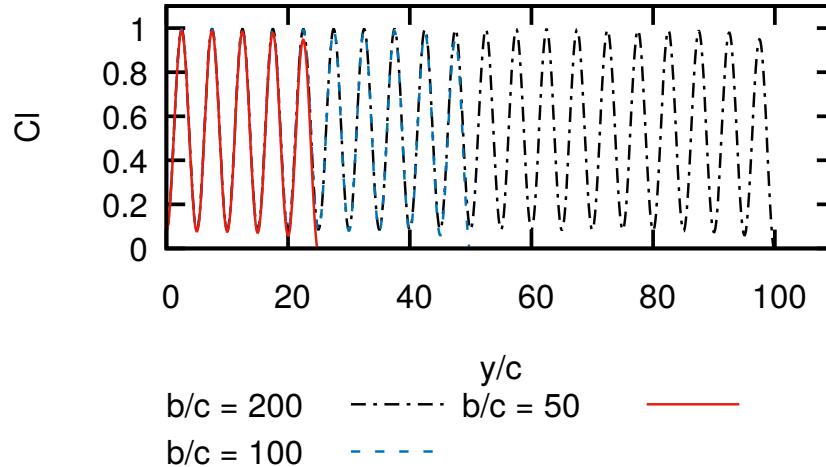


Figure 5.5 – Effect of the span on the lift distribution of wing with periodic twist.

Fig. 5.6 shows the solution of the same problem using the periodicity assumption proposed in this study. The computation is carried out with one ( $b/c = 5$ ) and three ( $b/c = 15$ ) twist periods between the imposed periodicity condition. The spanwise periodic VLM allows to recover the solution of the large aspect ratio wing, at a significantly lower computational cost since only one and three twist periods are meshed. The lift coefficient with 10 chordwise panels is also shown, which does not change the lift coefficient. Fig. 5.7 shows the  $\Gamma$  distribution with 1 and 10 spanwise cells. As one can see, the grid has an effect on the  $\Gamma$  distribution but not on the sectional lift distribution.

In conclusion, the proposed NL-VLM model is able to model infinite wing with an assumption on the periodicity of the solution. This method is also able to take into account viscous effects, including the post-stall regime.

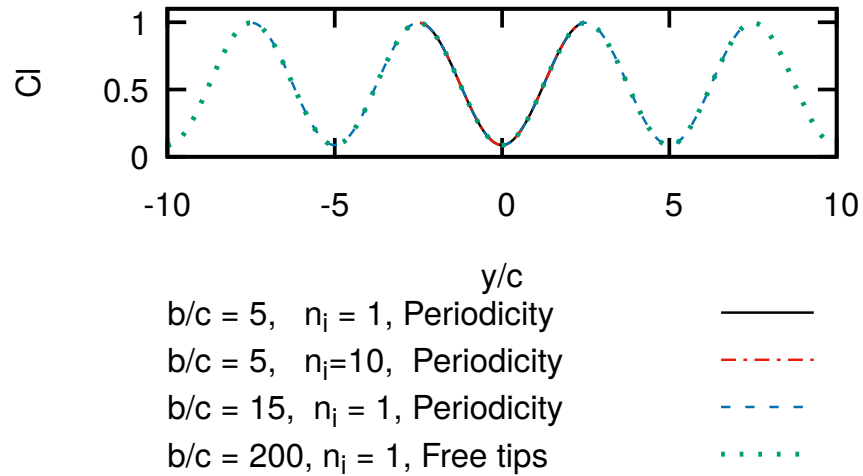


Figure 5.6 – Solution of the wing with periodic twist using the periodicity assumption.

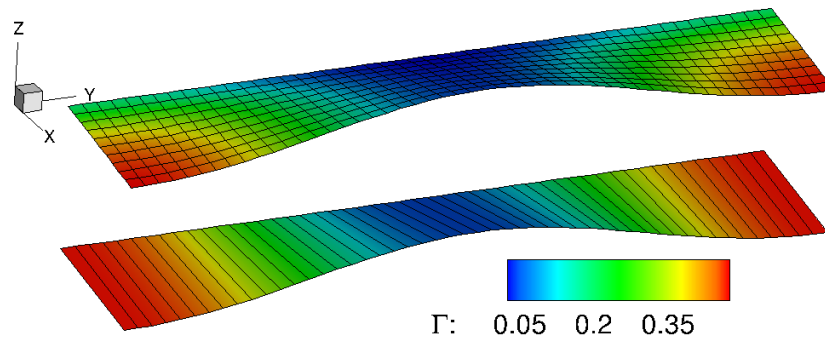


Figure 5.7 –  $\Gamma$  distribution over the periodic wing with 1 and 10 chordwise panels.

## 5.4 Analysis of the lift cell

### 5.4.1 Lifting line - Infinite Wing

This section investigates the infinite wing lifting line model proposed by Spalart (2014). Fig. 5.8 shows the lift coefficient and the effective angle of attack used for interpolation in the lift polar proposed by Spalart (2014). Two curves are shown for the lift coefficient. One is the lift coefficient interpolated from the lift polar at the effective angle of attack, The other is computed from the circulation  $\Gamma$  computed with the smoothed  $A_j$  and  $B_j$  Fourier coefficients. This analysis is done for a wing with a span of 10, at an angle of attack of  $16^\circ$  and with a filter width  $c_f = 0.23$ . A thousand points are used to discretize the wing and 200 terms are kept in the Fourier series. The latter is very large considering the fact that the Gaussian filter reduces the impact of modes with high wavenumbers. As one can see,

the solution of our implementation reproduces the one of Spalart (2014). However, one can observe that the Gaussian filter causes a large deviation of the lift coefficient from the one interpolated inside the lift polar. Nonetheless, the global lift coefficient is the same up to  $10^{-6}$ . Hence the filter reduces the sharp features of the lift distribution with a very small impact on the integrated lift force. One can also observe that the minimum lift coefficient is 1.2, which is the asymptotic value of the manufactured lift polar at high angles of attack. For this reason, the effective angle of attack can reach higher values with no effect on the lift coefficient. The maximal sectional lift coefficient corresponds to interpolation in the lift polar at the maximum lift coefficient angle of attack ( $15^\circ$ ). Hence, with this model the spanwise solution alternates between regions where the lift coefficient is interpolated in the post-stall regime and in the pre-stall regime. The solution is in the stall regime (negative slope of the  $C_l(\alpha)$  curve) only for a narrow band of sections.

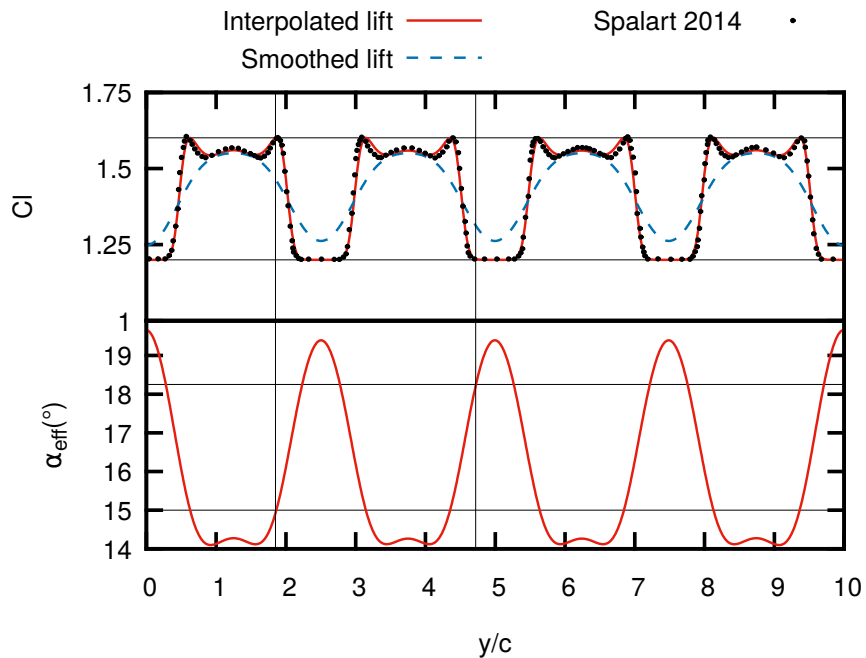


Figure 5.8 – Lift distribution and effective angle of attack of Spalart’s lifting line model.

As stated by Spalart (2014) this model has a bias towards the high wavenumber modes. Hence the Gaussian filter is necessary to obtain a converged solution or the number of modes must be limited. Fig. 5.9 shows the result with several number of Fourier modes and without the Gaussian filter. The lift cell phenomenon is only observed when the number of modes is at least 2. In this case, two cells are obtained. An interesting point is the fact that the number of cells increases with the number of modes and the model bifurcates towards the

highest wavenumber possible. For a higher number of modes the model fails to converge without the Gaussian filter. This figure also shows the fact that lift distribution is smoothed out even though the Gaussian filter is not used. In fact the Fourier Series is unable to closely follow the  $\Gamma$  distribution. Hence, in the iterative process the Fourier series gives a smooth distribution of  $w$ . Then sharp features in the lift distribution are found when interpolating inside the lift polar and fitting a Fourier Series in the  $\Gamma$  results in a smooth distribution.

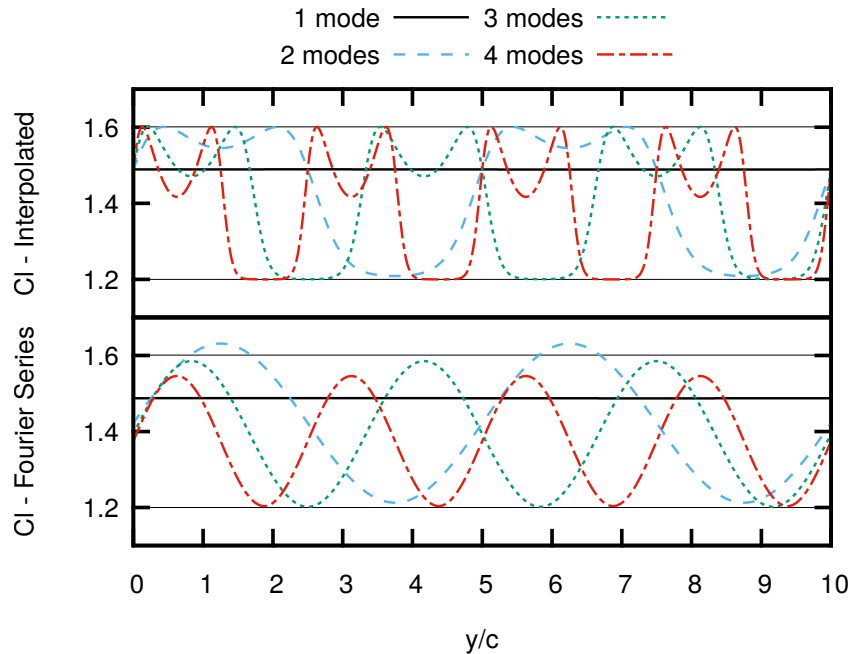


Figure 5.9 – Lift distribution of Spalart's lifting line model without the Gaussian filter.

As mentioned above, the lift coefficient cannot go below 1.2 in the high effective angle of attack range because it is the asymptotic value of the lift distribution. Test with a polar without an asymptotic value shows the fact that the model cannot stabilize to a steady-state solution if the slope of the lift curve remains negative.

#### 5.4.2 Lifting surface - Elliptic wing

To apply the NL-VLM model to a finite wing problem, first the case of a wing with an elliptic chord distribution is investigated. This test case presents the advantage that the downwash should be constant on the wing and thus the effective angle of attack should be constant. This means that the stall should occur at every wing section simultaneously. The elliptic wing is defined with a unitary chord at the root and the aspect ratio  $AR = b^2/S_{ref}$ .



The lift polar used for the viscous coupling is the one given in equation 5.19. Figs. 5.10 and 5.11 shows the effect of the artificial dissipation term on the lift and effective angle of attack distribution respectively. Simulations are done at an angle of attack of  $18^\circ$ . The NL-VLM model is able to converge to a solution in the post-stall regime without adding a dissipation term. However, as one can see in fig. 5.11, the effective angle of attack of some of the sections is unrealistically large. This is explained by the fact that the lift coefficient provided by the polar is constant for angles of attack higher than  $19^\circ$  (this angle of attack as well as the maximum lift coefficient angle are also shown in this graph). Hence, the NL-VLM model can increase the angle of attack correction to impact the linear VLM system of equations without impacting the viscous lift coefficient, which stays constant at 1.2. By comparing fig. 5.10 and fig. 5.11, one can observe that the parts of the lift distribution equal to 1.2 correspond to the sections where the effective angle of attack is greater than  $19^\circ$ . The other sections of the wing have an effective angle of attack lower than  $15^\circ$  (the maximum lift coefficient angle). One can also observe that no wing section has an effective angle of attack in the region where  $C_{l_\alpha}$  is negative. This means that the parts of fig. 5.10 where the lift coefficient is between 1.2 and 1.6 are in fact not stalled in the lift polar. This seems to indicate that the NL-VLM model does not allow a wing section to see a negative  $C_{l_\alpha}$ . Since an elliptic wing is considered, for which the whole wing stalls together, the NL-VLM forces some section to get un-stalled and other to be fully stalled.

Even though a solution can be obtained without the artificial viscosity term, this term smooth out the sharp discontinuity in the effective angle of attack distribution. The main effect of the smoothing is observed in fig. 5.11 where the very large effective local angles of attack decrease. As such the smoothing allows to correct the unrealistic effective angle of attack. As is the case for the lifting line model of Spalart (2014), adding this dissipation term creates two spanwise lift distributions. The first one is computed in the VLM system and the second one is the lift coefficient interpolated at the effective angle of attack. This is shown in fig. 5.12. Without the dissipation, the two ways of computing the lift coefficient return the same result. However when adding the dissipation, lift distributions with peaks similar to the one of Spalart (2014) are obtained. It is interesting to note that artificial dissipation was added by Chattot (2004) as a numerical artefact to stabilize the  $\Gamma$  coupling algorithm without knowing its effect on the stabilization of the physical properties of the flow.

Fig. 5.13 shows the distribution of the circulation  $\Gamma$  on wings at several angles of attack using an artificial dissipation with  $\mu = 0.2$ . The wing is in the pre-stall regime for the angle of attack of  $17^\circ$  because the downwash causes the wing to be at a constant effective angle of

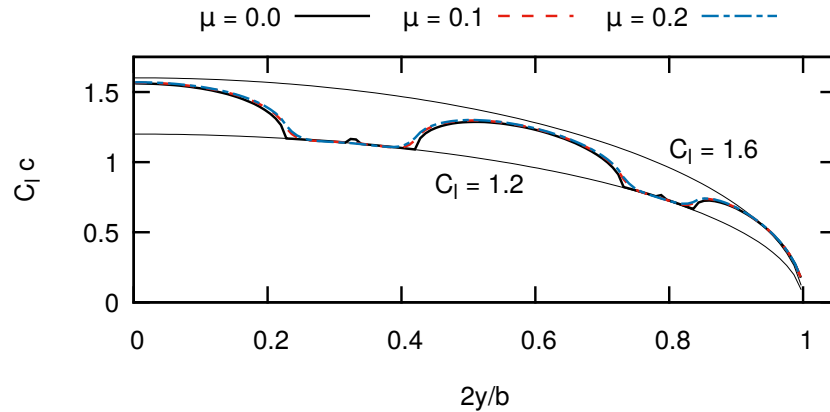


Figure 5.10 – Effect of the dissipation coefficient  $\mu$  on the lift distribution (elliptic wing,  $AR = 16.0$ ,  $\alpha = 18^\circ$ ).

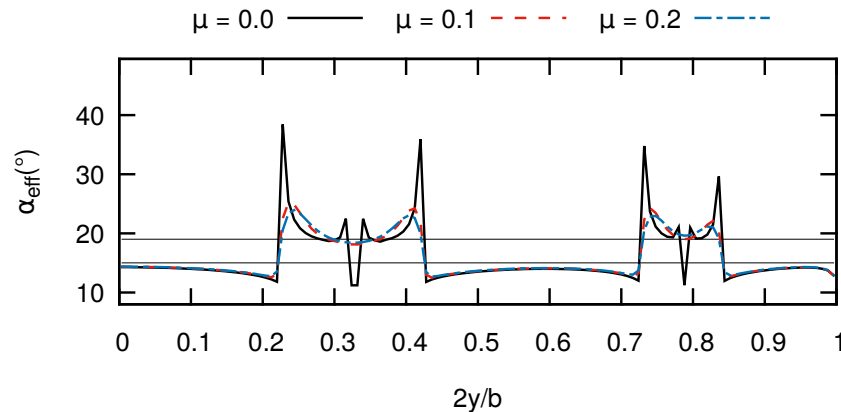


Figure 5.11 – Effect of the dissipation coefficient  $\mu$  on the effective angle of attack (elliptic wing,  $AR = 16.0$ ,  $\alpha = 18^\circ$ ).

attack lower than  $15^\circ$ . One can observe the cellular patterns in the solution for the angle of attack of  $18^\circ$  and  $19^\circ$ . For the angle of attack of  $20^\circ$ , the cells no longer occur because the wing is completely stalled. Fig. 5.14 shows the distribution of the lift coefficient multiplied by the local chords for several aspect ratios and geometrical angle of attacks. The lift coefficient is multiplied by the local chord to highlight the elliptic distribution of the lift force. As one can see, the elliptic lift distribution is obtained for low aspect ratio and low angles of attack. For the other aspect ratios, lift cells are observed. This is caused by the fact that the downwash is constant along the span and stronger for the lower aspect ratio. Thus, the wings with a lower aspect ratio reach the stall condition at a higher angle of attack. Two curves are used to highlight the boundaries of the region of the local lift polar where  $C_{l_\alpha}$  is negative ( $C_l = 1.2$  and  $C_l = 1.6$ ). As soon as the effective angle of attack becomes higher

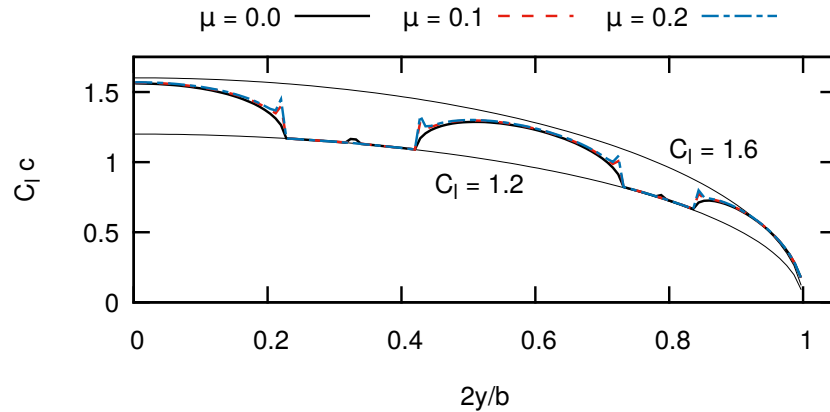


Figure 5.12 – Effect of the dissipation coefficient  $\mu$  on the lift coefficient interpolated at the effective angle of attack (elliptic wing,  $AR = 16.0$ ,  $\alpha = 18^\circ$ ).

than the maximum lift coefficient angle, lift cells occur. Also, the number of cells increases with the aspect ratio. When the wings of aspect ratios 16 and 20 reach the stall conditions they respectively have 3 and 4 lift cells. Hence, the variation of the number of cells appears to increase linearly with the aspect ratio for angles of attack slightly past the maximum lift coefficient angle. As the angle of attack is further increased the lift cells break down into smaller cells, up to the point where the wing is fully stalled and  $C_{lc} = 1.2$  (the asymptotic value of the manufactured lift polar) for the entire wing.

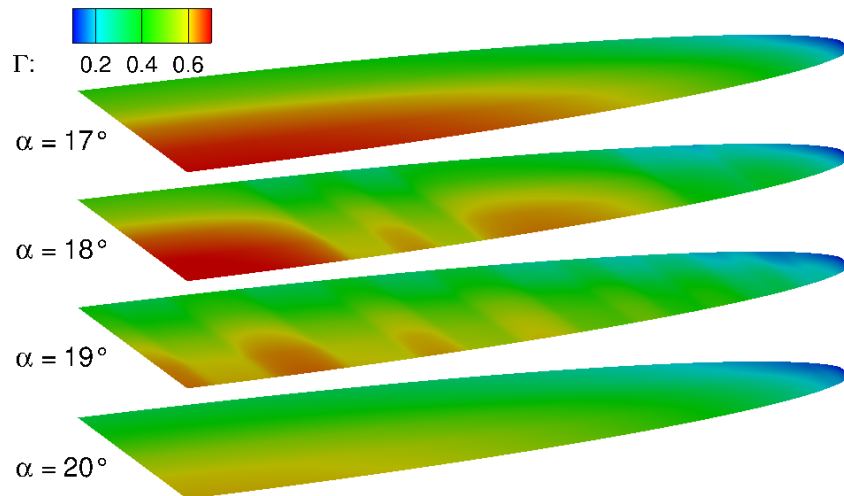


Figure 5.13 –  $\Gamma$  distribution at several angle of attack (elliptic wing,  $AR = 16.0$ ).

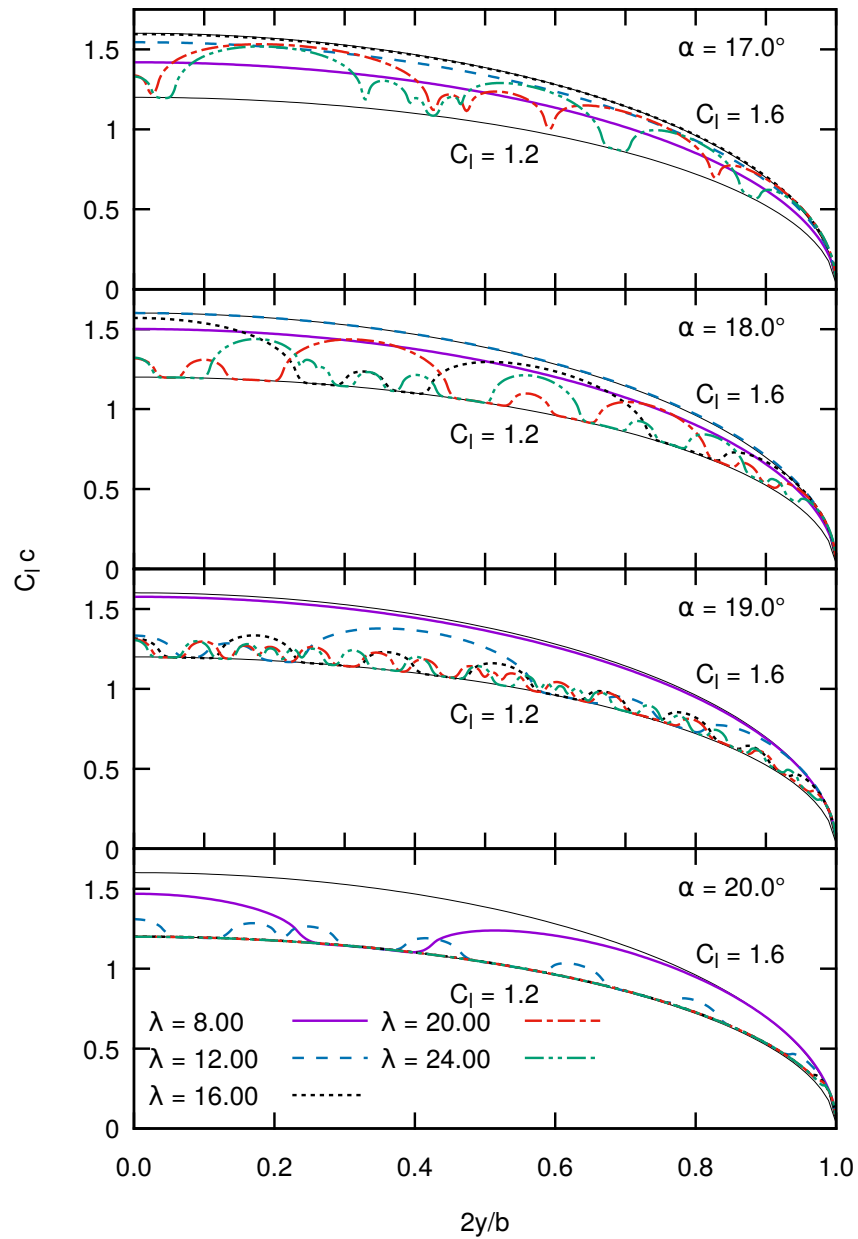


Figure 5.14 – Lift coefficient distribution of several aspect ratios at several angles of attack (elliptic wing).

The lift polar is another variable in the NL-VLM model. To characterize this effect, one can design a series of lift polar with different post-stall behavior based on the formulation of Spalart (2014) :

$$C_l(\alpha) = C_{l0} + C_{l\alpha,0}\alpha + 0.5(C_{l0} - C_{l\alpha,1}\alpha)(1 + \text{erf}((\alpha - \alpha_0)/\alpha_1)) \quad (5.21)$$

with the parameters given in Table 5.1. Fig. 5.15 shows these lift polars. The polar 2 is designed to remove the asymptotic behavior of the lift original polar from Spalart (2014) (polar 1). The polar 3 is selected to increase the negative slope of the lift polar, while the polars 4 and 5 decrease this slope.

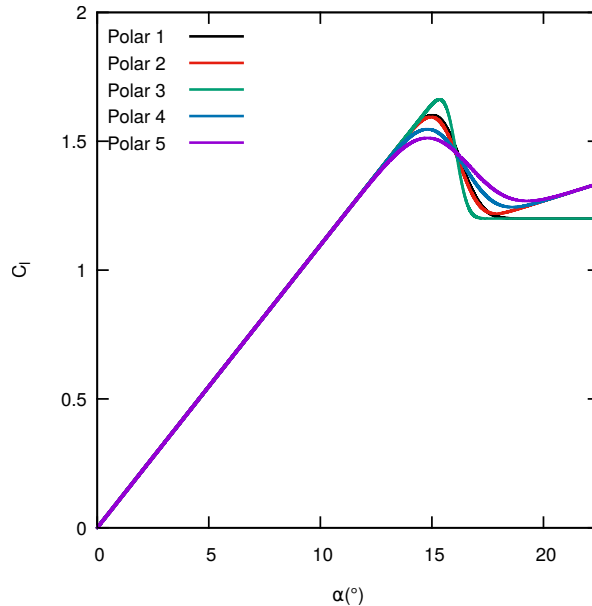


Figure 5.15 – Selection of manufactured lift curves.

Figs. 5.16 and 5.17 show the lift coefficient and the effective angle of attack computed with this selection of lift polars. In every case the grid is refined in both topological directions to obtain a grid independent solution and the size of the mesh changes from one case to the other. As one can see by comparing the solutions with the polar 1 and 2, adding a positive slope as the angle of attack goes to infinity helps to remove the non-physically large effective angle of attacks, which is an effect similar to adding the artificial dissipation. However, this does not change the number of lift cells and significantly affect the amplitude of the latter.

Table 5.1 – Parameters of the lift polar.

Polar	$C_{l0}$	$\alpha_0$	$\alpha_1$	$C_{l\alpha,0}$	$C_{l\alpha,1}$
Polar 1	1.20	0.28	0.02	$2\pi$	$2.0\pi$
Polar 2	0.72	0.28	0.02	$2\pi$	$1.5\pi$
Polar 3	0.72	0.28	0.01	$2\pi$	$1.5\pi$
Polar 4	0.72	0.28	0.03	$2\pi$	$1.5\pi$
Polar 5	0.72	0.28	0.04	$2\pi$	$1.5\pi$

This further emphasizes the fact that having  $C_{l_\alpha} = 0$  causes the viscous correction and the VLM system of equation to become decoupled. On the other end, changing the slope of the lift polar in the post stall regime significantly changes the number of cells. Decreasing this slope increases the number of cells, while increasing it decreases the number of cells. The criterion found by Gross *et al.* (2015) predicts that the wavelength of the cells increases with the norm of the lift slope, if the latter is negative. This tendency is the same as the one observed here. Another interesting point is the fact that a typical leading edge stall will exhibit a sharp reduction of the lift coefficient for angles of attack just past the maximum lift angle. This could be assimilated to an infinite slope which will result in very large stall cell wavelengths. Moreover, the range of angles of attack for which the stall cells are observed requires the effective angle of attack to be in the negative  $C_{l_\alpha}$  area. This region of the lift curve becomes smaller as the lift slope is increased. If this region becomes infinitely small, the elliptic wing will jump from the pre-stall regime to the post-stall one without the occurrence of the stall cells phenomenon. This can explain the fact that the stall cells are usually observed for wings with a trailing edge type of stall which is characterized by lift curves similar to the one used in this paper, as reported by Broeren and Bragg (2001).

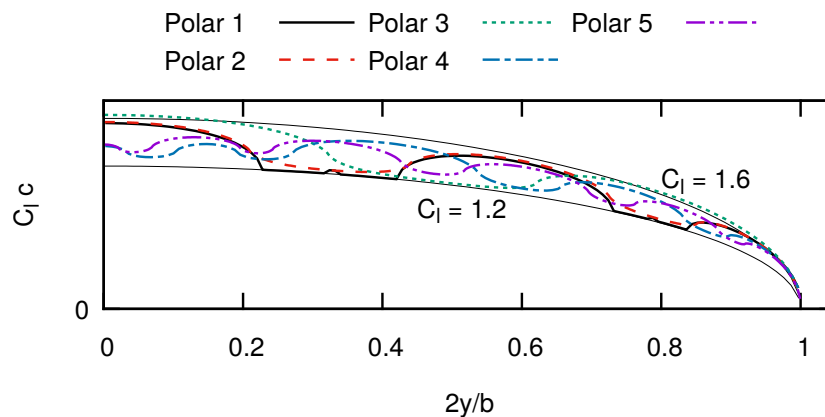


Figure 5.16 – Effect of the lift polar on the lift distribution (elliptic wing,  $AR = 16.0$ ,  $\alpha = 18^\circ$ ).

### 5.4.3 Lifting surface - Rectangular wing

Rectangular wings with free tips were studied by Winkelmann and Barlow (1980) with a Clark Y airfoil section. To compare with them, the case of a rectangular wing is now studied with the lift polar 5 of the previous section. The simulations are done with a symmetry plane, 8 cells in the chordwise direction and a spanwise grid spacing of  $0.025c$ . Fig. 5.18 shows the solution at an angle of attack of  $20^\circ$  for aspect ratio of 3, 6, 9 and 12. As observed

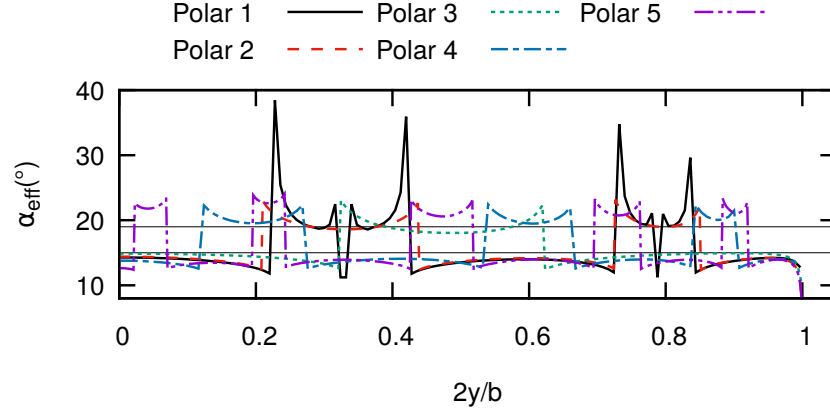


Figure 5.17 – Effect of the lift polar on the effective angle of attack (elliptic wing,  $AR = 16.0$ ,  $\alpha = 18^\circ$ ).

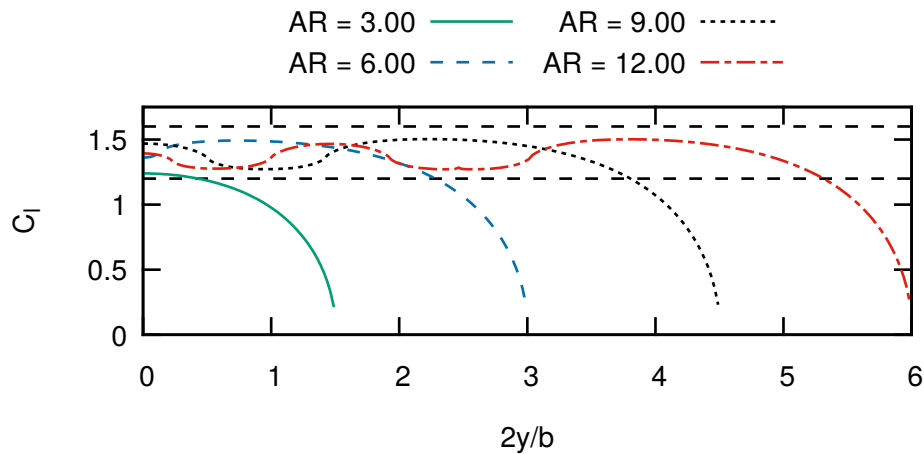
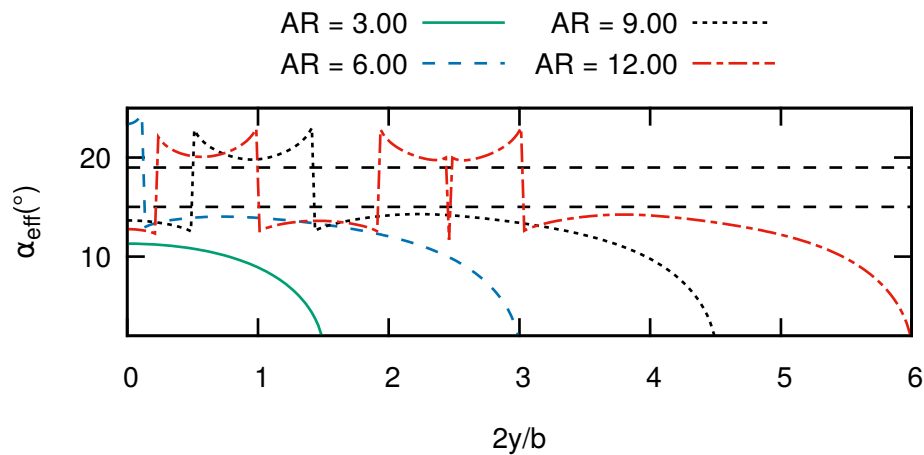
by Winkelmann and Barlow (1980) the number of lift cells is proportional to the aspect ratio of the wing. However, the aspect ratio of 3 is small for a Vortex Lattice Method and no cells are observed. For the other aspect ratio the number of cells is lower than the one observed by Winkelmann and Barlow (1980), who clearly had 2 cells for an aspect ratio of 6, while only one is observed here. This discrepancy can be explained by the lift polar used in the NL-VLM. For this reason, a new lift polar is designed to reproduce the experimental lift polar of the Clark Y airfoil at a Reynolds number of 400 000 (Lyon *et al.*, 1997). The parameter of the manufactured lift polar are selected to reproduce the  $C_{l_{max}}$  and early post-stall behavior. The lift polar is extended and a positive slope is added in the high angle of attack range, to get a better conditioning of the NL-VLM. The new lift curve is (polar 6) :

$$C_l(\alpha) = 0.35 + 1.8\pi\alpha + 0.5(0.18 - 1.6\pi\alpha)(1 + \text{erf}((\alpha - 0.28)/0.15)) \quad (5.22)$$

This lift curve is shown in fig. 5.20 and the spanload of the rectangular wings at an angle of attack of  $18.4^\circ$  (the same as in the experiments of Winkelmann and Barlow (1980)) is shown in fig. 5.21. The number of cells is reported in Table 5.2. The values obtained with this new polar are closer to the experimental one. This confirms that the lift polar is the main parameter which has an influence on the solution of the NL-VLM and that the phenomenon observed in the experiment is linked to an instability present in an inviscid model.

Table 5.2 – Number of stall cells compared to the experiments.

$AR$	Winkelmann and Barlow (1980)	Polar 5	Polar 6
3	1	0	0
6	2	1	2
9	3 to 5	2	5
12	5 to 6	4	7

Figure 5.18 – Effect of the aspect ratio on the lift coefficient distribution (rectangular wing,  $\alpha = 20^\circ$ , polar 5).Figure 5.19 – Effect of the aspect ratio on the effective angles of attack (rectangular wing,  $\alpha = 20^\circ$ , polar 5).



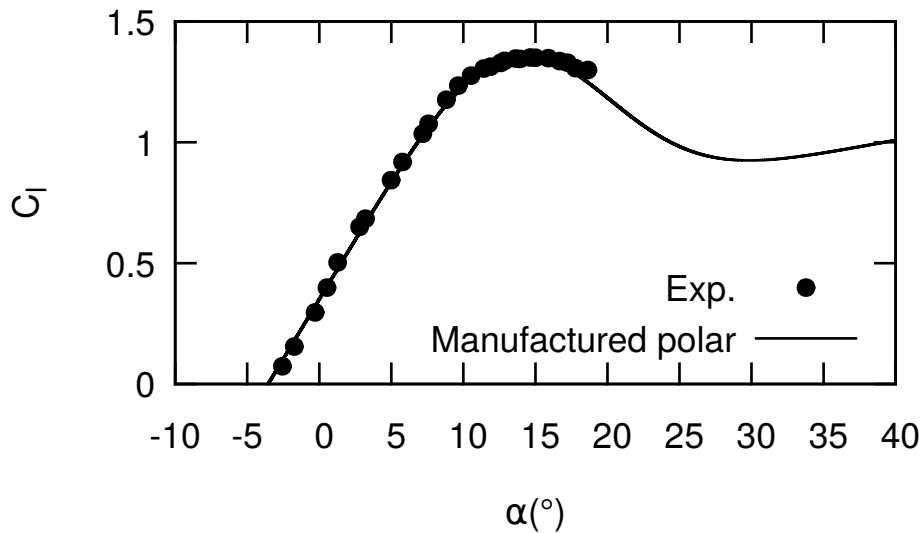


Figure 5.20 – Manufactured lift curve for the Clark Y airfoil based on the experiments (Lyon *et al.*, 1997).

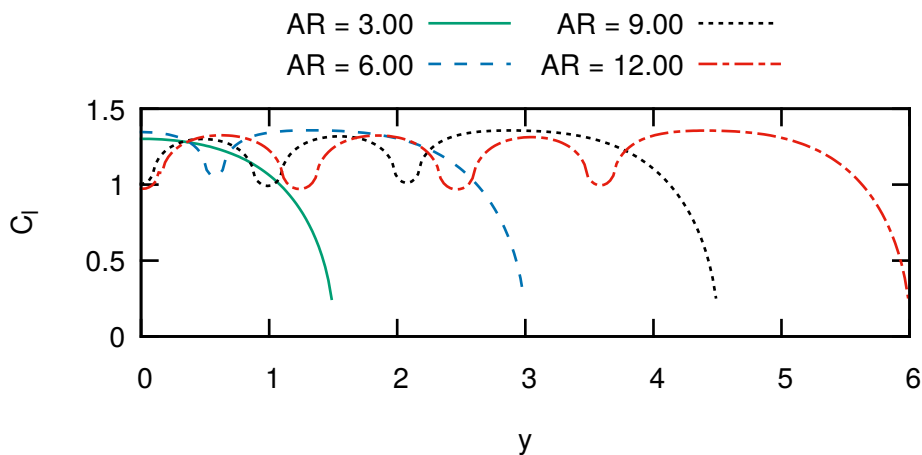


Figure 5.21 – Effect of the aspect ratio on the lift coefficient with the experimental lift curve (rectangular wing,  $\alpha = 18.4^\circ$ , polar 6).

#### 5.4.4 Lifting surface - Infinite wing

Finally, the solution of the lifting surface model with the hypothesis of periodicity in the spanwise direction is investigated. Fig. 5.22 shows the effect of the angle of attack on the solution for a meshed domain of a span of 2. This figure shows the solution with a mesh of 101 by 1 cells and the influence matrix is built using 300 periods on both sides of the simulated domain. The lift polar 5 of Table 5.1 is used. This case reproduces an infinite

wing. Hence, as long as the solution stays two-dimensional the induced angle of attack is zero and the wing will stall at the same angle of attack as the one of the prescribed lift polar. As one can see, the solutions of fig. 5.22 are two-dimensional for angles of attack below the stall angle ( $15^\circ$ ) and at very high angles of attack (greater than  $19^\circ$ ). In both conditions  $C_{l_\alpha} > 0$ . For angles of attack between these two values, stall cells occur. Hence, the stall cells occur in cases where  $C_{l_\alpha} < 0$ . However, the solution is not periodic within the computational domain. This is explained by the fact that the periodicity assumption is only imposed between the two edges of the computational domain. Thus, the interior of the domain remains free. Moreover, multiple solutions cannot be ruled out. Fig. 5.23 shows the effective angle distribution for these cases. As was observed previously, there is no section with an effective angle of attack where  $C_{l_\alpha}$  is negative. The polar used has a positive slope as the angle of attack goes to infinity. For this reason, the effective angle of attack remains in a realistic range.

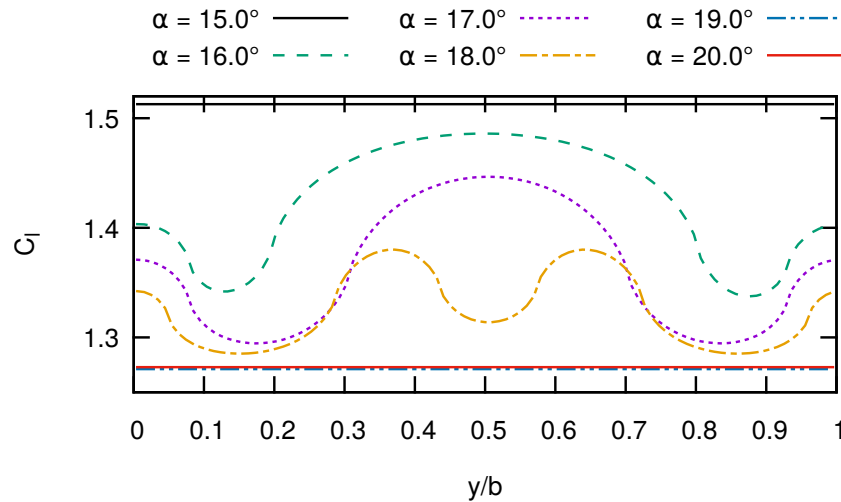


Figure 5.22 – Effect of the angle of attack on the lift distribution (infinite wing,  $AR = 2.0$ ).

A free parameter of the model is the number of periods considered in the infinite wing assumption. The greater this number, the smaller are the influence coefficients which are neglected in the infinite wing assumption. Fig. 5.24 shows the effect of this parameter for the same case. One can observe that the number of periods must be greater than 100 to remove the truncation effect, and a constant solution is obtained if one refines this parameter. A study of the mesh refinement in the spanwise direction has been carried out, with no significant variation on the solution.

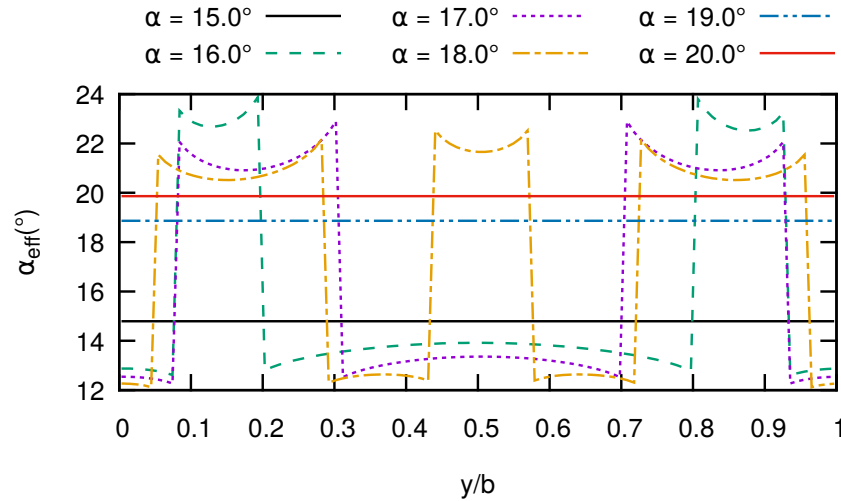


Figure 5.23 – Effect of the angle of attack on the sectional effective angle distribution (infinite wing,  $AR = 2.0$ ).

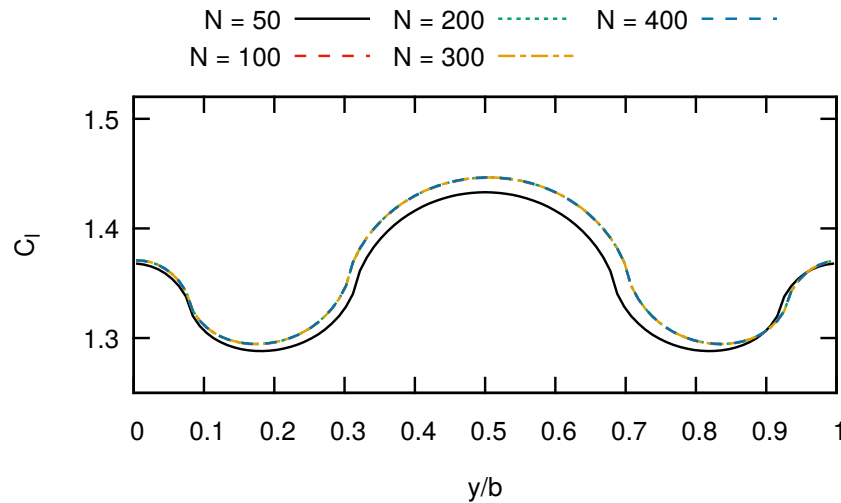


Figure 5.24 – Effect of the number of spanwise period on the lift distribution (infinite wing,  $AR = 2.0$ ).

One can now study the effect of the size of the computational domain on the lift cells. To do so, the span of the domain is increased and the number of grid cells is increased to keep the size of the grid cells constant. The number of periodicity is adapted to keep the neglected influence coefficients at a distance of  $600c$ . This criterion is selected because the influence coefficients decay with the distance and using a constant number of periodicity would result in a large computational cost for the larger mesh. Fig. 5.25 shows the effect of the aspect ratio. As expected the number of lift cells increases with the aspect ratio. This relation is

linear. However, when the aspect ratio is high, the solution becomes noisy in the middle of the computational domain. This effect remains unexplained.

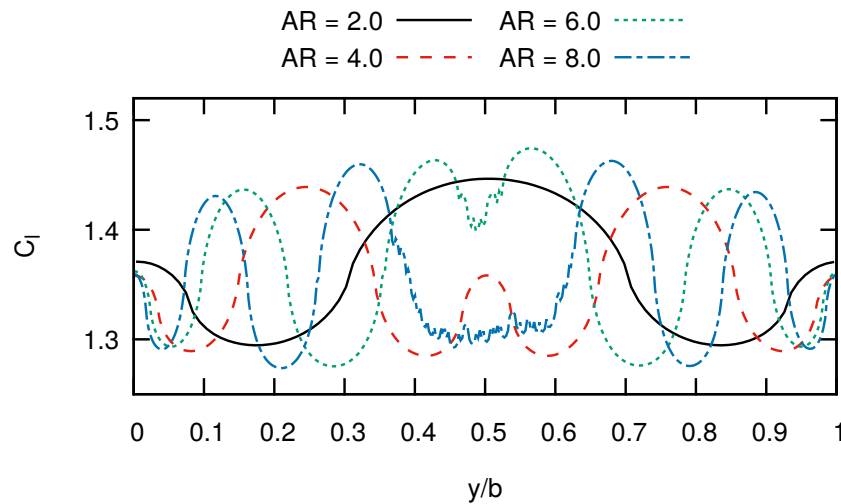


Figure 5.25 – Effect of the aspect ratio on the lift distribution of infinite wings.

Finally, one can add the artificial viscosity term. This effect is shown in fig. 5.26 and 5.27. As it was the case for the finite wing, this parameter has the effect of smoothing out the effective angle of attack and the lift distribution but the solution remains similar.

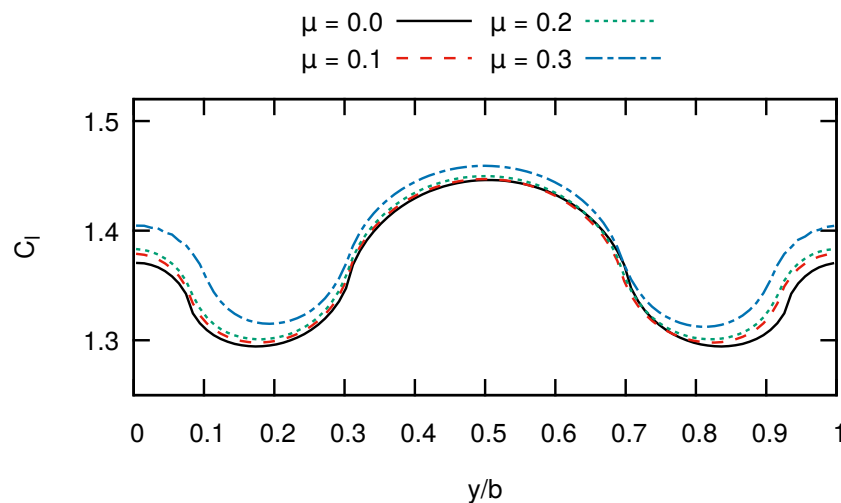


Figure 5.26 – Effect of the artificial dissipation on the lift distribution (infinite wing,  $AR = 2.0$ ).

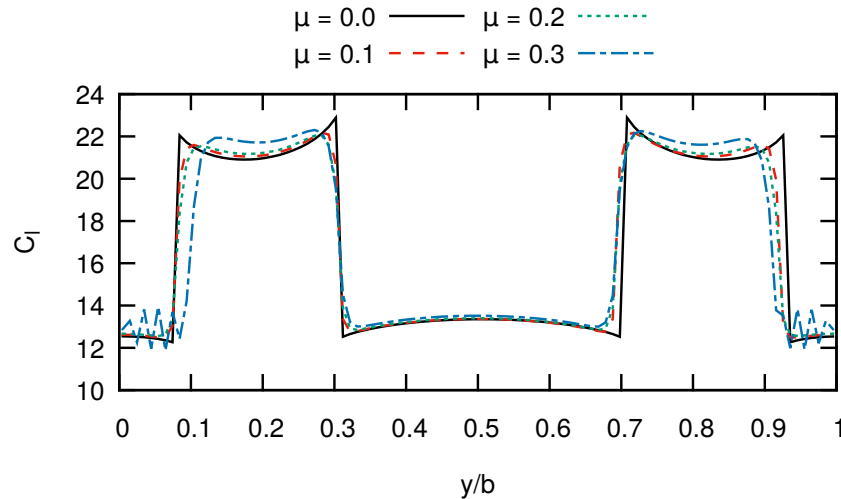


Figure 5.27 – Effect of the artificial dissipation on the effective angle distribution (infinite wing,  $AR = 2.0$ ).

## 5.5 Conclusion

A lifting surface model is applied towards the study of stall cells, thereby extending the lifting line model of Spalart (2014). To this end, the non-linear Vortex Lattice Method proposed by Gallay and Laurendeau (2015) is used. Contrary to the model of Spalart, this model does not use a spectral transformation so that solutions can be non-periodic within the bound of the computational domain. This lifting surface model uses an  $\alpha$ -based coupling with a lift polar to include viscous and compressibility effects and an artificial viscosity is added to smooth out discontinuity in the solution. The NL-VLM model is first verified and characterized for canonical cases. In particular, the paper introduces a mathematical modification to compute infinite wings by including a periodicity condition. This allows to simulate infinite wings with a spanwise grid refinement sufficient to simulate phenomenon with a size of the order of the chord length. The case of elliptic, rectangular and infinite wings in the post-stall regimes were analyzed. For all these cases, an instability is observed as soon as the slope of the lift versus angle of attack relation is negative. This behavior is expected from the analysis presented by Spalart (2014) and Gross *et al.* (2015). Contrary to the model of Spalart, which requires the use of a smoothing factor to obtain a converged solution, the NL-VLM converges to a solution without adding the artificial dissipation. Adding this term smooths out the solution, but does not change the number of stall cells. Another observation is the fact that adding a dissipation to the NL-VLM model results in two lift distributions. The first one being the one of the viscous coupling and the other the one of the inviscid

model. Without dissipation, these two lifts are the same. A similar behavior is observed with the model of Spalart. Finally, solutions are in qualitative agreement to the results of Winkelmann and Barlow (1980) on a rectangular wing without the need of adding any particular filter. The lifting surface model allows to include parameters like the sweep angle, taper ratio and twist. As such, this model provides a low-cost model for the prediction of the wavelength of the stall cells, which could be used in wing design.

### **Acknowledgment**

This work is financially supported by the Natural Sciences and Engineering Research Council of Canada (NSERC), the Canada Research chair Programs and Office National d'Études et de Recherches Aérospatiales (ONERA).

## CHAPTER 6 GENERAL DISCUSSION

Stall cells and buffet cells have been studied using several level of approximation from a high-fidelity hybrid RANS/LES model (ZDES) to an inviscid model with viscous correction (NL-VLM). The bulk of the results have been produced using Unsteady-Reynolds Averaged Navier-Stokes simulations (URANS) and global stability analyses, a method relying on a linearization of the flow around fixed points of the Reynolds Averaged Navier-Stokes (RANS) equations. The analyses have been done for infinite swept/unswept wings to exclude any three-dimensional effects coming from the geometry or the boundary conditions. The first part of the thesis uses unsteady numerical simulations to characterize the three-dimensional buffet and the stall cells. The second part uses global stability analyses and a reduced order model to propose explanations for both phenomena.

By carrying URANS (chapter 2) and ZDES (chapter 3) simulations on infinite swept wing configurations, one observes stall cells or buffet cells. In their study of so-called infinite swept wings, Iovnovich and Raveh (2015) obtained buffet cells. However, the computational domain was closed by a symmetry plane at the root of the wing and an extrapolation at the tip of the wing. This caused the presence of a  $\lambda$  shock near the root and the buffet cells looked as if they were generated at the tip of this  $\lambda$  shock. In the present study, the periodicity condition is closer to an infinite configuration. Thus no  $\lambda$  shock is present and the buffet cells are still observed. Hence, one must exclude the effect of the geometry as the root cause for this phenomenon. A similar phenomenon is observed at low speed in stall conditions.

The URANS simulations allow to characterize the effect of the sweep angle on the buffet/stall cells. It is found that the sweep angle has a minor effect on the wavelength of the cells. The exception is the unswept wing case where a higher number of cells is observed. On the other hand, the sweep angle has a strong effect on the frequency of the unsteady phenomenon. It is observed that the buffet and stall cells are convected in the spanwise direction when the wing is swept. For both phenomena the convection speed of the cells is proportional to the sweep angle. As such, the convection speed is null for the unswept wings. In the case of the subsonic stall, this results in steady stall cells and RANS simulations are converged within machine accuracy. In the transonic buffet case, an unsteady behavior is still observed in the form of a chordwise oscillation of the shock wave position. This oscillation of the shock wave position is observed for every sweep angle and its frequency is constant and can be linked to a two-dimensional instability. Finally, the frequency induced by the convection

of stall/buffet cells increases with the sweep angle since the convection speed increases.

One should note that the configurations in the numerical simulations are not truly infinite. In fact, the periodicity condition imposes a constraint on the solution inside the domain. Only wavelengths which are harmonics of the span of the computational domain can be observed. For this reason a parametric study on the span of the domain has been carried out at a constant sweep angle of 20 deg. The wavelength increases with the span of the wing, up to the point where another buffet cells can be formed and the wavelength is sharply reduced. This behavior is expected. However, it is not linear since the transition between 2 and 3 cells occurs when the aspect ratio is still lower than the largest wavelength with a single cell. A similar trend is shown in the results of fully converged steady solutions at a sweep angle of zero degree of He and Timme (2020a). The possibility of such solutions is hinted in chapter 4, based on the stability analyses. However, their existence was later proved by He and Timme (2020a). Their results also show a non-linear relation between the wing aspect ratio and the wavelength of the cells. This non-linear relation could be related to multiple flow solutions like the ones found by Kamenetskiy *et al.* (2014). In the case of the subsonic stall a simulation of the unswept wing with a span of 6 and 12 resulted in 4 and 8 cells respectively. This indicates that there is a preferential wavelength to the stall cells. However, a computation with a very large aspect ratio would be necessary to approach a real infinite wing.

As explained above, the convection of buffet cells induces a frequency which increases with the sweep angle. This is consistent with the observation in the literature of perturbations traveling in the spanwise direction for three-dimensional buffet over finite wings. This phenomenon is linked to the observation of a higher buffet frequency in 3-D than in 2-D. However, these studies were all carried out on wings typical of transport aircraft with a sweep angle higher than 25 degrees. The present study shows that the three-dimensional frequency could be lower than the two-dimensional one if the wing is swept at a lower angle. This is corroborated by the recent results of He and Timme (2020a) where fully converged steady RANS simulations of buffet cells were obtained. This has limited application since transonic aircraft have highly swept wings. Nevertheless it seems that the description of the 2-D buffet as a well-defined low frequency phenomenon and the 3-D one as a higher frequency broadband unsteadiness is somewhat inaccurate. In the present study, two dominant unsteady features are observed in the URANS simulations. The first one is the convection of buffet cells and the second one is a chordwise oscillation of the shock wave position at a constant frequency with respect to the sweep angle. This frequency is in the range expected



of the two-dimensional buffet phenomenon. This indicates that the two-dimensional and three-dimensional buffets have different origins. Moreover, in the theoretical infinite unswept wing case, the three-dimensional buffet can be steady. Hence, calling this phenomenon three-dimensional buffet is contrary to the definition of buffet as an unsteady phenomenon. For this reason the three-dimensional buffet could be more precisely defined as an instability akin to the stall cells. However, the URANS simulations do not explain the broadband spectrum observed numerically and experimentally for three-dimensional finite swept wings. The simplicity of the infinite swept wings could explain the well-defined frequency observed in the present study. The turbulent fluctuations, not present in the URANS simulations, could also be an explanation for the broadband spectrum. However, the ZDES simulation presented in chapter 3 is in qualitative agreement with the URANS ones. It exhibits a well-marked peak which can be associated with the convection of the buffet cells. Hence the resolution of turbulent fluctuations does not significantly change the unsteady behavior, with the exception of a high frequency which is probably linked to a Kelvin-Helmholtz instability. However, a ZDES simulation with a longer signal and a closer agreement to the experiments could be invaluable.

Following the unsteady numerical simulations, global stability analyses are used (chapter 4) to study the buffet and stall cells. These analyses show unstable three-dimensional modes which are responsible for the transition from spanwise invariant solutions (with or without a sweep angle) to three-dimensional ones with periodic flow structures in the spanwise direction. The stability analyses allow to identify the shape, growth rate and frequency of the modes in the linear regime. For the case of the stall cells over the NACA4412 airfoil, the stability analyses predict correctly the wavelength and the frequency of the stall cells. In the case of the transonic buffet, the linearly unstable mode has a smaller wavelength than the one observed in the non-linear URANS simulations in the saturated regime. However, the frequency is consistent with flow structures convected at the same velocity as the one in the URANS simulations. For this reason the stall cells and buffet cells can be linked to a global unstable mode. Moreover, the onset of this mode for the buffet and stall test case corresponds to the angle of attack for which the slope of the lift against the angle of attack becomes negative.

URANS simulations with the initial condition set as the steady base-flows of the stability analyses have been carried out. These simulations are consistent with the stability analyses results. In the case of the subsonic stall on the unswept wing, the flow becomes three-dimensional with the wavelength predicted by the stability analyses and settles to a steady solution with the same wavelength in the saturated regime. For the transonic buffet, the

flow becomes three-dimensional with the number of cells predicted by the stability analyses. However, the number of cells changes between the linear and the non-linear regime. Hence, the stability analysis predicts the initial bifurcation from the steady spanwise invariant flow to a three-dimensional state. However, the modification in the wavelength following the initial transition to a three-dimensional flow remains to be explained.

To further emphasize the similarity between stall cells and buffet cells, stability analyses of a set of base-flows on a NACA0012 airfoil at a high Reynolds number of 10 million and with Mach numbers varying from 0.2 to 0.72 were carried out. In these analyses an unstable three-dimensional mode was found for every Mach number. Moreover, a constant wavenumber normalized by the separation height was found across these unstable modes. This suggests that there is a relation between the size of the flow separation and the wavelength of the unstable mode which further supports the hypothesis that stall cells and buffet cells are akin to one another.

At last, the explanation of the stall cells based on the lifting line theory by Spalart (2014) was expanded to a lifting surface model (chapter 5). In contrary to the model of Spalart, no filtering term is required to obtain solutions in qualitative agreement to the experiments. Such a numerical artefact helped to get smooth solutions, without affecting the number of cells. Also, grid independent solutions were obtained. An interesting feature of this model is the fact that only the lift versus angle of attack polar is provided to the model. Hence, it has no sensitivity to the topology of the flow separation and strictly predicts stall cells when the slope of this lift polar becomes negative. For this reason, the stall cells seem to be linked to an instability between the circulation of the wing spanwise sections. The mechanism occurs as follows: If a wing section stalls, its circulation diminishes following the Kutta-Joukowski theorem. This will cause the downwash on neighbor wing sections to increase and thus to stay in the pre-stall regime. The effective angle of attack of the stalled section will increase, which will lead it to be further stalled. In the end, the solution reaches a state where some sections are in the pre-stall regime and some are in the post stall regime, where the  $C_{l_\alpha}$  becomes positive again. If this regime does not exist, the feedback loop will fail to find a new equilibrium and the solution diverges.

From the point of view of the numerical methods, the thesis proposes a fully discrete method to carry out the stability analyses of spanwise invariant base-flows with a periodicity assumption of the perturbations in the spanwise direction (BiGlobal stability analysis). This method was adapted from the literature (Schmid *et al.*, 2017) to be applied to the stall and

buffet problems. This method has a lower computational cost than fully three-dimensional analyses and does not require tedious mathematical developments to include the spanwise periodicity assumption. As such, this method can be readily applied to a black-box CFD software. Another numerical development of the thesis is the introduction of the non-linear Vortex Lattice Method as a model for the stall cells. The computational cost of this method is low since the Vortex-Lattice Method is a low-fidelity model and two-dimensional RANS computations are now routinely used in the industry. This makes the method suitable for uses in preliminary design. A periodicity assumption for the Vortex Lattice Method is also proposed.

## CHAPTER 7 CONCLUSION

In conclusion, URANS simulations allowed to characterize the buffet cells and stall cells and to observe a similar unsteady behavior between the two phenomena. These simulations support the observation of the higher buffet frequency on aircraft wing, but also predict a lower frequency if the wing is swept at a lower angle. To the author's knowledge the stall cells were only studied on unswept wing, but one should expect an unsteady behavior on swept wings. These conclusions on the behavior of stall cells and buffet cells are consistent with the stability analyses which correctly predict the bifurcation from the two-dimensional to the three-dimensional state, showing that a similar global instability is responsible for the stall cells and buffet cells. Moreover, this mode exists for every Mach number from the subsonic to the transonic flow regime. For this reason, one can conclude that the buffet cells are caused by an instability akin to the stall cell one, in agreement with the project working hypothesis. Although the description of this phenomenon as three-dimensional buffet is practical in applied aerodynamics, it might not be accurate since the so-called buffet cells can be steady. Moreover, this description implies that the two-dimensional and three-dimensional (buffet cells) are a variation of the same phenomenon while they are in fact two different phenomena involved in the unsteady buffet flow. A description with a shock boundary layer interaction superimposed on a three-dimensional stall cell type instability is more accurate.

Such an instability can be found in an inviscid potential flow model with viscous correction. With a low order model like this one, only the lift against the angle of attack is provided to the model. Hence this stall cell instability is linked to a negative slope of the lift polar. This is also the case in the global stability analyses and URANS simulations of the NACA4412 stall case and the OALT25 buffet case. For this reason the explanation of the stall/buffet cells as a feedback loop between the circulation of the wing sections is a plausible model.

Future work on the topic of stall/buffet cells should aim to elucidate the discrepancies between the wavelength of the unstable mode in the transonic regime and the URANS simulation one. Nonlinear interactions are a possible explanation. In the same order, the variation of the buffet cells wavelength on infinite swept wings should be further investigated since this study and the work of He and Timme (2020a) exhibit a non-linear relation between the aspect ratio of the wing and the number of cells. At last, an explanation for the broadband buffet spectrum on three-dimensional finite swept wings remains to be found. A possible explanation is proposed by Timme (2020), who observed multiple modes which potentially become

unstable at the same time. The complexity of the geometry could also be an explanation. The models presented in this thesis should also be oriented towards an application in design since both the subsonic stall and transonic buffet are boundaries of aircraft flight envelope.

## REFERENCES

- ABBAS-BAYOUMI, A. and BECKER, K., “An industrial view on numerical simulation for aircraft aerodynamic design,” *Journal of Mathematics in Industry*, vol. 1, no. 1, p. 10, 2011, doi: 10.1186/2190-5983-1-10.
- AIDUN, C. K. and CLAUSEN, J. R., “Lattice-Boltzmann Method for Complex Flows,” *Annual Review of Fluid Mechanics*, vol. 42, no. 1, pp. 439–472, 2010, doi: 10.1146/annurev-fluid-121108-145519.
- ÅKERVIK, E., BRANDT, L., HENNINGSON, D. S., HOEPFFNER, J., MARXEN, O., and SCHLATTER, P., “Steady solutions of the Navier-Stokes equations by selective frequency damping,” *Physics of Fluids*, vol. 18, no. 6, p. 068102, 2006, doi: 10.1063/1.2211705.
- ALLMARAS, S., “Analysis of a local matrix preconditioner for the 2-D Navier-Stokes equations.” AIAA Paper 1993-3330, 1993, doi: 10.2514/6.1993-3330.
- ARNOLDI, W. E., “The principle of minimized iterations in the solution of the matrix eigenvalue problem,” *Quarterly of applied mathematics*, vol. 9, no. 1, pp. 17–29, 1951.
- BALDWIN, B. and LOMAX, H., “Thin-layer approximation and algebraic model for separated turbulent flows.” AIAA Paper 1978-0257, 1978, doi: 10.2514/6.1978-257.
- BARKLEY, D., GOMES, M. G. M., and HENDERSON, R. D., “Three-dimensional instability in flow over a backward-facing step,” *Journal of Fluid Mechanics*, vol. 473, pp. 167–190, Dec. 2002, doi: 10.1017/S002211200200232X.
- BAYLY, B. J., ORSZAG, S. A., and HERBERT, T., “Instability Mechanisms in Shear-Flow Transition,” *Annual Review of Fluid Mechanics*, vol. 20, no. 1, pp. 359–391, Jan. 1988, doi: 10.1146/annurev.fl.20.010188.002043.
- BENDER, E., ANDERSON, B., and P.J., Y., “Vortex generator modeling for Navier-Stokes codes.” ASME Paper FEDSM99-6919, 1999.
- BENEDDINE, S., “Characterization of unsteady flow behavior by linear stability analysis,” Ph.D. dissertation, Paris-Saclay, 2017.
- BENOIT, B. and LEGRAIN, I., “Buffeting prediction for transport aircraft applications based on unsteady pressure measurements.” AIAA Paper 1987-2356, 1987, doi: 10.2514/6.1987-2356.
- BÉRARD, A. and ISIKVEREN, A. T., “Conceptual Design Prediction of the Buffet Envelope of Transport Aircraft,” *Journal of Aircraft*, vol. 46, no. 5, pp. 1593–1606, 2009, doi: 10.2514/1.41367.
- BERTAGNOLIO, F., SØRENSEN, N. N., and RASMUSSEN, F., “New Insight Into the Flow Around a Wind Turbine Airfoil Section,” *Journal of Solar Energy Engineering*, vol. 127, no. 2, pp. 214–222, 2005, doi: 10.1115/1.1861927.

BLAZEK, J., *Computational Fluid Dynamics: Principles and Applications*, 3rd ed. Oxford: Butterworth-Heinemann, 2015.

BOEING COMMERCIAL AIRPLANES, “Statistical Summary of Commercial Jet Airplane Accidents: Worldwide Operations 1959-2014,” Seattle, Washington, United States, 2014.

BOLDS-MOOREHEAD, P. J., CHANEY, V. G., LUTZ, T., and VAUX, S., “Stalling transport aircraft,” *The Aeronautical Journal*, vol. 117, no. 1198, pp. 1183–1206, 2013, doi: 10.1017/S0001924000008812.

BONNE, N., “Stabilité de l’interaction onde de choc/ couche limite laminaire,” Ph.D. dissertation, Paris-Saclay, Paris, 2018.

BONNIFET, V., “Prédiction du phénomène de tremblement sur un profil d’aile avec une approche LES de type PANS-RSM,” Ph.D. dissertation, Sorbonne Université, Paris, France, 2018.

BONNIFET, V., GEROLYMOS, G. A., and VALLET, I., “Transonic Buffet Prediction using Partially Averaged Navier-Stokes.” American Institute of Aeronautics and Astronautics, Jun. 2017, doi: 10.2514/6.2017-3955.

BOURGAULT-CÔTÉ, S., GHASEMI, S., MOSAHEBI, A., and LAURENDEAU, É., “Extension of a Two-Dimensional Navier–Stokes Solver for Infinite Swept Flow,” *AIAA Journal*, vol. 55, no. 2, pp. 662–667, 2017, doi: 10.2514/1.J055139.

BRAGG, B. M., HEINRICH, D. C., BALOW, F. A., and ZAMAN, K. B. M. Q., “Flow oscillation over an airfoil near stall,” *AIAA Journal*, vol. 34, no. 1, pp. 199–201, 1996, doi: 10.2514/3.13045.

BRAGG, M. B., HEINRICH, D. C., and ABDOLLAH, K., “Low-frequency flow oscillation over airfoils near stall,” *AIAA Journal*, vol. 31, no. 7, pp. 1341–1343, 1993.

BRION, V., DANDOIS, J., ABART, J.-C., and PAILLART, P., “Experimental analysis of the shock dynamics on a transonic laminar airfoil,” *Progress in Flight Physics*, vol. 9, pp. 365–386, 2017, doi: 10.1051/eucass/2016090365.

BROEREN, A. P. and BRAGG, M. B., “Flowfield Measurements over an Airfoil During Natural Low-Frequency Oscillations near Stall,” *AIAA Journal*, vol. 37, no. 1, pp. 130–132, 1999, doi: 10.2514/2.678.

BROEREN, A. P. and BRAGG, M. B., “Spanwise Variation in the Unsteady Stalling Flowfields of Two-Dimensional Airfoil Models,” *AIAA Journal*, vol. 39, no. 9, pp. 1641–1651, 2001, doi: 10.2514/2.1501.

BRUNET, V. and DECK, S., “Zonal-Detached Eddy Simulation of Transonic Buffet on a Civil Aircraft Type Configuration.” AIAA Paper 2008-4152, 2008, doi: 10.2514/6.2008-4152.

BUSQUET, D., “Study of a high Reynolds number flow around a two dimensional airfoil at stall; an approach coupling a RANS framework and bifurcation theory,” Ph.D. dissertation, Institut Polytechnique de Paris, 2020.

BUSQUET, D., MARQUET, O., RICHEZ, F., JUNIPER, M. P., and SIPP, D., “Global stability analysis of turbulent flows around an airfoil near stall,” in *EUROGEN 2017*, Madrid, Spain, 2017.

CAMBIER, L., HEIB, S., and PLOT, S., “The Onera elsA CFD software: Input from research and feedback from industry,” *Mechanics & Industry*, vol. 14, no. 3, pp. 159–174, DOI: 10.1051/meca/2013056, 2013.

CASACUBERTA, J., GROOT, K. J., TOL, H. J., and HICKEL, S., “Effectivity and efficiency of selective frequency damping for the computation of unstable steady-state solutions,” *Journal of Computational Physics*, vol. 375, pp. 481–497, Dec. 2018, doi: 10.1016/j.jcp.2018.08.056.

CEBECI, T., SHAO, J. P., KAFYEKE, F., and LAURENDEAU, É., “Boundary -Layer Equations,” in *Computational Fluid Dynamics Fo Engineers*. Springer Berlin Heidelberg, 2005.

CHABERT, T., DANDOIS, J., and GARNIER, É., “Experimental closed-loop control of separated-flow over a plain flap using extremum seeking,” *Experiments in Fluids*, vol. 57, no. 3, p. 37, Mar. 2016, doi: 10.1007/s00348-016-2123-y.

CHAOUAT, B., “The State of the Art of Hybrid RANS/LES Modeling for the Simulation of Turbulent Flows,” *Flow, Turbulence and Combustion*, vol. 99, no. 2, pp. 279–327, 2017, doi: 10.1007/s10494-017-9828-8.

CHATTOT, J.-J., “Analysis and Design of Wings and Wing/Winglet Combinations at Low Speeds.” AIAA Paper 2004-220, 2004, doi: 10.2514/6.2004-220.

CHEN, S. and DOOLEN, G. D., “Lattice Boltzmann Method for Fluid Flows,” *Annual Review of Fluid Mechanics*, vol. 30, no. 1, pp. 329–364, 1998, doi: 10.1146/annurev.fluid.30.1.329.

CHRISTODOULOU, K. N. and SCRIVEN, L. E., “Finding leading modes of a viscous free surface flow: An asymmetric generalized eigenproblem,” *Journal of Scientific Computing*, vol. 3, no. 4, pp. 355–406, 1988, doi: 10.1007/BF01065178.

CITRO, V., LUCHINI, P., GIANNETTI, F., and AUTERI, F., “Efficient stabilization and acceleration of numerical simulation of fluid flows by residual recombination,” *Journal of Computational Physics*, vol. 344, pp. 234–246, 2017, doi: 10.1016/j.jcp.2017.04.081.

COLES, D. and WADCOCK, A. J., “Flying-Hot-wire Study of Flow Past an NACA 4412 Airfoil at Maximum Lift,” *AIAA Journal*, vol. 17, no. 4, pp. 321–329, Apr. 1979, doi: 10.2514/3.61127.



CROUCH, J. D., GARBARUK, A., and MAGIDOV, D., “Predicting the onset of flow unsteadiness based on global instability,” *Journal of Computational Physics*, vol. 224, no. 2, pp. 924–940, 2007, doi: 10.1016/j.jcp.2006.10.035.

CROUCH, J. D., GARBARUK, A., MAGIDOV, D., and TRAVIN, A., “Origin of transonic buffet on aerofoils,” *Journal of Fluid Mechanics*, vol. 628, p. 357, Jun. 2009, doi: 10.1017/S0022112009006673.

CROUCH, J. D., GARBARUK, A., and STRELETS, M., “Global instability in the onset of transonic-wing buffet,” *Journal of Fluid Mechanics*, vol. 881, pp. 3–22, Dec. 2019, doi: 10.1017/jfm.2019.748.

CROUCH, J., GARBARUK, A., MAGIDOV, D., and TRAVIN, A., “Origin and Structure of Transonic Buffet on Airfoils.” AIAA Paper 2008-4233, 2008, doi: 10.2514/6.2008-4233.

CROUCH, J. D., GARBARUK, A., and STRELETS, M., “Global Instability Analysis of Unswept and Swept-Wing Transonic Buffet Onset.” AIAA Paper 2018-3229, 2018, doi: 10.2514/6.2018-3229.

CROW, S. C., “Stability theory for a pair of trailing vortices,” *AIAA Journal*, vol. 8, no. 12, pp. 2172–2179, 1970, doi: 10.2514/3.6083.

CUNHA, G., PASSAGGIA, P.-Y., and LAZAREFF, M., “Optimization of the selective frequency damping parameters using model reduction,” *Physics of Fluids*, vol. 27, no. 9, p. 094103, 2015, doi: 10.1063/1.4930925.

DANDOIS, J., “Experimental study of transonic buffet phenomenon on a 3D swept wing,” *Physics of Fluids*, vol. 28, no. 1, p. 016101, 2016, doi: 10.1063/1.4937426.

DANDOIS, J., MARY, I., and BRION, V., “Large-eddy simulation of laminar transonic buffet,” *Journal of Fluid Mechanics*, vol. 850, pp. 156–178, 2018, doi: 10.1017/jfm.2018.470.

DECK, S., GAND, F., BRUNET, V., and BEN KHELIL, S., “High-fidelity simulations of unsteady civil aircraft aerodynamics: Stakes and perspectives. Application of zonal detached eddy simulation,” *Philosophical Transactions of the Royal Society A: Mathematical, Physical and Engineering Sciences*, vol. 372, 2014, doi: 10.1098/rsta.2013.0325.

DECK, S., “Zonal-Detached-Eddy Simulation of the Flow Around a High-Lift Configuration,” *AIAA Journal*, vol. 43, no. 11, pp. 2372–2384, 2005, doi: 10.2514/1.16810.

DECK, S., “Numerical Simulation of Transonic Buffet over a Supercritical Airfoil,” *AIAA Journal*, vol. 43, no. 7, pp. 1556–1566, 2005, doi: 10.2514/1.9885.

DECK, S., “Recent improvements in the Zonal Detached Eddy Simulation (ZDES) formulation,” *Theoretical and Computational Fluid Dynamics*, vol. 26, no. 6, pp. 523–550, 2012, doi: 10.1007/s00162-011-0240-z.

DECK, S. and RENARD, N., “Towards an enhanced protection of attached boundary layers in hybrid RANS/LES methods,” *Journal of Computational Physics*, vol. 400, p. 108970, Jan. 2020, doi: 10.1016/j.jcp.2019.108970.

DELL'ORSO, H. and AMITAY, M., "Parametric Investigation of Stall Cell Formation on a NACA 0015 Airfoil," *AIAA Journal*, pp. 1–13, 2018, doi: 10.2514/1.J056850.

DELL'ORSO, H., TUNA, B. A., and AMITAY, M., "Measurement of Three-Dimensional Stall Cells on a Two-Dimensional NACA0015 Airfoil," *AIAA Journal*, vol. 54, no. 12, pp. 3872–3883, 2016, doi: 10.2514/1.J054848.

DISOTELL, K. J. and GREGORY, J., "Time-Resolved Measurements of Cellular Separation on a Stalling Airfoil." AIAA Paper 2015-1501, 2015, doi: 10.2514/6.2015-1501.

EDWARDS, J. R. and CHANDRA, S., "Comparison of eddy viscosity-transport turbulence models for three-dimensional, shock-separated flowfields," *AIAA Journal*, vol. 34, no. 4, pp. 756–763, 1996, doi: 10.2514/3.13137.

EDWARDS, J., "Transonic shock oscillations calculated with a new interactive boundary layer coupling method." AIAA Paper 1993-0777, 1993, doi: 10.2514/6.1993-777.

ELIMELECH, Y., ARIELI, R., and IOSILEVSKII, G., "The three-dimensional transition stages over the NACA-0009 airfoil at Reynolds numbers of several ten thousand," *Physics of Fluids*, vol. 24, no. 2, p. 024104, 2012, doi: 10.1063/1.3682377.

FELDHUSEN-HOFFMANN, A., STATNIKOV, V., KLAAS, M., and SCHRÖDER, W., "Investigation of shock–acoustic-wave interaction in transonic flow," *Experiments in Fluids*, vol. 59, no. 1, p. 15, Jan. 2018, doi: 10.1007/s00348-017-2466-z.

FRANCIOLINI, M., DA RONCH, A., DROFELNIK, J., RAVEH, D., and CRIVELLINI, A., "Efficient infinite-swept wing solver for steady and unsteady compressible flows," *Aerospace Science and Technology*, vol. 72, pp. 217–229, 2018, doi: 10.1016/j.ast.2017.10.034.

FUKUSHIMA, Y. and KAWAI, S., "Wall-Modeled Large-Eddy Simulation of Transonic Airfoil Buffet at High Reynolds Number," *AIAA Journal*, vol. 56, no. 6, pp. 1–18, 2018, doi: 10.2514/1.J056537.

GALBRAITH, M. C., ALLMARAS, S. R., and HAIMES, R., "Full Potential Revisited: A Medium Fidelity Aerodynamic Analysis Tool," in *55th AIAA Aerospace Sciences Meeting*. Grapevine, Texas: American Institute of Aeronautics and Astronautics, Jan. 2017, doi: 10.2514/6.2017-0290.

GALLAIRE, F., MARQUILLIE, M., and EHRENSTEIN, U., "Three-dimensional transverse instabilities in detached boundary layers," *Journal of Fluid Mechanics*, vol. 571, pp. 221–233, Jan. 2007, doi: 10.1017/S0022112006002898.

GALLAY, S. and LAURENDEAU, E., "Nonlinear Generalized Lifting-Line Coupling Algorithms for Pre/Poststall Flows," *AIAA Journal*, vol. 53, no. 7, pp. 1784–1792, 2015, doi: 10.2514/1.j053530.

GALLAY, S. and LAURENDEAU, E., "Preliminary-Design Aerodynamic Model for Complex Configurations Using Lifting-Line Coupling Algorithm," *Journal of Aircraft*, vol. 53, no. 4, pp. 1145–1159, Jul. 2016, doi: 10.2514/1.C033460.

GALLAY, S., “Algorithmes de couplage RANS et écoulement potentiel,” Ph.D. dissertation, Polytechnique Montréal, 2016.

GARNIER, E. and DECK, S., “Large-Eddy Simulation of Transonic Buffet over a Supercritical Airfoil,” in *Turbulence and Interactions*, DEVILLE, M., LÊ, T.-H., and SAGAUT, P., Eds. Springer, Berlin, Heidelberg, 2010, pp. 135–141, doi: 10.1007/978-3-642-14139-3\_16.

GHASEMI, S., MOSAHEBI, A., and LAURENDEAU, E., “A Two-Dimensional/Infinite Swept Wing Navier-Stokes Solver.” AIAA Paper 2014-0557, 2014, doi: 10.2514/6.2014-0557.

GIANNELIS, N. F., VIO, G. A., and LEVINSKI, O., “A review of recent developments in the understanding of transonic shock buffet,” *Progress in Aerospace Sciences*, vol. 92, pp. 39–84, 2017, doi: 10.1016/j.paerosci.2017.05.004.

GIANNELIS, N. F., LEVINSKI, O., and VIO, G. A., “Influence of Mach number and angle of attack on the two-dimensional transonic buffet phenomenon,” *Aerospace Science and Technology*, vol. 78, pp. 89–101, 2018, doi: 10.1016/j.ast.2018.03.045.

GONCALVES, E. and HOUEVILLE, R., “Turbulence model and numerical scheme assessment for buffet computations,” *International Journal for Numerical Methods in Fluids*, vol. 46, no. 11, pp. 1127–1152, 2004, doi: 10.1002/flid.777.

GOPINATH, A. and JAMESON, A., “Time Spectral Method for Periodic Unsteady Computations over Two- and Three- Dimensional Bodies.” AIAA Paper 2005-1220, 2005, doi: 10.2514/6.2005-1220.

GOVAERTS, W., “Stable Solvers and Block Elimination for Bordered Systems,” *SIAM Journal on Matrix Analysis and Applications*, vol. 12, no. 3, pp. 469–483, Jul. 1991, doi: 10.1137/0612034.

GREGORY, N., QUINCEY, V. G., O’REILLY, C. L., and HALL, D. J., “Progress Report on Observations of Three-Dimensional Flow Patterns obtained during Stall Development on Aerofoils, and on the Problem of Measuring Two-Dimensional Characteristics,” Aeronautical Research Council, Tech. Rep. C.P. No. 1146, 1971.

GROSS, A. and FASEL, H., “Numerical Investigation of Separation for Airfoils.” AIAA Paper 2011-3438, 2011, doi: 10.2514/6.2011-3438.

GROSS, A., FASEL, H. F., and GASTER, M., “Criterion for Spanwise Spacing of Stall Cells,” *AIAA Journal*, vol. 53, no. 1, pp. 272–274, 2015, doi: 10.2514/1.J053347.

GROSSI, F., BRAZA, M., and HOARAU, Y., “Prediction of Transonic Buffet by Delayed Detached-Eddy Simulation,” *AIAA Journal*, vol. 52, no. 10, pp. 2300–2312, 2014, doi: 10.2514/1.j052873.

HAAS, A. P., BROWNE, O. M., FASEL, H. F., and BREHM, C., “A Numerical Jacobian Based Linearized Compressible Navier-Stokes Solver For Hypersonic Boundary-Layer Stability.” AIAA Paper 2017-4520, 2017, doi: 10.2514/6.2017-4520.

- HALL, K. C., THOMAS, J. P., and CLARK, W. S., “Computation of Unsteady Nonlinear Flows in Cascades Using a Harmonic Balance Technique,” *AIAA Journal*, vol. 40, no. 5, pp. 879–886, 2002, doi: 10.2514/2.1754.
- HALL, K. C., EKICI, K., THOMAS, J. P., and DOWELL, E. H., “Harmonic balance methods applied to computational fluid dynamics problems,” *International Journal of Computational Fluid Dynamics*, vol. 27, no. 2, pp. 52–67, 2013, doi: 10.1080/10618562.2012.742512.
- HARTMANN, A., FELDHUSEN, A., and SCHRÖDER, W., “On the interaction of shock waves and sound waves in transonic buffet flow,” *Physics of Fluids*, vol. 25, no. 2, p. 026101, Feb. 2013, doi: 10.1063/1.4791603.
- HARTMANN, A., KLAAS, M., and SCHRÖDER, W., “Coupled Airfoil Heave/Pitch Oscillations at Buffet Flow,” *AIAA Journal*, vol. 51, no. 7, pp. 1542–1552, Jul. 2013, doi: 10.2514/1.J051512.
- HASHIMOTO, A., ISHIDA, T., AOYAMA, T., OHMACHI, Y., YAMAMOTO, T., and HAYASHI, K., “Current Progress in Unsteady Transonic Buffet Simulation with Unstructured Grid CFD Code.” AIAA Paper 2018-0788, 2018, doi: 10.2514/6.2018-0788.
- HE, W., GIORIA, R. S., PÉREZ, J. M., and THEOFILIS, V., “Linear instability of low Reynolds number massively separated flow around three NACA airfoils,” *Journal of Fluid Mechanics*, vol. 811, pp. 701–741, 2017, doi: 10.1017/jfm.2016.778.
- HE, W. and TIMME, S., “Resolvent Analysis of Shock Buffet on Infinite Wings.” VIRTUAL EVENT: AIAA Paper 2020-2727, Jun. 2020, doi: 10.2514/6.2020-2727.
- HE, W. and TIMME, S., “Triglobal Shock Buffet Instability Study on Infinite Wings.” AIAA Paper 2020-1986, Jan. 2020, doi: 10.2514/6.2020-1986.
- HESS, J. and SMITH, A., “Calculation of potential flow about arbitrary bodies,” *Progress in Aerospace Sciences*, vol. 8, pp. 1–138, 1967, doi: 10.1016/0376-0421(67)90003-6.
- HOARAU, Y., SHIA-HUI, P., SCHWANBORN, D., and ALISTAIR, R., *Progress in Hybrid RANS-LES Modelling : Papers Contributed to the 6th Symposium on Hybrid RANS-LES Methods, 26-28 September 2016, Strasbourg, France*, ser. Notes on Numerical Fluid Mechanics and Multidisciplinary Design. Cham Springer International Publishing, 2018, no. 137.
- HOSANGADI, P. and GOPALARATHNAM, A., “A Low-Order Method for Prediction of Separation and Stall on Unswept Wings,” *arXiv preprint arXiv:2006.00107*, 2020.
- HUANG, J., XIAO, Z., LIU, J., and FU, S., “Simulation of shock wave buffet and its suppression on an OAT15A supercritical airfoil by IDDES,” *Science China Physics, Mechanics and Astronomy*, vol. 55, no. 2, pp. 260–271, 2012, doi: 10.1007/s11433-011-4601-9.
- HUERRE, P. and MONKEWITZ, P. A., “Local and global instabilities in spatially developing flows,” *Annual Review of Fluid Mechanics*, vol. 22, pp. 473–537, 1990.

IORIO, M. C., GONZÁLEZ, L. M., and FERRER, E., “Direct and adjoint global stability analysis of turbulent transonic flows over a NACA0012 profile,” *International Journal for Numerical Methods in Fluids*, vol. 76, no. 3, pp. 147–168, 2014, doi: 10.1002/fld.3929.

IOVNOVICH, M. and RAVEH, D. E., “Reynolds-Averaged Navier-Stokes Study of the Shock-Buffer Instability Mechanism,” *AIAA Journal*, vol. 50, no. 4, pp. 880–890, 2012, doi: 10.2514/1.j051329.

IOVNOVICH, M. and RAVEH, D. E., “Numerical Study of Shock Buffet on Three-Dimensional Wings,” *AIAA Journal*, vol. 53, no. 2, pp. 449–463, 2015, doi: 10.2514/1.j053201.

ISHIDA, T., ISHIKO, K., HASHIMOTO, A., AOYAMA, T., and TAKEKAWA, K., “Transonic Buffet Simulation over Supercritical Airfoil by Unsteady-FaSTAR Code.” AIAA Paper 2016-1310, 2016, doi: 10.2514/6.2016-1310.

ISHIDA, T., HASHIMOTO, A., OHMICH, Y., AOYAMA, T., and TAKEKAWA, K., “Transonic Buffet Simulation over NASA-CRM by Unsteady-FaSTAR Code.” AIAA Paper 2017-0494, 2017, doi: 10.2514/6.2017-0494.

JACQUIN, L., MOLTON, P., DECK, S., MAURY, B., and SOULEVANT, D., “Experimental Study of Shock Oscillation over a Transonic Supercritical Profile,” *AIAA Journal*, vol. 47, no. 9, pp. 1985–1994, 2009, doi: 10.2514/1.30190.

JAMESON, A., “The Evolution of Computational Methods in Aerodynamics,” *Journal of Applied Mechanics*, vol. 50, pp. 1052–1070, 1983, doi: 10.1115/1.3167188.

JAMESON, A. and BAKER, T., “Solution of the Euler equations for complex configurations.” AIAA Paper 1983-1929, 1983, doi: 10.2514/6.1983-1929.

JAMESON, A., SCHMIDT, W., and TURKEL, E., “Numerical solution of the Euler equations by finite volume methods using Runge Kutta time stepping schemes.” AIAA Paper 1981-1259, 1981, doi: 10.2514/6.1981-1259.

JAMESON, A., “Time dependent calculations using multigrid, with applications to unsteady flows past airfoils and wings.” AIAA Paper 1991-1596, 1991, doi: 10.2514/6.1991-1596.

JAMESON, A. and YOON, S., “Lower-upper implicit schemes with multiple grids for the Euler equations,” *AIAA Journal*, vol. 25, no. 7, pp. 929–935, 1987, doi: 10.2514/3.9724.

JORDI, B. E., COTTER, C. J., and SHERWIN, S. J., “Encapsulated formulation of the selective frequency damping method,” *Physics of Fluids*, vol. 26, no. 3, p. 034101, 2014, doi: 10.1063/1.4867482.

JORDI, B. E., COTTER, C. J., and SHERWIN, S. J., “An adaptive selective frequency damping method,” *Physics of Fluids*, vol. 27, no. 9, p. 094104, 2015, doi: 10.1063/1.4932107.

KAFYEKE, F., PIPERNI, P., and ROBIN, S., “Application of KTRAN Transonic Small Disturbance Code to the Challenger Business Jet Configuration with Winglets,” in *Aerospace Technology Conference and Exposition*, Oct. 1988, p. 881483, doi: 10.4271/881483.

KAMENETSKIY, D. S., BUSSOLETTI, J. E., HILMES, C. L., VENKATAKRISHNAN, V., WIGTON, L. B., and JOHNSON, F. T., “Numerical Evidence of Multiple Solutions for the Reynolds-Averaged Navier–Stokes Equations,” *AIAA Journal*, vol. 52, no. 8, pp. 1686–1698, 2014, doi: 10.2514/1.J052676.

KATZ, J., “Large-scale vortex-lattice model for the locally separated flow overwings,” *AIAA Journal*, vol. 20, no. 12, pp. 1640–1646, 1982, doi: 10.2514/3.7998.

KATZ, J. and PLOTKIN, A., *Low-Speed Aerodynamics*, 2nd ed. Cambridge: Cambridge University Press, 2001, doi: 10.1017/CBO9780511810329.

KITSIOS, V., RODRÍGUEZ, D., THEOFILIS, V., OOI, A., and SORIA, J., “BiGlobal stability analysis in curvilinear coordinates of massively separated lifting bodies,” *Journal of Computational Physics*, vol. 228, no. 19, pp. 7181–7196, 2009, doi: 10.1016/j.jcp.2009.06.011.

KOIKE, S., UENO, M., NAKAKITA, K., and HASHIMOTO, A., “Unsteady Pressure Measurement of Transonic Buffet on NASA Common Research Model.” AIAA Paper 2016-4044, 2016, doi: 10.2514/6.2016-4044.

KONTOGIANNIS, A., PARENTEAU, M., and LAURENDEAU, E., “Viscous-Inviscid Analysis of Transonic Swept Wings using 2.5D RANS and Parametric Shapes.” AIAA Paper 2019-2116, 2019, doi: 10.2514/6.2019-2116.

LAWSON, S., GREENWELL, D., and QUINN, M. K., “Characterisation of Buffet on a Civil Aircraft Wing.” AIAA Paper 2016-1309, 2016, doi: 10.2514/6.2016-1309.

LE BALLEUR, J. and GIRODOUX-LAVIGNE, P., “Viscous-Inviscid Strategy and Computation of Transonic Buffet,” in *Symposium Transsonicum III*. Springer, Berlin, Heidelberg, 1989, pp. 49–63.

LEE, B. H. K., “Oscillatory shock motion caused by transonic shock boundary-layer interaction,” *AIAA Journal*, vol. 28, no. 5, pp. 942–944, May 1990, doi: 10.2514/3.25144.

LEE, B. H. K., “Self-sustained shock oscillations on airfoils at transonic speeds,” *Progress in Aerospace Sciences*, vol. 37, no. 2, pp. 147–196, 2001, doi: 10.1016/s0376-0421(01)00003-3.

LEHOUCQ, R. B., SORENSEN, D. C., and YANG, C., *ARPACK Users’ Guide: Solution of Large-Scale Eigenvalue Problems with Implicitly Restarted Arnoldi Methods*. Society for Industrial and Applied Mathematics, 1998, doi: 10.1137/1.9780898719628.

LEPAGE, A., DANDOIS, J., GEERAERT, A., MOLTON, P., TERNOY, F., DOR, J. B., and COUSTOLS, E., “Transonic buffet alleviation on 3D wings: Wind tunnel tests and closed-loop control investigations,” *Advances in aircraft and spacecraft science*, vol. 4, no. 2, pp. 145–167, 2017, doi: 10.12989/aas.2017.4.2.145.

LIOU, M.-S., “A Sequel to AUSM: AUSM+,” *Journal of Computational Physics*, vol. 129, no. 2, pp. 364–382, 1996, doi: 10.1006/jcph.1996.0256.

LIOU, M.-S., “Ten years in the making - AUSM-family.” AIAA Paper 2001-2521, 2001, doi: 10.2514/6.2001-2521.

LIU, D. and NISHINO, T., “Numerical analysis on the oscillation of stall cells over a NACA 0012 aerofoil,” *Computers & Fluids*, vol. 175, pp. 246–259, Oct. 2018, doi: 10.1016/j.compfluid.2018.08.016.

LYON, C., BROEREN, A. P., GIGUÈRE, P., GOPALARATHNAM, A., and SELIG, M. S., “Summary of Low-Speed Airfoil Data,” Tech. Rep., 1997.

MANNI, L., NISHINO, T., and DELAFIN, P.-L., “Numerical study of airfoil stall cells using a very wide computational domain,” *Computers & Fluids*, vol. 140, pp. 260–269, 2016, doi: 10.1016/j.compfluid.2016.09.023.

MANOLESOS, M. and VOUTSINAS, S. G., “Geometrical characterization of stall cells on rectangular wings: Geometrical characterization of stall cells,” *Wind Energy*, vol. 17, no. 9, pp. 1301–1314, 2013, doi: 10.1002/we.1634.

MANOLESOS, M. and VOUTSINAS, S. G., “Experimental investigation of the flow past passive vortex generators on an airfoil experiencing three-dimensional separation,” *Journal of Wind Engineering and Industrial Aerodynamics*, vol. 142, pp. 130–148, 2015, doi: 10.1016/j.jweia.2015.03.020.

MANOLESOS, M., PAPADAKIS, G., and VOUTSINAS, S. G., “Experimental and computational analysis of stall cells on rectangular wings: Experimental and CFD analysis of stall cells,” *Wind Energy*, vol. 17, no. 6, pp. 939–955, 2014, doi: 10.1002/we.1609.

MARQUET, O., LOMBARDI, M., CHOMAZ, J.-M., SIPP, D., and JACQUIN, L., “Direct and adjoint global modes of a recirculation bubble: Lift-up and convective non-normalities,” *Journal of Fluid Mechanics*, vol. 622, p. 1, Mar. 2009, doi: 10.1017/S0022112008004023.

MARTINELLI, L., “Calculations of viscous flows with a multigrid method,” Ph.D. dissertation, Princeton University, 1987.

MASINI, L., TIMME, S., and PEACE, A. J., “Analysis of a civil aircraft wing transonic shock buffet experiment,” *Journal of Fluid Mechanics*, vol. 884, p. A1, Feb. 2020, doi: 10.1017/jfm.2019.906.

MASINI, L., TIMME, S., CIARELLA, A., and PEACE, A., “Influence of Vane Vortex Generators on Transonic Wing Buffet: Further Analysis of the Bucolic Experimental Dataset,” in *52nd 3AF International Conference on Applied Aerodynamics*, Lyon, France, 2017.

MASINI, L., TIMME, S., and PEACE, A. J., “Scale-Resolving Simulations of a Civil Aircraft Wing Transonic Shock-Buffet Experiment,” *AIAA Journal*, pp. 1–17, Jul. 2020, doi: 10.2514/1.J059219.

MASKEW, B., “Program VSAERO theory document: A computer program for calculating nonlinear aerodynamic characteristics of arbitrary configurations,” NASA Ames Research Center, Moffett Field, California, United States, Contractor Report NASA CR-4023, 1987.

MAVRIPLIS, D., “Multigrid Strategies for Viscous Flow Solvers on Anisotropic Unstructured Meshes,” *Journal of Computational Physics*, vol. 145, no. 1, pp. 141–165, Sep. 1998, doi: 10.1006/jcph.1998.6036.

MCCULLOUGH, G. B. and GAULT, D. E., “Example of three representative types of airfoil-section stall at low speed,” National Advisory Committee for Aeronautics, Moffett Field, California, United States, Technical Note NACA TN 2502, 1951.

MCDEVITT, J. B. and OKUNO, A. F., “Static and dynamic pressure measurements on a NACA 0012 airfoil in the Ames High Reynolds Number Facility,” NASA Ames Research Center, Moffett Field, California, United States, Technical Report NASA-TP-2485, 1985.

MCMULLEN, M., JAMESON, A., and ALONSO, J., “Application of a non-linear frequency domain solver to the Euler and Navier-Stokes equations.” AIAA Paper 2002-0120, 2002, doi: 10.2514/6.2002-120.

MCMULLEN, M., JAMESON, A., and ALONSO, J., “Acceleration of convergence to a periodic steady state in turbomachinery flows.” AIAA Paper 2001-0152, 2001, doi: 10.2514/6.2001-152.

MCMULLEN, M. S., “The Application of the Non-Linear Frequency Domain Methods to the Euler and Navier-Stokes Equations,” Ph.D. dissertation, Stanford University, 2003.

MEMMOLO, A., BERNARDINI, M., and PIROZZOLI, S., “Scrutiny of buffet mechanisms in transonic flow,” *International Journal of Numerical Methods for Heat & Fluid Flow*, pp. 00–00, Apr. 2018, doi: 10.1108/HFF-08-2016-0300.

MENTER, F. R., “Two-equation eddy-viscosity turbulence models for engineering applications,” *AIAA Journal*, vol. 32, no. 8, pp. 1598–1605, 1994, doi: 10.2514/3.12149.

METTOT, C., RENAC, F., and SIPP, D., “Computation of eigenvalue sensitivity to base flow modifications in a discrete framework: Application to open-loop control,” *Journal of Computational Physics*, vol. 269, pp. 234–258, 2014, doi: 10.1016/j.jcp.2014.03.022.

MOLTON, P., DANDOIS, J., LEPAGE, A., BRUNET, V., and BUR, R., “Control of Buffet Phenomenon on a Transonic Swept Wing,” *AIAA Journal*, vol. 51, no. 4, pp. 761–772, 2013, doi: 10.2514/1.j051000.

MOSS, G. F. and MURDIN, P. M., “Two-Dimensional Low-Speed Tunnel Tests on the NACA 0012 section Including Measurements Made During Pitching Oscillations at the Stall,” Aeronautical Research Council, Tech. Rep. C.P. No. 1145, 1971.

MURMAN, E. M. and COLE, J. D., “Calculation of plane steady transonic flows,” *AIAA Journal*, vol. 9, no. 1, pp. 114–121, Jan. 1971, doi: 10.2514/3.6131.



OHMACHI, Y., ISHIDA, T., and HASHIMOTO, A., “Numerical Investigation of Transonic Buffet on a Three-Dimensional Wing using Incremental Mode Decomposition.” AIAA Paper 2017-1436, 2017, doi: 10.2514/6.2017-1436.

OHMACHI, Y., ISHIDA, T., and HASHIMOTO, A., “Modal Decomposition Analysis of Three-Dimensional Transonic Buffet Phenomenon on a Swept Wing,” *AIAA Journal*, vol. 56, no. 10, pp. 3938–3950, Oct. 2018, doi: 10.2514/1.J056855.

PALADINI, E., DANDOIS, J., SIPP, D., and ROBINET, J.-C., “Analysis and Comparison of Transonic Buffet Phenomenon over Several Three-Dimensional Wings,” *AIAA Journal*, vol. 57, no. 1, pp. 379–396, 2019, doi: 10.2514/1.J056473.

PALADINI, E., “Insight on transonic buffet instability: Evolution from two-dimensional aerofoils to three-dimensional swept wings,” Ph.D. Thesis, École Nationale Supérieure d’Arts et Métiers, Paris, France, 2018.

PALADINI, E., MARQUET, O., SIPP, D., ROBINET, J.-C., and DANDOIS, J., “Various approaches to determine active regions in an unstable global mode: Application to transonic buffet,” *Journal of Fluid Mechanics*, vol. 881, pp. 617–647, Dec. 2019, doi: 10.1017/jfm.2019.761.

PALADINI, E., BENEDDINE, S., DANDOIS, J., SIPP, D., and ROBINET, J.-C., “Transonic buffet instability: From two-dimensional airfoils to three-dimensional swept wings,” *Physical Review Fluids*, vol. 4, no. 10, p. 103906, Oct. 2019, doi: 10.1103/PhysRevFluids.4.103906.

PARENTEAU, M., LAURENDEAU, É., and CARRIER, G., “Combined high-speed and high-lift wing aerodynamic optimization using a coupled VLM-2.5D RANS approach,” *Aerospace Science and Technology*, vol. 76, pp. 484–496, May 2018, doi: 10.1016/j.ast.2018.02.023.

PARENTEAU, M. and LAURENDEAU, É., “Nonlinear Frequency-Domain Solver for Vortex Lattice Method,” *AIAA Journal*, pp. 1–10, 2018, doi: 10.2514/1.J056704.

PARENTEAU, M., SERMEUS, K., and LAURENDEAU, E., “VLM Coupled with 2.5D RANS Sectional Data for High-Lift Design.” AIAA Paper 2018-1049, 2018, doi: 10.2514/6.2018-1049.

PAUL, R. C. and GOPALARATHNAM, A., “Iteration schemes for rapid post-stall aerodynamic prediction of wings using a decambering approach,” *International Journal for Numerical Methods in Fluids*, vol. 76, no. 4, pp. 199–222, 2014, doi: 10.1002/flid.3931.

PICCOLA, J., “Flight Test Guide For Certification Of Transport Category Airplanes,” Federal Aviation Administration, Advisory Circular AC 25-7C, 2012.

PICCELLA, F., LOISEAU, J.-C., LUSSEYRAN, F., ROBINET, J.-C., CHERUBINI, S., and PASTUR, L., “Successive bifurcations in a fully three-dimensional open cavity flow,” *Journal of Fluid Mechanics*, vol. 844, pp. 855–877, Jun. 2018, doi: 10.1017/jfm.2018.169.

PIERCE, N. A. and GILES, M. B., “Preconditioned multigrid methods for compressible flow calculations on stretched meshes,” *Journal of Computational Physics*, vol. 136, no. 2, pp. 425–445, 1997, doi: 10.1006/jcph.1997.5772.

PLANTE, F. and LAURENDEAU, É., “Acceleration of Euler and RANS solvers via Selective Frequency Damping,” *Computers & Fluids*, vol. 166, pp. 46–56, 2018, doi: 10.1016/j.compfluid.2018.01.027.

PLANTE, F. and LAURENDEAU, É., “Simulation of Transonic Buffet Using a Time-Spectral Method,” *AIAA Journal*, pp. 1–13, Jan. 2019, doi: 10.2514/1.J057224.

PLANTE, F., DANDOIS, J., SARTOR, F., and LAURENDEAU, E., “Study of Three-Dimensional Transonic Buffet on Swept Wings.” AIAA Paper 2017-3903, 2017, doi: 10.2514/6.2017-3903.

PLANTE, F., DANDOIS, J., BENEDDINE, S., SIPP, D., and LAURENDEAU, É., “Numerical Simulations and Global Stability Analyses of Transonic Buffet and Subsonic Stall,” in *54 Th 3AF International Conference on Applied Aerodynamics*. FP63-AERO2019-plante, 2019.

PLANTE, F., DANDOIS, J., and LAURENDEAU, É., “Similarities Between Cellular Patterns Occurring in Transonic Buffet and Subsonic Stall,” *AIAA Journal*, vol. 58, no. 1, pp. 71–84, 2019, doi: 10.2514/1.J058555.

RAVEH, D. and DOWELL, E., “Frequency lock-in phenomenon for oscillating airfoils in buffeting flows,” *Journal of Fluids and Structures*, vol. 27, no. 1, pp. 89–104, 2011, doi: 10.1016/j.jfluidstructs.2010.10.001.

RIBEIRO, A. F., SINGH, D., KÖNIG, B., FARES, E., ZHANG, R., GOPALAKRISHNAN, P., LI, Y., and CHEN, H., “Buffet Simulations with a Lattice-Boltzmann based Transonic Solver.” AIAA Paper 2017-1438, 2017, doi: 10.2514/6.2017-1438.

RICHEZ, F., LEGUILLE, M., and MARQUET, O., “Selective frequency damping method for steady RANS solutions of turbulent separated flows around an airfoil at stall,” *Computers & Fluids*, vol. 132, pp. 51–61, 2016, doi: 10.1016/j.compfluid.2016.03.027.

ROBINET, J.-C., “Bifurcations in shock-wave/laminar-boundary-layer interaction: Global instability approach,” *Journal of Fluid Mechanics*, vol. 579, p. 85, May 2007, doi: 10.1017/S0022112007005095.

RODRÍGUEZ, D. and THEOFILIS, V., “Structural changes of laminar separation bubbles induced by global linear instability,” *Journal of Fluid Mechanics*, vol. 655, pp. 280–305, Jul. 2010, doi: 10.1017/S0022112010000856.

RODRÍGUEZ, D. and THEOFILIS, V., “On the birth of stall cells on airfoils,” *Theoretical and Computational Fluid Dynamics*, vol. 25, pp. 105–117, 2011, doi: 10.1007/s00162-010-0193-7.

ROE, P., “Approximate Riemann solvers, parameter vectors, and difference schemes,” *Journal of Computational Physics*, vol. 43, no. 2, pp. 357–372, 1981, doi: 10.1016/0021-9991(81)90128-5.

ROOS, F., “The buffeting pressure field of a high-aspect-ratio swept wing.” AIAA Paper 1985-1609, 1985, doi: 10.2514/6.1985-1609.

RUMSEY, C. L., SLOTNICK, J. P., LONG, M., STUEVER, R. A., and WAYMAN, T. R., “Summary of the First AIAA CFD High-Lift Prediction Workshop,” *Journal of Aircraft*, vol. 48, no. 6, pp. 2068–2079, Nov. 2011, doi: 10.2514/1.C031447.

RUMSEY, C., “NASA Langley Research Center Turbulence Modeling Resource,” <https://turbmodels.larc.nasa.gov/>, 2017.

RUMSEY, C. L., SLOTNICK, J. P., and SCLAFANI, A. J., “Overview and Summary of the Third AIAA High Lift Prediction Workshop.” AIAA Paper 2018-1258, 2018, doi: 10.2514/6.2018-1258.

SAAD, Y. and SCHULTZ, M. H., “GMRES: A Generalized Minimal Residual Algorithm for Solving Nonsymmetric Linear Systems,” *SIAM Journal on Scientific and Statistical Computing*, vol. 7, no. 3, pp. 856–869, Jul. 1986, doi: 10.1137/0907058.

SARLAK, H., FRÈRE, A., MIKKELSEN, R., and SØRENSEN, J., “Experimental Investigation of Static Stall Hysteresis and 3-Dimensional Flow Structures for an NREL S826 Wing Section of Finite Span,” *Energies*, vol. 11, no. 6, p. 1418, Jun. 2018, doi: 10.3390/en11061418.

SARTOR, F. and TIMME, S., “Reynolds-Averaged Navier-Stokes Simulations of Shock Buffet on Half Wing-Body Configuration.” AIAA Paper 2015-1939, 2015, doi: 10.2514/6.2015-1939.

SARTOR, F. and TIMME, S., “Mach number effects on buffeting flow on a half wing-body configuration,” *International Journal of Numerical Methods for Heat & Fluid Flow*, vol. 26, no. 7, pp. 2066–2080, 2016, doi: 10.1108/HFF-07-2015-0283.

SARTOR, F. and TIMME, S., “Delayed Detached–Eddy Simulation of Shock Buffet on Half Wing–Body Configuration,” *AIAA Journal*, vol. 55, no. 4, pp. 1230–1240, 2017, doi: 10.2514/1.J055186.

SARTOR, F., METTOT, C., and SIPP, D., “Stability, Receptivity, and Sensitivity Analyses of Buffeting Transonic Flow over a Profile,” *AIAA Journal*, vol. 53, pp. 1980–1993, 2015, doi: 10.2514/1.j053588.

SCHEWE, G., “Reynolds-number effects in flow around more-or-less bluff bodies,” *Journal of Wind Engineering and Industrial Aerodynamics*, vol. 89, no. 14-15, pp. 1267–1289, 2001, doi: 10.1016/S0167-6105(01)00158-1.

SCHMID, P. J., DE PANDO, M. F., and PEAKE, N., “Stability analysis for  $n$ -periodic arrays of fluid systems,” *Physical Review Fluids*, vol. 2, no. 11, Nov. 2017, doi: 10.1103/PhysRevFluids.2.113902.

SHUR, M. L., SPALART, P. R., STRELETS, M. K., and TRAVIN, A. K., “A hybrid RANS-LES approach with delayed-DES and wall-modelled LES capabilities,” *International Journal of Heat and Fluid Flow*, vol. 29, no. 6, pp. 1638–1649, 2008, doi: 10.1016/j.ijheatfluidflow.2008.07.001.

SIPP, D., MARQUET, O., MELIGA, P., and BARBAGALLO, A., “Dynamics and Control of Global Instabilities in Open-Flows: A Linearized Approach,” *Applied Mechanics Reviews*, vol. 63, no. 3, p. 030801, 2010, doi: 10.1115/1.4001478.

SORENSEN, D. C., “Implicit Application of Polynomial Filters in a  $k$ -Step Arnoldi Method,” *SIAM Journal on Matrix Analysis and Applications*, vol. 13, no. 1, pp. 357–385, Jan. 1992, doi: 10.1137/0613025.

SPALART, P. R. and VENKATAKRISHNAN, V., “On the role and challenges of CFD in the aerospace industry,” *The Aeronautical Journal*, vol. 120, no. 1223, pp. 209–232, 2016, doi: 10.1017/aer.2015.10.

SPALART, P. R., JOU, W.-H., STRELETS, M., and ALLMARAS, S. R., “Comments on the Feasibility of LES for Wings, and on a Hybrid RANS/LES Approach,” in *Advances in DNS/LES*, LIU, C., LIU, Z., and SAKELL, L., Eds. Columbus, Ohio, United States: Greyden Press, 1997, pp. 137–147.

SPALART, P. R., DECK, S., SHUR, M. L., SQUIRES, K. D., STRELETS, M. K., and TRAVIN, A., “A New Version of Detached-eddy Simulation, Resistant to Ambiguous Grid Densities,” *Theoretical and Computational Fluid Dynamics*, vol. 20, no. 3, pp. 181–195, 2006, doi: 10.1007/s00162-006-0015-0.

SPALART, P., “Trends in turbulence treatments.” AIAA Paper 2000-2306, 2000, doi: 10.2514/6.2000-2306.

SPALART, P. R., “Young-Person’s Guide to Detached-Eddy Simulation Grids,” NASA Langley Research Center, Tech. Rep. NASA CR-2001-211032, 2001.

SPALART, P. R., “Detached-Eddy Simulation,” *Annual Review of Fluid Mechanics*, vol. 41, no. 1, pp. 181–202, 2009, doi: 10.1146/annurev.fluid.010908.165130.

SPALART, P. R., “Prediction of Lift Cells for Stalling Wings by Lifting-Line Theory,” *AIAA Journal*, vol. 52, no. 8, pp. 1817–1821, 2014, doi: 10.2514/1.J053135.

SPALART, P. R., “Philosophies and fallacies in turbulence modeling,” *Progress in Aerospace Sciences*, vol. 74, pp. 1–15, 2015, doi: 10.1016/j.paerosci.2014.12.004.

SPALART, P. R. and ALLMARAS, S. R., “A One-Equation Turbulence Model for Aerodynamic Flows.” AIAA Paper 1992-0439, 1992, doi: 10.2514/6.1992-439.

SPALART, P., “Strategies for turbulence modelling and simulations,” *International Journal of Heat and Fluid Flow*, vol. 21, no. 3, pp. 252–263, 2000, doi: 10.1016/S0142-727X(00)00007-2.

SUGIOKA, Y., NAKAKITA, K., and ASAI, K., “Non-intrusive unsteady PSP technique for investigation of transonic buffet,” in *ICAS-2016*, 2016.

SUGIOKA, Y., KOIKE, S., NAKAKITA, K., NUMATA, D., NONOMURA, T., and ASAI, K., “Experimental analysis of transonic buffet on a 3D swept wing using fast-response pressure-sensitive paint,” *Experiments in Fluids*, vol. 59, no. 6, Jun. 2018, doi: 10.1007/s00348-018-2565-5.

SWANSON, R. and TURKEL, E., “On central-difference and upwind schemes,” *Journal of Computational Physics*, vol. 101, no. 2, pp. 292–306, 1992, doi: 10.1016/0021-9991(92)90007-L.

TAIRA, K., BRUNTON, S. L., DAWSON, S. T. M., ROWLEY, C. W., COLONIUS, T., MCKEON, B. J., SCHMIDT, O. T., GORDEYEV, S., THEOFILIS, V., and UKEILEY, L. S., “Modal Analysis of Fluid Flows: An Overview,” *AIAA Journal*, vol. 55, no. 12, pp. 4013–4041, 2017, doi: 10.2514/1.J056060.

TATSUMI, S., MARTINELLI, L., and JAMESON, A., “A new high resolution scheme for compressible viscous flows with shocks.” AIAA Paper 1995-0466, 1995, doi: 10.2514/6.1995-466.

THEOFILIS, V., HEIN, S., and DALLMANN, U., “On the origins of unsteadiness and three-dimensionality in a laminar separation bubble,” *Philosophical Transactions of the Royal Society A: Mathematical, Physical and Engineering Sciences*, vol. 358, no. 1777, pp. 3229–3246, Dec. 2000, doi: 10.1098/rsta.2000.0706.

THEOFILIS, V., “Advances in global linear instability analysis of nonparallel and three-dimensional flows,” *Progress in Aerospace Sciences*, vol. 39, no. 4, pp. 249–315, 2003, doi: 10.1016/S0376-0421(02)00030-1.

THEOFILIS, V., “Global Linear Instability,” *Annual Review of Fluid Mechanics*, vol. 43, no. 1, pp. 319–352, 2011, doi: 10.1146/annurev-fluid-122109-160705.

THIERY, M. and COUSTOLS, E., “Numerical prediction of shock induced oscillations over a 2D airfoil: Influence of turbulence modelling and test section walls,” *International Journal of Heat and Fluid Flow*, vol. 27, no. 4, pp. 661–670, 2006, doi: 10.1016/j.ijheatfluidflow.2006.02.013.

THOMAS, J. and DOWELL, E., “Discrete Adjoint Design Optimization Approach for Increasing Transonic Buffet Onset Angle-of-Attack.” AIAA Paper 2015-3435, 2015, doi: 10.2514/6.2015-3435.

TIMME, S. and SARTOR, F., “Passive Control of Transonic Buffet Onset on a Half Wing-Body Configuration,” in *International Forum on Aeroelasticity and Structural Dynamics*, Saint Petersburg, Russia, 2015.

TIMME, S., “Global instability of wing shock buffet,” *arXiv preprint arXiv:1806.07299*, 2018.

TIMME, S., “Global Shock Buffet Instability on NASA Common Research Model.” San Diego, California: AIAA Paper 2019-0037, Jan. 2019, doi: 10.2514/6.2019-0037.

TIMME, S., “Global instability of wing shock-buffet onset,” *Journal of Fluid Mechanics*, vol. 885, p. A37, Feb. 2020, doi: 10.1017/jfm.2019.1001.

TIMME, S. and THORMANN, R., “Towards Three-Dimensional Global Stability Analysis of Transonic Shock Buffet.” AIAA Paper 2016-3848, 2016, doi: 10.2514/6.2016-3848.

VAN DAM, C., “The aerodynamic design of multi-element high-lift systems for transport airplanes,” *Progress in Aerospace Sciences*, vol. 38, no. 2, pp. 101–144, Feb. 2002, doi: 10.1016/S0376-0421(02)00002-7.

VAN LEER, B., “Flux-vector splitting for the Euler equations,” in *Eighth International Conference on Numerical Methods in Fluid Dynamics*, ARAKI, H., EHLERS, J., HEPP, K., KIPPENHAHN, R., WEIDENMÜLLER, H. A., ZITTARTZ, J., and KRAUSE, E., Eds. Berlin, Heidelberg: Springer Berlin Heidelberg, 1982, vol. 170, pp. 507–512, doi: 10.1007/3-540-11948-5\_66.

WALES, C., GAITONDE, A. L., JONES, D. P., AVITABILE, D., and CHAMPNEYS, A. R., “Numerical continuation of high Reynolds number external flows,” *International Journal for Numerical Methods in Fluids*, vol. 68, no. 2, pp. 135–159, Jan. 2012, doi: 10.1002/flid.2497.

WEIHS, D. and KATZ, J., “Cellular patterns in poststall flow over unswept wings,” *AIAA Journal*, vol. 21, no. 12, pp. 1757–1759, 1983, doi: 10.2514/3.8321.

WINKELMANN, A. E. and BARLOW, J. B., “Flowfield Model for a Rectangular Planform Wing beyond Stall,” *AIAA Journal*, vol. 18, no. 8, pp. 1006–1008, 1980, doi: 10.2514/3.50846.

WITHERDEN, F., JAMESON, A., and ZINGG, D., “The Design of Steady State Schemes for Computational Aerodynamics,” in *Handbook of Numerical Analysis*. Elsevier, 2017, vol. 18, pp. 303–349, doi: 10.1016/bs.hna.2016.11.006.

XIAO, Q., TSAI, H.-M., and LIU, F., “Numerical Study of Transonic Buffet on a Supercritical Airfoil,” *AIAA Journal*, vol. 44, no. 3, pp. 620–628, Mar. 2006, doi: 10.2514/1.16658.

XU, S., TIMME, S., and BADCOCK, K. J., “Krylov subspace recycling for linearised aerodynamics analysis using DLR-TAU,” in *International Forum on Aeroelasticity and Structural Dynamics*, 2015.

YON, S. A. and KATZ, J., “Study of the Unsteady Flow Features on a Stalled Wing,” *AIAA Journal*, vol. 36, no. 3, pp. 305–312, 1998, doi: 10.2514/2.372.

YOON, S. and JAMESON, A., “Lower-upper Symmetric-Gauss-Seidel method for the Euler and Navier-Stokes equations,” *AIAA Journal*, vol. 26, no. 9, pp. 1025–1026, 1988, doi: 10.2514/3.10007.

ZAMAN, K. B. M. Q., BAR-SEVER, A., and MANGALAM, S. M., “Effect of acoustic excitation on the flow over a low- Re airfoil,” *Journal of Fluid Mechanics*, vol. 182, pp. 127–148, 1987, doi: 10.1017/S0022112087002271.

ZAMAN, K. B. M. Q., MCKINZIE, D. J., and RUMSEY, C. L., “A natural low-frequency oscillation of the flow over an airfoil near stalling conditions,” *Journal of Fluid Mechanics*, vol. 202, pp. 403–442, 1989, doi: 10.1017/S0022112089001230.

ZARUTSKAYA, T. and ARIELI, R., “On Vortical Flow Structures at Wing Stall and Beyond.” AIAA Paper 2005-4913, 2005, doi: 10.2514/6.2005-4913.

ZHANG, W. and SAMTANEY, R., “BiGlobal linear stability analysis on low-Re flow past an airfoil at high angle of attack,” *Physics of Fluids*, vol. 28, no. 4, p. 044105, 2016, doi: 10.1063/1.4945005.

## APPENDIX A Appendice to article 2

### OAT15A analysis

As verification for the implementation of the method proposed by Schmid *et al.* (2017), we have carried out a global linear stability analysis of transonic buffet of an OAT15A aerofoil in the same regime as in Crouch *et al.* (2019). A grid with the same property and the same numerical setup as the ones used for the OALT25 aerofoil are used. Fig. A.1 shows the growth rate and the frequency of the 2-D mode with respect to  $\beta$ . The results of Crouch *et al.* (2019) are also presented. One can observe that the frequencies and growth rates are close to the values found by Crouch *et al.* (2019). The trend with respect to the wavenumber is also the same. This agreement verifies the method used in this paper.

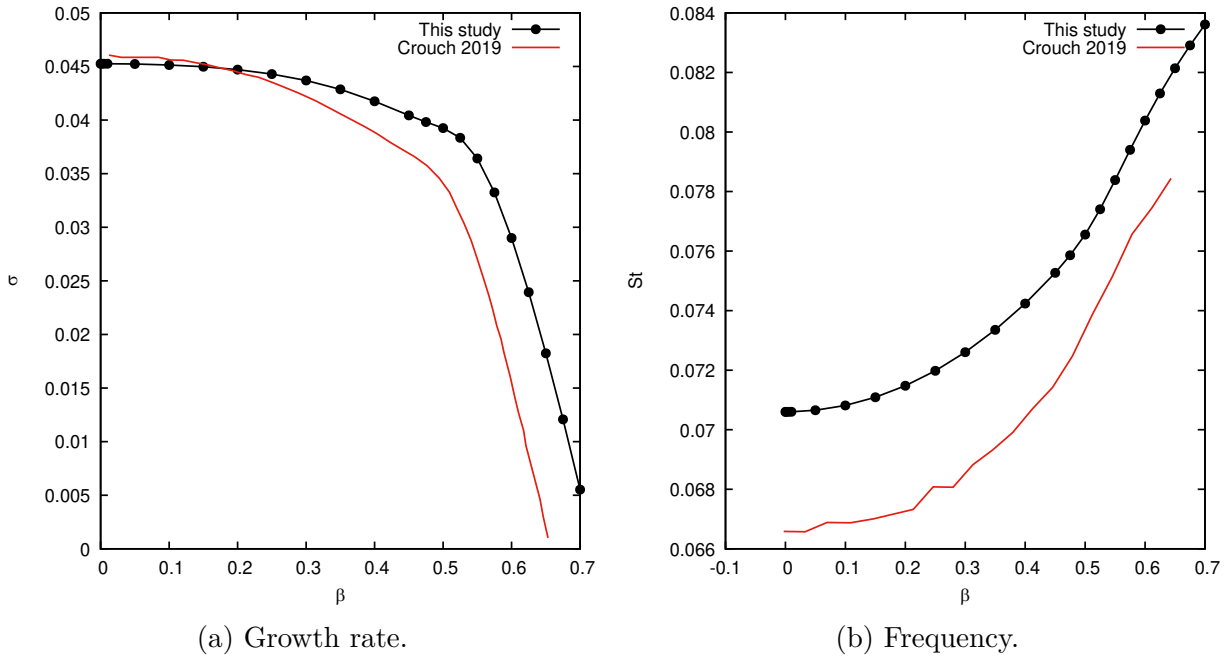


Figure A.1 – Effect of the wavenumber of the 2-D buffet mode (OAT15A,  $Re = 3 \times 10^6$ ,  $\alpha = 3.5^\circ$ ,  $\delta = 0^\circ$ ).

### Separation Metrics

This section reports separation metrics for a set of base-flows obtained in this paper. The maximum backflow velocity in the  $x$  direction  $\min(V_x)$ , the separation location  $x_s$  and the reattachment location  $x_r$ , the separation thickness measured in the direction normal to the wall  $h_s$ , the length of the separation area  $l_s = x_r - x_s$  and the projection of the separation length in the direction normal to the inflow  $l = l_s \sin \alpha$ .



Table A.1 lists the metrics of the recirculation bubble of the NACA4412 base-flows at a Reynolds number of 350 000. In every base-flow a trailing edge type separation is observed. For the base-flow on the lower branch, two zones where the backflow velocity is high are obtained. One is near the leading edge, and the other near the trailing edge. Only the maximum of these two velocities is reported.

Table A.2 lists some of the metrics of the separation zone for the base-flows of the OALT25 aerofoil at a Reynolds number of 3 million. In every case the recirculation is present from the shock wave to the trailing edge. However, for the lower angle of attack the recirculation is thicker at the shock foot and near the trailing edge. For this reason, two separation zone thicknesses ( $h_{s1}$  and  $h_{s2}$ ) are reported. These two zones of the recirculation bubble can be seen in fig A.2.

Table A.3 reports the separation metrics of the NACA0012 base-flows at a Reynolds number of  $10^7$ . For the specific case of Mach number of 0.3 and 0.4 a small recirculation bubble is obtained at the foot of a small shock wave near the leading edge. The metrics are reported for the second trailing edge type of separation. For higher Mach number, flow separation occurs at the shock foot. For the Mach number of 0.2, only a trailing edge type separation is obtained.

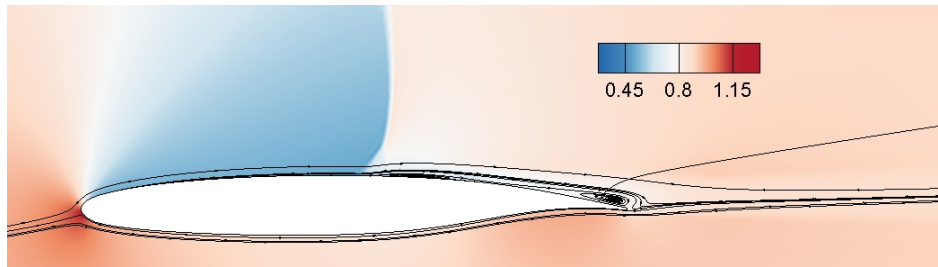


Figure A.2 – Density contours of the base-flow (OALT25,  $M = 0.7352$ ,  $Re = 3 \times 10^6$ ,  $\alpha = 4.0^\circ$ ,  $\delta = 0^\circ$ ).

Table A.1 – Description of the recirculation bubble associated with the NACA4412 base-flows

$\alpha$	$\delta$	$\min(V_x)$	$x_s$	$x_r$	$h_s$	$l_s$	$l$
14	0.	-0.163	0.618	1.	0.066	0.382	0.092
15.	0.	-0.187	0.518	1.	0.098	0.482	0.125
15.	10.	-0.186	0.518	1.	0.098	0.482	0.125
15.	20.	-0.184	0.527	1.	0.097	0.474	0.123
15.	30.	-0.180	0.538	1.	0.096	0.462	0.120
15.	40.	-0.174	0.562	1.	0.093	0.438	0.113
16.	0.	-0.203	0.434	1.	0.141	0.566	0.156
17.	0.	-0.209	0.351	1.	0.196	0.649	0.190
18.	0.	-0.210	0.286	1.	0.253	0.714	0.221
19.	0.	-0.208	0.212	1.	0.323	0.788	0.256
20.	0.	-0.205	0.146	1.	0.413	0.854	0.292
17. (lower branch)	0.	-0.265	0.100	1.	0.481	0.899	0.263
18. (lower branch)	0.	-0.244	0.108	1.	0.537	0.891	0.275
19. (lower branch)	0.	-0.225	0.005	1.	0.594	0.994	0.324
20. (lower branch)	0.	-0.220	0.004	1.	0.641	0.996	0.341

Table A.2 – Description of the recirculation bubble associated with the OALT25 base-flows

$\alpha$	$\delta$	$\min(V_x)$	$x_s$	$x_r$	$h_{s1}$	$h_{s2}$	$l_s$	$l$
3.5	0.	-0.115	0.563	1.	0.013	0.003	0.437	0.027
4.0	0.	-0.163	0.521	1.	0.024	0.007	0.479	0.033
4.0	10.	-0.160	0.521	1.	0.024	0.006	0.479	0.033
4.0	20.	-0.155	0.521	1.	0.024	0.006	0.479	0.033
4.0	30.	-0.146	0.521	1.	0.023	0.006	0.479	0.033
4.0	40.	-0.130	0.520	1.	0.023	0.005	0.480	0.033
4.5	0.	-0.212	0.480	1.	0.035	0.010	0.520	0.041
5.0	0.	-0.251	0.433	1.	0.047	0.014	0.567	0.049
6.0	0.	-0.301	0.338	1.	0.074	N/A	0.662	0.069
7.0	0.	-0.327	0.249	1.	0.105	N/A	0.751	0.092
8.0	0.	-0.341	0.162	1.	0.140	N/A	0.838	0.117
9.0	0.	-0.348	0.080	1.	0.181	N/A	0.920	0.144

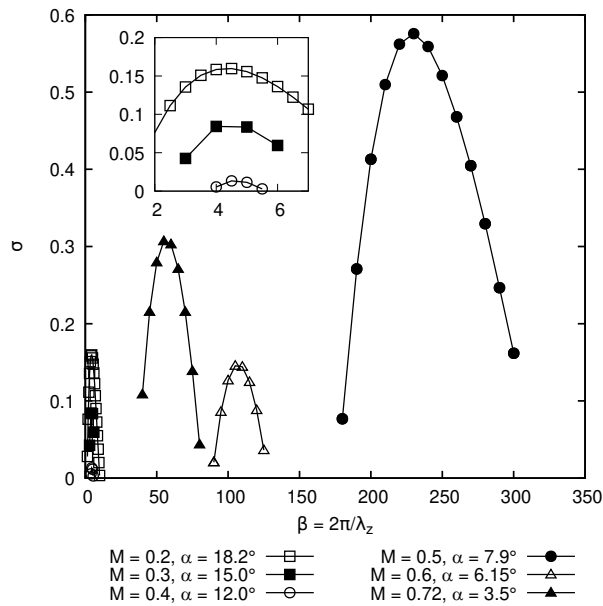
Table A.3 – Description of the recirculation bubble associated with the NACA0012 base-flows

Mach	$\alpha$	$\min(V_x)$	$x_s$	$x_r$	$h_s$	$l_s$	$l$
0.20	18.20	-0.189	0.581	1.000	0.061	0.419	0.131
0.30	15.00	-0.181	0.564	1.000	0.052	0.436	0.113
0.40	12.00	-0.169	0.544	1.000	0.051	0.456	0.095
0.50	7.90	-0.274	0.060	0.090	0.001	0.029	0.004
0.60	6.15	-0.215	0.163	0.226	0.002	0.063	0.007
0.72	3.50	-0.174	0.380	0.506	0.004	0.126	0.008

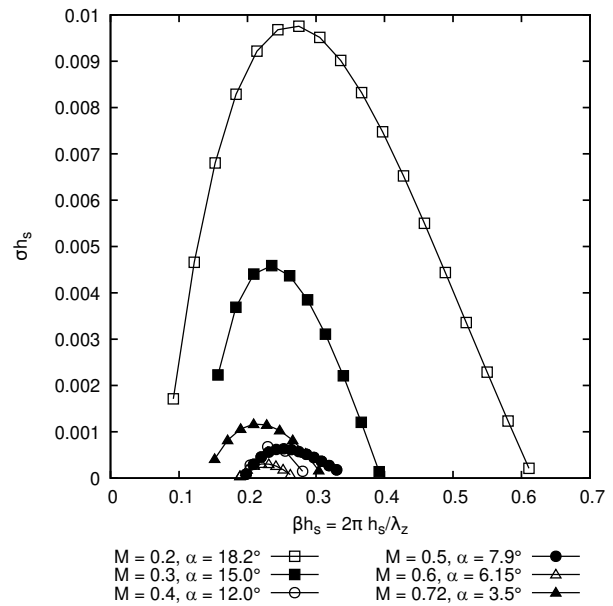
### Scaling of the 3D unstable modes

In the section 4.6 of the article, a scaling of the wavenumber of the stall and buffet cells by the separation height was proposed. Two other scalings were investigated, the scaling by the length of the separation  $l_s$  and projection of the separation length in the direction normal to the inflow  $l$ . These scalings are shown in fig. A.3. By using the length of the separation, a proper scaling is obtained for the subsonic and transonic cases separately. But this scaling does not hold between these two flow regimes. The scaling by the projection of the separation length does not hold between Mach numbers.

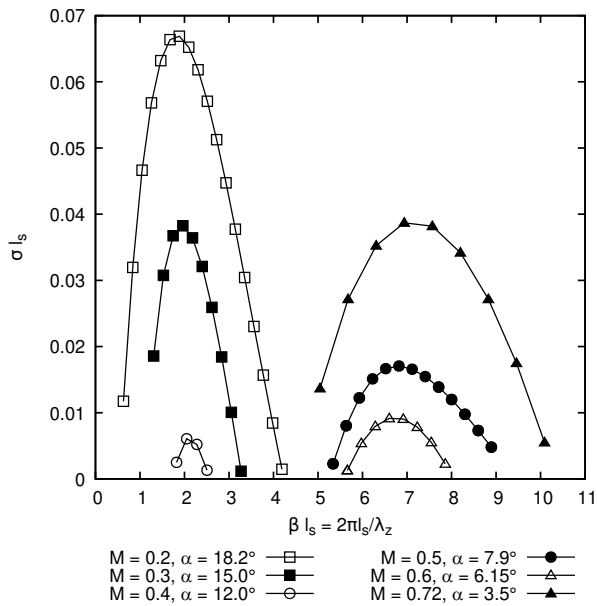
For the case of the NACA0012 aerofoil, the height of the separation zone has been found to be a proper scaling to relate the size of the buffet cells and stall cells. Fig. A.4 shows the application of this scaling factor to the NACA4412 aerofoil in stall conditions and the OALT25 aerofoil in buffet conditions. The application of this scaling results in values of the normalized wavenumber  $\beta h_s$  around 0.3 and 0.2 for the NACA4412 and the OALT25 respectively at the onset of the instabilities.



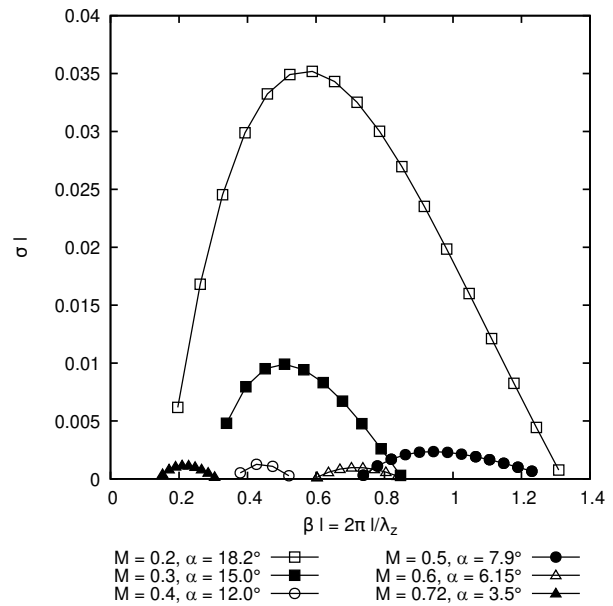
(a) Normalized by the chord length.



(b) Normalized by the separation height.

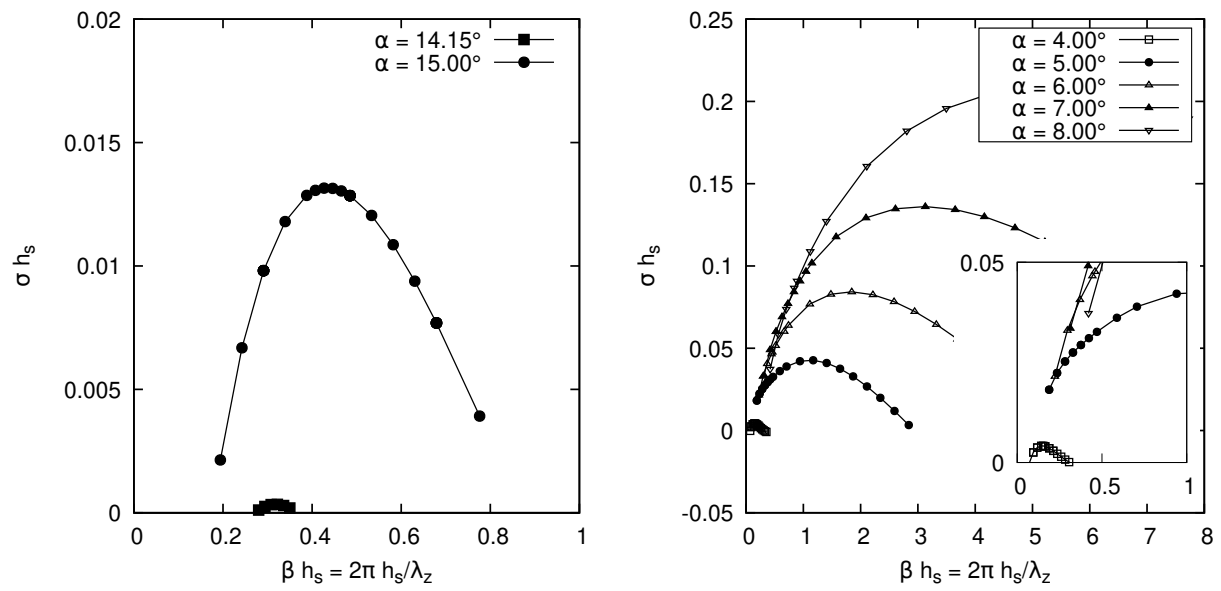


(c) Normalized by the separation length.



(d) Normalized by the projection of the separation length.

Figure A.3 – Effect of the Mach number and angle of attack on the growth rate of the three-dimensional mode (NACA0012,  $Re = 10^7$ ,  $\delta = 0^\circ$ ).



(a) NACA4412,  $M = 0.2$ ,  $Re = 350\,000$  and  $\delta = 0.0$  (b) OALT25,  $M = 0.7352$ ,  $Re = 3 \times 10^6$  and  $\delta = 0.0$

Figure A.4 – Scaling of the three-dimensional modes by the separation height.

## APPENDIX B Newton continuation

### Numerical method

In the chapters 2 and 4, the case of a NACA4412 airfoil at a Reynolds number of 350 000 and a Mach number of 0.2 was studied. For this test case two solution branches were observed. Nevertheless, no link was reported between these two branches. However, previous work by Wales *et al.* (2012) showed that these two solution branches are in fact a single series of solutions linked by a continuous set of converged solutions. To obtain these solutions, one must use a continuation technique based on a Newton algorithm. The SFD technique as well as a Newton continuation method has been used to converge the solutions presented in chapters 2 and 4. The latter was carried out by starting with two solutions  $\mathbf{W}_{i-2}$  and  $\mathbf{W}_{i-1}$ , such that  $\mathbf{R}(\mathbf{W}_{i-2}) = \mathbf{R}(\mathbf{W}_{i-1}) = 0$ , computed with the elsA flow solver. With  $\mathbf{R}$  the residual, which is the summation of the convective fluxes, viscous fluxes and source terms of the RANS equations, including the turbulence model. From these solutions, one uses a linear extrapolation to get an estimate of the next solution  $\bar{\mathbf{W}}_i$ :

$$\bar{\mathbf{W}}_i = \mathbf{W}_{i-1} + h \frac{\mathbf{W}_{i-1} - \mathbf{W}_{i-2}}{|\mathbf{W}_{i-1} - \mathbf{W}_{i-2}|} \quad (\text{B.1})$$

at an angle of attack

$$\alpha_i = \alpha_{i-1} + h \frac{\alpha_{i-1} - \alpha_{i-2}}{|\alpha_{i-1} - \alpha_{i-2}|} \quad (\text{B.2})$$

with  $h$  a user-selected step length. Then the solution is corrected using a Newton algorithm to converge the real solution  $\mathbf{W}_i$ . The Newton algorithm is derived from the RANS equations with the turbulence model, which can be written in simplified form as:

$$\mathbf{V} \frac{\partial \bar{\mathbf{W}}_i}{\partial t} + \mathbf{R}(\bar{\mathbf{W}}_i) = 0 \quad (\text{B.3})$$

With a forward Euler scheme this equation reads:

$$\mathbf{V} \frac{\bar{\mathbf{W}}_i^{n+1} - \bar{\mathbf{W}}_i^n}{\Delta t} + \mathbf{R}(\bar{\mathbf{W}}_i^{n+1}) = 0 \quad (\text{B.4})$$

One can linearize the residual as:

$$R(\bar{\mathbf{W}}_i^{n+1}) \approx R(\bar{\mathbf{W}}_i^n) + \left. \frac{\partial \mathbf{R}}{\partial \mathbf{W}} \right|_{\bar{\mathbf{W}}_i^n} (\bar{\mathbf{W}}_i^{n+1} - \bar{\mathbf{W}}_i^n) \quad (\text{B.5})$$

Combining the equations B.4 and B.5, the new solution is :

$$\bar{\mathbf{W}}_i^{n+1} = \bar{\mathbf{W}}_i^n - \left( \frac{\mathbf{V}}{\Delta t} + \frac{\partial \mathbf{R}}{\partial \mathbf{W}} \Big|_{\bar{\mathbf{W}}_i^n} \right)^{-1} R(\bar{\mathbf{W}}_i^n) \quad (\text{B.6})$$

The time step  $\Delta t$  can go to infinity if the solution estimate is in the convergence radius, but can be defined as a local time step with a CFL condition for more stability. This CFL number can be increased with the residual convergence. The Jacobian  $\frac{\partial \mathbf{R}}{\partial \mathbf{W}}$  is computed with the fully discrete approach presented in chapter 4. Thus, this scheme has a quadratic convergence rate and converges in a few iterations. These sub-iterations are carried out until  $R(\bar{\mathbf{W}}_i^{n+1}) = 0$ . Then  $\mathbf{W}_i = \bar{\mathbf{W}}_i^{n+1}$  and the process is restarted from equations B.1 and B.2 for the next angle of attack. As such, this method is a predictor corrector one. However, one can see that at the limit of the solution branch  $\frac{\partial \mathbf{W}}{\partial \alpha} \rightarrow \infty$ . For this reason, this method will fail to find the solution past this folding point. To solve this issue, one can use the pseudo-arclength technique (Wales *et al.*, 2012; Busquet, 2020). The difference between the Newton and pseudo-arclength methods is shown in Figure B.1. Of course in these figures  $\mathbf{W}$  represents all the degrees of freedom of the RANS equations. In the case of the Newton iteration, the solution is corrected at a constant angle of attack. Hence, the iteration will only be able to find a solution on the lower branch. In the application this solution is not in the convergence radius, and the solver will diverge. The pseudo-arclength method works by adding the continuation parameter (here the angle of attack) to the degrees of freedom. Hence, one needs to add an equation for this new variable. This equation restricts the solution domain to the hyperplane normal to the gradient between previous solutions. This allows the method to follow the solution branch even if there is a folding point, as schematized in Figure B.1b.

Since  $\alpha$  is now a dependent variable, one must define a new independent variable. This is done by adding a new parameter  $\gamma$  which is the linearization of the arclength between two solutions and the new independent variables are  $\mathbf{X} = [\mathbf{W}, \alpha]$ . The added equation is:

$$g(\mathbf{W}, \alpha, \gamma) = \frac{\partial \mathbf{W}}{\partial \gamma} \Delta \mathbf{W} + \frac{\partial \alpha}{\partial \gamma} \Delta \alpha - \Delta \gamma = 0 \quad (\text{B.7})$$

Hence the equation B.6 becomes :

$$\begin{bmatrix} \frac{\partial \mathbf{R}(\mathbf{X})}{\partial \mathbf{X}} + \frac{\mathbf{V}}{\Delta t} \\ \frac{\partial g}{\partial \mathbf{X}} \end{bmatrix} \begin{pmatrix} \Delta \mathbf{W} \\ \Delta \alpha \end{pmatrix}^n = \begin{bmatrix} \frac{\partial \mathbf{R}(\mathbf{W}, \alpha)}{\partial \mathbf{W}} + \frac{\mathbf{V}}{\Delta t} & \frac{\partial \mathbf{R}(\mathbf{W}, \alpha)}{\partial \alpha} \\ \frac{\partial g}{\partial \mathbf{W}} & \frac{\partial g}{\partial \alpha} \end{bmatrix} \begin{pmatrix} \Delta \mathbf{W} \\ \Delta \alpha \end{pmatrix}^n = \begin{pmatrix} -\mathbf{R}(\mathbf{W}) \\ -g \end{pmatrix}^n \quad (\text{B.8})$$

With,  $\frac{\partial g}{\partial \mathbf{X}} = \frac{\mathbf{X}_{i-1} - \mathbf{X}_{i-2}}{|\mathbf{X}_{i-1} - \mathbf{X}_{i-2}|}$  and the term  $\frac{\partial \mathbf{R}(\mathbf{W}, \alpha)}{\partial \alpha}$  is evaluated using a finite difference after computing the residual with a perturbed  $\alpha$ . For convenience, Wales *et al.* (2012) write this system as:

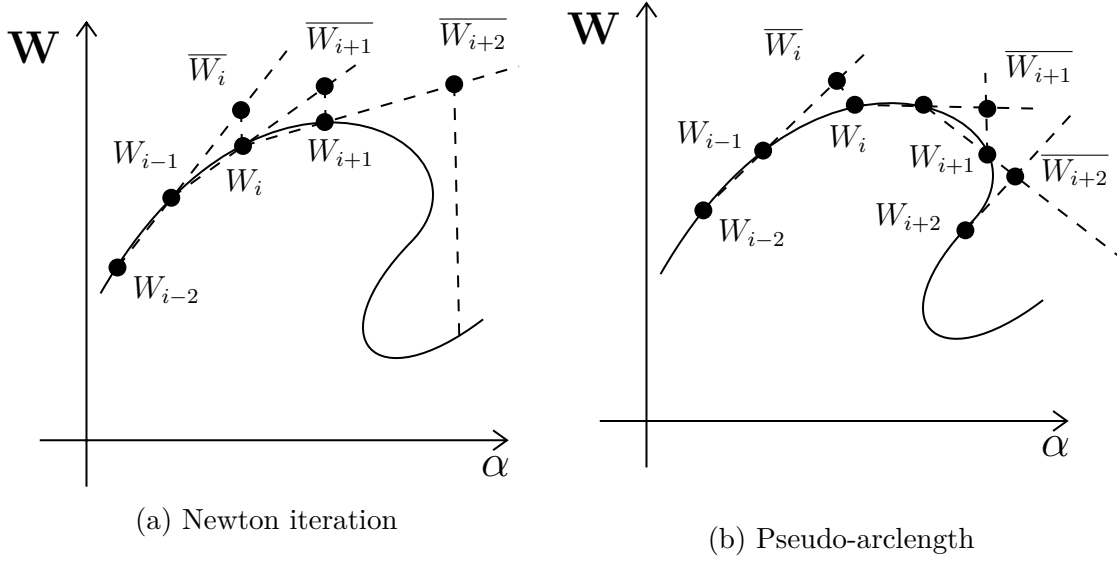


Figure B.1 – Continuation method. (Adapted from Wales *et al.* (2012))

$$\begin{bmatrix} A & b \\ c^T & d \end{bmatrix} \begin{pmatrix} x \\ y \end{pmatrix} = \begin{pmatrix} f \\ g \end{pmatrix} \quad (\text{B.9})$$

and the solution procedure of Govaerts (1991) is used

$$A^T w = c \quad (\text{B.10})$$

$$\delta^* = d - w^t b \quad (\text{B.11})$$

$$Av = b \quad (\text{B.12})$$

$$\delta = d - c^t v \quad (\text{B.13})$$

$$y_1 = \frac{g - w^t f}{\delta^*} \quad (\text{B.14})$$

$$f_1 = f - b y_1 \quad (\text{B.15})$$

$$g_1 = g - d y_1 \quad (\text{B.16})$$

$$A\xi = f_1 \quad (\text{B.17})$$

$$y_2 = \frac{g_1 - c^t \xi}{\delta} \quad (\text{B.18})$$

$$x = \xi - v y_2 \quad (\text{B.19})$$

$$y = y_1 + y_2 \quad (\text{B.20})$$

This method prevents the inversion of the complete left-hand side. This is advantageous because the complete matrix is large and, even though the portion A of the matrix is sparse,



$c$  and  $d$  are dense vectors which can significantly increase the cost of the inversion.

## Numerical results

Figure B.2 shows the lift polar obtained using the Newton continuation and the pseudo-arclength method. Using this techniques, it is possible to obtain a set of solutions connecting the two branches of solutions previously shown in Figure 4.2. As such, there is in fact only one solution branch. This result is also shown for several sweep angles. One can observe that the sweep angle has an effect on these lift polars. This effect is small for the low angle of attacks, near the starting point of the continuation method, but becomes larger as the angle of attack increases.

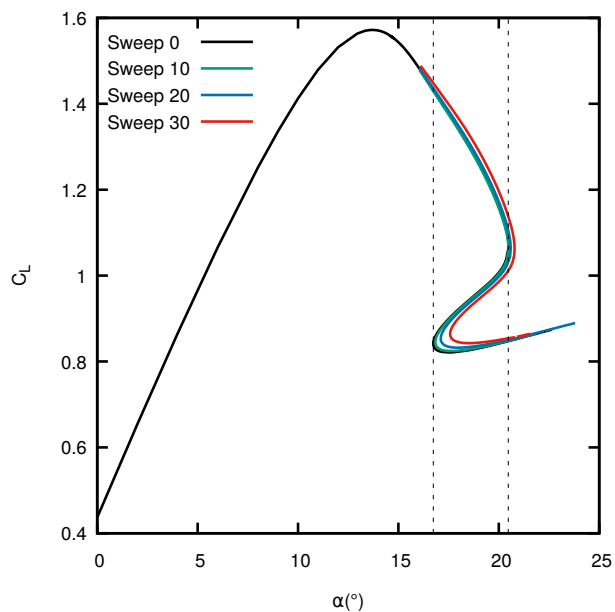


Figure B.2 – Lift curve for the 2-D steady solutions with the pseudo-arclength method (NACA4412,  $Re = 350\,000$ ,  $M = 0.2$ ).

All these solutions are fully converged and thus proper base-flows for a global stability analysis. Figure B.3 shows the base-flows and the unstable two-dimensional modes on the three branches. Hence, three base-flows and three unstable modes can be found for a single flow condition. The spectrum obtained by following the two-dimensional mode from the upper branch (black) to the lower one (blue) by passing through the middle one (red) is shown in Figure B.4. One can observe that the solutions on the middle branch fill the discontinuity between the upper and lower branches.

Figure B.5 shows the growth rate of the three-dimensional stall cell modes along the continuous solution branch. The points in red are located on the middle branch. One can observe the growth rate is maximal on the middle branch between 17.0 deg and 18.0

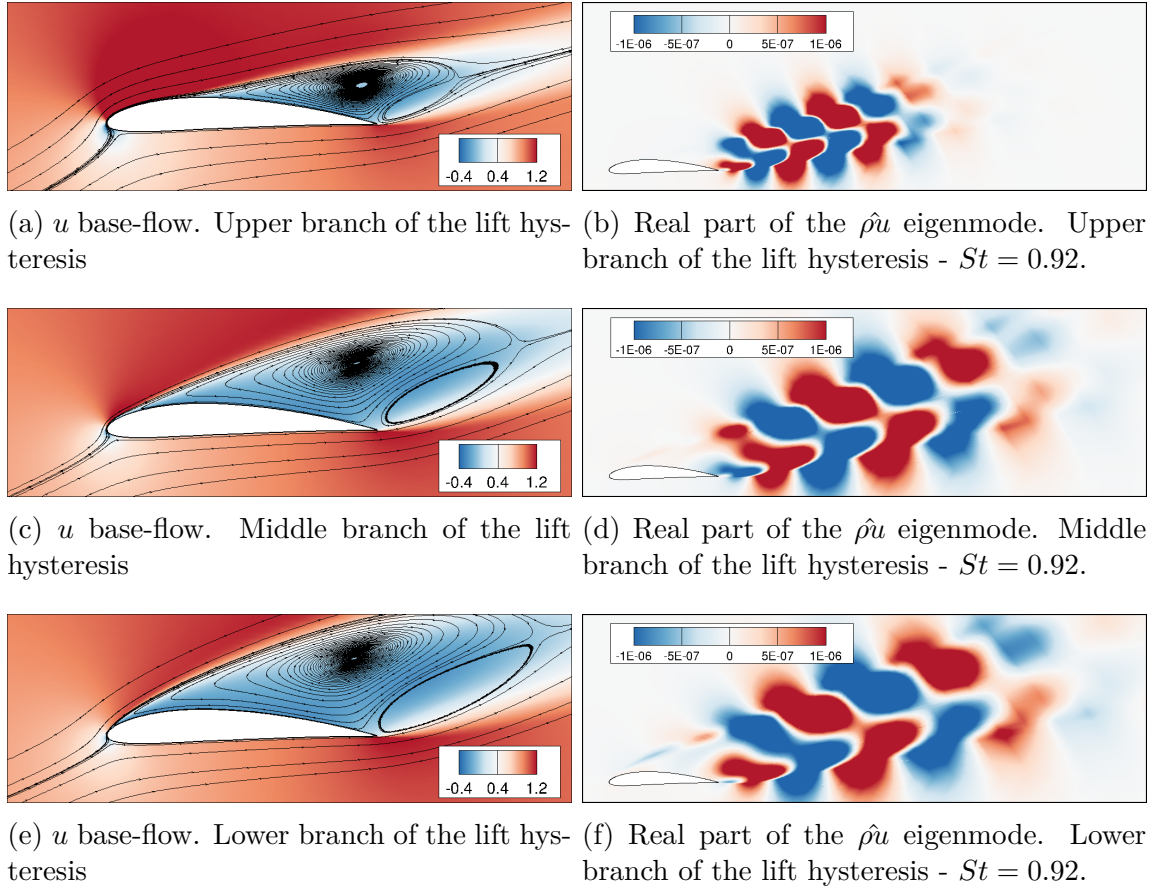


Figure B.3 – Flow visualisation of the (a): base-flow and (b): 2-D unstable mode on the two branches of the lift hysteresis (NACA4412,  $M = 0.2$ ,  $Re = 350\,000$ ,  $\alpha = 18.0^\circ$ ,  $\delta = 0.0^\circ$ ,  $\beta = 0.0$ .)

deg which is near the inflection point of the lift polar. The variation of the growth rate also flattens on the middle branch of the lift hysteresis. Nevertheless these unstable modes connect continuously the lower and upper branches of the lift polar.

Chapter 4 analysed in detail the case at an angle of attack of  $15^\circ$  on the upper branch. Figure B.6 shows the growth rate and the Strouhal number of the three-dimensional mode found on the upper branch of the lift polar at an angle of attack of  $18^\circ$ . The trend observed for an angle of attack of  $15^\circ$  holds. The sweep angle has a stabilizing effect and the Strouhal number is proportional to the sweep angle and the wavenumber. Figure B.7 shows the growth rates and the Strouhal numbers on the middle branch for several sweep angles. The growth rates are larger than those on the upper branch (Figure B.6a), which is consistent with the results in Figure B.5. The mode is also unstable over a broader range of  $\beta$ . This is true up to the point where the mode is unstable for  $\beta = 0$  which is a two-dimensional mode. For the Strouhal number, the proportionality to the wavenumber and sweep angle is still true, but the constant found in the URANS simulations at an angle of attack of  $15^\circ$  does not hold.

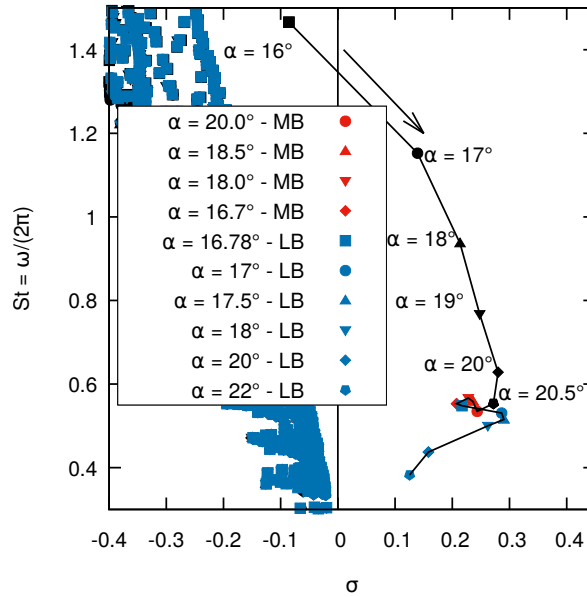


Figure B.4 – Effect of the angle of attack on the spectra of the 2-D unstable mode (NACA4412,  $M = 0.2$ ,  $Re = 350\,000$ ,  $\delta = 0.0^\circ$ ,  $\beta = 0$ ).

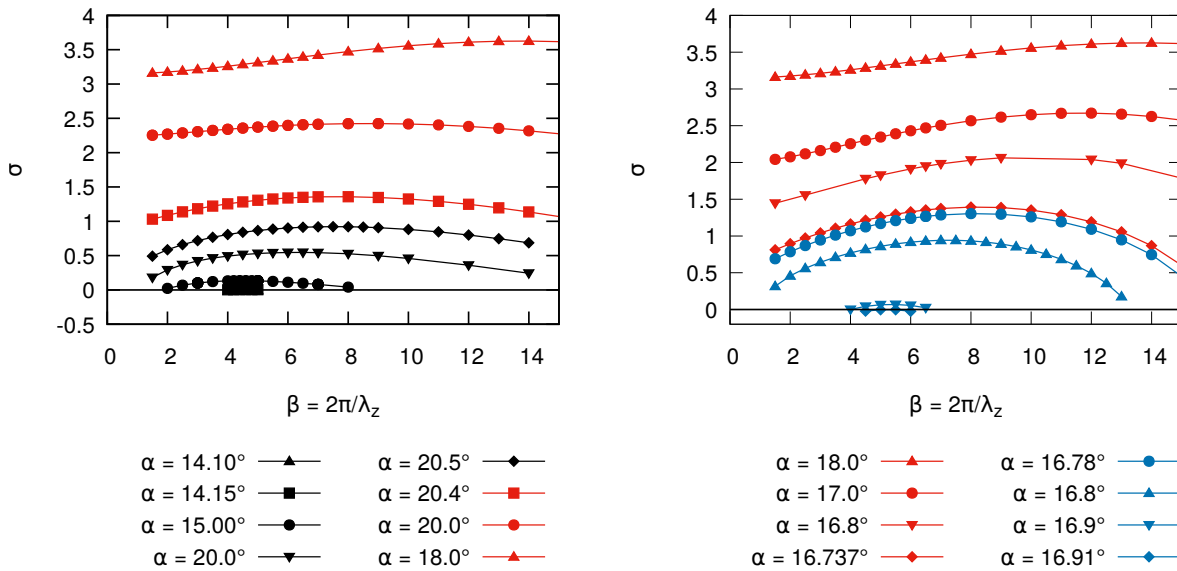


Figure B.5 – Effect of the angle of attack on the growth rate of the unstable mode (NACA4412,  $M = 0.2$ ,  $Re = 350\,000$ ,  $\delta = 0.0^\circ$ ).

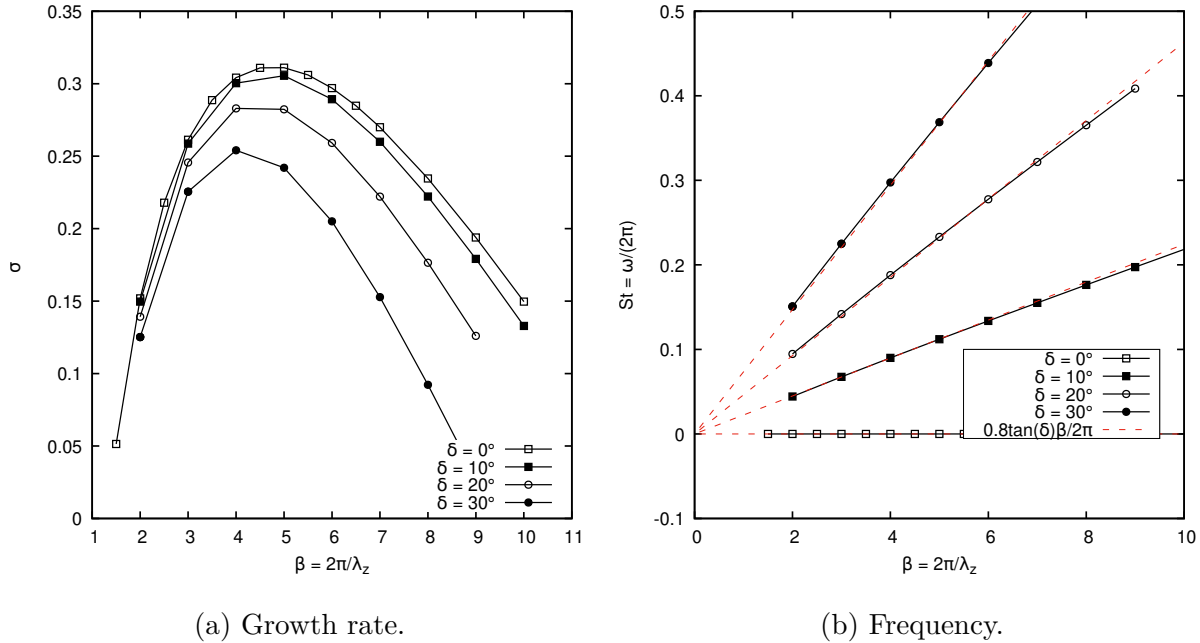


Figure B.6 – Effect of the sweep angle on the growth rate and frequency of the 3-D unstable mode (NACA4412,  $M = 0.2$ ,  $Re = 350\,000$ ,  $\alpha = 18.0^\circ$ , upper branch, black: stability analysis, red: URANS simulations ( $\alpha = 15.0^\circ$ )).

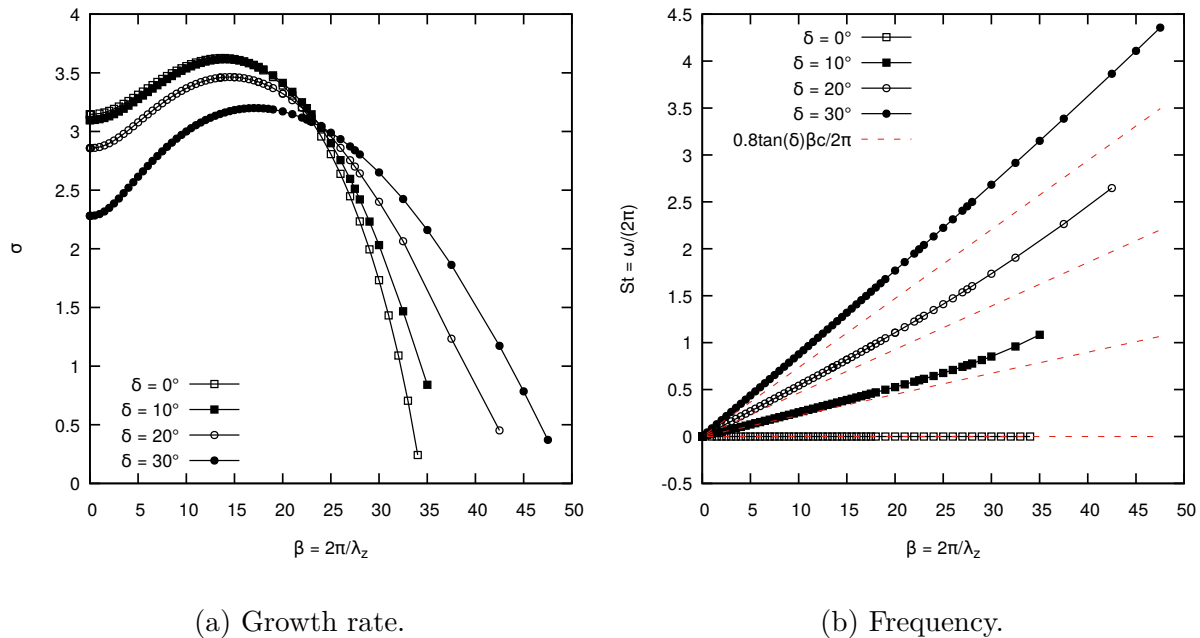


Figure B.7 – Effect of the sweep angle on the growth rate and frequency of the 3-D unstable mode (NACA4412,  $M = 0.2$ ,  $Re = 350\,000$ ,  $\alpha = 18.0^\circ$ , middle branch, black: stability analysis, red: URANS simulations ( $\alpha = 15.0^\circ$ )).

## APPENDIX C Stall cell convection analysis in the transonic buffet case

### Pressure maps

For brevity, only one graph of the pressure extracted along a line parallel to the leading edge was shown in the chapters 2 and 4. Here the prime superscripts are dropped when denoting the  $(x'y', z')$  referential,  $l_{ref} = c = 1.0$  and  $V_{ref} = 1.0$  to simplify the notation. This appendix provides these graphs for a longer time sample and for several sweep angles. Several lines of extraction are also shown. Figures. C.1, C.2 and C.3 show the pressure-time plot for sweep angles of 10 deg, 20 deg and 30 deg respectively and the instantaneous pressure coefficient at  $t = 0$ . The two subplots show two extraction lines at  $x = 0.1$  and  $0.4$ . For every sweep angle the pressure extraction on a line at  $x = 0.1$  only exhibit a two-dimensional unsteadiness. However, the pressure variation is small since these probes are located on the supersonic plateau, where the pressure is nearly constant in the buffet cycle. For the other probes, the convection behavior is also observed and the pressure fluctuations are more important. The convection speed can be identified on every line of extraction behind the shock wave location.

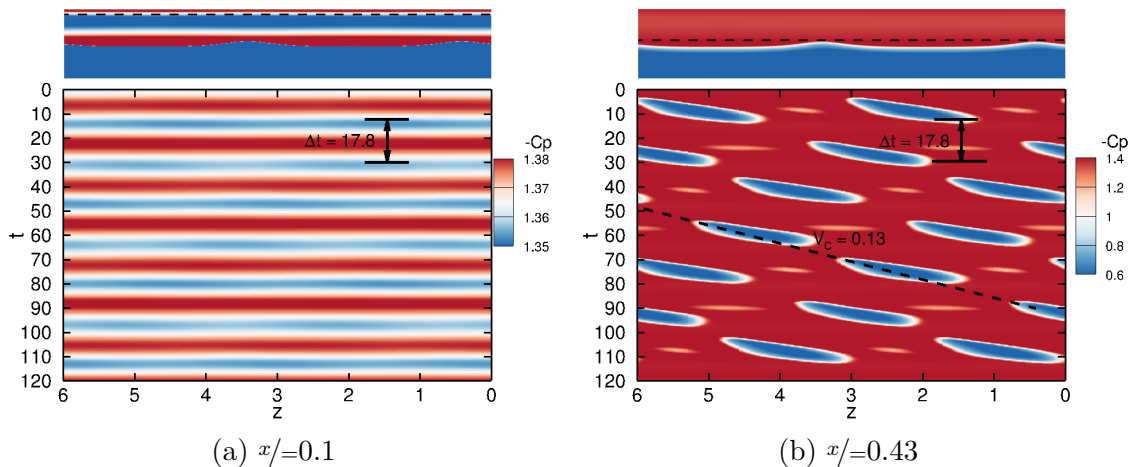


Figure C.1 – Extraction of the pressure on a line parallel to the leading edge (OALT25,  $M = 0.7352$ ,  $Re = 3 \times 10^6$ ,  $\alpha = 4^\circ$ ,  $\delta = 10^\circ$ ).

### Cross-spectrum

One can also study the convection of the stall cells using cross spectrum analyses. First, Figure C.4 shows the spectra of the pressure coefficient at several position along the chord. The selection of the spanwise position is irrelevant since infinite swept wings are considered. The same dominant frequencies as in Figure 4.9 are found. However, the frequencies associated with the convection of buffet cells are mostly observed aft of the shock wave position.

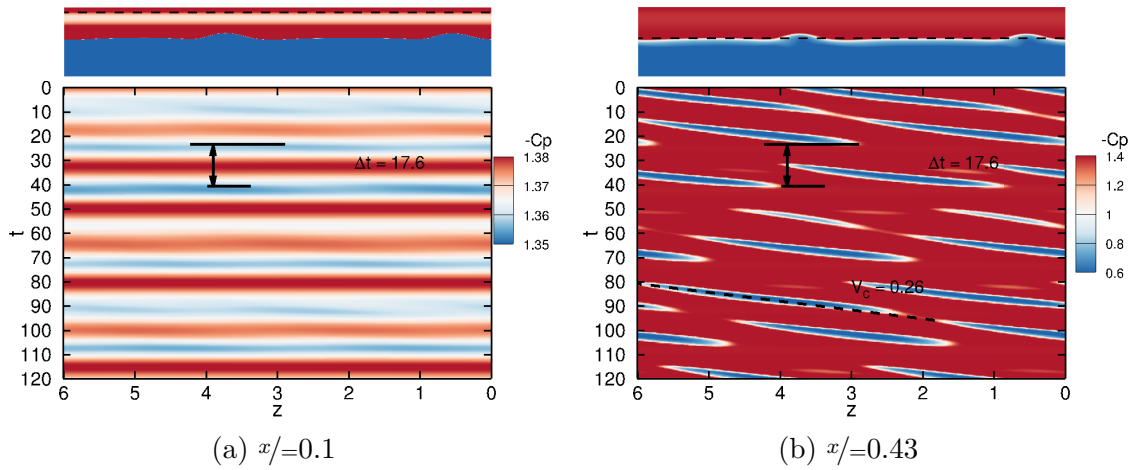


Figure C.2 – Extraction of the pressure on a line parallel to the leading edge (OALT25,  $M = 0.7352$ ,  $Re = 3 \times 10^6$ ,  $\alpha = 4^\circ$ ,  $\delta = 20^\circ$ ).

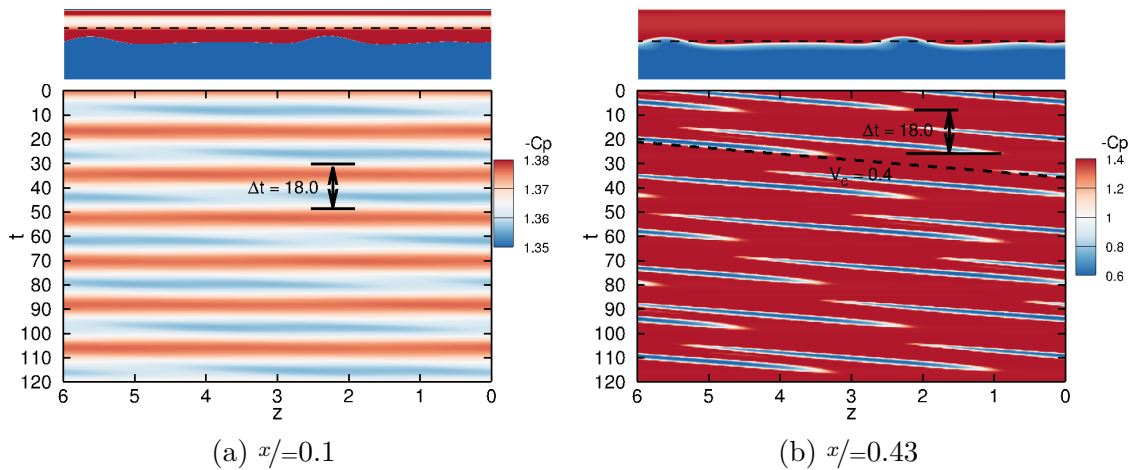


Figure C.3 – Extraction of the pressure on a line parallel to the leading edge (OALT25,  $M = 0.7352$ ,  $Re = 3 \times 10^6$ ,  $\alpha = 4^\circ$ ,  $\delta = 30^\circ$ ).

In contrary the low frequency associated with two-dimensional buffet ( $St = 0.06$ ) is also observed upstream of the shock wave position, but with a lower amplitude. This is consistent with the pressure maps results.

Next, one can look at the coherence (Figures C.5a, C.7a and C.9a) and the phase (Figures C.5b, C.7b and C.9b) of the signals in the spanwise direction for sweep angles of 10, 20 and 30 degrees respectively. These analyses allow to compute the convection velocity associated with a specific frequency as :

$$V_C = 2\pi f \frac{\Delta z}{\Delta \phi} \quad (\text{C.1})$$

The results of these analyses are summarized in the Tables C.1, C.2 and C.3.

The spectra at a sweep angle of 20 degrees are dominated by the two-dimensional buffet ( $St = 0.062$ ), the stall cell convection ( $St = 0.090$ ) and its first harmonic ( $St = 0.179$ ). The convection speed of the two convection modes ( $V_C = 0.26$ ) is consistent with previous analyses. This can be confirmed by looking at the inverse Fourier modes at these respective frequencies in Figure C.8. For the Strouhal number of 0.0621 the mode has no spanwise modulation, indicating the 2D buffet mode. The mode at a Strouhal number of 0.0899 contains the number of stall cells and this number is doubled for the Strouhal number of 0.1791. Moreover these two modes have the same spanwise convection speed ( $V_C = 0.26$ ). The two other dominant frequencies are more complex. However, these modes show more or less the wavelength of the buffet cells and are at Strouhal numbers which are the summation and difference between the two-dimensional buffet and stall cell convection ones. We can interpret these modes as the multiplication of two modes in the convective terms of the Navier-Stokes equations. By considering the first one as a standing wave with the frequency of the two-dimensional buffet ( $\omega_1$ ) and an amplitude  $\hat{p}_1$ . The second one is a traveling wave with the frequency and wavenumber of the buffet cells convection ( $\omega_2, \beta_2$ ) and an amplitude  $\hat{p}_2$ .

$$p(t, x) = \hat{p}_1(e^{i\omega_1 t} + e^{-i\omega_1 t})\hat{p}_2(e^{i(\omega_2 t - \beta_2 x)} + e^{-i(\omega_2 t - \beta_2 x)}) \quad (\text{C.2})$$

$$= \hat{p}_1\hat{p}_2 \left[ e^{i((\omega_1 + \omega_2)t - \beta_2 x)} + e^{i((\omega_1 - \omega_2)t + \beta_2 x)} + e^{i((\omega_2 - \omega_1)t - \beta_2 x)} + e^{i((- \omega_2 - \omega_1)t + \beta_2 x)} \right] \quad (\text{C.3})$$

Hence we find the combinations of frequencies observed in the spectra ( $\omega_1 + \omega_2, \omega_1 - \omega_2$  and  $\omega_2 - \omega_1$ ). These frequencies ( $\omega_3$ ) are also traveling waves and by definition have an apparent convection speed of  $V_{C,3} = \omega_3/\beta_2$ . By the same definition  $\beta_2 = \omega_2/V_{C,2}$ . Thus, the convection speed can be expressed as  $V_{C,3} = V_{C,2}\omega_3/\omega_2$ . Hence, the convection speed of these modes can be related to the convection speed of the buffet cells and the frequencies of the two combined modes. This convection speed agrees with the finding of the cross-spectrum analyses. For these reasons, these modes are the non-linear interaction between the two dominant modes.

For the sweep angle of 10 deg, many peaks can be identified in the spectra. Some of these are associated to the stall cell convection and its harmonic ( $St = 0.045, 0.09, 0.135$  and  $0.180$ ). In these cases the convection speed  $V_C = 0.135$  is obtained. The two-dimensional buffet is also present with a Strouhal number of 0.06 and a convection speed equal to zero. The Fourier modes at these frequencies are presented in Figure C.6. The other frequencies are more complex, but all have a frequency which is the summation or difference between other dominant frequencies. Moreover, the wavelengths correspond to the ones of the harmonic of the convection mode included in the mode. For example, the Strouhal number of 0.195 is the summation of the two-dimensional buffet (0.06) and the second harmonic of the stall cell

convection (0.135) and has a wavelength of 1.0, the third of the one of the stall cell convection ( $\lambda_z = 3.0$ ). Another complex case is the Strouhal number of 0.18 which is a harmonic of both the two-dimensional buffet and the convection of stall cells.

The case at a sweep angle of 30 deg is even more complex. In this case, the convection of stall cells ( $St = 0.135$ ) and the two-dimensional buffet ( $St = 0.055$ ) are still observed. A mode which is a sub-harmonic of the stall cells convection is present ( $St = 0.067$ ). Two modes which are interactions between the stall cells convection and the two-dimensional buffet are observed ( $St = 0.079$  and  $0.191$ ) with the wavelength of the convection mode ( $\lambda_z = 3.0$ ). Other modes include the sub-harmonic of the convection of stall cells and the two-dimensional buffet ( $St = 0.012$  and  $0.122$ ). Two frequencies ( $St = 0.034$  and  $0.09$ ) have a wavelength close to two (which is also observed in their Fourier modes). This is not a harmonic or sub-harmonic of the buffet cells convection. As such, these modes remain unexplained.



Table C.1 – Summary of the convection speed and spanwise wavelength associated with specific frequencies in the pressure spectrum (OALT25,  $M = 0.7352$ ,  $Re = 3 \times 10^6$ ,  $\alpha = 4^\circ$ ,  $\delta = 10^\circ$ ,  $x = 0.4$ )

Physical mechanism	$S_t$	$\frac{\Delta\phi}{\Delta z}$	$V_C$	$\lambda_z$
Interaction between 2D buffet and buffet cells ( $St = 0.060 - 0.045 = 0.015$ )	0.015	-2.11	-0.045	-2.988
Interaction between 2D buffet and buffet cells harmonic ( $St = 0.090 - 0.06 = 0.03$ )	0.029	4.21	0.043	1.492
Buffet cells convection	0.045	2.10	0.134	2.985
Two-dimensional buffet	0.060	0.00	0.000	$\infty$
First harmonic of the buffet cells convection	0.090	4.19	0.135	1.498
Interaction between 2D buffet and buffet cells ( $St = 0.060 + 0.045 = 0.105$ )	0.106	2.10	0.317	2.993
Second harmonic of the buffet cells convection	0.135	6.32	0.134	0.994
Interaction between 2D buffet and buffet cells harmonic ( $St = 0.090 + 0.06 = 0.150$ )	0.150	4.19	0.225	1.499
Third harmonic of the buffet cells convection and second harmonic of 2D buffet	0.180	8.40	0.135	0.748
Interaction between 2D buffet and second buffet cells harmonic ( $St = 0.135 + 0.06 = 0.195$ )	0.195	6.29	0.195	0.999
Interaction between 2D buffet and second buffet cells harmonic ( $St = 0.18 + 0.06 = 0.124$ )	0.240	8.50	0.177	0.739

Table C.2 – Summary of the convection speed and spanwise wavelength associated with specific frequencies in the pressure spectrum (OALT25,  $M = 0.7352$ ,  $Re = 3 \times 10^6$ ,  $\alpha = 4^\circ$ ,  $\delta = 20^\circ$ ,  $x = 0.4$ )

Physical mechanism	$S_t$	$\frac{\Delta\phi}{\Delta z}$	$V_C$	$\lambda_z$
Interaction between 2D buffet and buffet cells ( $St = 0.090 - 0.06 = 0.03$ )	0.029	2.19	0.083	2.867
Two-dimensional buffet	0.062	0.00	0.000	$\infty$
Buffet cells convection	0.090	2.19	0.258	2.870
Interaction between 2D buffet and buffet cells ( $St = 0.090 + 0.06 = 0.150$ )	0.150	2.14	0.441	2.938
First harmonic of the buffet cells convection	0.179	4.38	0.257	1.434

Table C.3 – Summary of the convection speed and spanwise wavelength associated with specific frequencies in the pressure spectrum (OALT25,  $M = 0.7352$ ,  $Re = 3 \times 10^6$ ,  $\alpha = 4^\circ$ ,  $\delta = 30^\circ$ ,  $x = 0.4$ )

Physical mechanism	$St$	$\frac{\Delta\phi}{\Delta z}$	$V_C$	$\lambda_z$
Interaction between 2D buffet and sub-harmonic of buffet cells ( $St = 0.067 - 0.055 = 0.012$ )	0.012	1.08	0.070	5.797
Interaction between the first harmonic of two-dimensional buffet and the buffet cells convection ( $St = 0.135 - 0.112 = 0.022$ )	0.022	2.19	0.063	2.857
	0.034	3.28	0.065	1.915
Interaction between the first harmonic of two-dimensional buffet and sub-harmonic of buffet cells ( $St = 0.112 - 0.067 = 0.045$ )	0.045	-1.11	-0.255	-5.974
Two-dimensional buffet	0.055	0.000	0.000	$\infty$
Sub-harmonic of buffet cells	0.067	1.100	0.382	5.716
Interaction between 2D buffet and buffet cells ( $St = 0.135 - 0.055 = 0.08$ )	0.079	2.203	0.225	2.852
	0.090	3.304	0.171	1.902
First harmonic of two-dimensional buffet	0.112	0.002	0.000	$\infty$
Interaction between 2D buffet and sub-harmonic of buffet cells ( $St = 0.67 + 0.055 = 0.122$ )	0.122	1.100	0.697	5.712
Buffet cells convection	0.135	2.204	0.385	2.851
Interaction between 2D buffet and buffet cells ( $St = 0.135 + 0.055 = 0.19$ )	0.191	2.204	0.545	2.851

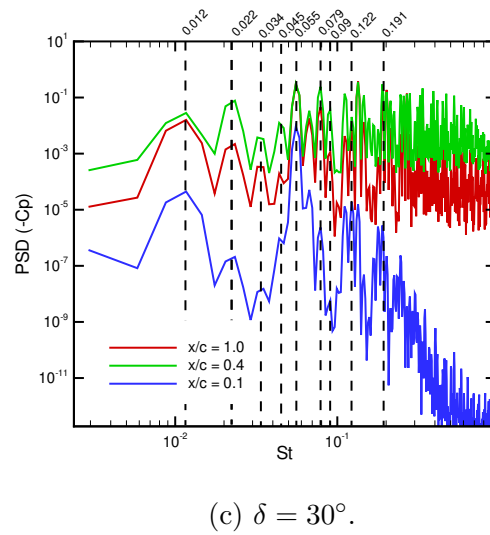
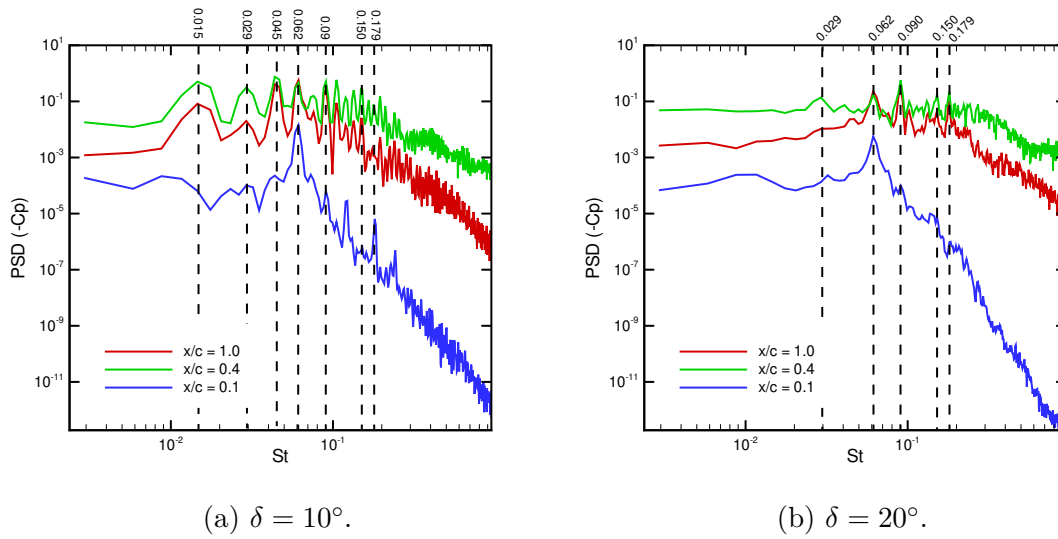


Figure C.4 – Power spectral density of the pressure coefficient at several position along the chord (OALT25,  $M = 0.7352$ ,  $Re = 3 \times 10^6$ ,  $\alpha = 4^\circ$ ,  $\delta = 10^\circ$ ).

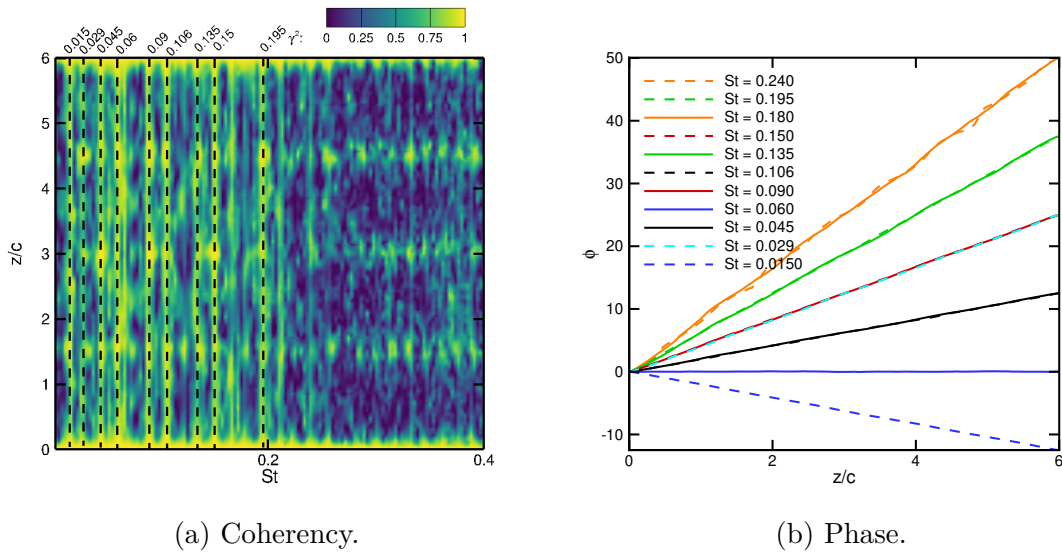


Figure C.5 – Cross-spectrum analysis for a line of sensors at  $x/c = 0.4$  (OALT25,  $M = 0.7352$ ,  $Re = 3 \times 10^6$ ,  $\alpha = 4^\circ$ ,  $\delta = 10^\circ$ ).

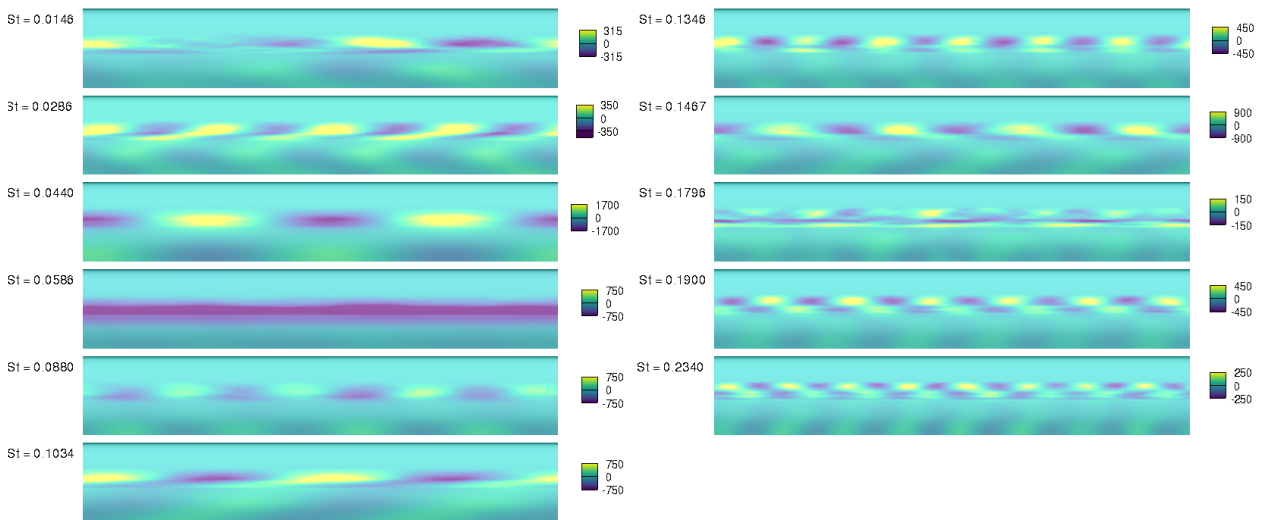
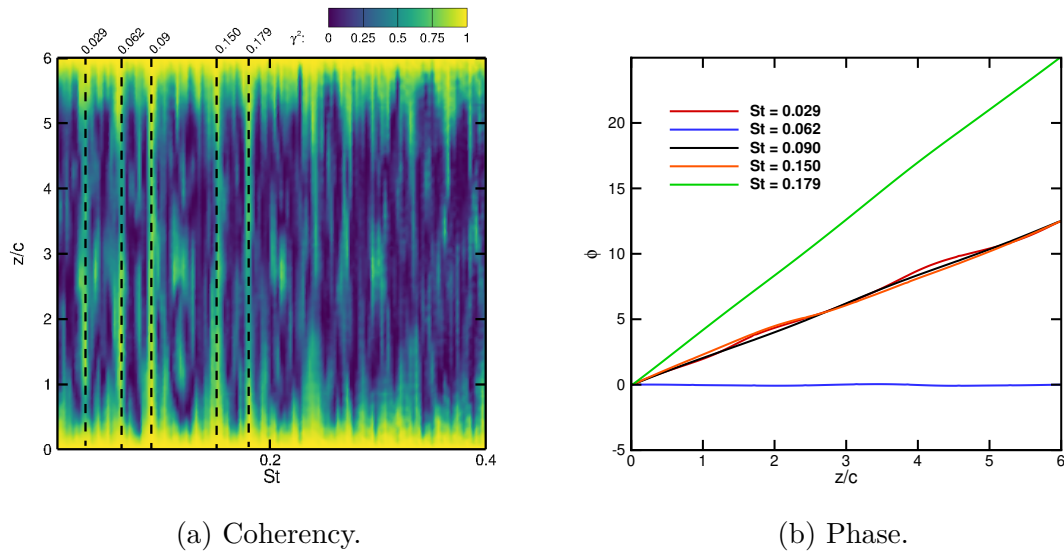


Figure C.6 – Inverse Fourier mode on the wing suction side at the dominant frequencies (OALT25,  $M = 0.7352$ ,  $Re = 3 \times 10^6$ ,  $\alpha = 4^\circ$ ,  $\delta = 10^\circ$ ).



(a) Coherency.

(b) Phase.

Figure C.7 – Cross-spectrum analysis for a line of sensors at  $x/c = 0.4$  (OALT25,  $M = 0.7352$ ,  $Re = 3 \times 10^6$ ,  $\alpha = 4^\circ$ ,  $\delta = 20^\circ$ ).

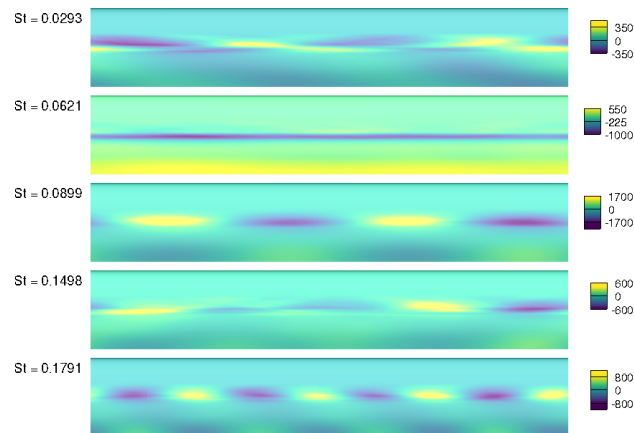


Figure C.8 – Inverse Fourier mode on the wing suction side at the dominant frequencies (OALT25,  $M = 0.7352$ ,  $Re = 3 \times 10^6$ ,  $\alpha = 4^\circ$ ,  $\delta = 20^\circ$ ).

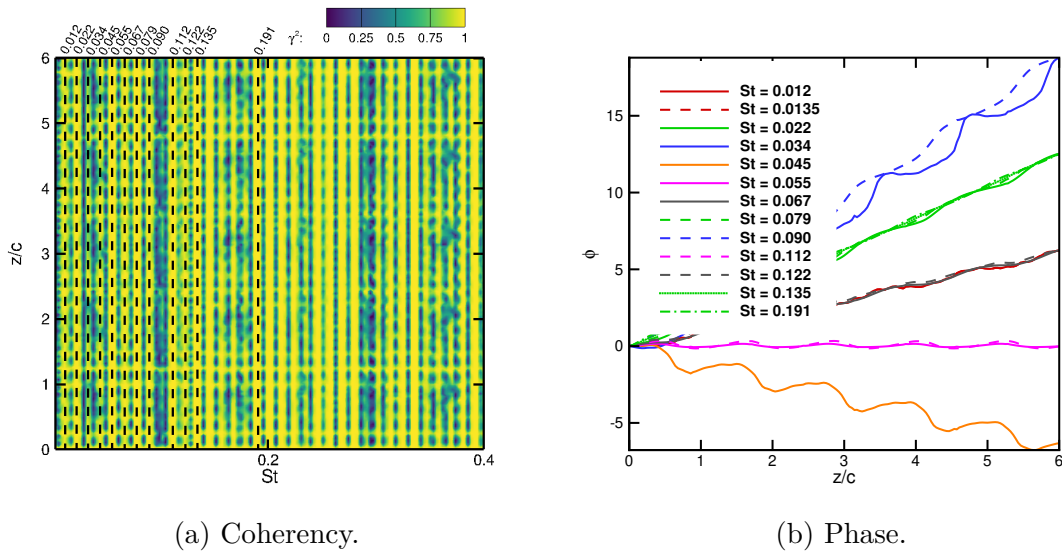


Figure C.9 – Cross-spectrum analysis for a line of sensors at  $x/c = 0.4$  (OALT25,  $M = 0.7352$ ,  $Re = 3 \times 10^6$ ,  $\alpha = 4^\circ$ ,  $\delta = 30^\circ$ ).

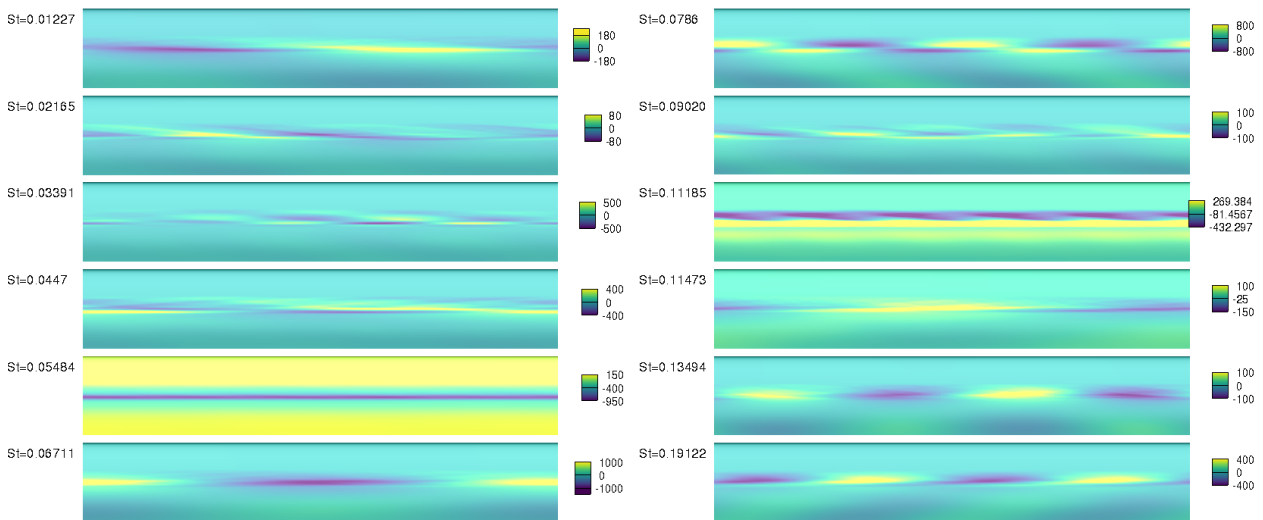


Figure C.10 – Inverse Fourier mode on the wing suction side at the dominant frequencies (OALT25,  $M = 0.7352$ ,  $Re = 3 \times 10^6$ ,  $\alpha = 4^\circ$ ,  $\delta = 30^\circ$ ).